# Proton and Positron Acceleration from Ultra-Intense Lasers

by

**Shaun Kerr**

A thesis submitted in partial fulfillment of the requirements for the degree of

**Doctor of Philosophy**

in

**Photonics and Plasmas**

**Department of Electrical and Computer Engineering**
**University of Alberta**

# Abstract

Ultra-intense lasers ($I > 10^{18}$ W/cm$^2$) irradiating solid targets can produce bright, energetic (MeV) beams of protons, with potential applications from fusion energy to tumour treatment. Spatially and spectrally controlling these particle beams remains a challenge, however, and experimental and computational work performed for this thesis seeks to address these issues.

In one typical acceleration process relativistic electrons driven by the laser form an escaping electron cloud, which accelerates protons away from the target surface, called target normal sheath acceleration (TNSA). For thick (mm), high-Z targets, positrons are generated in the target from high-energy x-rays and accelerated by the same TNSA electron cloud. Due to their low mass and rapid acceleration, positrons can act as a probe of transient field features. Experimental results from the OMEGA EP laser show multi-peak modulations developing in the positron spectra when the laser energy exceeds one kilojoule. Detailed 2D particle-in-cell simulations using the LSP code were carried out, and suggest that for high laser energies, multiple acceleration phases are present in the TNSA process and leave signatures in the positron spectrum. They also give insight into the influence of the proton contaminant layer and target geometry on the positron acceleration process.

Experimental work was also done to demonstrate an alternative acceleration mechanism - collisionless shockwave acceleration (CSA) - which could

offer better control of the proton beam spectrum. CSA occurs when plasma pressure drives an electrostatic shock that reflects ions ahead of it, generating quasi-monoenergetic ion beams. The CSA experiment was performed using the ultra-intense, $\lambda = 1.054\,\mu\text{m}$ Titan laser at the Jupiter Laser Facility. Near-critical density targets were used to maximize laser coupling, while tailored density profiles on both the front and rear sides of the target were necessary to create a shock and inhibit the strength of TNSA fields that would obscure the CSA spectrum. Density shaping was achieved experimentally by using a nanosecond beam to expand Mylar foils, and a carefully timed, ultra-intense picosecond pulse to drive shocks in the decompressing foils at the optimal density profile. Narrow energy spread proton and ion beams were observed using an Imaging Proton Spectrometer (IPS), with characteristics consistent with generation from CSA. This is believed to be the first observation of highly energetic ($\gg 1$ MeV) proton beams from CSA with a $\lambda = 1.054\,\mu\text{m}$ laser.

# Preface

This thesis is an original work by Shaun Kerr. Some of the research conducted for this thesis was done in collaboration with researchers from the University of Alberta, Lawrence Livermore National Laboratory (LLNL), and other institutions and universities. The introduction in Chapter 1, theoretical background in Chapter 2, discussion of experimental techniques in Chapter 3, simulation background in Chapter 4, computational study in Chapter 6, ion data analysis in Chapter 7 and conclusion in Chapter 8 are my original work. They were written by myself and edited by Professor Robert Fedosejevs. For the shock acceleration work in Chapter 7 I was responsible for collecting and analyzing the ion data, which was the key result of the project.

Chapter 5 discusses the analysis techniques I developed and used for the Imaging Proton Spectrometer (IPS) data. The experimental and computational tests of the IPS modulations described in Appendix A were designed and performed by me, with the exceptions of the foil test and data collected by Professor Louis Willingale, Dr. Hui Chen and Dr. Andrew Hazi (as noted in the text). The IPS was designed by Dr. Chen [1]. Dr. Hazi provided extensive guidance in the operation and usage of the diagnostic. The data dewarping technique originated with Dr. Arthur Pak. Assistance with the diagnostic analysis was provided by Prof. Fedosejevs, Dr. Hazi and Dr. Pak.

The particle-in-cell (PIC) simulation studies in Chapter 4 and Chapter 6 were performed by me. The analysis of the results and conclusions are mine, with input from Prof. Fedosejevs, Dr. Chen and Dr. Anthony Link. I heavily modified a simulation setup provided by Dr. Link. Dr. Link also generated the initial electron source used in those simulations from laser-plasma PIC simulations he performed. The PIC code used, LSP, was developed by Voss Scientific, LLC, and modified by Ohio State University and Dr. Link. This computational investigation was motivated by experimental data collected by

Dr. Chen, Gerald Jackson Williams and Jaebum Park at the OMEGA EP laser facility in the Laboratory for Laser Energetics. This data was published in the manuscript: H. Chen, A. Link, Y. Sentoku, P. Audebert, F. Fiuza, A. Hazi, R. F. Heeter, M. Hill, L. Hobbs, A. J. Kemp, G. E. Kemp, S. Kerr, D. D. Meyerhofer, J. Myatt, S. R. Nagel, J. Park, R. Tommasini, and G. J. Williams, "The scaling of electron and positron generation in intense laser-solid interactions", Phys. Plasmas **22**, 056705 (2015). My contribution to this manuscript was collecting and analyzing experimental data at the Titan laser, which was not included in this thesis.

The experiments described in Chapter 7 were performed at the Jupiter Laser Facility at LLNL. The data reported has been submitted for publication as A. Pak, S. Kerr, N. Lemos, A. Link, P. Patel, F. Albert, L. Divol, B. B. Pollock, D. Haberberger, D. Froula, M. Gauthier, S. H. Glenzer, A. Longman, L. Manzoor, R. Fedosejevs, S. Tochitsky, C. Joshi, and F. Fiuza, "Collisionless shock acceleration of narrow energy spread ion beams from mixed species plasmas using 1 µm lasers". I was responsible for fielding the Imaging Proton Spectrometer (IPS), the primary ion diagnostic, and I collected, analyzed and helped interpret the IPS data. I also assisted with other aspects of the experimental setup and data collection, along with the experimental team of A. Pak, N. Lemos, A. Link, M. Gauthier, A. Longman, and L. Manzoor. The original concept was proposed by Dr. Fiuza in [2]. The experiment was designed and guided by Dr. Pak, who was also responsible for the manuscript composition. The remaining authors aided in experimental design, data interpretation and the manuscript text. The HYDRA hydrodynamic simulations were performed by A. Link, and the PIC simulations shown in the chapter figures were performed by F. Fiuza. The LSP PIC simulation for escaping and trapped hot electrons described in the chapter was setup by A. Link; I ran it and analyzed the output.

# Acknowledgements

I would first like to thank my supervisors, Professor Robert Fedosejevs at the University of Alberta and Dr. Hui Chen at Lawrence Livermore National Laboratory (LLNL), for the mentorship, expertise, and opportunities they provided me. I first heard Professor Fedosejevs discuss fusion energy in a 2$^{nd}$ year undergraduate lecture, and ever since the idea has fascinated me. As an advisor he gave me the chance to work at the forefront of the field, and I strive to meet his standards of scientific excellence, hard work, and diligence in everything I do. Dr. Chen generously agreed to supervise an unknown 1$^{st}$ year graduate student on one of her experiments, and then more generously allowed me to continue be involved with her work in the years since. She opened my eyes to topics and possibilities I would never have known otherwise.

I have had the good fortune to work with and learn from many people at Lawrence Livermore National Laboratory. My experimental work would not have been possible without the support of the Jupiter Laser Facility staff over many (many) experimental campaigns, and I would like to thank Scott Andrews, Jim Bonlie, Carl Bruns, Chuck Cadwalader, Bob Cauble, Rob Costa, Gary Freeze, and Beth Mariott for their patience and help. I would like to thank Andy Hazi for mentoring me, and sharing his deep understanding of the Imaging Proton Spectrometer and physics in general. I am grateful to have worked closely with Art Pak for the collisionless shock work; I learned much from him about perseverance and the scientific method. Without the guidance of Anthony Link, in both experiments and LSP simulations, I never would have made the progress I did. I would like to thank Scott Wilks for his insight and feedback on my simulation work, Gregory Elijah Kemp for offering me time on his experiment, and Harry McLean for hosting my stay at LLNL. I am grateful to my collaborators Nicolai Brejnholt, Drew Higginson, Andreas Kemp, Nuno Lemos, Tammy Ma, Derek Mariscal, Sabrina Nagel and Prav Patel. Lastly,

I want to thank my fellow (ex) students, Edward Marley, Jaebum Park, and Gerald Jackson Williams for their friendship and collaboration over the years of grad school. In particular, I want to thank Jaebum and his family for inviting me into their home and introducing me to Oakland.

At the University of Alberta I would like to thank Professor Ying Tsui and Dr. Henry Tiedje, and my colleagues Zhijiang Chen, Chandra Curry, Hal Friesen, Andrew Longman, Laila Manzoor, Raj Masoud, Mianzhen Mo, and Travis Schoepp. In particular, Mianzhen's guidance and companionship throughout my degree was vastly appreciated.

One of the highlights of this degree has been working with many great people from an array of institutions. From SLAC I would like to thank Frederico Fiuza for guiding the shock acceleration project, as well as Maxence Gauthier. I would like to thank Joohwan Kim, Chris McGuffey, Jonathan Peebles and Professor Farhat Beg from UCSD, Matt Hill at AWE, Daniel Barnak at the University of Rochester, Mario Manuel and Mingsheng Wei at General Atomics, and Hiroshi Sawada at the University of Nevada, Reno. Professor Joao Jorge Santos at the University of Bordeaux allowed me to participate in his fascinating and challenging work, and I would like to thank him and his protégés Xavier Vaisseau and Pierre Forestier Colleoni. I would also like to thank Alessio Morace at the University of Osaka for enlivening the field.

Finally, I want to thank my family for supporting me no matter where in the world I was. Without the support of my parents, John and Pat Kerr, my siblings, Laura and Daniel, and my grandmother, Charlotte, I would not have completed this journey.

# Contents

# List of Tables

# List of Figures

# List of Abbreviations

| | |
|---|---|
| ASE | Amplified Spontaneous Emission |
| BOA | Breakout Afterburner |
| CPA | Chirped Parametric Amplification |
| CSA | Collisionless Shock Acceleration |
| EPPS | Electron Proton Positron Spectrometer |
| FI | Fast Ignition |
| FWHM | Full Width Half Maximum |
| HED | High Energy Density |
| ICF | Inertial Confinement Fusion |
| IP | Image Plate |
| IPS | Imaging Proton Spectrometer |
| LLNL | Lawrence Livermore National Laboratory |
| LP | Long Pulse (nanosecond duration) |
| LPI | Laser Plasma Interaction |
| OPCPA | Optical Parametric Chirped Pulse Amplification |
| PIC | Particle in Cell |
| PM | Plasma Mirror |
| PSL | Photo Stimulated Luminescence |
| RPA | Radiation Pressure Acceleration |
| SP | Short Pulse (picosecond duration) |
| SLAC | SLAC National Accelerator Laboratory (Stanford) |
| SR | Steradian |
| TCC | Target Chamber Centre |
| TP | Thomson Parabola |
| TNSA | Target Normal Sheath Acceleration |

| | |
|---|---|
| ps | picosecond ($10^{-12}$ second) |
| fs | femtosecond ($10^{-15}$ second) |
| keV | Kiloelectronvolt ($10^{3}$ eV) |
| MeV | Megaelectronvolt ($10^{6}$ eV) |
| GeV | Gigaelectronvolt ($10^{9}$ eV) |
| $1\omega$ | 1054 nm wavelength light |
| $2\omega$ | 527 nm wavelength light |

# Chapter 1
# Introduction

Beams of energetic protons have many applications, ranging from ultrafast imaging of fields in high energy density (HED) physics to radiotherapy and isotope generation in health care. Interest in protons is driven by their characteristic energy deposition curve, known as a Bragg peak, whereby protons lose energy primarily at the end of their range. This peak is illustrated in Figure 1.1. Energetic protons also tend to travel ballistically through the majority of their range of travel, as efficient collisions with nuclei are rare; consequently proton beams are relatively insusceptible to scattering. In contrast, photons deposit the majority of their energy at the start of their path, while electrons scatter significantly in matter. As many applications require beam dose to be delivered to a specific location, these properties make proton beams highly desirable and advantageous. The chief applications of proton beams are outlined in this chapter. The experimental work reported for this Ph.D aimed to demonstrate a novel acceleration mechanism that would allow greater spectral control of laser-generated proton beams, enhancing their applicability to these applications.

Positrons, the antimatter counterpart to electrons, are produced in copious amounts and accelerated to relativistic energies in ultra-intense laser-matter interactions. They are of interest both for fundamental physics, such as understanding astrophysical phenomena, and as a probe of the complex accelerating fields that occur in laser-matter interactions. Most work to date has focused on the first application, with beams of relativistic, laser-generated positrons potentially giving insight into similar beams believed to exist in gamma-ray bursts, among other astrophysical processes. The use of positrons as a probe

relies on their light mass (relative to protons and heavier ions) which allows them to undergo rapid acceleration and experience transient field features. This novel probe application of laser-generated positrons was explored using detailed simulations that were matched to experimental results.

## 1.1 Applications of Energetic Proton Beams

### 1.1.1 Bragg Peak

The average energy loss of a beam of charged particles in matter, known as its stopping power $S$, is governed by the Bethe-Bloch equation [37, 38]. It is typically normalized by the mass density, $\rho$, of the target material to give the form:

$$\frac{S}{\rho} = -\frac{\mathrm{d}E}{\rho \mathrm{d}x} \tag{1.1}$$

$$= 4\pi N_A r_e^2 m_e c^2 \frac{Z}{A}\frac{z^2}{\beta^2}\left[\ln\frac{2m_e c^2\gamma^2\beta^2}{I} - \beta^2 - \frac{\delta}{2} - \frac{C}{Z}\right] \tag{1.2}$$

where $E$ is the mean energy loss, $x$ is the distance travelled, $N_A$ is Avogadro's number, $r_e = e^2/4\pi\epsilon_0 m_e^2$ is the classical electron radius, $m_e$ is the mass of an electron, $Z$ is the atomic number of the material, $A$ is the atomic weight of the material, $z$ is the charge of the incident particle, $\beta = v/c$ is the normalized velocity of the particle, $\gamma = 1/\sqrt{(1-\beta^2)}$ is the Lorentz factor, $I$ is the mean excitation potential of the material, $\delta$ is the correction factor from electron shielding and $C$ is the shell correction item. From Equation (1.2) can be seen that $S \propto 1/v^2$, which indicates that as the proton slows its stopping increases dramatically. This dependency gives rises to the Bragg peak.

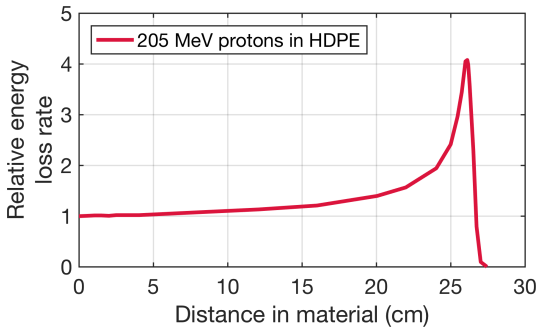


Figure 1.1: The energy loss curve for 250 MeV protons in high density polyethylene (HDPE). The signature Bragg peak is evident. From [3].

### 1.1.2 Proton Radiography

The most widely used application of laser-produced protons to date has been as an innovative diagnostic for other laser-plasma experiments, called proton radiography or deflectometry [39, 40, 41, 42]. A laser-generated proton beam is directed towards the primary laser-plasma interaction (LPI) region, where the protons are deflected by the Lorentz and electrostatic forces from the time-varying electromagnetic fields and an imprint is made in the spatial distribution of the beam. By recording this proton signal, either as imprint pits on CR-39 plastic film or on radiochromic film (RCF - see Section 3.2.3) high spatial resolution images of the interaction fields can be captured.

The proton radiography beam can be generated either through long pulse driven De$^3$He and DD fusion reactions [43], or short pulse target normal sheath acceleration (TNSA - see Section 2.3) [40]. The fusion approach yields well controlled, monoenergetic beams of 14.7 and 3 MeV protons, but has a low flux due to its isotropic nature and can only be fielded at large scale laser facilities. The yield into $4\pi$ steradians is $\sim 10^9$ protons at OMEGA [43] and $\sim 10^{10}$ protons at NIF [44], giving $8 \times 10^7$ and $8 \times 10^8$ protons/steradian, respectively. TNSA beams, in contrast, are highly directional, have a broad energy spectrum and can be generated at smaller scale, short pulse laser facilities. Yields reach $10^{10}$ protons in a $\sim 40^\circ$ full cone opening, giving an order of magnitude

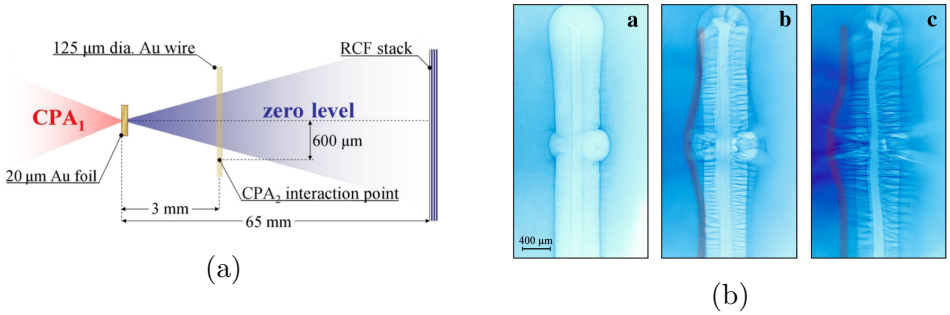


Figure 1.2: Examples of proton radiograph, showing sheath field instability formation along a wire target. (a) Setup, with 'CPA' indicating an intense short pulse generating the TNSA proton beam. (b) Proton RCF images for a) ∼10 ps, b) ∼30 ps, and c) ∼50 ps. Images from [4, 5].

improvement in flux. The broadband source energy allows time-resolved images of fields to be captured in RCF stacks through the time of flight effect. The beam is laminar, with a slight divergence, and can be treated as coming from a virtual point source behind the generation target. The desired image magnification, therefore, is achieved simply by setting the correct distances between the source, target, and detector. Examples of an experimental setup and radiography images from [4, 5] are shown in Figure 1.2.

### 1.1.3 Radioisotope Generation

Radioisotopes are a critical component of medical imaging, with the most commonly used isotope, Technetium 99m ($^{99m}$Tc), given to millions of patients each year [45]. Currently over 90% of the world's supply of $^{99m}$Tc comes from five nuclear reactors, most of which are nearing the end of their lifespans. The largest production facility, the National Research Universal reactor in Chalk River, Ontario, Canada, is scheduled to close in March 2018 [46]. The expense and safety considerations of constructing nuclear reactors has led to extensive interest in alternative approaches to isotope generation [47].

Laser-generated protons offer another potential approach to isotope generation, as they produce protons of sufficient energy (5-30 MeV) and flux to

generate macroscopic quantities of isotopes, such as $^{99m}$Tc from molybdenum-99 [45]. In an experiment performed at the Vulcan Petawatt Laser Facility, 50 J of laser energy in 0.5 – 1 ps pulses were used to generate 8.25 kBq of radioactivity from a TNSA proton beam onto a secondary Mo target. For an enriched, 99.54% pure Mo target it was calculated that 85.3 kBq would be produced, and ∼1 GBq in 20 minutes with a 10 Hz laser [45]. Current laser systems are unsuitable for practical isotope production due to their low shot rate, but high repetition rate, diode-pumped systems are in development [48, 49] and could be competitive with cyclotron production within a decade [45]. The ultimate goal would be a table-top system that could be widely used and replace the centralized production facilities currently used.

Laser driven proton beams can also be used to generate the short-lived isotopes used in positron emission tomography (PET), such as $^{11}$C, $^{13}$N, $^{15}$O and $^{18}$F. The half lives of these isotopes is between 20 – 120 minutes, making on-site, real-time production necessary [50]. Production of $^{11}$C and $^{13}$N from lasers has been demonstrated [50, 51], but higher repetition rate lasers are necessary for practical application.

### 1.1.4 Proton Radiotherapy

The localized energy deposition of the Bragg peak makes protons the ideal particle for treating cancers near critical regions such as the brain or eye [52], as well as minimizing dose to avoid long-term effects in children with cancers [53]. As can be seen in Figure 1.3, traditional radiation therapy particles such as x-rays have a very broad energy deposition compared to protons, which is non-ideal [6]. 'Hadrontherapy' using protons is currently available only at specialized cyclotron-based facilities which are extremely expensive to construct ($100–225 million); consequently the number of these facilities worldwide is limited [54]. Laser-based facilities have the potential to be much more cost-effective, and therefore more widely available.

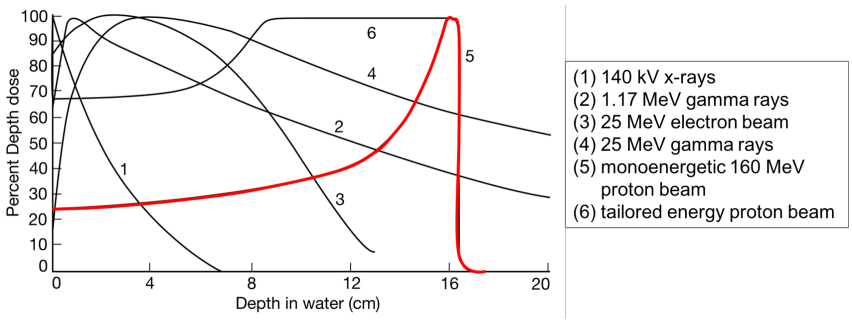


Figure 1.3: Depth dose distributions for a variety of particle beams. The proton radiotherapy, highlighted in red, delivers more localized energy deposition. From [6].

The ideal proton radiotherapy beam is monoenergetic, very high energy (up to ∼250 MeV) and tunable; this allows penetration of deep tissue ($> 20$ cm) and controlled location of deposition [6]. Traditional accelerators (cyclotrons and synchrotrons) produce proton beams with energy spreads of $\Delta E/E \approx 0.1\%$ [55]. The particle energy from synchrotrons can be controlled directly by the guiding magnetic field; cyclotrons can produce only a single energy range, and therefore energy tuning is achieved by energy loss in foils and energy-selecting transport systems. The typical spectrum from TNSA is broadband and limited in maximum energy to ∼90 MeV, and therefore not very favourable for this application. Typical treatment doses are on the order of ∼1 Gy in $1-3$ minutes; this corresponds to $10^{12}$ protons total or $10^{10}$ protons per second (∼2 nA) [55]. Such levels are easily achievable with accelerators, but represent a challenge for laser-based sources. TNSA can produce up to $10^{10}$ protons per shot, but without the energy selection, beam focusing or repetition rates necessary to reach $10^{10}$ protons/second on target. The shot-to-shot consistency of TNSA sources to date has also been very poor, while radiotherapy demands a ∼5% variation for dose control.

Meeting the requirements of radiotherapy with laser-based sources is very challenging, and necessitates large advances in both acceleration techniques and laser and target technology. Conventional TNSA is unsuited for this

purpose, but other proton acceleration mechanisms are being explored that could potentially deliver much improved beam characteristics (see Section 2.4 and Chapter 7). In all cases a high repetition rate laser will be necessary to deliver the required dose in a reasonable amount of time. Diode-pumped laser systems, operating at up to 10 Hz, are very promising for this reason [48, 49]. High rep-rate targets such as liquid jets [56] or liquid crystal films [57] must be developed in parallel.

## 1.2 Inertial Confinement Fusion

Stars, through their immense mass and gravitational fields, can reach the pressures and temperatures necessary for fusion naturally. Mankind, however, must use cleverer schemes to create fusion energy on Earth. The challenge is confining an extremely hot plasma long enough for fusion reactions to occur and propagate as a chain reaction within the fuel. Research into fusion energy is divided into two approaches: (1) Magnetic confinement fusion confines the burning plasma with magnetic fields, typically in a donut-shaped device called tokamak. (2) Inertial confinement fusion (ICF) heats a plasma to fusion temperatures and pressures over such a small timescale that the inertia of the fuel itself provides confinement.

ICF can be achieved in a controlled manner using lasers, which can transfer MJ of energy to a mm-scale target within nanoseconds. Even these small spatial and temporal scales, however, are not enough to overcome the thermal and radiation losses of a plasma at keV-temperatures. Consequently, central hot spot ignition has been developed [58]. In this approach only a small central volume at the core of a spherically imploding target reaches fusion temperatures and densities. Once fusion reactions start occuring, $\alpha$-particles from deuterium-tritium (DT) fusion heat the remaining bulk of the fuel and achieve a full burn.

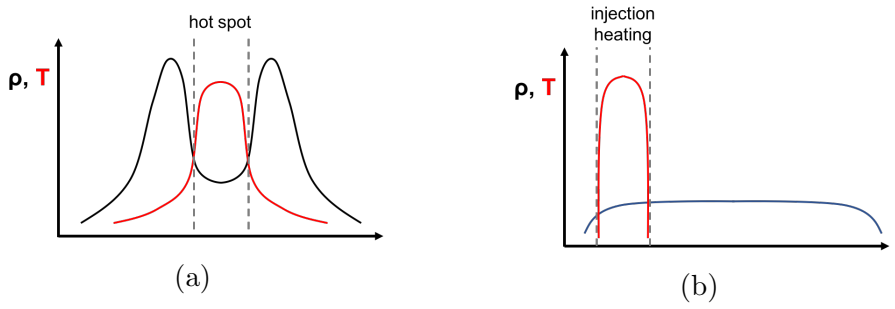


Figure 1.4: Illustrations of temperature and density spatial profiles for compressed fuel cores in (a) the isobaric, central hot spot ICF approach and (b) the isochoric, fast ignition approach. In (a) the central hot spot has a low density relative to the outer core but a higher temperature. For fast ignition in (b) the density is relatively constant and the heating is localized at the ignitor interaction region.

The central hot spot is a region of low density, high temperature plasma, and is in pressure equilibrium with the high density, low temperature bulk target plasma. This is the isobaric model [59]. The density and temperature profiles of the central hot spot in this model are plotted in Figure 1.4a. For ignition a central hot spot temperature of $\geq 5$ keV is required with an areal density $\rho r = 0.3 - 0.4$ mg/cm$^2$; this is determined by the range of 3.5 MeV fusion $\alpha$-particles, which must be stopped within the compressed fuel to achieve self-heating. The core must reach a pressure of $\sim$200 Gbar and a maximum density $\rho \geq 200$ g/cm$^3$. The density value is set by the gain requirement: sufficient fuel must be present and a large enough fraction must be burned (20–30%) for break-even, $E_{\text{out}} \geq E_{\text{in}}$ [60].

### 1.2.1 Proton Fast Ignition

An alternate to the central hot spot approach, known as fast ignition (FI), proposes using an intense, short pulse laser to spark the fusion reaction of an imploding fuel capsule. Decoupling the compression and heating steps greatly relaxes the compression requirements, and allows the hot spot and the surrounding fuel to be out of pressure equilibrium [61]. This is the isochoric

model of ICF. FI requires significantly lower stagnation pressure, which in turn allows for much slower and more stable implosion velocities. Mixing of fuel and ablator shell material in the hot spot, the bane of traditional ICF because it reduces the temperature of the hot spot, is of reduced importance since the critical heating step is transferred to the ignitor beam.

The hydrodynamic disassembly time of the compressed fuel core is $10-40$ ps, and the ignitor beam must have a corresponding duration [62]. For a reference density of $\rho = 300$ g/cm$^3$, optimistic 1D models indicate that $10-20$ kJ of energy must be deposited in the core. The hot spot temperature must reach $\sim$10 keV, and the beam spot size must be on the order of the compressed core size, $10-40$ µm. Compared to hot spot ignition the gain could increase by $2-10\times$, due to both increased fuel mass in the target and reduced compression energy [61, 63].

The challenge with FI is effectively coupling ignitor laser energy to the fuel core. Electrons are directly and efficiently accelerated by the laser, but occur in highly divergent, overly energetic beams that couple inefficiency to the dense core (electron energies of 0.5 – 1 MeV are necessary to stop in the core, while typical energies from ultra-intense LPI are 1 – 100 MeV). These issues substantially increase the ignition parameters given above. In contrast, protons deposit energy readily in their Bragg peak, can be focused with careful target design [64] and could feasibly be used for FI with a range of energy distributions [65].

The parameters for proton FI in the ideal case (flat spatial and temporal profiles) were given in Roth *et al.* [7] using a compressed core profile from [63]. Here $E_{\text{opt}}$ is beam energy, $t_{\text{opt}}$ is pulse duration and $r_{\text{opt}}$ is beam spot radius.

$$E_{\text{opt}} = 140/\hat{\rho}^{1.85} \text{ kJ} \tag{1.3}$$

$$t_{\text{opt}} = 54/\hat{\rho}^{0.85} \text{ ps} \tag{1.4}$$

$$r_{\text{opt}} = 60/\hat{\rho}^{0.97} \text{ µm} \tag{1.5}$$

where $\hat{\rho} = \rho/(100\text{g/cm}^3)$. Proton energies of 15 – 23 MeV were assumed, which are readily within the energies possible with current laser systems. The deposition curves in the core are plotted in Figure 1.5a.

Conversion efficiency and beam divergence are critical for the success of proton fast ignition. Simulations that take into account realistic beam properties and target geometries have indicated up to 20 kJ of energy in protons is required [8]; the ignitor laser energy could then approach 400 kJ for a relatively high conversion efficiency of 5%. Increasing the conversion efficiency from laser to proton energy is critical to driving down this pulse energy. Likewise, controlling the proton beam divergence is highly important for coupling to the target core and reducing the drive requirements. Understanding the electric field behaviour on the proton target is the first step to controlling beam divergence.

## 1.3 Laboratory Astrophysics

The ability of high power lasers to generate high-energy-density systems has opened up the study of astrophysical phenomena in the laboratory [66]. Most work in this area has focused on nanosecond interactions, with investigations of magnetic field generation from Weibel instability in intermingling plasmas [67] and equations of state relevant to stellar bodies [68]. Ultra-intense, short pulse lasers open the possibility of exploring relativistic plasmas and pair production, which are relevant to extreme astrophysical events.

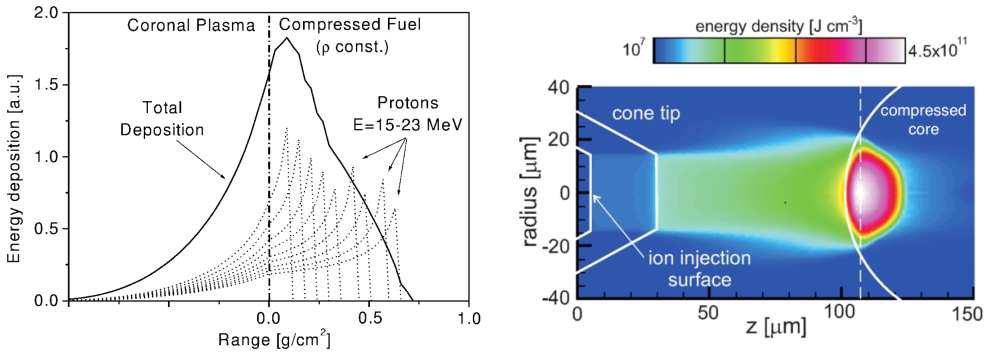


(a) (b)

Figure 1.5: (a) Energy deposition curves for protons in a compressed fuel core, in a 1D model. The range of initial proton energies allows the full core region to be irradiated. From [7]. (b) Energy deposition isocontours from a 2D simulation with a realistic injection cone and core plasma. Beam divergence has a large effect on energy deposited. From [8].

### 1.3.1 Fireball Model of Gamma-ray Bursts

One such event is a cosmic fireball, as is believed to occur for neutron star mergers or black holes but has never been studied in the laboratory. The fireball model was introduced to account for astronomical observations of gamma-ray bursts, which show photons with up to 100 MeV energies and a power-law distribution, $N(E)dE \sim E^{-2}dE$. This non-Planckian distribution indicates that the source plasma is not optically thick, yet MeV photons should produce pairs in the reaction $\gamma\gamma \rightarrow e^{-}e^{+}$ such that the region is no longer optically thin [66]. The resolution to this "compactness problem" is to have the source plasma moving at relativistic velocities towards the observer. In this case the photons are blue-shifted to the observed high energies $h\nu_{obs}$ in the observer frame, while in the source frame their energy is reduced by a Lorentz factor $h\nu_{obs}/\gamma$, pair production is reduced, thermalization occurs through the Compton process and the plasma remains optically thin [69]. The relativistic shock that characterizes this process is expected to undergo Weibel filamentation. The growth rate of this process, and the various processes it can mediate such as collisionless shock formation and particle acceleration [70] have motivated

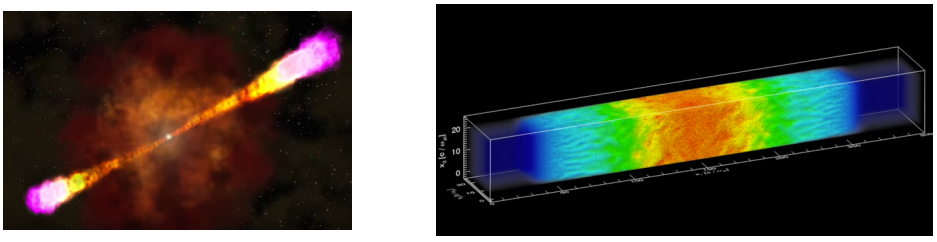

(a) (b)

Figure 1.6: (a) Rendering of cosmic gamma ray burst. (b) Simulated electron-positron jet. From the Michigan Institute for Plasma Science and Engineering.

investigation.

Work by Chen *et al.* shows that laser-produced positrons form energetic, dense and directional plasmas that could be uniquely suited for studying the relativistic fireball model [23, 71, 72]. The challenge is achieving a positron density comparable to the electron density, as positron generation is a secondary process and has several orders less particles. Different target geometries have been used to get comparable densities in localized regions [73], but a true relativistic, neutral beam of electrons and positrons has not yet been realized. It was observed that positron production has a non-linear scaling with laser energy, $N_{e+} \propto E_L^2$, while electron production scaling is linear, $N_{e-} \propto E_L$ [72]. These favourable rates suggest that with 10 kJ class lasers such as ARC on NIF [74] and LFEX on Gekko [75] it will be possible to create relativistic, equal density electron-positron plasmas with $N_{e+} \approx 10^{14}$. While the present intensities of these laser systems limits their ability to generate positrons, future upgrades and modifications such as focusing plasma mirrors [76] could overcome this limitation.

# Chapter 2
# Physics of LPI and Particle Acceleration

The physics of particle acceleration from short pulse laser-plasma interactions is multi-stage and multi-process, and therefore a wide variety of phenomenon must be introduced. This chapter is structured as follows: First general plasma physics relevant to ultra-intense laser-plasma interaction (LPI) is covered. The various mechanisms that produce relativistic, 'hot' electrons are then discussed. Finally the details of ion acceleration are reviewed.

## 2.1 Ultra-intense LPI

The electric field of a laser with $I = 1 \times 10^{19}$ W/cm$^2$ is on the order of $10^{12}$ V/m, which is sufficient to quickly ionize the surface of a target through field ionization. A plasma several times the critical density, $n_{\text{crit}}$, is generated, and a standing wave is formed with an evanescent component penetrating to a skin depth of $l_s = \sim c/\omega_{\text{plasma}}$. Here $n_{\text{crit}}$ is defined in Equation (2.1), $c = 2.998 \times 10^9$ m/s is the speed of light and $\omega_{\text{plasma}}$ is the plasma frequency, defined in Equation (2.2). For a plasma in local thermal equilibrium (LTE) the ionization state can be determined statistically using the Saha-Boltzmann equation [77]. Plasmas produced with short pulse lasers, however, are typically in non-LTE states due the rapidly varying fields and spatial gradients (density, temperature) involved. In this case non-trivial rate equations must be solved to determine the ionization state [78].

Electron acceleration varies as the plasma density changes from underdense, where the laser light can propagate, to overdense, where the pulse is reflected. The critical density that defines the transition from underdense to

overdense regions is given by:

$$n_{\text{crit}} = \frac{m_e \epsilon_0 \omega_{\text{laser}}^2}{e^2} \tag{2.1}$$

where $m_e = 9.109 \times 10^{-31}$ kg is the mass of an electron, $\epsilon_0 = 8.854 \times 10^{-12}$ F/m is the permittivity of free space, $\omega_{\text{laser}}$ is the frequency of the laser and $e = 1.602 \times 10^{-19}$ C is the fundamental charge. Physically this corresponds to the density at which the laser frequency equals the plasma frequency, $\omega_{\text{laser}} = \omega_{\text{plasma}}$, and the plasma response can negate the incident light. The plasma frequency is given by:

$$\omega_{\text{plasma}} = \left( \frac{e^2 n_e}{\epsilon_0 m_e} \right)^{1/2} \tag{2.2}$$

where $n_e$ is the electron density. The laser will penetrate the underdense plasma until it reaches the critical surface, where $n_e = n_{\text{crit}}$. For many of the cases outlined in this thesis the nanosecond prepulse of a $\lambda = 1054$ nm ($1\omega$) beam will create a large, 10's µm underdense plasma [79]. When the laser pulse has very low prepulse, such as with a frequency-doubled, $\lambda = 527$ nm ($2\omega$) beam or with a plasma mirror, the underdense preplasma region will be small (typically $\ll 10\,\mu$m) and the main pulse interacts primarily with the overdense target surface.

When the quiver velocity of an electron – the velocity it reaches in an oscillating electric field – approaches the speed of light, the beam is said to be relativistic. At these high intensities, the normalized laser amplitude is often cited:

$$a_0 = \frac{v_{\text{osc}}}{c} = \frac{eE_0}{m_e c \omega_0} \tag{2.3}$$

where $v_{\text{osc}} = eE_0/m_e\omega_0$ is the peak velocity of an electron in an oscillating electric field, $E_0$, in the non-relativistic case $a_0 < 1$. The relativistic regime corresponds to $a_0 > 1$. For a $\lambda \approx 1\,\mu$m wavelength laser such as Titan at $1\omega$

an intensity of $I_0 = 1.4 \times 10^{18}$ W/cm$^2$ gives $a_0 = 1$; for frequency-doubled $2\omega$ ($\sim$0.5 µm) the necessary intensity is $I_0 = 5.4 \times 10^{18}$ W/cm$^2$. At these intensities the electrons can be accelerated to relativistic velocities within a single laser cycle. As the electron motion becomes relativistic its effective mass increases by the Lorentz factor, $\gamma = 1/\sqrt{1 - v^2/c^2}$, and the interaction of the laser with the plasma becomes modified. The time averaged Lorentz factor is $\hat{\gamma} = \sqrt{1 + v_{\text{osc}}^2/2c^2} = \sqrt{1 + a_0^2/2}$, and the critical density is increased by this factor, $n'_{\text{crit}} = \hat{\gamma} n_{\text{crit}}$. This effect, known as 'relativistic transparency', allows ultra-intense lasers with $a_0 > 1$ to penetrate further into plasmas than classical theory would predict.

The refractive index of a plasma is:

$$n_r = \sqrt{1 - \frac{\omega_{\text{plasma}}^2}{\omega^2}} \tag{2.4}$$

For electrons moving at relativistic velocities the plasma frequency is reduced by the average Lorentz factor, $\omega_{\text{plasma}}^2 \rightarrow \omega_{\text{plasma}}^2/\hat{\gamma}$. As a result the refractive index $n_r$ increases locally at the intense centre of the laser beam, and there is a positive lensing effect that can focus the laser [80].

## 2.2 Hot Electron Generation

A population of relativistic, super-thermal electrons is generated in intense laser-plasma interactions. These 'hot electrons' arise from a variety of mechanisms depending upon the plasma and laser conditions involved, and the dominant effect can be difficult to isolate in an experimental setting. Nonetheless, as energetic electrons are the drivers and intermediaries for the other phenomena that occur with intense LPI, a grasp of the processes involved is crucial to understanding the field. The primary mechanisms are outlined here.

### 2.2.1 Collisional Absorption

For non-relativistic laser intensities ($a_0 < 0$) collisional absorption, or inverse bremsstrahlung, occurs in underdense plasmas. The laser couples directly to the electrons via the oscillating electric field, which transfer thermal energy to ions through collisions. At high intensities these processes are essentially multiphoton since the energy transferred is much more then the energy of a single photon [81]. The electron-ion collisions heat the plasma, and the absorption coefficient scales according to the equation:

$$\kappa_{ib} \propto \frac{Z n_e^2}{T_e^{3/2}(1 - n_e/n_{\text{crit}})^{1/2}} \tag{2.5}$$

where $T_e$ is the electron temperature. The strong inverse dependence on $T_e$ means that as a plasma is heated, inverse bremsstrahlung becomes less important [82]. For typical short pulse laser interactions the plasmas is heated so rapidly that collisionless processes dominate. However, collisional absorption must be considered for both the low intensity foot of ultra-intense, short pulse lasers and the intrinsic low intensity of nanosecond pulse lasers.

### 2.2.2 Resonant Absorption

When a component of the incident electric field of the laser is in the direction of the density gradient, i.e. $p$-polarized light, plasma waves can be driven at the critical density point in the plasma profile. This process is resonant at the critical surface, where the frequency of the plasma waves is equal to that of the laser, $\omega_{pe} = \omega_0$, and the amplitude of the waves becomes large. These waves transfer energy to thermal particles, either when they are collisionally damped (for cold plasmas) or through wave breaking (for hot plasmas) [83]. So called 'resonant absorption' can be efficient, but only for longer scalelengths that are not usually reached with the inherent short pulse prepulse.

The absorption fraction of light depends upon the self-similar parameter

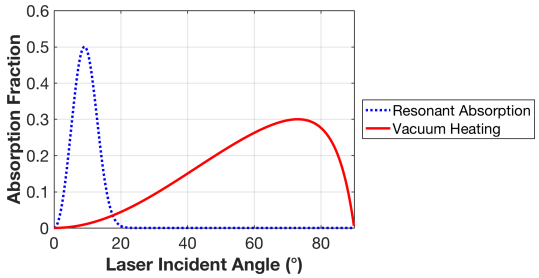


Figure 2.1: Absorption into energetic electrons versus laser angle of incidence for the resonant absorption ($p$-polarization) and vacuum heating mechanisms. The simplified resonant absorption calculation uses $\lambda = 1\,\mu\text{m}$, $L_n = 20\,\mu\text{m}$, and is scaled to match the more accurate peak value of 0.5 [9]. The vacuum heating curve is scaled to a peak value of 0.3, a typical value [10].

$\xi = (kL_n)^{1/3} \sin\theta_{\text{laser}}$, where $k = 2\pi/\lambda$ is the wave vector, $L_n$ is the $1/e$ density scalelength and $\theta_{\text{laser}}$ is the laser angle of incidence. The resultant absorption as a function of incident angle is insensitive to the actual wave damping mechanism and can be approximated by [84]:

$$\eta_{ra}(\xi) \simeq 2.6\xi^2 \exp\left(\frac{-2\xi^3}{3}\right)^2 \tag{2.6}$$

This relationship is valid for long scalelength plasmas, where $kL_n \gg 1$; it correctly captures the trend of absorption, but overestimates the peak value. More precise modelling gives a maximum absorption of $\sim$50% from resonance absorption [9]. The angular absorption curve from Equation (2.6) is plotted in Figure 2.1, scaled to a maximum value of 0.5.

### 2.2.3 Vacuum Heating

Vacuum heating, or 'Brunel absorption', occurs when an intense laser is incident on an overdense plasma with a sharp vacuum interface [85]. Electrons present on the surface of the target are accelerated outwards into vacuum during a single half cycle cycle of the laser pulse and then sent into the target. In this overdense region there is no restoring laser field beyond the skin depth, $\delta_s \approx c/\omega_{\text{plasma}}$, and the accelerated electrons can travel freely into the target

depositing their energy. The particles can reach the quiver velocity in the incident electric field, $v_{\rm osc} = eE/m_e\omega$. The source of electrons on the surface is either thermal motion or field emission from the intense electric fields of the laser.

The plasma density gradient controls the transition between resonant absorption and vacuum heating. For very steep gradients there is not enough plasma for significant resonance to occur, and the amplitude of electron oscillations will be $x_p \approx eE/m_e\omega^2 = v_{\rm osc}/\omega$. If this distance is larger then the plasma scalelength, $v_{\rm osc}/\omega > L_n$, electrons will be driven into the target and vacuum heating will occur as described above.

From a capacitor approximation model developed by Brunel and simplified by Gibbon [86], which neglects the magnetic fields, electrons accelerated by vacuum heating are treated as a moving sheet that obtains a velocity $v \simeq 2v_{\rm osc} \sin\theta_{\rm laser}$ after a single laser cycle. By assuming that all electrons in this sheet penetrate the target and accounting for imperfect reflectivity and relativistic motion, the absorbed power versus $\theta_{\rm laser}$ can be calculated. In the relativistic limit of $a_0 \gg 1$ the angular absorption behaviour is:

$$\eta_{\rm vh}^{\rm rel} = \frac{4\pi\alpha}{(\pi+\alpha)^2} \tag{2.7}$$

where $\alpha(\theta_{\rm laser}) = \sin^2\theta_{\rm laser}/\cos\theta_{\rm laser}$. The absorption is strongly peaked at $\theta = 73^\circ$ and goes to zero at normal incidence, where no component of the laser electric field directs particles into the target. The maximum absorption depends upon the laser intensity and plasma density, and is not predicted by this calculation. The absorption curve versus laser angle is plotted in Figure 2.1, scaled to a typical maximum absorption value of 0.3 [10].

### 2.2.4 J × B Heating & Ponderomotive Force

For ultra-high laser intensities, $a_0 > 1$ and electrons reach relativistic velocities in a single laser cycle. Two forces then become significant: the $v \times B$ component of the Lorentz force, and the ponderomotive force. The latter arises from the strongly non-uniform Gaussian spatial distribution of laser beams [87]. Electrons that are initially near the centre of the Gaussian beam will be accelerated radially away, where the beam intensity (and hence restoring force) is weaker, and therefore experience a net energy gain. The classical ponderomotive force can be expressed as a gradient of the electric field [86]:

$$F_P = -\frac{e^2}{4m_e\omega^2}\nabla(E^2) \tag{2.8}$$

The relativistic $v \times B$ Lorentz force introduces forward motion, and the net result is that electrons are accelerated forward at a given angle, $\cos\theta_{\text{electrons}} = \sqrt{(\gamma-1)/(\gamma+1)}$, and with velocities $\sim v_{\text{osc}}$. This acceleration mechanism, known as J × B heating, drives electrons twice per laser cycle, resulting in highly directional, characteristic bunches at $\omega_{J\times B} = 2\omega_{\text{laser}}$.

The random fluctuations in energy gain over laser cycles and between particles gives electron acceleration a highly stochastic nature, and the ensemble hot electron energies tend to resemble a Maxwellian distribution [88]. Combined with the 'cold' background electrons present in a bulk target, a two-temperature energy distribution is typically observed in electron spectra. When $I > 10^{18}$ W/cm$^2$, $J \times B$ heating is dominant and the hot electron temperature, $T_{\text{hot}} = k_B T_e$, follows a ponderomotive scaling [89]:

$$\begin{aligned} T_{\text{hot}} &\approx m_e c^2(\gamma - 1) \\ &= m_e c^2 \left[(1 + a_0^2)^{1/2} - 1\right] \\ &= 511 \left[(1 + 0.73 I_{18} \lambda_{\mu m}^2)^{1/2} - 1\right] \text{ keV} \end{aligned} \tag{2.9}$$

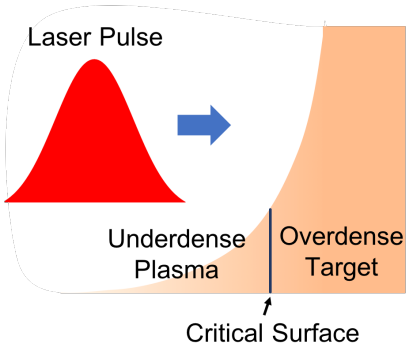


Figure 2.2: Diagram of laser interaction with a target with preplasma.

where $k_B = 8.617 \times 10^{-5}$ eV/K is the Boltzmann constant, the time averaged relativistic factor is $\gamma = (1 + a_0^2)^{1/2}$, and the electron momentum is set by the quiver velocity and expressed in terms of the normalized amplitude $a_0 = eE_0/m_e c\omega_0 = p_{\text{osc}}/m_e c$. Equation (6.5) is given in units of $10^{18}$ W/cm$^2$ and µm for intensity and wavelength, respectively.

## 2.3 Target Normal Sheath Acceleration (TNSA)

Highly energetic ($> 1$ MeV), forward directed beams of laser-generated protons were first reported in 2000 [90, 91, 92]. Since then extensive research efforts have been devoted to understanding and controlling these proton beams. The straightforward physics picture will be outlined first, then several models will be given that aim to predict parameters of the accelerated protons.

The basic physics picture of proton acceleration from ultra-intense lasers was put forth by Wilks *et al.* shortly after the first experimental observations [93]. The mechanism, known as target normal sheath acceleration (TNSA), occurs as follows:

1. Highly energetic, 'hot' electrons are generated at the front surface of a target irradiated with an ultra-intense, short pulse laser. The process by which these electrons are created is not crucial for the following steps, although the energy scaling and efficiency of the overall process depends

strongly on which of the many electron acceleration modes is dominant.

2. The hot electrons, which are relativistic and moving at close to the speed of light, quickly travel through the target. The first and most energetic particles escape and the target becomes positively charged, confining the majority of the electrons to the target [29]. Still highly energetic, these trapped electrons drive charge separation and establish a strong ($\sim$TV/m) electrostatic field on the rear surface.

3. Protons present on the surface of the target are ionized and accelerated by the sheath field normal to the rear plane. These protons, along with the electron cloud, form a moving, quasi-neutral beam that accelerates outward until the hot electron pressure is no longer sufficient to drive charge separation. This smooth, non-stochastic acceleration gives TNSA proton spectra a characteristic sharp cutoff energy. The source of protons is a thin, ubiquitous hydrocarbon contaminant layer that covers all surfaces unless specific steps, such as target heating under vacuum, are taken [94].

These steps are illustrated in Figure 2.3. Section 2.2, above, outlines the processes that create hot electrons, and the following sections cover analytic TNSA models and effects that can modify it. Section 2.4 outlines other proton acceleration methods.

### 2.3.1 Fluid Models

The fundamental models of TNSA by Wilks *et al.* [93] and Mora [12] use fluid descriptions of plasma expansion into vacuum to represent the hot electron cloud and proton beam. The model of Mora will be detailed here, as it provides an accurate yet simple picture of TNSA physics. The initial setup is a semi-infinite plasma slab with a perfect step in ion density and a sigmoidal electron

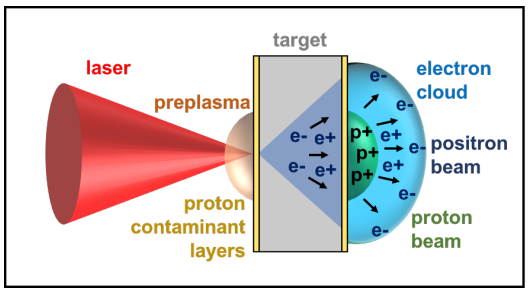


Figure 2.3: The target normal sheath acceleration (TNSA) process. Electrons on the front surface are accelerated to relativistic energies by an ultra-intense laser, then travel through the target and establish an electron cloud on the rear surface. Protons (present on the surface of the target) and positrons (generated inside the target from the energetic electrons) are accelerated by the strong electric fields established by the electron cloud.

density (Figure 2.4a). The electrons are assumed to follow the Boltzmann distribution:

$$n_e = n_{e_0} \exp\left(\frac{e\phi}{k_B T_e}\right) \tag{2.10}$$

where $n_{e_0} = Z n_{i_0}$ is the initial electron density in the unperturbed plasma region ($x = -\infty$), $Z$ is the charge state, $n_{i_0}$ is the initial ion density, and $\phi$ is the electrostatic potential, which goes to 0 at $x = \infty$. The Boltzmann distribution is valid under the conditions that the fields present are purely electrostatic ($E = -\nabla\phi$), they evolve slowly compared to the electron response, and the fluids are isothermal. The ions are initially cold and at rest. The rapid electron response assumption is reasonable for MeV-energy electrons. Subsequent work, detailed below, addresses the assumption of isothermal fluids [95].

The potential obeys the Poisson equation:

$$\epsilon_0 \frac{\partial^2 \phi}{\partial x^2} = e(n_e - Z n_i) \tag{2.11}$$

which is assumed to hold as the plasma expands. The potential boundary conditions are $\phi(-\infty) = 0$ and $\phi(\infty) = -\infty$. The ion motion is found using the fluid equations for continuity and motion:

$$\frac{\partial n_i}{\partial t} + \frac{\partial (n_i v_i)}{\partial x} = -n_i \frac{\partial v_i}{\partial x} \tag{2.12}$$

$$\frac{\partial v_i}{\partial t} = -C_s \frac{dn_i}{dx} \tag{2.13}$$

where $C_s = \sqrt{Z k_B T_e / m_i}$ is the ion acoustic velocity and $m_i$ is the ion mass. A self-similar solution can be found for the plasma expansion with $v_i = C_s + x/t$, for $x + C_s t > 0$. Quasi-neutrality must be assumed, such that $n_e = Z n_i = n_{e_0} \exp(-x/C_s t - 1)$. The self-similar sheath electric field can be found:

$$E_{\text{self-similar}} = \frac{k_B T_e}{e C_s t} \tag{2.14}$$

The self-similar solution becomes undefined when the local Debye length, $\lambda_D = (\epsilon_0 k_B T_e / n_e e^2)^{1/2}$, becomes larger than the self-similar scalelength, $C_s t$. This occurs at early times, $\omega_{pi} t < 1$, where $\omega_{pi} = (n_{e_0} Z e^2 / m_i \epsilon_0)^{1/2}$ is the ion plasma frequency with the initial, unperturbed electron density. The position of the front at later times can be estimated from the equality $\lambda_D = C_s t$. Mora calculated a more accurate front position by interpolating from numerical results. The electric field he found was:

$$E_{\text{front}} \simeq \left( \frac{2\omega_{pi} t}{(2e + \omega_{pi}^2 t^2)^{1/2}} \right) E_{\text{self-similar}} \tag{2.15}$$

The ion energy spectrum can then be calculated. It has an exponential fall-off in energy and a well defined cutoff, which for large times ($\omega_{pi} t \gg 1$) is:

$$E_{\max} \approx 2 T_{\text{hot}} \left[ \ln \left( \tau_p + \sqrt{1 + \tau_p} \right) \right]^2 \tag{2.16}$$

where $\tau_p = \omega_{pi} t / \sqrt{2 \exp(1)}$ is the normalized time. Figure 2.4b gives examples of the calculated proton energy spectra. Mora's model, having a constant electron temperature, predicts unbounded proton energy gain and plasma expansion. Fuchs *et al.* found an acceleration cutoff time of $t_{\text{acc}} \approx 1.3 \tau_{\text{laser}}$ to be

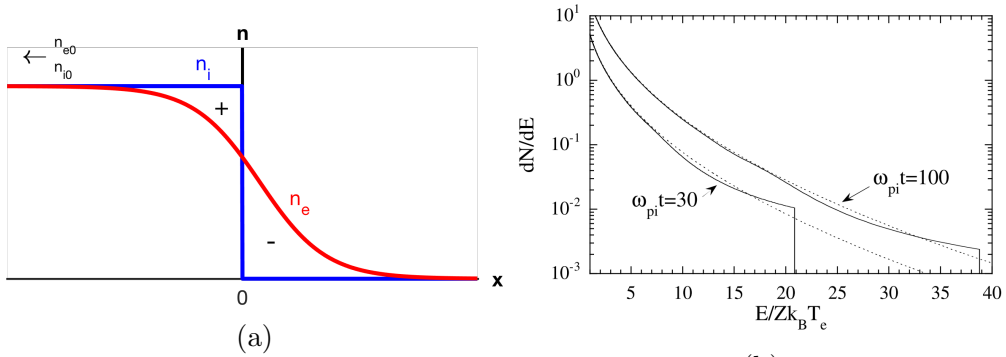


(a) (b)

Figure 2.4: (a) Initial plasma profile for the Mora model, with a step-like ion density and an electron sheath. Based on a diagram in [11]. (b) Proton spectra calculated by Mora for two times. The dotted curves are from the analytic, self-similar solution, and the solid curves are from 1D Lagrangian simulations. For example, if $Z = 1$, $k_B T_e = 500$ keV, and $n_{e_0} = n_{i_0} = 10^{22}$ cm$^{-3}$, the predicted cutoff energies would be 11 MeV and 19 MeV at times of 0.2 ps ($\omega_{\rm pi} t = 30$) and 0.8 ps ($\omega_{\rm pi} t = 100$), respectively. Figure from [12].

in good agreement with experimental and simulated maximum proton energies [96]. That the acceleration time should be proportional to the laser pulse, $\tau_{\rm laser}$ is consistent, as during this period hot electrons are continuously being generated and the plasma is approximately isothermal. In their treatment the hot electron density on the rear surface, $n_{e_0}$, was estimated by an electron beam cone, with the initial size set by the laser spot, cone length equal to the target thickness, and the final spot determined by the electron beam divergence half-angle ($\theta_{\rm beam} \approx 25°$). Ballistic electrons were assumed.

Wilks *et al.* note that the self-similar scalelength is the plasma scalelength, $C_s t = L_n$ [93], giving the relationship:

$$E_{\rm max} \propto \frac{T_{\rm hot}}{L_n} \tag{2.17}$$

The definition of plasma scalelength is typically given as a exponential function $n(x) = n_0 \exp(-x/L_n)$. Equation (2.17) establishes a scaling relationship with $\rm T_{hot}$, which for relativistic intensities can be estimated from the ponderomotive scaling in Equation (6.5). Accordingly, $E_{\rm max} \propto (I\lambda)^{1/2}$, a scaling that has been

verified for 10–25 µm foils at intensities up to $6 \times 10^{20}$ W/cm$^2$ [97].

An adiabatic model of expansion from Mora addresses the isothermal assumption by taking into account the cooling of the hot electron cloud and the finite target size [95]. The total energy available to the protons is set by the plasma thickness, hence this model avoids the infinite energy gain and arbitrary acceleration time cutoff of the isothermal model. When compared to experiment results, however, this model proved to be less accurate than the simpler isothermal model in some cases [98]. It agreed better for multi-picosecond laser pulses, and experimental matching was further improved when the acceleration time was capped to account for lateral expansion of the electron cloud [97].

The isothermal Mora model of TNSA has been modified to incorporate various effects that dominate depending upon specific experimental conditions. For small targets, refluxing of electrons maintains a higher electron density, resulting in enhanced proton acceleration. To include this phenomenon Buffechoux *et al.* suggested increasing the acceleration time in Equation (2.16), the maximum proton energy relation, by the time for significant expansion of the proton layer, $\tau_{\text{expansion}} \approx 6\omega_{pi}^{-1}$ [99]. The ion plasma frequency $\omega_{pi}$ gives the response time of the ions, and the coefficient has been determined to be in good agreement with simulation and experimental results. To account for finite beam spot sizes with ultra-thin, 25 nm thick targets, Brenner *et al.* proposed adding an additional acceleration time, $\tau_{\text{escape}} = D_L/2v_e$, where $D_L$ is the diameter of the sheath and $v_e$ is the average lateral velocity of the hot electrons [100]. This term approximates the time necessary for electrons to escape the initial sheath spot through lateral expansion. Good agreement was found between experimental results and this modified model [100].

Yogo *et al.* developed a modification to account for multi-picosecond, constant intensity pulses [101]. For these conditions the hot electron temperature was found to grow beyond ponderomotive scaling and show a significant time

dependence, $T_{\text{hot}}(t)$. This time-dependent term was inserted into the fluid model equations and solved for proton energy. Fit parameters from 1D PIC simulations were used to define the temporal profile, $T_{\text{hot}}(t)$, and the time-dependent ion acoustic velocity. The final ion velocity was found by integrating acceleration time from the arrival time of the first peak to a set decay time (approximately twice the total pulse duration). With these parameters the model was found to agree with experiment for pulse lengths up to 6 ps, the maximum measured.

### 2.3.2 Other TNSA Models

A model by Passoni *et al.* calculates the electrostatic field that develops before significant proton expansion has occurred [102, 103]. Only electrons trapped in the target by the sheath field are considered, while the target ions are stationary and the protons are treated as test particles in the quasi-stationary electric field. For $T_{\text{hot}} \gg 1$, the maximum proton energy is given by:

$$E_{\text{max}} = k_B T_{\text{hot}} \frac{e^{\varphi_{\text{max}}}(\varphi_{\text{max}} - 1) + 1}{e^{\varphi_{\text{max}}} - 1} \tag{2.18}$$

where $\varphi_{\text{max}}$ is the maximum of the sheath potential energy, in units of $k_B T_e$, and must be estimated. An empirical scaling law, $\varphi_{\text{max}} = 4.8 + 0.8\ln(E_{\text{laser}}[J])$, was proposed. This model is valid only for a short period of time early in the acceleration process, but gives surprisingly accurate results for laser pulse durations up to ~1 ps [98].

Schreiber *et al.* and Zeil *et al.* describe TNSA using a surface charge determined from laser parameters and an assumption of electron beam divergence, which yields a charge density on the rear surface of the target for a given target thickness [104, 105]. The potential is then solved, resulting in an implicit function for maximum proton energy. Integrating to the laser pulse duration

gives an approximate relationship [105]:

$$E_{\max} \approx E_{\infty} \tanh^2 \left( \frac{\tau_{\text{laser}}}{2\tau_0} \right) \tag{2.19}$$

where $\tau_0 = R/v(\infty) = R/(2E_{\infty}/m_p)^{1/2}$, $R$ is the radius of the electron cloud on the rear surface, and $E_{\infty} = Qe^2/(2\pi\epsilon_0 R)$ is the sheath potential barrier for a total charge $Q$. To find the electron cloud radius a half angle divergence of 45° was assumed for Titan-class lasers, based on experimental observations.

### 2.3.3 Effect of Prepulse

The presence of a preplasma alters the density profile on the front surface of a target, which can result in significantly different electron generation mechanisms becoming predominant (Section 2.2). The altered hot electron temperature and density, in turn, affect the proton spectra as was described in Section 2.3.1. Amplified spontaneous emission (ASE) is the usual cause of preplasma; the ns-scale prepulse from ASE can generate a plasma with with a scalelength in the 10's of µm.

These effects have been studied using two beam experiments, with a long pulse beam to create a controlled preplasma and a high contrast short pulse to minimize inherent prepulse. By varying the delay between the two pulses the expansion time of the surface plasma was controlled, setting the plasma scalelength for the short pulse. It was found that proton cutoff energy and conversion efficiency are maximized for scale lengths of 30-60 µm with 25 µm thick targets [106]. At scalelengths $> 100$ µm the beam was seen to filament, reducing the laser intensity. An additional effect occurs when the shock driven by the prepulse has time to propagate through the target and disrupt the rear surface; in this case the rear scalelength $L_n$ increases and TNSA is inhibited through a reduced accelerating field [107]. This effect introduces a relationship between ASE and target thickness, which produces an optimal thickness for a

given laser system [108].

An effect that has typically been ignored in theoretical and simulated treatments of LPI is that of the ps-scale prepulse, due to the deviation from an ideal Gaussian temporal profile. Recent investigations have shown that this ps-prepulse has a significant effect on electron and proton generation for 'ultraclean' laser systems, and must be accounted for in order to accurately model TNSA proton energies [109].

### 2.3.4 Effect of Sheath Field Dynamics

The sheath field due to the electron cloud is highly dynamic, and its evolution over time has important effects on particle acceleration. The process occurs as follows: Hot electrons are created while the laser pulse is present and travel at ∼c. They cross the target on timescales of 10–100's of femtoseconds, and the first and most energetic particles escape and charge the target like a capacitor [29]. Less energetic and late electrons are then confined to the target by the electrostatic field established by the target charging, and form an electron cloud. It is this electron cloud that forms the sheath field.

The confined hot electrons are reflected in the forward direction by the sheath field but retain their transverse momentum, and therefore spread laterally in the target [110]. The charge cloud expands until it reaches the target edges, where there is no more plasma to sustain a neutralizing return current, and the hot electrons are again arrested. The electric density at the edges builds, and after approximately a plasma period (∼100's fs) the electrons are reflected inward [111]. Two-dimensional particle-in-cell simulations give evidence for this sheath reverberation in the target, with the potential at the centre of the target peaking a second time due to reflected electrons [99, 111].

The reflected electrons also revisit the target front surface if the target is thin, an effect known as refluxing. A 'thin' target is defined as one in which the time for a hot electron to make a round trip in the target, thickness $T$,

is less than the laser pulse duration, $tau_{\text{laser}}$: $2T/c < \tau_{\text{laser}}$ [112]. Refluxing electrons can increase the local hot electron density in the sheath field within a small enough timescale to boost TNSA [99, 113]. An added boost to hot electron density is given by the minimal electron beam divergence in a thin target. The effect of refluxing has also been shown through K-alpha x-ray emission from buried tracer layers [114, 115].

The speed of the lateral expansion of the charge cloud also determines the timescale for sheath decay and rebound. A key parameter is the time it takes for hot electrons to leave and return to the target centre, defined as $\tau = D_{\text{target}}/v_{\perp}$, where $D_{\text{target}}$ is the target diameter. Simulations performed by McKenna *et al.* found a transverse speed of $v_{\perp} = 0.75c$ [111], while Buffechoux *et al.* found a similar value of 0.7c [99]. In the latter case an explanation was given that electrons are largely ballistic at relativistic velocities, and if they are traveling at a speed of c their transverse velocity is simply set by their direction. The laser was incident at $\theta_{\text{laser}} = 45°$, giving $v_{\perp} = \cos(45°) \times c = 0.7c$. Expansion through a thin current layer has also been found to be important for large incidence angles and p-polarized light [116].

Three-dimension effects can play an important role. Simple models such as Mora's assume planar expansion, while evidence from proton radiography and PIC simulations indicates that the electron cloud on the target rear forms a bell shape (with a forward velocity of $3 - 4 \times 10^7$ m/s) [41, 117, 118]. Accounting for the realistic expansion profile in models has allowed for better matches with data [97].

One promising technique to improve TNSA yield is using multiple pulses, separated by the order of a picosecond, to optimize the acceleration conditions. Simulations suggest that the enhancement is due to both front surface and rear surface effects [119], with better laser-electron coupling on the front surface from a longer scalelength plasma and a pre-seeded TNSA bunch on the rear surface that enhances the driving electric field. This effect has been observed

experimentally, with 100 µm Au targets showing proton yield improvements of 2-3× [120] and 5 µm Au targets giving increases of >10× [121]. The latter results, reported by Brenner *et al.*, claimed a record 15% conversion efficiency. The best yield was found with a separation of 1 ps and a 1:10 intensity ratio between the first and second pulses. Further theoretical calculations were carried out by Volpe *et al.* indicating that, for thick targets (∼100 µm), even more improvement could perhaps be obtained using three pulses [122].

## 2.4 Other Ion Acceleration Mechanisms

Several other proton acceleration mechanisms have been observed or proposed. The goal of investigation into these alternate schemes is to reach higher maximum ion energies, higher conversion efficiencies and/or more controlled spectra compared to TNSA.

### 2.4.1 Hole Boring

The compression of a plasma surface under the radiation pressure of a laser can generate ion beams, in a process known as hole boring. Radiation pressure, given by $P_L = 2I/c$ for perfect reflection, can reach Gbars for $I > 10^{19}$ W/cm$^2$. These extreme pressures can significantly accelerate light ions, such as protons, in a 'snowplow' process that was first theoretically outlined for relativistic intensities by Wilks *et al.* [89]. An estimate of the hole boring velocity can be made by assuming momentum conservation between the incident light and the outgoing ions:

$$\frac{v_{\mathrm{hb}}}{c} = \sqrt{\frac{n_{\mathrm{crit}}}{n_e}\frac{Zm_e}{m_i}\frac{a_0^2}{2}} \tag{2.20}$$

where $m_i = Am_p$ is the ion mass, $A$ is the atomic number, and $m_p = 1.673 \times 10^{-27}$ kg is the mass of a proton. Typical hole boring velocities from

Equation (2.20) are $v_{\mathrm{hb}} \approx 0.02c$. A relativistic extension to multi-species plasmas was outlined in Robinson *et al.* [34], giving an energy of:

$$E_{\mathrm{hb}} = m_i c^2 \left[ \frac{2\Xi}{1 + 2\sqrt{\Xi}} \right] \tag{2.21}$$

where $\Xi = I/m_i n_i c^3$ is a dimensionless 'pistoning parameter' and $n_i$ is the ion density. This relativistically correct form is important for ultra-high intensities ($I > 5 \times 10^{21}$ W/cm$^2$) and low density targets such as liquid hydrogen [34]. In order for momentum transfer to be maximized, absorption of the laser light must be minimized. Practically this is accomplished by using circularly polarized light, which does not efficiently heat electrons [123]. Despite this approach, holing boring is not an effective acceleration scheme at current laser intensities [124].

### 2.4.2 Radiation Pressure Acceleration

Radiation pressure acceleration (RPA) is closely related to hole boring, as both are driven by the radiation pressure of the beam. RPA, however, utilizes ultra-thin targets (nanometer-scale) such that the whole target is accelerated as a single plasma [125]. This is also known as light sail acceleration [126], and is predicted to become significant for intensities above $10^{22}$ W/cm$^2$ [125]. Seeing evidence of RPA at lower intensities requires suppressing the TNSA protons in foils, as is possible with circular polarization [127, 128], or using gaseous targets with longer wavelength $CO_2$ lasers to interact with critical density [129]. Ultra-clean lasers are necessary to allow the nm thick foil targets to survive irradiation until the arrival of the main pulse. Investigation into RPA is motivated by the extremely high conversion efficiencies predicted by simple models, which suggest that a major part of the laser energy can be converted to ion energy for highly relativistic intensities [125]; more realistic approaches give lower but still significant conversion efficiencies [126].

### 2.4.3 Breakout Afterburner

When a laser pulse can penetrate an ultra-thin target, breakout afterburner (BOA) can occur [130]. In this mechanism the target becomes relativistically transparent to the ultra-intense laser pulse, allowing it to accelerate electrons directly at the rear of the target. The energy in electrons is then transferred to ions. A linearly polarized pulse must be used to efficiently produce hot electrons. Experimentally, carbon ions with energies to 1 GeV (83 MeV/amu) have been observed from BOA [131]. Conversion efficiencies into ions of up to ∼10% are predicted for favourable conditions [132].

### 2.4.4 Collisionless Shockwave Acceleration

Collisionless shockwave acceleration (CSA) uses plasma pressure instead of radiation pressure to accelerate particles. An ion density discontinuity, established by hole boring from a short pulse laser, drives a shockwave from the high density, high pressure downstream region to the low density, low pressure upstream region. At the interface of this shock, charge separation occurs and a strong electrostatic field is established; the resulting moving potential can reflect ions ahead of it at up to twice the shock velocity [133]. Because of the role of electrostatic fields, CSA is also called electrostatic shock acceleration. The reflected ion distribution is highly monoenergetic. For CSA to occur the background electrons must be very energetic (∼MeV), and therefore energy must be efficiently coupled from the laser to the plasma. This can be done using targets near the critical density of the laser wavelength. The theory of CSA is covered in detail in Section 7.1.

CSA was first reported experimentally by Haberberger *et al.* using a $\lambda = 10\,\mu\text{m}$ $CO_2$laser and a gas jet target [133]. Proton energies up to ∼22 MeV were observed in highly monoenergetic peaks. Translating this work to more common $\lambda = 1\,\mu\text{m}$ lasers is challenging, because of the lack of near-critical

density targets for this wavelength and the strong influence of sheath fields. Fiuza *et al.* proposed using an exponentially decaying rear density profile to minimize TNSA signal and velocity dispersion from sheath fields [2, 33]. Work done for this degree has experimentally demonstrated CSA in this regime for the first time - see Chapter 7.

# Chapter 3
# Methodologies

Experiments were conducted primarily using two ultra-intense lasers: the Titan laser at the Jupiter Laser Facility in Lawrence Livermore National Laboratory, California, and the OMEGA EP laser at the Laboratory for Laser Energetics in Rochester, New York. These facilities use Chirped Pulse Amplification (CPA) to achieve $I > 1 \times 10^{19}$ W/cm$^2$ in 1 – 10 ps pulses. They utilize Optical Parametric CPA (OPCPA) front end preamplifiers in order to reduce the prepulse level on the final laser pulse. In this chapter the operation and configuration of these laser systems is detailed. Additionally, the main diagnostics and tools used on these experiments are described, with the exception of the Imaging Proton Spectrometer, which is covered in Chapter 5.

## 3.1 Ultra-Intense Short Pulse Lasers

Modern ultrashort lasers are made possible by Chirped Pulse Amplification (CPA). An idea borrowed from radar and first applied to optical lasers in 1985 [134], CPA stretches the laser pulse in time to reduce its intensity and thereby allow higher levels of amplification to take place without damaging the amplifiers. Typical stretched pulselengths are on the order of nanoseconds. After amplification the pulse is compressed in time and focused down to ultrahigh intensities. The key to the CPA process (as well as its limiting factor) is the compressor gratings, which shorten the pulse and must withstand the fluence of the fully amplified beam.

To allow amplification of pulses with minimum prepulse the technology of Optical Parametric CPA (OPCPA) was developed. First proposed for

petawatt level systems by Dubietis *et al.* in 1991 [135] and demonstrated at a petawatt level by Ross *et al.* in 2000 [136], parametric amplification uses a $2^{\text{nd}}$ order nonlinear optical process to transfer energy from a pump beam to a seed beam in a crystal. A weak idler beam is also output, with a frequency such that $\omega_{\text{pump}} = \omega_{\text{signal}} + \omega_{\text{idler}}$ [137]. As a parametric process, OPCPA only occurs when the pump pulse is present and therefore requires a pump pulse duration similar to that of the seed pulse. CPA allows the primary pulse to be temporally stretched to match nanosecond-duration pump lasers. This allows amplification of the laser pulse over many orders of magnitude in the front end of the laser, without introducing large amounts of amplified spontaneous emission (ASE). This is an enabling technology allowing high contrast, ultrahigh intensities to be generated by lasers such as Titan, with $I > 10^{20}$ W/cm$^2$.

Within a laser gain medium, a fraction of the spontaneous emission will be along the laser axis and get amplified along with the main pulse. This ASE creates a pedestal in the laser envelop that can reach ionizing levels nanoseconds before the main pulse (Figure 3.1). The laser contrast, or difference between the peak pulse intensity and intensity at a given time before the main pulse, is therefore limited by ASE in the system. Techniques such as frequency doubling and plasma mirrors can be used to 'clean' the pulse and remove ASE, and are discussed below. In many cases, however, some amount of prepulse is present, which can generate preplasma and significantly influence the interaction physics (see Section 2.1 and Section 2.3.3).

### 3.1.1 The Titan Laser

Experimental work was primarily performed using the Titan laser, at the Jupiter Laser Facility (JLF) in Lawrence Livermore National Laboratory (LLNL), California. It is an intermediate scale Nd:glass laser capable of reaching intensities of $\sim 1 \times 10^{20}$ W/cm$^2$. The primary, 1054 nm short pulse beam has energies of 150 – 300 J in 0.7 – 30 ps, and with a spot size of $\sim$10 µm. A

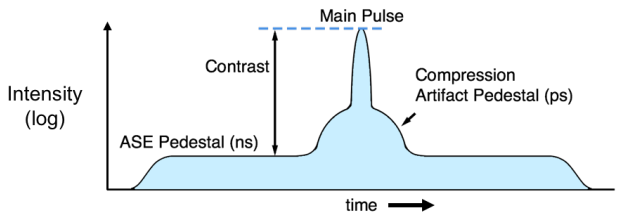


Figure 3.1: A typical pulse intensity profile for a CPA laser. The ASE prepulse is a pedestal rising nanoseconds before the main pulse. The main pulse also deviates from a perfect Gaussian due to a picosecond-scale pedestal from compression.

second, long pulse beam is available which can deliver up to 800 J of energy in 10 ns [138].

The master oscillator initiates the beam with ∼200 fs pulses, which are stretched to 1.6 ns with an Offner pulse stretcher. Three-stage OPCPA then takes place, amplifying the beam from 1 nJ to 20 mJ. This front-end preamplifier is pumped by a 5 Hz, 1053 nm beam, amplified by a regenerative amplifier and Nd:YLF 4-pass amplifier to 1.5 J. Before driving the OPCPA the pump beam is frequency doubled to 526 nm in a BBO ($\beta$-barium borate) crystal. The laser next travels through a series of rod and disk Nd:glass amplifiers, pumped by flashlamps, resulting in the final energy of 100–200 J. After being magnified to 25 cm in diameter the beam is compressed with two 40 cm $\times$ 80 cm dielectric gratings. Finally the s-polarized, 25 cm diameter beam is focused to a 10–15 µm full-width half-maximum spot at target chamber centre (TCC) with a dielectric-coated, f/3 off-axis parabola (OAP). The resulting maximum intensity is $\sim 1 \times 10^{20}$ W/cm$^2$ with the minimum pulse duration of 0.7 ps. The Titan laser chain is shown in Figure 3.2. The standard angle of incidence on targets is 16° to prevent potentially damaging back-reflection from reaching the compressor gratings .

The Titan laser can be operated in frequency doubled mode ($2\omega$), with a wavelength $\lambda = 527$ nm. Second harmonic generation (SHG) is a nonlinear process, with the energy of the secondary harmonic light depending upon the

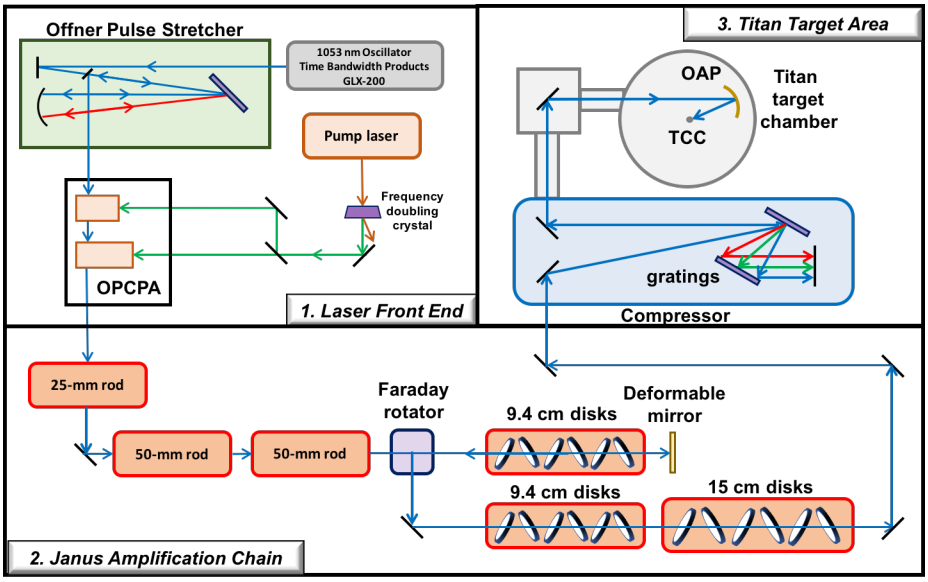


Figure 3.2: The Titan laser chain. The operation is described in the text. This diagram is an updated version of a diagram by Cliff Chen.

square of the intensity of the first harmonic light, $E_{2\omega} \propto I_{1\omega}^2$ [137]. SHG therefore increases the difference between the low intensity prepulse and the high intensity main pulse, and this improved intensity contrast is a major advantage of the $2\omega$ beam. The disadvantage is the much lower pulse energy, a maximum of 50 J, due to energy lost in both the conversion process and the sub-aperture doubling crystal. The limited crystal size reduces the beam diameter from 25 to 20 cm. This crystal is 2 mm thick KDP and is located in the compressor chamber. A typical spot for the $2\omega$ beam is shown in Figure 3.3.

The second, nanosecond beam can provide 300-800 J pulses in $1\omega$ or $2\omega$. This 'long pulse' beam is amplified using the same Nd:glass amplifier configuration as the short pulse beam. It can be injected in the target chamber at a variety of angles and is timed independently to the short pulse, allowing for various applications such as shock or plasma generation. The laser is focused using an $F = 0.5$ m lens, but typically a phase plate is used that acts to increase the spot size and make it approximately spatially uniform [139]. Phase plates are available to give 500 µm and 800 µm diameter beams.

Prepulse in the short pulse is monitored on shot using a water-cell detector

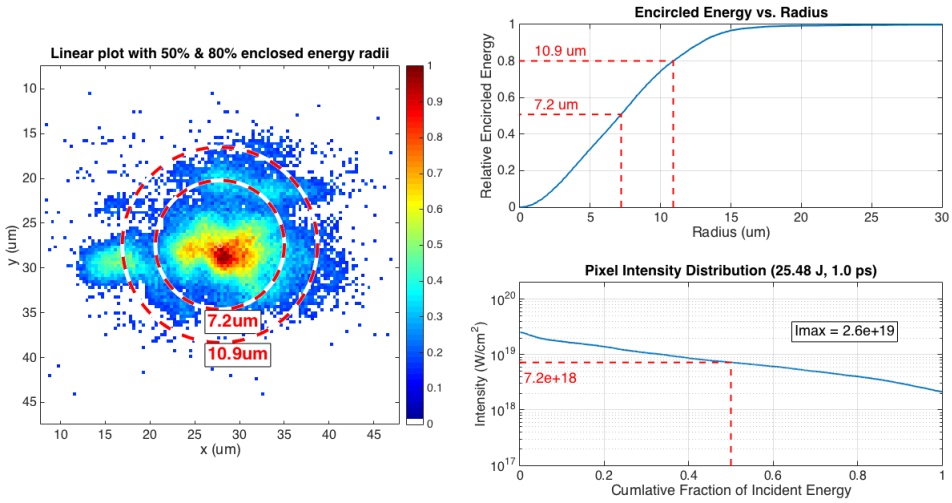


Figure 3.3: A typical laser spot for the frequency-doubled, 527 nm beam.

[79]. Leakage light from a mirror in the compressor is focused into a water-cell, which breaks down at high intensities to shield the detector. Light transmitted before the breakdown is measured with a fast photo-diode, with a rise time of 35 ps, and a GHz oscilloscope. Low energy shots allow calibration with a calorimeter at TCC. A typical Titan prepulse arrives several nanoseconds before the main pulse and contains 5 – 20 mJ of energy.

### 3.1.2 The OMEGA EP Laser

Positron data was collected at the OMEGA EP laser in the Laboratory for Laser Energetics (LLE) in Rochester, New York. This is a large scale, petawatt-class laser build as an extension to the 60-beam, long pulse OMEGA facility (EP = extended performance). EP consists of two, 1054 nm short-pulse beam-lines, each of which is capable of delivering up to 1.3 kJ on target in 1-100 ps. Beam energies of 1.5 kJ can be reached if no blast shield is used. Intensities can reach $\sim 1 \times 10^{20}$ W/cm$^2$ with a spot size of 30 µm [13].

The EP beam begins with a sub-picosecond pulse, is stretched by an Offner triplet stretcher then amplified by two stages of OPCPA. These stages increase the energy from ∼1 nJ to ∼100 mJ. Subsequent amplification occurs in a

beamline similar to those at the National Ignition Facility (NIF): A 7-disk booster amplifier stage, followed by 4 passes through an 11-disk, 40 cm cavity amplifier. A Pockels cell then ejects the beam, sending it back through the booster amplifier and to the 40 × 140 cm tile-grating compressor. In contrast to Titan, deformable mirrors are used both within the cavity amplifier and after the compressor. A dielectric, f/2 off-axis parabola focuses the beam. Typical spots contain 80% of their energy within 15–20 µm. The OMEGA EP laser chain is shown in Figure 3.4.

The contrast of the EP beam was improved significantly with a front-end upgrade in 2012 [140]. An OPA stage was added before the stretcher to amplify the seed pulse while it is still picoseconds in length. This allows the gain in the primary OPCPA stages to be lowered; consequently the amplification of the parametric fluorescence, which forms the nanosecond ASE pedestal, is decreased. Additionally, the small temporal window of ps OPCPA increases the inherent contrast of the pulse. The positron data used in Chapter 6 was taken before this upgrade was implemented, however.

### 3.1.3 Plasma Mirrors

In addition to second harmonic generation (SHG), the contrast of a short pulse laser can be improved by using plasma mirrors (PMs). PMs are simply transparent optics which, by operating at a carefully chosen laser fluence, act as optical switches. The low intensity laser pedestal is transmitted and therefore removed from the pulse, but as the pulse ramps up in energy the PM starts ionizing (through multi-photon ionization, among other processes) and once $n_{e^-} = n_{\text{crit}}$ all subsequent light is reflected. In this manner the main pulse is preserved with a much reduced pedestal, and the laser contrast is improved by up to ∼100 [141]. An example of a PM is shown in Figure 3.5a.

For ps duration pulses, the parameters of a PM are a trade-off between reflectivity and beam spot quality [141]. Increased reflectivity can be achieved

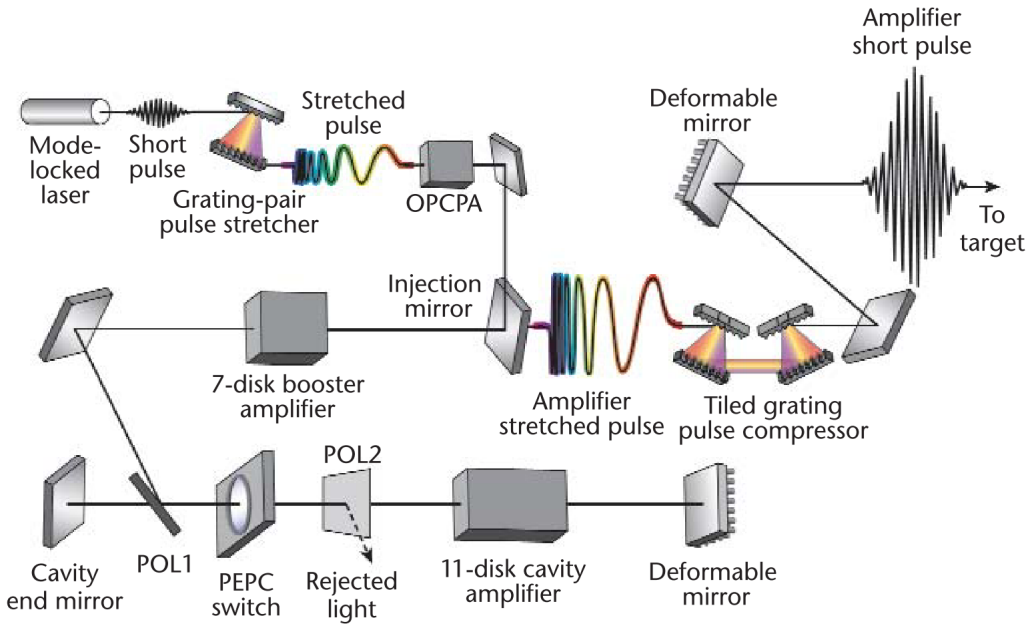


Figure 3.4: The OMEGA EP laser chain, from [13]. The operation is described in the text. PEPC = large aperture Pockels cell, POL = polarizers.

by reducing the laser spot size on the PM to increase fluence and trigger earlier ionization; the increased irradiation, however, will drive increased plasma expansion that will deform the plasma surface and introduce phase front errors. Reflectivities of $70 - 90\%$ are achievable with fluences between 10 – 100 J/cm$^2$. A PM was used in the shock acceleration experiment, and the reflectivity vs. fluence was measured with a calorimeter (Figure 3.5b). The details of its parameters are given in Section 7.2.

The surface of the PM optic is significantly ablated by the main pulse and must be replaced after each use; this makes a quick alignment system essential. For use at Titan the PM was placed as the final optic, after the OAP. Compared to SHG, a PM has the advantage of much reduced equipment requirements: no doubling crystal or specialized $2\omega$ optics are necessary. The original wavelength is also preserved, while reflectivity is similar or better to SHG conversion efficiency.

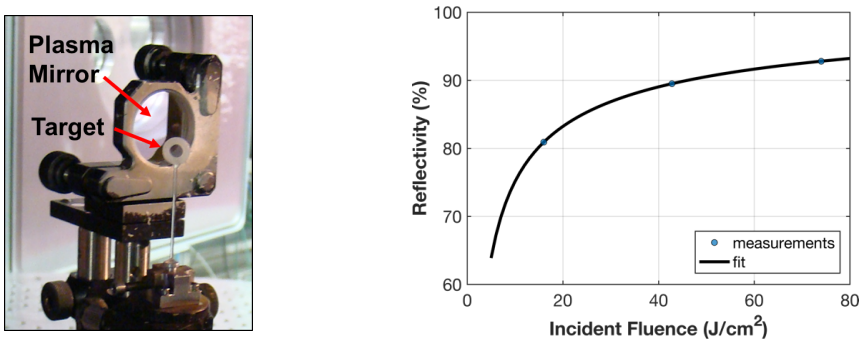


(a) (b)

Figure 3.5: (a) The plasma mirror and target used in the shock acceleration experiment. (b) Measured reflectivity of the plasma mirror vs. peak incident fluence.

## 3.2 Diagnostics

A variety of diagnostics are used to characterize the beams of particles emitted from intense, short pulse LPI. The usage of two of these diagnostics, the EPPS and radiochromic film, is outlined here. The primary detection medium, image plate, is also described. Usage of the Imaging Proton Spectrometer, the primary ion diagnostic, is given in detail in Chapter 5.

### 3.2.1 Electron-Proton-Positron Spectrometer

The Electron-Proton-Positron Spectrometer (EPPS) was used to measure escaping electrons and positrons. It is a compact, magnet-based spectrometer that uses the Lorentz force to disperse particles in space and give a measurement of particle energy:

$$F = q\vec{v} \times \vec{B} \tag{3.1}$$

The EPPS uses 0.8 T permanent magnets and the detection medium is an image plate, which is described in the next section. It was optimized for electron and positron energy measurements in the range of 0.1 – 300 MeV,

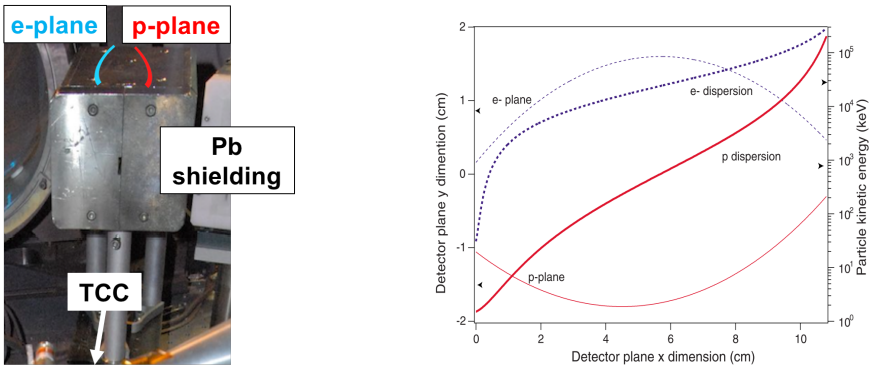


(a) (b)

Figure 3.6: (a) Picture of the EPPS fielded on experiment, with the measurement planes drawn for illustration. It is shown inside its Pb housing. (b) EPPS dispersion for positive and negative particles. From [14].

and has dual channels to allow both positive and negative particles to be measured simultaneously [14]. Protons are also measured, however the small internal travel space causes them to be dispersed less compared to the IPS, and the resulting signal is spatially concentrated and frequently saturated. The entrance pinhole used was a $100 \times 100\,\mu m$ square. This was found to balance spectral resolution and signal for the present cases. The spectrometer is typically fielded with thick, lead shielding to reduce background from high energy x-rays and gamma rays. A diagram of the EPPS and its dispersion are given in Figure 3.6.

### 3.2.2 Image Plates

Both the EPPS and IPS use image plate (IP) detectors, which were originally developed for medical x-ray applications but have been widely adopted by physicists for the uniquely challenging environment of intense laser-plasma experiments. IPs record a temporary image of incident ionizing radiation and are reusable, resistant to damage and have a dynamic signal range of >4 orders [142]. IPs contain a BaFBr:Eu2+ phosphor-crystal layer that absorbs ionizing radiation, exciting electrons to a meta-stable state and producing a latent

image of the initial signal. For readout, illumination with red light further excites electrons in the meta-stable state, causing electron/hole recombination that produces blue light; this signal is known as photo-simulated luminescence or PSL and is proportional to the energy absorbed from the ionizing radiation. At JLF a Fuji FLA 7000 scanner was used to raster-scan IPs with a 633 nm HeNe laser and capture the 400 nm stimulated photons with a photomultiplier tube. BAS-TR image plates (blue, uncoated) were used with the IPS due to their lack of a mylar layer covering the active layer. This prevents energy loss of the ions in the coating, which can be significant for lower energy particles. BAS-MS plates were used with the EPPS; these plates have a 9 µm mylar protective layer before the active layer that makes them more durable while having negligible effect on electron and positron energies.

The raw data, in quantum level units, is converted to absolute PSL using an ImageJ script and the scanner settings. The conversion equation is:

$$\mathrm{PSL} = \left(\frac{R_{\mu\mathrm{m}}}{100}\right)^2 \left(\frac{4000}{S}\right) 10^{L\left(\frac{P}{2^{16}-1}-0.5\right)} \tag{3.2}$$

where $R_{\mu\mathrm{m}}$ is the spatial resolution in µm, the sensitivity $S$ determines the photomultiplier tube voltage, the latitude $L$ sets either 4 or 5 orders of dynamic range and $P$ is the scanned pixel value. Typical settings for the IPS rear image plate are $R = 50\,\mu\mathrm{m}$, $S = 4000$ and $L = 5$.

Image plate signal decreases over time as the meta-stable sites decay, and for consistency should be scanned the same time after exposure for each experiment. The decay rate has been well characterized and is accounted for in the data analysis [18]. Absolute calibrations giving the number of particles per PSL signal have been done for x-rays [143], electrons [144], and ions (see Section 5.1.1).

### 3.2.3 Radiochromic Film

Radiochromic film (RCF) is another highly useful medical technology adapted for short pulse laser experiments. The film provides high spatial resolution images of proton beams. RCF polymerizes immediately when exposed to ionizing radiation, with no chemical processing required, and is not affected by optical light, allowing easy handling. The change in optical density is proportional to the received dose, and can be measured using densitometers or flatbed optical scanners [145]. The latter method was used due to the easy accessibility and speed of modern scanners. The incident particle flux and energy can then be calculated using established calibrations [146].

RCF can also provide spectral information of proton beams by using stacked layers of film, as depicted in Figure 3.7a. Due to the Bragg peak in proton stopping power, each layer primarily receives dose from the narrow energy band of protons that stop in it. Contributions from unstopped protons are found by working backward in the stack. Often aluminum filters are inserted between film layers to conserve film and increase spectral separation. Energy deposition on each layer is calculated using the Monte Carlo, particle transport codes Geant4 [147] and TRIM [148]. An example of energy deposition curves is given in Figure 3.7b.

The types of RCF used in this work were EBT-3 and HD-V2. EBT3 is a symmetric film with a 30 µm active layer between two 125 µm polyester layers. HD-V2 is an asymmetric film with a bare 8 µm active layer on top of a 97 µm polyester layer. The thin active layer of HD-V2 makes it ideal for measuring high flux beams, such as the low energy component of a TNSA spectrum, and therefore is often used as the first layers in a film stack. EBT3, with its relatively thick active layer, is then used for subsequent layers to measure the low fluxes of protons at higher energies.

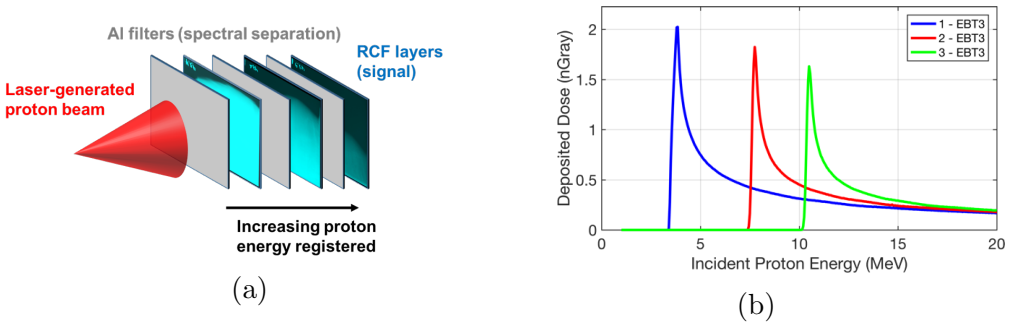


Figure 3.7: (a) Diagram of a radiochromic film stack. (b) Proton energy deposition curves for each RCF layer, showing dominant energy absorption due to Bragg peak. Calculated using Geant4.

# Chapter 4
# LSP Simulations of TNSA of Protons and Positrons

## 4.1 Particle-in-Cell Techniques

Extensive simulations were performed using the particle-in-cell (PIC) code LSP. The PIC technique is a powerful but computationally demanding approach to modelling plasmas. Conceptually straightforward, it models individual particles and their interaction with electromagnetic fields. This fundamental treatment of particles allows PIC to handle non-Maxwellian distributions, which are often created in ultra-intense laser-plasma interactions and cannot be modelled with hydrodynamic codes. PIC uses two basic simplifications to maintain manageable computational requirements. First, weighted 'macroparticles' are used to represent large numbers of real particles (Figure 4.1a). Realistic particles numbers can be up to $10^{23}$ for solid densities, which is not feasible to be simulated; typical PIC runs have $N = 10^5$ – $10^9$ macroparticles. Second, interactions are not calculated directly between macroparticles; instead fields are defined at nodes on a grid, and interpolated to positions between nodes (Figure 4.1b). This allows the complexity of PIC runs to scale like $O(N)$, instead of the $O(N^2)$ scaling for direct, particle-to-particle interactions, and is equivalent to working with charge density in a given region [15]. The grid introduces several restrictions, namely wavelengths smaller then the grid spacing (cell size) cannot be resolved, and interactions between particles within a cell (collisions) must be treated separately (see section 4.1.3). Full-scale, 3D PIC simulations are still often impractical, and consequently 2D simulations are the standard. This introduces an additional source of error in the fields: in 2D PIC simulations fields fall-off $\propto 1/r$, unlike the true $1/r^2$ in 3D. For many

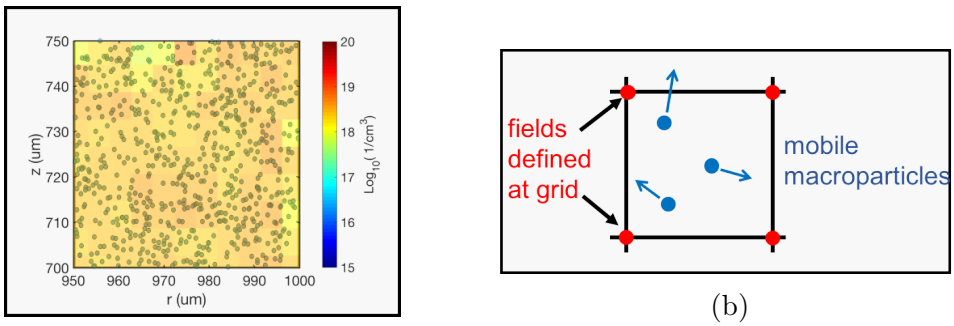


(a) (b)

Figure 4.1: Basic PIC components. (a) Plasmas are formed from weighted macroparticles. (b) Fields are calculated on a grid, and interpolated to particles.

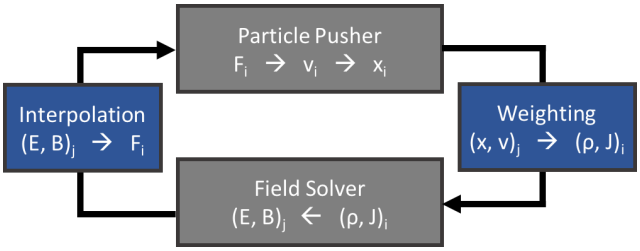


Figure 4.2: The cycle of calculations in a PIC time step. From [15].

cases, however, 2D PIC simulations prove adequate for exploring the salient physics features of plasma systems. Simulations in 3D RZ cylindrical can also be used to more accurately model field behaviour [149].

The fundamental algorithm of a PIC consists of two components: a *particle pusher*, which takes the forces and calculates updated particle positions, and a *field solver*, which calculates the electromagnetic fields on the grid given the charge and current distributions. A time step consists of both components, and is illustrated in Figure 4.2. The details of these components in the LSP code will be discussed in the next two sections.

### 4.1.1 Field Solver

Electromagnetic fields are solved through the finite-difference, time-domain (FTDT) approach on a Yee staggered mesh. Calculations are performed us-

ing the leap frog method and second order, centred derivates. This standard explicit approach has strict time step requirements in order for numerical stability to be maintained. The electron plasma and cyclotron frequencies must be resolved such that $\omega_p \Delta t < 2$ and $\omega_c \Delta t < 2$. The Courant limit $c\Delta t \leq \Delta x$, which requires that particles not travel more then one cell per time step to ensure stability, must also be obeyed.

A key advantage of the LSP code is its implementation of implicit algorithms, which allows future field/particle values to be calculated through a combination of present and future values. Implicit simulations do not need to resolve the plasma and cyclotron frequencies to maintain stability, and therefore large time steps can be used. This allows solid density plasmas to be handled with greatly reduced computational requirements. The direct implicit algorithm uses an equal split of electric field at the old and new positions and times.

The electromagnetic field equations are:

$$\frac{\partial \boldsymbol{E}}{\partial t} = \nabla \times \boldsymbol{B} - \boldsymbol{J} - \langle \boldsymbol{S} \rangle \cdot E \tag{4.1}$$

$$\frac{\partial \boldsymbol{B}}{\partial t} = -\nabla \times \boldsymbol{E} \tag{4.2}$$

where $\boldsymbol{J}$ is the current density from the first particle push and $\boldsymbol{S}$ is the susceptibility tensor constructed from particle charge and current on the grid. The finite-difference forms of Equation (4.1) and Equation (4.2) can be solved iteratively using the Alternating Direct Implicit (ADI) method, or directly using matrix inversion (Matrix Solution) and a two $\Delta t/2$ steps [150]. The latter allows large time steps and greatly relaxes the plasma frequency constraint $\omega_p \Delta$, but must resolve the cyclotron frequency $\omega_c \Delta t < 5$ [16]. The improved runtimes resulting from the larger time step mean that the Matrix Solution solver is typically employed.

### 4.1.2 Particle Pusher

LSP uses the Boris technique for particle pushing, in which the electric and magnetic components of the Lorentz force are separated into a half push for the electric field, a rotation with the magnetic field, then the remaining electric field push [151]. The 'averaged' explicit algorithm uses spatially averaged fields from the grid and is momentum conserving (no particle self-forces). The implicit advancement of particle momentum uses an energy conserving 'primary' push which finds the electromagnetic solution for each particle position. The explicit constraint that the Debye length must be resolved, $\lambda_D/\Delta t < 1$, or numerical heating will occur is significantly relaxed with the implicit primary option. This allows solid density plasmas to be simulated with much large cell sizes then would otherwise be possible.

The particle push formula is:

$$\boldsymbol{p}_{n+1/2} = \boldsymbol{p}_{n-1/2} + \Delta t \left[ \boldsymbol{a}_n + (\boldsymbol{p}_{n-1/2} + \boldsymbol{p}_{n+1/2}) \times \frac{q}{2\gamma_n mc} \boldsymbol{B}_n(\boldsymbol{x}_n) \right] \tag{4.3}$$

where $n$ is the time step index, $\Delta t$ is the time step, $m$ is the mass of the particle, $c$ is the speed of light, and $\gamma$ is the Lorentz factor. The explicit algorithm uses electric field values at the current time:

$$\boldsymbol{a}_n = \frac{q}{m} \boldsymbol{E}_{\boldsymbol{n}}(\boldsymbol{x}_{\boldsymbol{n}}) \tag{4.4}$$

The implicit push uses an average of the old electric field value and the future value:

$$\boldsymbol{a}_n = \frac{1}{2} \left[ \boldsymbol{a}_{n-1} + \frac{q}{m} \boldsymbol{E}_{n+1}(\boldsymbol{x}_{n+1}) \right] \tag{4.5}$$

This is accomplished by splitting the push into two steps [152]. The first push stage ignores the future field values, i.e. $\boldsymbol{E}_{n+1}(\boldsymbol{x}_{n+1}) = 0$, while the

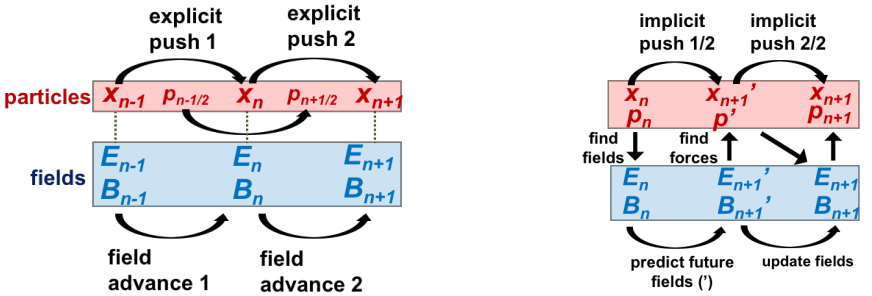


(a) (b)

Figure 4.3: The order in which particle pushes and field updates are carried out in LSP. (a) The standard explicit leapfrog algorithm. (b) The direct implicit push, carried out in two stages. Values with ticks (') are calculated using the predictive algorithm. From [16].

second predicts the field values at the next time step, $\boldsymbol{E}_{n+1}(\boldsymbol{x}_{n+1})$, from a linear expansion of Maxwell's equations and the particle's equations of motion after the first push. The cumulative error from this prediction is corrected gradually [150]. The order of operations for this direct implicit scheme is shown in Figure 4.3b.

An inertial fluid algorithm is available, which improves energy conservation by calculating an ensemble velocity for particles within a cell and adding a pressure gradient term, $P_e \nabla V_e / n_i m_i$, to the equations of motion. This greatly reduces the number of particles necessary to conserve energy; a kinetic particle description might require ∼100 particles per cell while equal or better accuracy can be achieved with $< 10$ fluid particles. Hybrid operation is possible, with kinetic species interacting with fluid species, and particles can be migrated between fluid and kinetic descriptions based on their kinetic energy and temperature. The fluid technique is typically used to described cold, high density electrons, such as the bulk of a solid laser target, that form the background for energetic kinetic electrons accelerated by the laser. In practise, the chief advantage of fluid particles is that the lower particle count allows simulations to be run to much longer times.

### 4.1.3 Collisions

Ultra-intense LPI on solid target leads to plasmas that are initially cold and very density ($\sim 10^{23}$ cm$^{-3}$), a regime in which collisions cannot be neglected. Coulomb forces between particles in PIC codes are separated into two categories: (1) long range interactions, where the separation between the particles is greater then a cell length, and (2) short range interactions between particles within a cell. Physically, the cutoff between these interactions is set by the electron Debye length. Long range interactions are handled with the electromagnetic fields defined by the grid, and represent collective effects. Short range interactions are defined as collisions for PIC codes, and in LSP are handled using either the Jones model (the default) or the binary collision model [151].

The Jones model simplifies collisions by assuming a particle distribution, and sampling from this distribution to scatter particles [153]. In each cell the mean momentum for each particle species, in each direction, is calculated and used to create drifting Maxwellian distributions. This effectively establishes a "collision field" as a grid property, which is the 'friction' term output for LSP scalar files (for fluid species the pressure gradient plays the same role). Collision are then modelled by taking each particle, sampling a particle from the Maxwellian distribution, and elastically scattering them in the center-of-mass frame of the sampled particle. The implementation of this algorithm uses the grid quantities of $n$, $T$ and $< v >$ to find the collision field, and the force due to collisions is included in the Lorentz particle push.

The Binary Collision Model (BCM) is the more accurate but computationally intense method, in which pairs of particles within a cell are assembled at random and scattered off each other. The BCM technique originates with Takizuka and Abe [154], and was extended by Nanbu to follow the Spitzer collision rate and treat many small angle collisions by one large angle collision [155]. The BCM model should be used when the particle velocity distribution

is not Maxwellian. It conserves momentum and energy exactly when Spitzer collision rates are valid.

The probability of scattering for both the Jones and Binary algorithms is determined by the Spitzer collision frequency, by default. For a Maxwellian distribution the Spitzer rate is given by:

$$\nu_{ei} = \frac{n_e e^4}{16\pi\epsilon_0^2 m_e^{1/2}(K_B T_e)^{3/2}} \ln\Lambda \tag{4.6}$$

For low temperatures, such as room temperature, Equation (4.6) becomes unrealistically large due to the $T^{-3/2}$ dependence. To handle this regime (solid density, temperatures on the order of an eV) the Lee-More-Desjarlais (LMD) model [156, 157] can optionally be used to find collision rates. To determine conductivity the LMD model uses an electron density calculated from both quantum atomic theory (Thomas-Fermi ionization) and statistical treatments (non-ideal Saha ionization). Particle interactions are found using fits to quantum mechanical atomic models. It should noted that the ionization state considered by LMD is not related to the ionization state in LSP simulations, which is handled using a separate algorithm. The LMD collision rates can be used with the Jones PIC collisional algorithm; the BCM model can only use Spitzer collision rates, though recent work has sought to modify it to allow the LMD model [158]. An alternative approach is to cap the Spitzer collision frequency to avoid unrealistic low temperature values. A typical capped rate is $\nu_{ei} = 10^{16}$ Hz.

Lastly a dE/dx Monte Carlo model is available for highly non-collisional species in dense mediums. Particles with this model do not collide with each other or other dE/dx species. Angular scattering and energy loss is handled using cross-sections, with ions using the Li and Petrasso model [159]. Particles can be migrated between scattering (Jones or Binary) and dE/dx models based on energy thresholds.

### 4.1.4 Particle Generation and SAK Modifications

Secondary particles are generated in LSP using Monte Carlo calculations done by the Integrated Tiger Series (ITS) code, which is built into LSP [160]. Electrons in the ITS medium with energies above 5 keV undergo ITS transport calculations, which determine energy loss, scattering and secondary particle generation. Secondary particles which can be produced are Bremsstrahlung photons and electron-positron pairs, which are created exclusively through the Bethe-Heitler mechanism (Section 6.1). An external cross-section file from the XGEN component of ITS is required for the elements used.

For the positron simulations the SAK (Swiss Army Knife) version of LSP was used; this was developed at Ohio State University, primarily by Chris Orban and Anthony Link. It includes many modifications to ITS that allow positrons to be handed properly. Knock-on electron production (ionization from electron-ion collisions) was disabled through an SAK directive, as it is not integrated with the LSP ionization routines and therefore does not conserve charge (i.e. electrons are generated with no corresponding change in ion ionization state). Photon energy loss through Compton scattering (inelastic electron-photon scattering) is included, but the corresponding energy gain by electrons was disabled with an SAK directive to conserve charge. Several SAK modifications are necessary to keep low energy particles on the grid, but not be destroyed or unnecessarily transported by ITS. SAK also fixes various errors in the LSP scattering algorithm that are present in version 10 of the code. The Coulomb logarithm calculation is fixed, as well as the angular scattering algorithm. The ion contribution to scattering is calculated from the ion atomic number, instead of the ion charge, to be consistent with ITS. Lastly, an SAK directive is necessary to enable dE/dx scattering of positrons.

Positron results from the SAK version of LSP have been compared with experiment and good agreement has been found. The total number of escaping positrons from simulation matched experimental data well, falling in the

middle of the experimental range which had shot-to-shot variation of ∼50% [23]. It also agreed with an analytic model [161] to within ∼15%. Additionally, with fields turned off (no electron refluxing) the positron yield from LSP was shown to be within ∼20% of Geant4 Monte Carlo results, which do not model fields [23]. The stopping power and scattering of dE/dx electrons has been benchmarked by Dr. Drew Higginson, and good agreement was found with published models [162]. Additional quantitative matches between LSP simulations and experiments have been published. Higginson *et al.* modelled K$\alpha$ x-ray emission from hot electrons in cone-wire targets, and found agreement in laser-to-K$\alpha$ conversion to within the experimental uncertainty of ∼35% [163]. Schollmeier *et al.* modelled TNSA with detailed preplasma from 3D hydrodynamic simulations, and the results matched experimental proton cutoff energies to $< 7\%$ [109].

## 4.2 Effect of Proton Layer Parameters

Realistic modelling of TNSA protons and sheath field evolution depends upon accurately simulating the contaminant layer, from which the proton beam originate. Experimentally, the contaminant layer is ∼10 Å thick and consists of hydrogen, carbon and oxygen from hydrocarbons and water; x-ray photoemission spectroscopy has been used to determine a hydrogen atomic density of $2.24 \times 10^{23}$ cm$^{-3}$ for an Au foil [164]. Typical PIC cell sizes are 20 nm - 1 µm, much larger then 1 nm, and resolving such a thin layer would drastically increase the computational time of simulations. One approach taken is to use a thicker contaminant layer with reduced proton density, such that the total number of protons was roughly conserved. Additionally, the oxygen and carbon species were usually neglected. Testing was performed to determine the validity of these approximations. The proton energy spectra were created from all the particles on the grid. For all simulations a 1 ps injected electron source

was used to drive TNSA in a 50 µm target. The electron source was derived from a Titan-like LPI simulation with $I = 8 \times 10^{19}$ W/cm$^2$ and a realistic pre-plasma. Experimental data for 50 µm foil targets from the Z-Petawatt laser, which has similar characteristics to the Titan laser ($I_{peak} = 2 \times 10^{20}$ W/cm$^2$, $E \approx 100$ J, $\tau < 1$ ps, large ns-scale prepulse) showed a proton cutoff energy of ~45 MeV [109].

### 4.2.1 Cell size

The first test was the effect of cell size relative to the contaminant layer thickness. A 1 µm proton layer was defined with $n = 10^{20}$ cm$^{-3}$, and the cell size in this layer was varied from 10 nm to 1 µm (corresponding to 100 – 1 cells per layer). Figure 4.4a shows the imprint of cell size on the proton macroparticle distribution. Bands of macroparticles are visible, with the number of bands proportional to the number of cells in the initial proton layer; the beam is being driven from the bottom towards the top. The effect on proton density at late times is shown in Figure 4.4b; there appears to be little change in the general distribution of the proton beam, however transverse density perturbations seem to be seeded by the macroparticle bands. These would affect the simulated beam uniformity. The resulting energy spectra appear to be unaffected, as shown in Figure 4.4c. This suggests that if the maximum proton energy is the main parameter of interest, minimizing cell size below a given threshold is not necessary. The threshold observed was 1 cell per layer (1 µm); at this resolution the TNSA beam was not accurately modelled, as shown in Figure 4.4b.

### 4.2.2 Density

The effect of proton layer density was also studied, by varying it from $10^{19}$ – $10^{23}$ cm$^{-3}$. The layer thickness was 1 µm and cell size in the layer was 0.1 µm. The number of macroparticles per cell was not changed with density, and

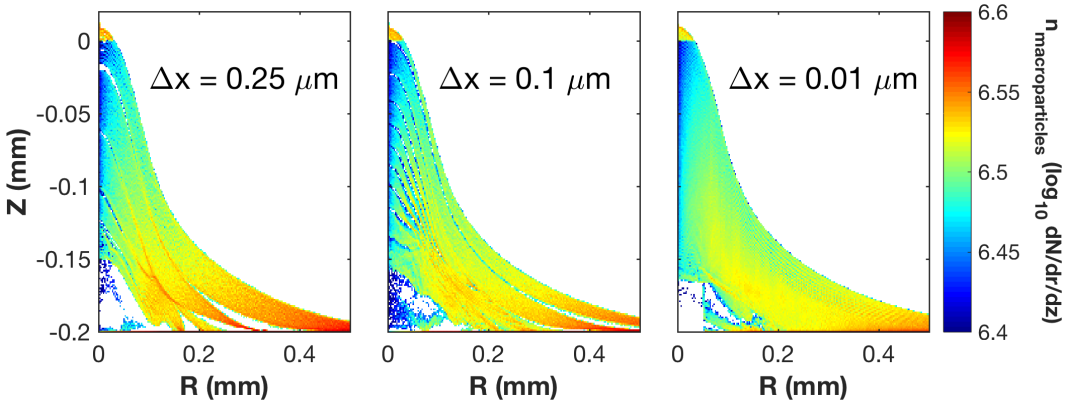


(a)

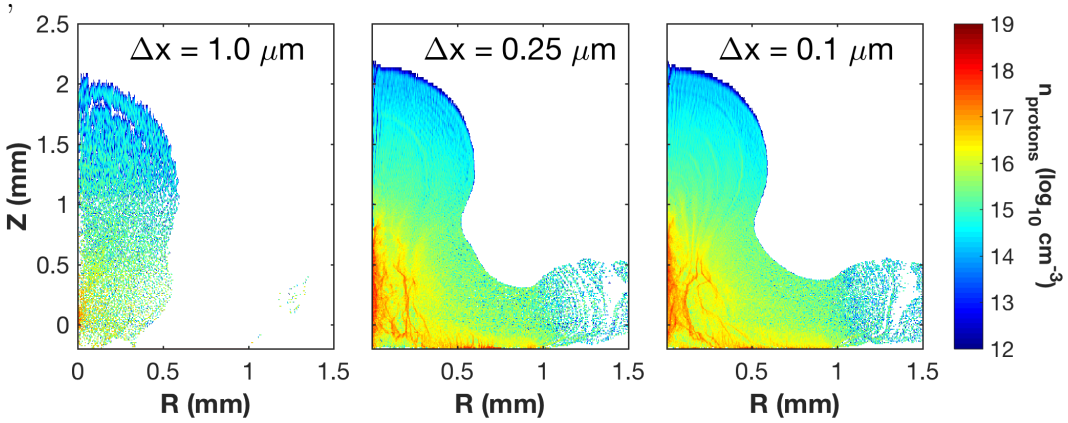


(b)

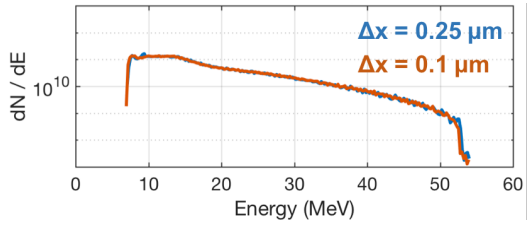


(c)

Figure 4.4: Test of proton layer resolution and TNSA. The electron source is injected from the bottom through a 50 µm thick Au target (not shown). (a) Distribution (density) of proton macroparticles for cell sizes of 0.25 µm (4 cells/layer), 0.1 µm (10 cells/layer) and 0.01 µm (100 cells/layer) at $t = 3.5$ ps. The proton layer was initially 1 µm thick with $n = 10^{20}$ cm$^{-3}$. Clear imprints of the initial particle distribution can be seen, varying with cell size. (b) Proton density at $t = 25$ ps, showing transverse density perturbations which vary with cell size. The TNSA proton beam is not resolved properly for a cell size of 1 µm (1 cell/layer). (c) Similar energy spectra result for both 0.25 µm and 0.1 µm cases.

therefore the macroparticle weighting was different in each case. The proton energy spectra are shown in Figure 4.5a. There is a maximum proton energy for $10^{20}$ – $10^{21}$ cm$^{-3}$; at higher and lower densities the cutoff decreases, and at $10^{23}$ cm$^{-3}$ there is minimal acceleration. The proton beam profiles are plotted in Figure 4.5b, and indicate that macroparticle weighting becomes an issue above $10^{22}$ cm$^{-3}$. The lower maximum proton energy seen in the $n = 10^{19}$ cm$^{-3}$ case appears to be due to depletion of the proton layer, which causes weaker electric fields at the proton front and stronger fields near the surface of the target. The lower energy of the $n = 10^{22}$ cm$^{-3}$ case is likely due to decreased fields in the higher density plasma, and also a lack of macroparticle statistics. A typical experimental maximum proton energy for a similar laser source is ∼45 MeV, as discussed above [109], which would suggest best agreement with a density of $10^{21}$ – $10^{22}$ cm$^{-3}$ from these tests. It should be noted, however, that experimental conditions such as preplasma and laser intensity profile were not matched in these simulations and so exact agreement in not expected.

### 4.2.3 Macroparticle Weighting

Tests were performed for three proton densities $n_p$: $10^{21}$, $10^{22}$ and $10^{23}$ cm$^{-3}$. For each density three particle per cell (ppc) values were used, with approximately a factor of four between each: 49, 225, and 900. Proton layer thickness was constant at 1 µm. For $n_p = 10^{21}$ cm$^{-3}$ the beam has converged for all ppc values. The $n_p = 10^{22}$ cm$^{-3}$ case appears to have converged by 225 ppc, based on a well resolved cutoff energy. It is unclear where the additional energy comes from in the time history for higher ppc values. The $n_p = 10^{23}$ cm$^{-3}$ case has too poor statistics to determine convergence from the energy spectrum, but the time history suggests that 225 and 900 ppc have a similar behaviour, distinct from 49 ppc.

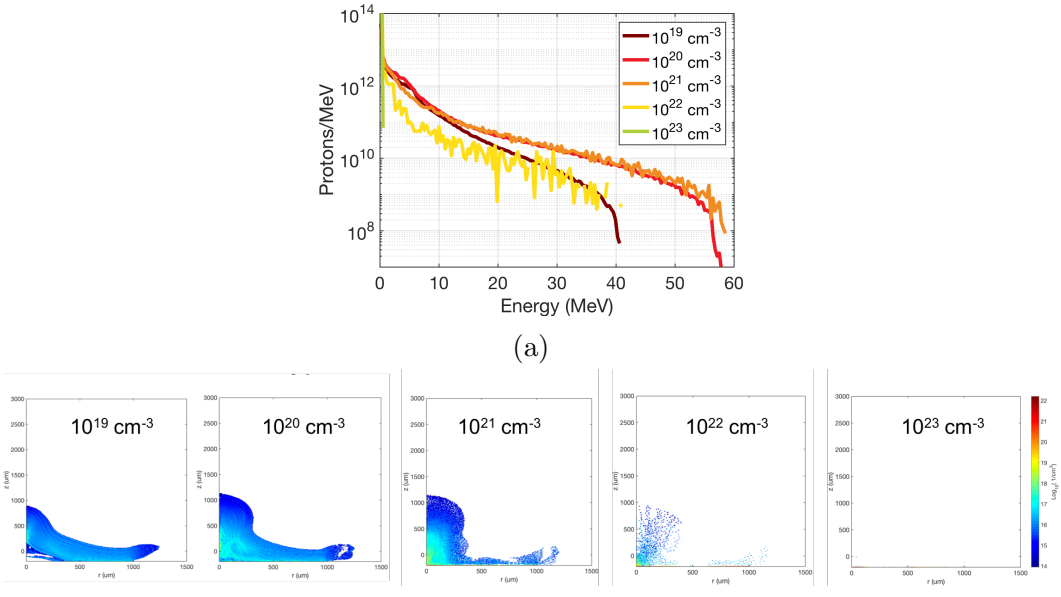


Figure 4.5: Test of proton layer density. (a) Proton spectra for varying initial densities, showing a similar cutoff at $10^{21}$ - $10^{22}$ cm$^{-3}$ and decreasing energies at other densities. (b) Proton beam density profiles. Macroparticle weighting appears to be an issue for $10^{22}$ cm$^{-3}$ and no acceleration occurs for $10^{23}$ cm$^{-3}$.

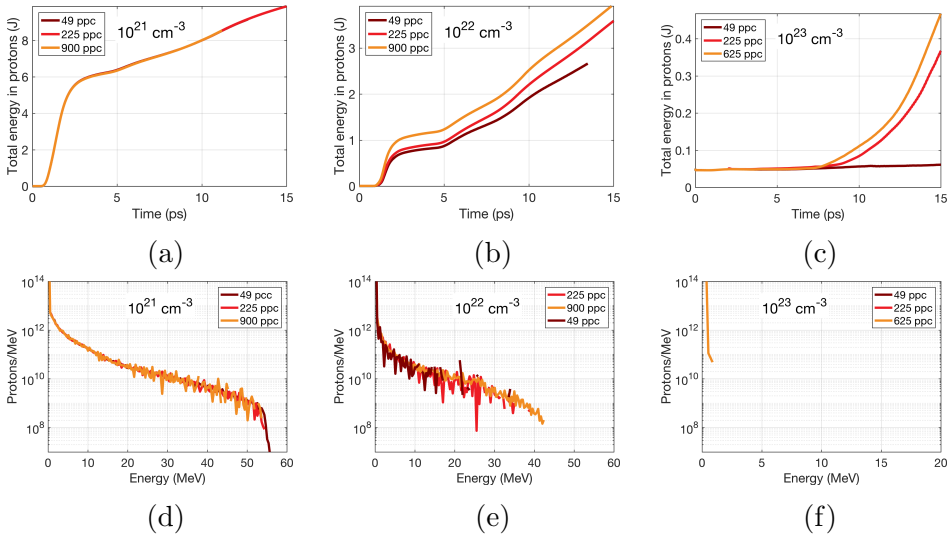


Figure 4.6: Test of macroparticle weighting with different particles per cell (ppc), for densities $n_p$ of (a, d) $10^{21}$ cm$^{-3}$, (b, e) $10^{22}$ cm$^{-3}$ and (c, f) $10^{23}$ cm$^{-3}$. Top: time history of energy in all protons on the grid. Botton: proton spectra at t = 10 ps. The initial layer thickness was 1 µm. The $n_p = 10^{21}$ cm$^{-3}$ case is converged for all ppc values. The $n_p = 10^{22}$ cm$^{-3}$ case is converged by 225 ppc. The $n_p = 10^{23}$ cm$^{-3}$ case does not experience significant acceleration, and therefore convergence is difficult to judge.

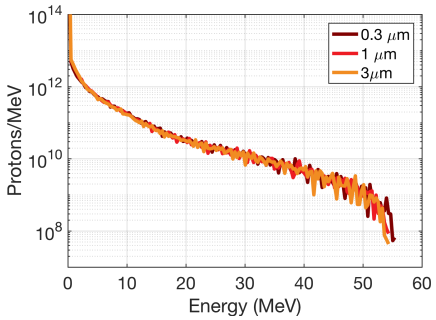


Figure 4.7: Test of proton layer initial thickness, with $n_p = 10^{21}$ cm$^{-3}$ and cell size $\Delta x = 0.1\,\mu$m. All thicknesses give similar TNSA spectra.

### 4.2.4 Thickness

The initial thickness of the proton layer was not found to have an impact on the proton beam, provided the layer was adequately resolved. To determine this the thickness was set to 0.3, 1 and 3 µm, with a density of $10^{21}$ cm$^{-3}$ and a cell size of 0.1 µm. The spectra are shown in Figure 4.7, and are identical in all cases. This is consistent with the TNSA model, where the sheath field peaks on the surface of the proton layer and then gets gradually screened out inside the beam. Protons at the back of the layer have no influence on the front, and provided the layer is not depleted (every proton accelerated) similar spectra should result for different thicknesses. Proton depletion has only been observed for laser energies exceeding 1 kJ [165].

### 4.2.5 Carbon Ions

The contaminant layer is typically defined only with protons, to simplify the simulations. This neglects the heavier ions, carbon and oxygen, that are also present in real contaminant layers. To determine the accuracy of this simplification a run was performed with a carbon species uniformly mixed with the protons in the contaminant layer. The proton density was $n_{\text{protons}} = 10^{21}$ cm$^{-3}$ and the carbon density was $n_{\text{carbon}} = 0.5 \times 10^{21}$ cm$^{-3}$; this 2:1 ratio was chosen as a simple test case to represent $CH_2$ plastic, and closely approximates the

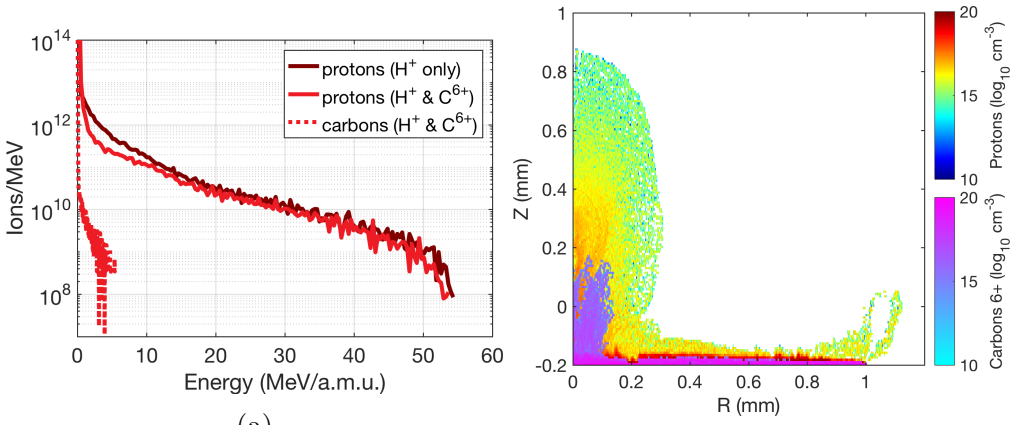


(a) (b)

Figure 4.8: Test of the presence of carbon ions in the contaminant layer. The layer was 1 µm thick, with proton density $n_p = 10^{21}$ cm$^{-3}$ in both cases and carbon density $n_c = 5 \times 10^{20}$ cm$^{-3}$. (a) Carbon and proton spectra. The maximum proton energy remains the same when carbons are present, while the low energy protons are reduced in number. (b) Density plot with proton and carbon beams overlaid, showing limited expansion of carbon ions.

ratio in hydrocarbons with long chains. The carbon species was fully ionized. Figure 4.8a compares this run to a proton-only run with the same proton density. A similar proton cutoff is reached, and the proton spectra are comparable until low energies. This is consistent with the shielding effects of the carbon ions, which experience reduced acceleration and smaller plasma expansion due to their lower charge-to-mass ratio. Protons are quickly accelerated in front of the carbons, where they experience the full sheath field and reach similar maximum energies to the proton-only case. Lower energy protons correspond to those that are in the back of the beam, where carbons are present and reduce the accelerating fields.

### 4.2.6 Summary of Tests

The above tests indicate that proton density in the initial layer is the critical factor, with similar acceleration between $10^{20}$ – $10^{21}$ cm$^{-3}$ and a reduction at higher and low densities. Initial layer thickness does not affect the beam, provided that it is resolved by several cells (at least 3-4). Finer cell sizes

may reduce artificial transverse modulations, which influence beam quality, but appear to have no affect on the final spectrum. Macroparticle weighting is important, and the particle per cell value necessary for convergence depends up the density used. Finally, mixing carbon ions with protons in the initial layer does not change the proton spectrum at higher energies ($> 20$ MeV), while at lower energies there is a reduction in accelerated protons. This confirms the initial assumption that carbons can be safely neglected in the simulations while still capturing most of the TNSA beam properties.

# Chapter 5
# The Imaging Proton Spectrometer

## 5.1 Properties and Analysis

The Imaging Proton Spectrometer (IPS) was the primary proton diagnostic for the experiments performed in Chapter 7. It is a magnetic spectrometer originally designed to measure low energy protons for stopping power experiments [1]. The detection method is image plates (Section 3.2.2) which can be loaded on the side for low energy protons (0 - 2.4 MeV) and the rear for high energy particles (> 2 MeV) (see Figure 5.1a). The width of the entrance slit can be adjusted using spacers, but was fielded at 100 µm for the work done here. The height of the slit is ∼5 cm, which allows 1D imaging to be performed; this is useful to distinguish between multiple sources, such as the main proton beam and emission from the target mounting stock (a common secondary source of protons). A nickel wire mesh across the slit provides a spatial fiducial, allowing protons to be traced back to their vertical entrance position. The magnetic field in the centre of the instrument is ∼0.3 T, the field minimum, and increases to ∼0.6 T close to the magnets (Figure 5.1b).

### 5.1.1 PSL to Ion Conversion

To determine particle flux from image plates a response function (PSL/proton) is required; two proton response functions have been published for TR image plates. Mancic *et al.* used a TNSA proton source and calibrated the IP response with RCF for 5-20 MeV protons and CR39 for lower energies [17]. Bonnet *et al.* modelled the energy deposition with Geant4, and experimentally

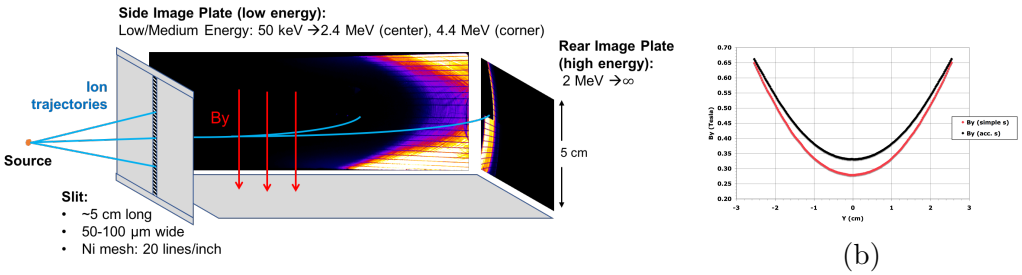


(a) (b)

Figure 5.1: (a) Diagram of the Imaging Proton Spectrometer (IPS), the primary ion diagnostic. (b) Magnetic field strength in the vertical direction, versus vertical position. Plotted from calculations for simple and accurate geometries. From Andy Hazi.

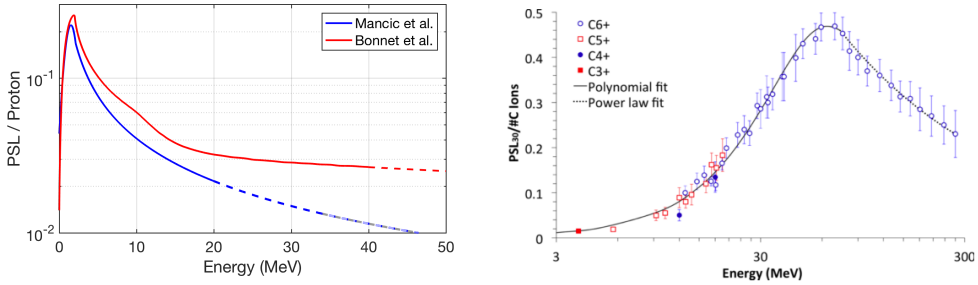


(a) (b)

Figure 5.2: (a) Comparison of Mancic *et al.* [17] and Bonnet *et al.* [18] proton response curves for TR image plates. Dashed lines indicate extrapolation beyond the published ranges. (b) Carbon response curves for TR image plates, from Doria *et al.* [19].

calibrated their curve with a proton accelerator and a silicon diode detector [18]. These responses are compared in Figure 5.2. It can be seen that there is significant disagreement for $> 2$ MeV protons, with Bonnet giving higher PSL/proton. The Bonnet response was selected over the Mancic response due to their thorough modelling and better controlled experimental calibration. In contrast to the highly variable laser-ion source used by Mancic *et al.*, Bonnet *et al.* used an ion accelerator to deliver mono-energetic proton beams with known intensities. Additionally, their beam fluences were measured with a silicon diode detector, which involves fewer assumptions then Mancic's RCF measurements. Bonnet *et al.* provided deposition calculations up to 40 MeV.

High energy ions were observed on the shock acceleration experiments, as discussed in Section 7.2.3. These could be either carbon or oxygen, as they have the same charge-to-mass ratio at full ionization, but carbon was assumed due to the greater abundance of carbon in Mylar ($C_{10}H_8O_4$). For PSL to ion conversion the carbon calibrations published in Doria *et al.* were used [19]. They utilized TNSA ions and CR39 to measure carbon energies up to 300 MeV, with a response that was relatively constant with charge state (Figure 5.2b). The lack of dependence on charge state is due to the behaviour of stopping power, which is determined solely by the incident ion's kinetic energy and its effective charge in matter [148].

### 5.1.2 Filter Correction

The IPS is solely a magnetic field-based diagnostic, and therefore does not provide discrimination between ions with different charge-to-mass ratios. To ensure a pure proton signal aluminum foils are often placed on the image plates, which filters out heavier ions. The foil thicknesses range from 12.5 µm (Reynolds kitchen wrap, a cheap and common foil) to 300 µm, with the thickness selected based on the breakthrough energies of protons and carbon ions (Figure 5.3). Carbon, in the form of hydrocarbons, is the most common non-Hydrogen element typically present in the contaminant layer [164]. Oxygen from water may also be present.

Ions lose energy as they travel through filters, resulting in an energy-dependent, energy downshift which can be significant for particles near the breakthrough energy (those that almost stop in the foil). The response of image plates is energy-dependent, and therefore this energy downshift must be accounted for to accurately determine ion number (Figure 5.4a). The following procedure was used to compensate for the filter effect. First the energy downshift was calculated using TRIM [20]. A TRIM input file containing a user-defined population of particles was generated using Matlab (Appendix C

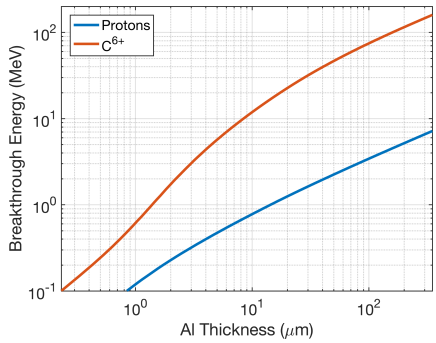


Figure 5.3: Proton and $C^{6+}$ breakthrough energies in aluminum. Calculated using SRIM [20].

1b), with energies spanning the energy range of interest and $> 10$ particles per energy bin. These particles were sent through an Al foil of a given thickness, the energies of the transmitted particles were recorded and the energy downshift of each particle used to create a power curve (Figure 5.4b). Each filter thickness required a different set of calculations.

The experimental spectra were filter-corrected using a Matlab function (Appendix C, 1d). The energy downshift curves were used to calculate the shifted spectra, which were then used for the PSL to ion number conversion (Section 5.1.1). The final spectra consisted of the corrected particles numbers along with the original energy values. Figure 5.4c and Figure 5.4d show this process for a sample $C^{6+}$ spectrum. The increase in effective filter thickness with non-normal angle of incidence was neglected. This is a reasonable approximation for the high energy rear image plate, where an estimated maximum angle from a circular (cyclotron) trajectory is 15°, resulting in a path increase of $\cos(15°) \approx 3.5\%$.

For particles very close to the breakthrough energy a fraction of the incident population will be transmitted through the filter due to energy straggling, i.e. broadening of the ion energy distribution as it propagates. TRIM was used to estimate the effect of this fractional breakthrough. A narrow energy group of particles was sent through a foil, with the number of particles per bin increased to give better statistics. The fraction of particles transmitted was recorded;

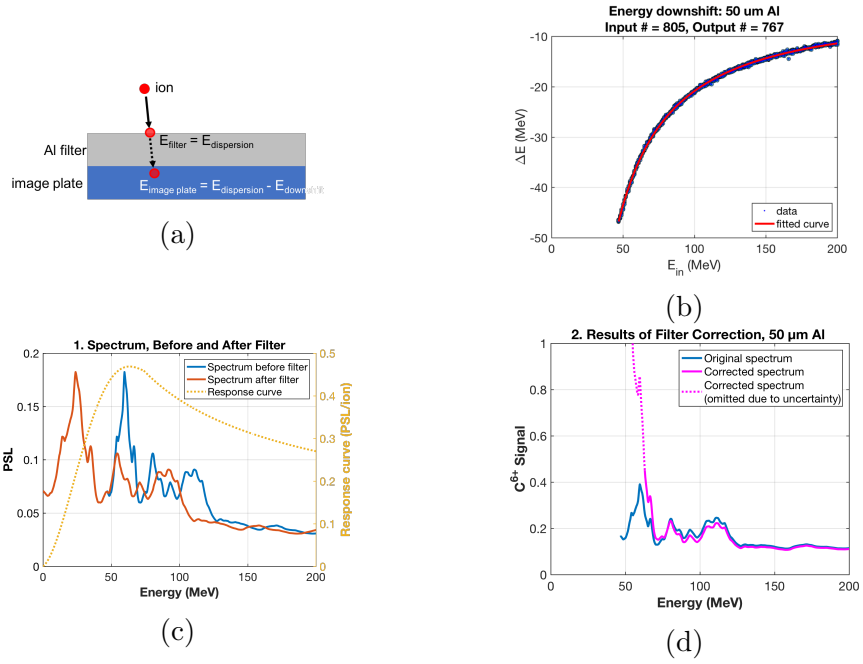


Figure 5.4: (a) Diagram of ion energy loss in filters. (b) Energy downshift for $C^{6+}$ ions in 50 µm Al. (c) Original spectrum (incident on filter) and downshifted filter (incident on image plate) with image plate response curve overlaid (dashed line, corresponding to right axis). (d) Original measured spectrum and spectrum corrected for filter effects. The large increase in signal near the cutoff, shown as a dashed line, is due to division by a small number as the breakthrough fraction becomes negligible, and is not physical.

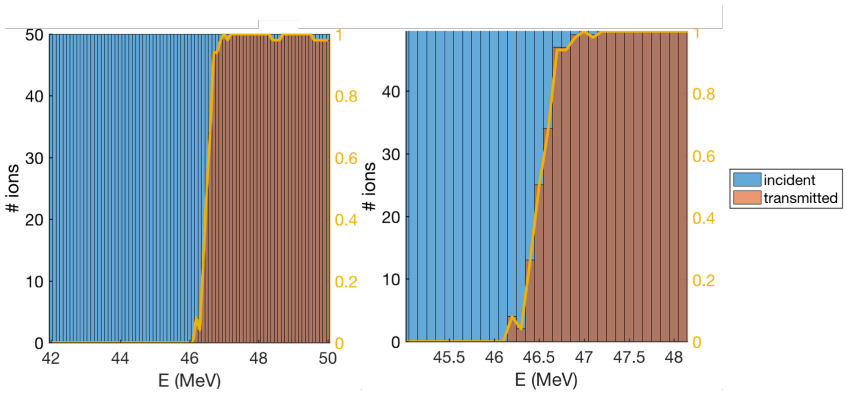


Figure 5.5: Fractional breakthrough of Carbon 6+ ions in 50 µm Al. Calculated using TRIM [20].

results are shown in Figure 5.5. For the given case ($C^{6+}$ ions in 50 µm Al) the energy range in which fractional breakthrough was a significant effect was ∼1 MeV. This is a relatively small range, and occurs within the ∼5 MeV spectral region (from the cutoff peak) where the standard filter correction is most uncertain due to a lack of particles, as shown in Figure 5.4d. Consequently, it was concluded that the high uncertainty near the filter cutoff makes fractional breakthrough compensation a higher order correction that is not important for the final spectra.

### 5.1.3 Background Subtraction

Background subtraction on the IPS is not straightforward, as there is no region of the spectrum that is guaranteed to be free of proton signal. This makes it necessary to calculate a background level from the high energy region of the spectrum, with the assumption that no proton signal is present above the proton cutoff. For a fitting region above 50 MeV this is a reasonable assumption; the highest energy TNSA protons reported to date are 85 MeV using the PHELIX laser and sub-micron targets, with much more optimal conditions then at Titan [166]. For 1D line-outs a linear fit was used; this was the simplest function that fit the background behaviour in the selected region.

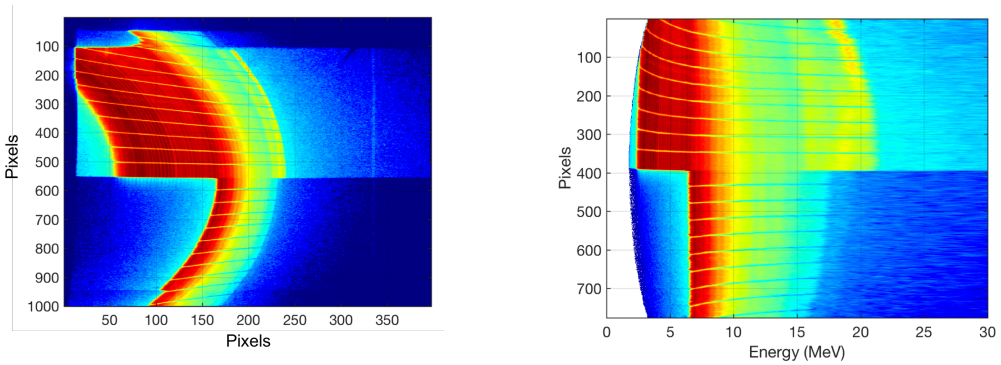


(a) (b)

Figure 5.6: (a) Raw data from the IPS rear image plate. (b) Dewarped spectrum.

### 5.1.4 Image Dewarping

The proton beams generated from near-critical density targets were spatially structured (Section 7.2.2), making it necessary to analyze the IPS signal off the central vertical axis. This required accounting for the curvature of the signal from the non-constant magnetic field, as can be seen in Figure 5.6. The approach taken was to find the $B(z)$, where z is vertical position in the spectrometer, using the breakthrough of protons in 300 µm Al as an energy reference. The dispersion was then interpolated for each z, i.e. each pixel in the vertical direction. This is an approximation which neglects the non-zero vertical momentum of the protons - it assumes a constant $z_0$ while in fact the particles traverse a range of z. The accuracy of this approach will be addressed shortly. A full 3D description of the magnetic field of the instrument, along with particle tracing, would be necessary to generating a more accurate 2D dispersion. This was the approach taken in [167], but was not available for the analysis here.

The relative magnetic field strength with height, B($z$), was found using the 6.5 MeV proton breakthrough energy in the 300 µm filter as a location reference (Figure 5.7). The particle path was then calculated with this B-field relationship. The motion of a charged particle in a constant magnetic field

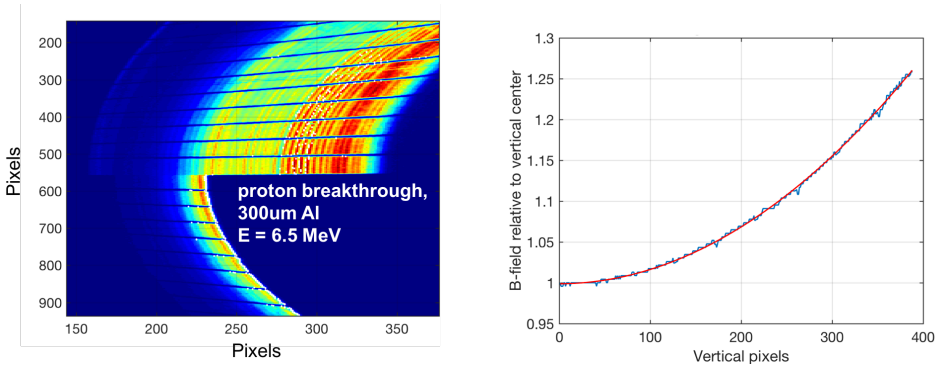


(a) (b)

Figure 5.7: (a) Spectrum showing proton breakthrough in 300 µm Al, giving reference pixel positions for E = 6.5 MeV protons. (b) Relative B-field strength.

is simply a circle with radius equal to the gyroradius $r_g = mv_\perp/Bq$. The dispersion, or position vs. energy relationship, can then be found from the intersection of this circle with the imaging plane. Choosing the origin of the coordinate system as shown in Figure 5.8 then gives the circle equation:

$$\begin{aligned} (x - x_0)^2 + (y - y_0)^2 &= r^2 \\ (r_g - d)^2 + L^2 &= r_g^2 \\ d^2 - 2r_g d + L^2 &= 0 \end{aligned} \tag{5.1}$$

This quadratic equation can be solved for d, the deflection distance. Using the magnetic field from the reference breakthrough energy of 6.5 MeV in 300 µm Al and stepping through the vertical pixels gives a 2D dispersion. The signal was then interpolated to an energy vector using this dispersion. A sample dewarped spectrum is shown in Figure 5.6.

The accuracy of this approach decreases with distance from the central axis, as the assumption of completely horizontal incidence becomes increasingly invalid. It also increases at energies far from the reference energy of 11.4 MeV. The error can be estimated by the degree in which the iso-energy contours depart horizontally from the central value, as the central axis dispersion is

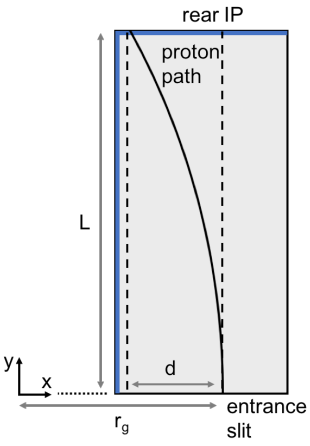


(a)

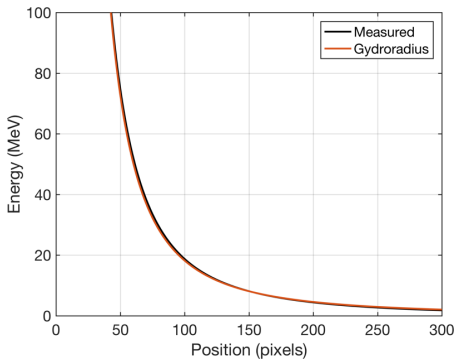


(b)

Figure 5.8: (a) Diagram of dispersion calculation in IPS, with the origin set at the gydroradius circle centre. The field was measured to rise over ∼1 cm near the entrance slit, with L = 15 cm. (b) Fields on the centre line.

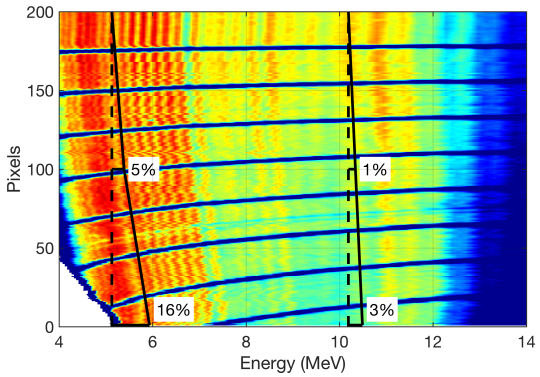


Figure 5.9: Estimation of IPS dispersion percent error using the interpolation dewarping technique.

known well (Figure 5.8). Figure 5.9 illustrates a sample error calculation. For energies close to 5 MeV the maximum error is 15% (IP edge), decreasing to <5% halfway between the IP edge and centre. For energies near 10 MeV the corresponding error was 3% and 1.5%. As the primary signal for the shock data was near the centre of the image plate and higher then 5 MeV, this degree of accuracy is acceptable. If more accuracy is needed for signal near the IP edge, a full 3D particle tracing approach would be necessary [167].

### 5.1.5 Solid Angle

The solid angle calculations for the IPS are more complicated then for a typical pinhole diagnostic, as the acceptance angle in the vertical direction is not bounded. Instead, angle in the slit direction must be calculated from the wire shadows, which provide a known spatial spacing at the slit entrance. The typical diverging source also means that the solid angle is not constant with energy or vertical pixel.

For line-outs on the central axis the solid angle is simplified. The approximation of negligible curvature is valid for the distances and solid angles given here, and therefore $\Omega \approx ab/d^2$. The slit width is known, and was $a = 100\,\mu\text{m}$ for the work here. The pixel height is known and set by the scanner resolution, but this corresponds to a smaller distance at the slit due to the magnification of the point source-like proton beam. This gives $b = R \times M = R \times L_{\text{IPS}}/d_{\text{IP}}$, where $R$ is the scanner resolution (either 50 or 100 µm), $L_{\text{IPS}} = 15\text{cm}$ is the distance from the IP to the slit, $d_{\text{IP}} = d_{\text{IPS}} + 15\text{cm}$ is the total distance from the source to the IP, and $d_{\text{IPS}}$ is the distance from the source to the IPS slit. The solid angle is then:

$$\Omega_{\text{central axis}} = \frac{100 \times 10^{-6}\text{m}}{d_{\text{IPS}}^2} R \left( \frac{0.15\text{m}}{d_{\text{IPS}} + 0.15\text{m}} \right) \tag{5.2}$$

For signals off of the central axis the magnification per pixel varies and this equation no longer holds. Figure 5.10 shows a 2D map of the solid angle for $d_{\text{IPS}} = 0.53m$.The map was generated using the Ni wire mesh (20 lines/inch) as a spacial fiducial. The magnification was calculated with the known 1.27 mm spacing between wires, and solid angle between wire shadows was assumed to be constant It can be seen that the solid angle varies by $< 5\%$ in the vertical direction and up to 15% in the energy axis (from 5 MeV to 20 MeV). These variations are large enough that when comparing signals with large angle or energy differences, the solid angle effect must be taken into account.

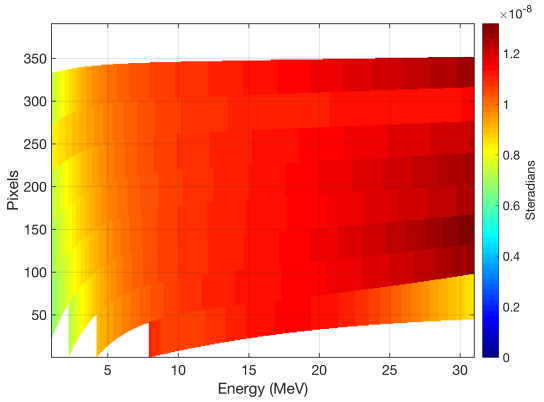


Figure 5.10: Map of IPS solid angle. Both upper and lower wire shadows are necessary to estimate solid angle, therefore regions near the edge of the IP cannot be calculated.

## 5.2 Spectral Oscillations

A unique and puzzling property of the IPS is that its spectra exhibit oscillations that are present for a wide variety of laser and target conditions. These oscillations can clearly be seen in Figure 5.7. Similar proton features have been observed with other diagnostics, though not as clearly or consistently as with the IPS. These previous observations are summarized in Appendix A, Section A.1. The consistency of the IPS oscillations, and the diverse set of experimental interactions for which they appear (solid density targets with and without preplasma, near critical density targets, $1\omega$ and $2\omega$ beams) indicates that the mechanism is highly robust, and unlikely to caused by a physical phenomenon that would be highly dependent on interaction conditions. A more likely source is the IPS itself, which is the common factor between all these experiments. The IPS is a relatively simple instrument, however, and the feature that could cause this behaviour is not obvious. A number of tests were done to try and determine the cause of the modulations; these test are described and summarized in Appendix A, Section A.2.

Simulations of the IPS and TNSA beams provide an additional avenue for exploring various theories of the modulations, and could guide experimental

testing. PIC is well suited to the task, as it handles collective plasma effects well, can model the generation and transport of TNSA beams, and easily renders the simple geometry of the IPS. The attempts undertaken to model the IPS modulations are described in Appendix A, Section A.3. However, at this point no simple explanation of the modulations has been found.

# Chapter 6
# Spectral Features of Laser-Generated Positrons

Relativistic, high flux positrons beams are a unique consequence of ultra-intense lasers interacting with thick, high Z solid targets. These beam could provide an opportunity to study astrophysical phenomenon such as the fireball model of gamma-ray bursts [168] in the laboratory, as well as fundamental physics of ultra-intense LPI. Numerous positron generation experiments were performed during the course of this degree using the Titan and OMEGA EP lasers, resulting in publications describing the beam emittance [169], scaling with laser parameters [23] and target material [170]. No work to date has dealt with positron spectral features, however, beyond pointing out that the characteristic quasi-monoenergetic spectral peak results from acceleration from the sheath field [71]. Data from high energy shots at OMEGA EP displayed spectral features not present for lower energy shots, and the origin of these features are investigated here using LSP simulations.

## 6.1 Positrons from Ultra-Intense LPI

Positrons are created and accelerated in intense LPI through a multi-step process, illustrated in Figure 6.1. The first step is the production of relativistic, hot electrons, discussed in detail in Chapter 2, which in turn generate bremsstrahlung photons with MeV energies. Photons with $E > 1.022$ MeV can interact with nuclei to create electron-positron pairs through the Bethe-Heitler (BH) process [171], which is the dominant mechanism for thick ($\sim$mm) targets. The more direct Trident process, where electrons interact directly with nuclei to produce pairs through a virtual photon, does not contribute significantly to

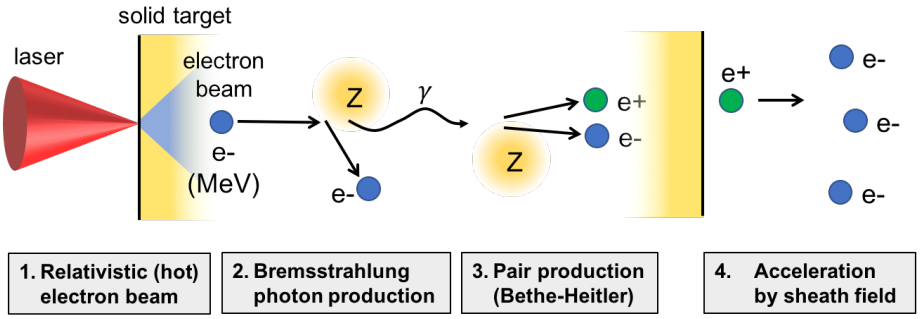


Figure 6.1: Stages of positron generation, from ultra-intense irradiation of a solid target.

the positron yield for thick targets; for a 1 mm target the ratio of positrons from the two processes is $N_{\mathrm{BH}}/N_{\mathrm{Trident}}\sim 400$ [71].

Laser-produced positrons from petawatt lasers were first observed in 1999 by Cowan *et al.* on the Petawatt facility [172]. Positrons from a modern OPCPA-based laser system with reduced prepulse were first reported by Chen *et al.* in 2009 using the Titan laser, with a 1000× increase in signal compared to the Petawatt result [71]. These positrons are directed along the laser axis and accelerated by the sheath field to much higher energies; this accelerating field is also responsible for TNSA protons [30]. The positron energy spectrum is quasi-monoenergetic, with an energy spread as low as 15%, due to their acceleration from a nearly constant sheath field potential. This is in contrast to protons, which are accelerated by the time-varying sheath field for a relatively long time, and experience different field strengths according to their positions. For reference, a 10 MeV positron travels at 0.9988c and will traverse a 100 $\mu$m region in 0.34 ps, while a 10 MeV proton moves at 0.1448c and travels the same distance in 2.30 ps.

The probability of an energetic electron creating a bremsstrahlung photon is given by the bremsstrahlung radiation differential cross section, which for

the relativistic Born approximation and an unscreened nucleus is [173]:

$$d\sigma_\gamma = \frac{4Z^2 r_0^2}{137}\frac{dk}{k}\left[1 + \left(\frac{E}{E_0}\right)^2 - \frac{2}{3}\frac{E}{E_0}\right]\left[\ln\left(\frac{2EE_0}{k}\right) - \frac{1}{2}\right] \tag{6.1}$$

where $Z$ is the atomic number, $r_0$ is the classical electron radius, $k$ is the energy of the emitted photon (in units of $m_e c^2$) and $E_0$ and $E$ are the initial and final energies of the electron (in units of $m_e c^2$). The Born approximation uses free particle wave functions which are perturbed to the first order in Z, and are estimated to be correct to within 10% for electron energies greater then 2 MeV [173]. Using the unscreened nucleus treatment is reasonable when $E_{e-} \gg E_{\text{binding}}$, which is the case for $E_{e-} \approx$ MeV and $E_{\text{binding}} \approx$ keV [174].

The probability of a photon generating an electron-positron pair from the Bethe-Heitler mechanism is given by the relativistic Bethe-Heitler cross section, which for an unscreened nucleus is [175]:

$$d\sigma_{e^+e^-} = \frac{4Z^2 r_0^2}{137k^3}\left[E_{e^+}^2 + E_{e^-}^2 + \frac{2}{3}E_{e^+}E_{e^-}\right]\left[\ln\left(\frac{2E_{e^+}E_{e^-}}{k}\right) - \frac{1}{2}\right]dE_{e^+} \tag{6.2}$$

where $E_{e^+}$ and $E_{e^-}$ are the birth energies of the positron and electron, respectively, in units of $m_e c^2$.

For a given electron input energy, $E_0$, the probability of pair production from the Bethe-Heitler process is proportional to the probability of generating a photon, then that photon producing a pair at some distance $d'$ from its birth position.

$$dP_{\gamma,e^-e^+} \propto (\sigma_\gamma)(\sigma_{e^+e^-}) \tag{6.3}$$

Assuming, for simplicity, that the initial electron and the generated photon travel normal into the target, the total probability of pair creation can be found by integrating over the full thickness of the target for the original electron (d) and the remaining thickness of the target for the photon ($x = \text{d} - \text{d}'$).

Integration is then performed over all photon energies and positron energies that satisfy the minimum energy necessary to create pairs ($k_{min} = 2m_e c^2 = 1.022$ MeV). For now, energy loss due to propagation is ignored. The result is:

$$P_{\gamma,e^-e^+} = \frac{n_i^2 \mathrm{d}^2}{2} \int_0^{E_0/2} \int_{k_{min}}^{E_0} d\sigma_\gamma(k, E_0) d\sigma_{e^+e^-}(E_{e^+}) \tag{6.4}$$

where $n_i$ is the ion number density. The cross section per atom for the production of Bremsstrahlung photons is proportional to $Z^2$ (Equation (6.1)) and the production of pairs from BH is also proportional to $Z^2$ (Equation (6.1)); therefore electron-to-positron generation from the bremsstrahlung/Bethe-Heitler process scales like $Z^4$. Due to this scaling high Z materials, such as gold (Z = 79), are typically used as targets to maximize positron yield. Monte Carlo calculations have shown, however, that the number of positrons emitted into a 1 steradian jet on the rear surface of a thick, high-Z target scales like $\sim Z^2$ [170]. This occurs because the increased pair production from higher Z elements is offset by increased Coulomb scattering that deflects or stops particles.

As positrons result from relativistic electrons created in ultra-intense LPI, understanding the generation of the electron beam is crucial to understanding the positron beam characteristics. The electron spectral distribution is described by the hot electron temperature, which for LPI with $I > 1 \times 10^{18}$ W/cm$^2$ is typically described by the ponderomotive scaling [89]:

$$T_{\mathrm{hot}} = 0.511 \left[ 1 + \left( \frac{I_{18} \lambda_{\mu m}^2}{1.37} \right)^{1/2} \right] \text{ MeV} \tag{6.5}$$

where $I_{18}$ is the laser intensity in $10^{18}$ $W/cm^2$ and $\lambda_{\mu m}$ is the wavelength in µm. Experimental results, however, indicate that the ponderomotive scaling does not accurately describe the observed trend of positron numbers vs. laser intensity. Positron production is dominated by the most energetic electrons,

which are primarily generated in the underdense plasma region on the target surface. For long plasma scalelengths self-generated fields can confine hot electrons to the laser channel, where they can gain energy efficiently through resonant betatron oscillations. This process was put forth by Pukhov *et al.* [24], who proposed a scaling law:

$$T_{\text{hot}} \approx 1.5(I_{18}\lambda^2)^{1/2} \text{ MeV} \tag{6.6}$$

This 'Pukhov' scaling agrees well with experimental data [72], and gives $T_{\text{hot}}$ of $4-6\times$ ponderomotive scaling.

The transport of electrons and positrons in the thick Au targets is important for the beam properties. The stopping of charged particles in matter depends up the energy of the incident particle and the atomic number, Z, of the material. The continuous slowing-down approximation (CSDA) for particle stopping is its path length in a material, assuming no energy gain from inelastic scattering; it is calculated as the integral of the reciprocal of the electron stopping power. The CSDA range gives a reasonable estimate of distance for energetic ions, which travel ballistically until near the end of their travel, but is insufficient for electrons which can scatter significantly. A monoenergetic beam of particles incident on a material will have a distribution of stopping distances due to the stochastic nature of scattering, and therefore the average range in the material, weighted by the distribution of ranges, is used to determine penetration in a target. This is the projected range. The energy loss of electrons in solid Au ($\rho = 19.3$ g/cm$^2$), as well as the CSDA and projected ranges are plotted in Figure 6.2. Positrons have stopping powers nearly identical to that of electrons, with a small correction factor due to the differing polarizations in matter ($< 3\%$ for the $E > 1$ MeV [21]) For the work here this correction is neglected, and electron stopping power is used for positrons.

The process of target normal sheath acceleration (TNSA) is described in

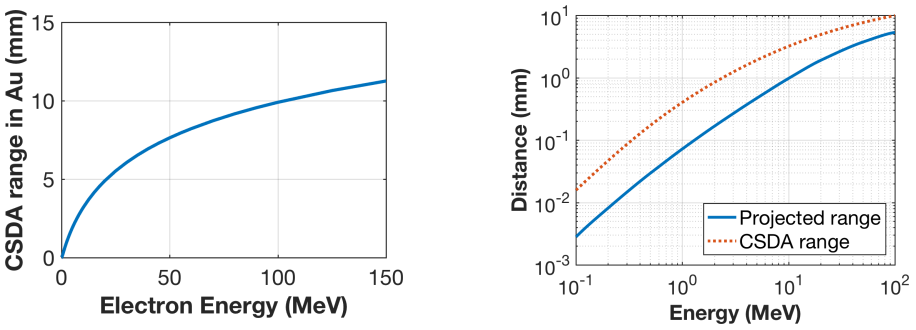


(a) (b)

Figure 6.2: Electron transport in Au. (a) CSDA ranges of energetic electrons in solid density, room temperature Au. Calculated using NIST total stopping powers [21]. (b) Projected range, which accounts for scattering [22] and CSDA range with no scattering [21]. Scattering leads to a detour factor of 2 – 5.

detail in Section 2.3, and therefore will only be summarized here. Relativistic, 'hot' electrons generated from ultra-intense LPI stream through the target, with the most energetic particles escaping and the rest confined to the rapidly charging target. These trapped electrons form an electron cloud, and their high pressure results in charge separation and strong electric fields (MeV/µm) on the surface of the target. These fields cause ions and positrons to be accelerated normal to the target surface. This process is well described by an isothermal expansion of the hot electron cloud into vacuum [12].

## 6.2 Experimental Data from OMEGA EP

The computational work described in this chapter was motivated by experimental data taken at the OMEGA EP laser by Hui Chen, and published in [23]. The targets were Au disks, 1 mm thick and 2 mm in diameter. Three scaling shots were taken with laser energies of 247 J, 800 J and 1500 J, while keeping the pulse duration constant at 10 ps and the spot size constant at R80 = 15 – 20 µm; the corresponding peak vacuum intensities were $6.9 \times 10^{18}$ W/cm$^2$, $2.1 \times 10^{19}$ W/cm$^2$ and $4.0 \times 10^{19}$ W/cm$^2$, respectively. The laser angle of incidence on the target was 0°. The energy of the last shot, 1.5 kJ, is outside

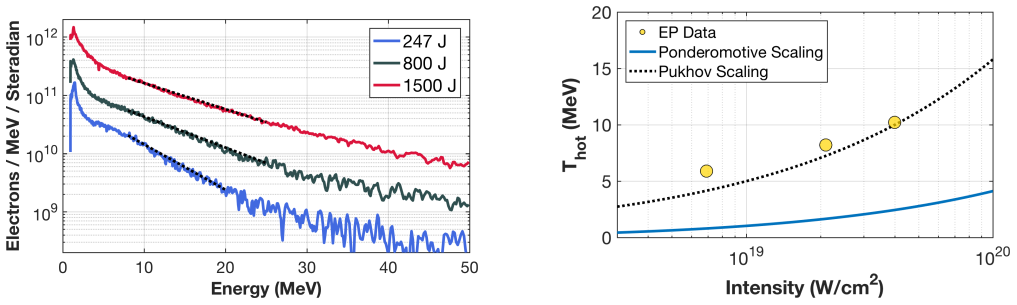


(a) (b)

Figure 6.3: (a) Experimental electron spectra from OMEGA EP for increasing energy shots [23]. (b) Scaling of $T_{hot}$ with intensity, showing best agreement with Pukhov scaling [24].

the normal operating range of EP and was only possible because the off-axis-parabola was being replaced, and therefore could be fielded without a lossy blast shield. The electron and positron spectra were measured simultaneously using an EPPS [14], 50 cm from the target and placed along target normal on the rear side of the target. Figure 6.3a plots the electron experimental data, which shows a typical trend of increasing temperature and absolute number with increasing energy and intensity. The scaling of $T_{hot}$ with intensity best matches Pukhov scaling, as shown in Figure 6.3b and discussed in Section 6.1.

The experimental positron spectra are given in Figure 6.4. The 247 J shot has a typical positron spectrum, with a single peak due to acceleration by an approximately constant sheath potential. Positrons are present at higher and lower energies due to variations in birth momenta and energy gain from the sheath, but at levels below the EPPS detection threshold [176]. As the laser energy was increased to 800 J a shoulder developed on the low energy side of the peak, while the peak energy shifted higher. At 1.5 kJ multiple peaks were seen, with two high energy peaks and a lower energy peak at approximately half the signal level. It was hypothesized that the multiple positron peaks were caused by the time-dependent evolution of the accelerating sheath field. Positrons are produced almost simultaneously with the laser and have low mass, and therefore could act like a probe of the rear surface potential at various times.

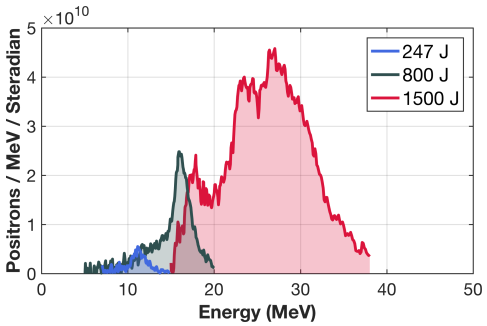


Figure 6.4: Experimental positron spectra from OMEGA EP for increasing energy shots [23]. An evolution in the positron spectral shape is observed, from a single peak to a peak with a low energy shoulder to multiple peaks.

Their relatively low number compared to the electrons ($n_{e+}/n_{e-} \approx 1/1000$) means they behave like test particles and do not significantly modify the target fields. The sheath field is known to be dynamic, and its evolution has been probed with proton radiography [41]. To date, however, no information has been extracted from positron spectral content. To investigate this hypothesis LSP simulations were conducted.

## 6.3 LSP Simulations of Positron Beams

Particle-in-cell simulations with the LSP code were used to model the positron beams. Transport simulations were chosen because full-scale, LPI simulations of the positron target are not computational feasible. Resolving the laser-matter interaction requires sub-fs time steps, which are prohibitive when running simulations to $t$ >40 ps; this is the length of time necessary to allow full development of the positron beam for a pulse duration of 10 ps. Additionally, a grid large enough to accommodate the targets – solid Au disks 2 mm in diameter and 1 mm thick – is impractical with cell sizes that resolve a laser wavelength ($\lambda/20 = 50$ nm). The two stage approach taken, with LPI and transport phases simulated separately, has been used successfully to model cone-wire targets [177] and spherical targets [64], among others. A schematic of the transport simulation box is given in Figure 6.5.

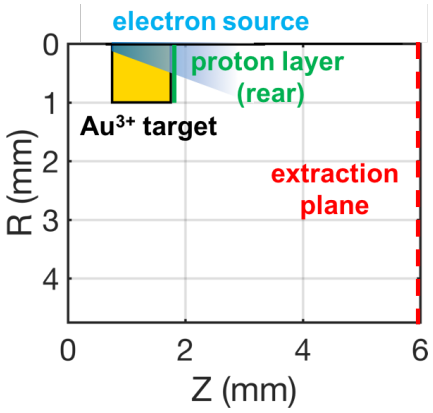


Figure 6.5: Diagram of the cylindrical transport simulation grid and plasmas. Only the primary extraction plane is shown. The cell sizes were 2 µm in the target, decreased smoothly to 0.25 µm in the rear proton layer and increased to $> 10$ µm near the grid edges.

The initial electron source was taken from a Titan-like LPI simulation performed by Tony Link. The laser was 0.7 ps in duration, with a $\sim$12 µm spot size, a double Gaussian spatial distribution, and peak intensity of $8 \times 10^{19}$ W/cm$^2$. A realistic preplasma from the 5-10 mJ Titan prepulse was modelled with a 2D HYDRA hydrodynamic simulation, and included in the LSP LPI simulation. All electrons that travelled 5 µm into the target were recorded, and their properties were used to generate discrete LSP functions. The injection functions were defined in 1 µm steps from R = 0 – 60 µm; each step had 10 energy bins, 3 angular bins per energy bin, and unique temporal functions for each space/energy/angle combination. In total 1800 unique injections were defined. To ensure charge neutralization of the target an equal amount of charge is injected in low energy protons; this is necessary because the plasma ionization state is not maintained from the LPI simulation. The transport simulations were performed in 2D cylindrical geometry, to more accurately model the $1/r^2$ fall-off of fields. The implicit treatment was chosen to allow large time steps (2 fs) without resolving $\omega_p$ in the solid density Au target. Fluid particles were used for the target ions and electrons, which greatly improves energy conservation for the long duration runs. The initial target temperature was

1 eV. Collisions between the cold background electrons and ions ($Au^{3+}$, p+) were modelled using the Lee-More-Desjarlais (LMD) model, and hot electrons and positrons were treated as test particles with continuously-slowing down, 'dedx' energy loss. The gold target had an ionization state of 3+, which was static to reduce computational complexity. Photon and positron generation was handled using cross-section tables created by the Xgen code and the Integrated Tiger Series (ITS) Monte-Carlo model, which is included in the LSP code. These processes were defined within the cylindrical target region, and the lower energy cutoff (below which Monte Carlo calculations are no longer performed) was 5 keV for both photons and electrons.

The SAKv22 (Swiss Army Knife) version of LSPv10 was used for these runs. As discussed in Section 4.1.4, SAK LSP has customizations that allow positron generation and dedx scattering to be handled property using the ITS model. Additionally, it allows the angle of injected electron to be defined, an essential feature to accurately model a realistic hot electron source. Positron annihilation was not included in the simulations. The lifetime of positrons in Au is ∼200 ps for thermalized particles [178]. This time scale is long compared to the transit time of positrons in the target, ∼3 ps, as well as the typical simulation runtime of 40–50 ps, and therefore annihilation can be neglected.

The escaping electron and positron spectra were captured by extraction planes placed at the boundaries of the simulation grid, 4.25 mm from the rear of the target. The position, momentum, and time of crossing of each particle was recorded, allowing the temporal evolution of the spectra to be reconstructed. Full scalar, field and particle dumps were recorded at 25 fs intervals.

A 1 µm contaminant layer was defined on the rear of the target, with a density of $n_p = 1 \times 10^{20}$ cm$^{-3}$. The cell size in this region was smoothly decreased to 0.25 µm to correctly resolve the sheath field. The importance of including a proton layer for positron acceleration is outlined in Section 6.3.2,

and the effect of the numerical parameters on the TNSA protons is examined in Section 4.2. No contaminant layers were present on the side or the front surfaces to minimize cell size requirements.

### 6.3.1 Electron Source Matching

The original electron source was modified to match the experimentally measured escaping electron source. The pulse was first stretched temporally, from its initial 0.7 ps duration to 7 ps; this approximated the 10 ps pulse used at OMEGA EP. To achieve this stretching a 10× scaling factor was applied to the temporal functions, while keeping all other properties constant. This simple temporal stretching neglects any physics that is unique to multi-picosecond interactions. In particular, it likely underestimates the hot electron temperature, as multi-ps pulses have been shown to have higher temperatures then ponderomotive scaling would predict [26, 101]. The time-dependent evolution of $T_{hot}$ for multi-picosecond interactions is also different from shorter interactions, which is not captured by this technique. Lastly, the $f = 2\omega$ electron bunches from $v \times B$ acceleration will also be temporally stretched to $f = \omega/5$. Despite these simplifications the stretched electron source provides a useful approximation of a 10 ps electron beam, and was used for LSP positron simulations published in [72]. The large scale of the Au targets required for positron generation also eases source matching requirements, as scattering in the 1 mm target will blur the source both spatially and temporally.

The second modification to the electron source was to scale the current in each energy bin to match different laser conditions. The electron spectrum can be characterized by two parameters:

1. Total energy in hot electrons, which for a given $T_{hot}$ sets the total charge/magnitude of the spectrum.

2. A temperature, $T_{hot}$, which sets the slope of the distribution. In some

cases multiple temperatures (slopes) are present.

Both of these parameters were adjusted and compared to experimental data to validate the resulting scaled electron sources.

The total energy in hot electrons is easily obtained in simulations but not measured on experiment. The conversion from laser energy to energy in hot electrons for multi-picosecond pulses is not well known, and consequently estimates were made based on combining published experimental and computational work for a range of pulse lengths. These works are shown in Figure 6.6. Ping *et al.* studied the intensity dependence of laser absorption with 150 fs pulses using an integrating sphere [25]. A factor of 0.6 was used to convert to hot electron kinetic energy, based on PIC simulations. A power fit to their data gives conversion to hot electrons scaling with intensity $CE(I) = 3.9 \times 10^{-6}(I)^{0.26} + 0.02$, which for an intensity of $4 \times 10^{19}$ W/cm$^2$ gives 0.35 conversion from laser to electrons. This is likely an underestimate of conversion for 10 ps pulses, as it has been demonstrated that pulses with multi-picosecond durations have enhanced absorption and conversion to hot electrons [26, 101]. Kemp and Divol performed 2D PIC simulations that gave up to 80% of laser energy into hot electrons for a 10 ps pulse and a constant (flat-top) intensity of $1.37 \times 10^{20}$ W/cm$^2$ (it should be noted that this beam power is not currently achievable experimentally). The increased absorption was attributed to plasma injected into the beam from the unstable interaction surface. This effect has been observed experimentally at the LFEX laser, where doubling the pulse duration from 1.5 to 3 ps with a flat-top intensity of $2.3 \times 10^{18}$ W/cm$^2$ increased the measured hot electron temperature from 0.45 to 1.10 MeV [101]. For pulses with Gaussian intensity profiles, experimental data from OMEGA EP shows hot electron temperatures increasing by 65–100% when pulse length is increased from 1 to 10 ps and peak intensity is held constant at $4 \times 10^{19}$ W/cm$^2$ [179]. Nilson *et al.* used copper K$\alpha$ x-ray emission measurements from Cu foils to find a conversation rate of $20 \pm 10\%$, which was

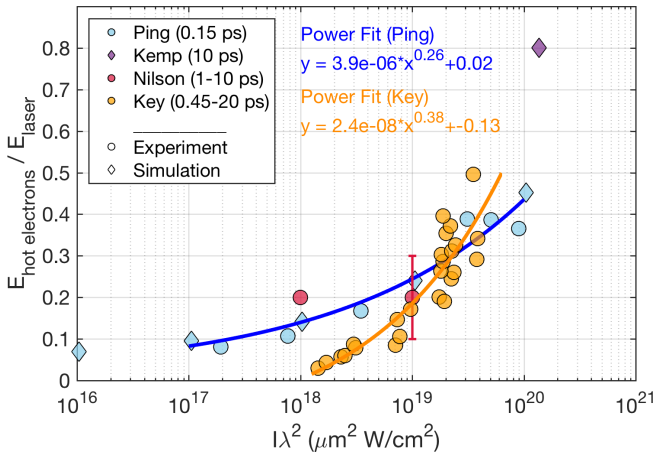


Figure 6.6: Intensity scaling of the conversion of laser energy to energy in hot electrons, for various pulse lengths and conditions and $\lambda = 1.054\,\mu\text{m}$ light. Data is from Ping *et al.* [25], Kemp and Divol [26], Nilson *et al.* [27] and Key *et al.* [28]

constant for 1–10 ps pulses [27]. The measurements from 10 ps, 1000 J pulses they report is the only experimental data of conversion efficiency for laser conditions similar to those of the 10 ps, 1500 J shot discussed in Section 6.2. Finally, Key *et al.* reported on copper K$\alpha$ emission from the Petawatt laser [28]. Their data fits a conversion curve $CE(I) = 2.4 \times 10^{-8}(I)^{0.38} - 0.13$; this is significantly different from Ping *et al.*, although there is agreement in the intensity region of interest at $\sim 4 \times 10^{19}$ W/cm$^2$. In summary, the expected conversion to hot electrons for $I = 4 \times 10^{19}$ W/cm$^2$ is in the range of 30 – 40%, and the effect of multi-picosecond interaction is likely to raise the expected value to the high end of the range. A conversion efficiency of 40% will henceforth be used for the high energy case.

Two different approaches to scaling the electron source were used. The first was a constant scaling, in which the scale factor for each energy bin was kept constant: $SF(E) = C$. This was done both for ease of implementation and to have a controlled study, and was equivalent to shifting the input spectrum to higher or lower energies while leaving the slope constant. Decoupling net charge and $T_{hot}$ in this manner is not possible experimentally, as both

increase with increasing laser intensity according to scaling laws (ponderomotive, Pukhov). The increased freedom in simulations, however, enables such parameter studies. The second approach was a weighted scaling, in which the scale factor was adjusted for each energy bin to modify both the distribution slope and absolute number: $SF(E) = G(E)$. This approach was used to achieve the best match with experiment. Both scalings were accomplished by replacing the temporal multipliers of the electron generation functions, which control the current density. As the source size was not changed during this process the current density was altered, which could affect the physics of the beam transport. Additionally, the angular distribution of the beam was not altered; the electron beam is known to become more directional for increasing laser intensity [180] and prepulse [181], but scattering in the 1 mm target will reduce this effect. Overall, modifying the source in this way is a powerful tool for investigating physics phenomenon which otherwise would be hard to access.

The escaping electron spectra for the constant scaling case are plotted in Figure 6.7, with the source properties (total electron energy and temperature) reported in Table 6.1. While the input electron spectra (not shown) are scaled by a constant amount, it can be seen that the escaping electron spectra are shifted by an energy dependent amount that varies with each case. This is due to the characteristic capacitance and charging of the target. In all cases the same amount of charge must escape for the potential barrier on the target to be high enough to trap all remaining electrons. At the same time the trapped charge will increase with scaling, which will modify the energies of the escaping electrons. The spectra are similar for the highest energy electrons ($E > 60$ MeV), but significantly modified at lower energies. This leads to a higher slope temperature for the 0.25 case compared to the higher scaled cases, but a lower absolute number for all energies.

In the second approach weighted scaling of the electron source was used

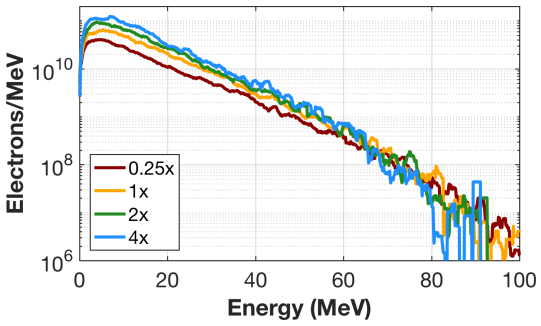


Figure 6.7: Escaping electron spectra for constant scaling of electron source. Even though the input spectra are scaled linearly, the escaping spectra are nonlinear due to the charging behaviour of the target.

| Case | Multiplier | E (J) | $T_{hot}$ (MeV) |
|---|---|---|---|
| 1 | ×0.25 | 133 | 12.0 |
| 2 | ×1 | 550 | 11.0 |
| 3 | ×2 | 1062 | 10.0 |
| 4 | ×4 | 2115 | 9.8 |

Table 6.1: Electron source parameters and $T_{hot}$ for escaping electrons from the constant scaling study. E is total energy in injected hot electrons.

to adjust both the temperature and magnitude of the electron distribution, in order to match the experimental conditions. $T_{hot}$ of the escaping electrons was measured experimentally and can also be determined in simulations from an extraction plane located far from the target; the distance was 4.25 mm from the target rear. The relationship between the input and escaping electron distributions is complex, and therefore matching of the electron source was done through an iterative process: an energy-weighted scaling was applied to the spectrum, which was then injected into a simulation. The escaping electron distribution and total energy were then compared to experiment, and the process was repeated with a new weighted scaling based on the previous matching. The best electron source matches generated are shown in Figure 6.8 for the low and high energy cases. The high energy case is the main area of interest, as the low energy case is the null case (no positron spectral features); consequently more effort was put into matching the high energy electron source. Total energy in the low energy LSP electron source was 137 J compared to an estimated energy of 74 J using an $E_{\text{laser}}$ to $E_{\text{hot electrons}}$ conversion factor of 0.3. For the high energy case the total energy in electrons in the LSP simulations was 870 J, compared to an estimated energy of 600 J with a conversion factor

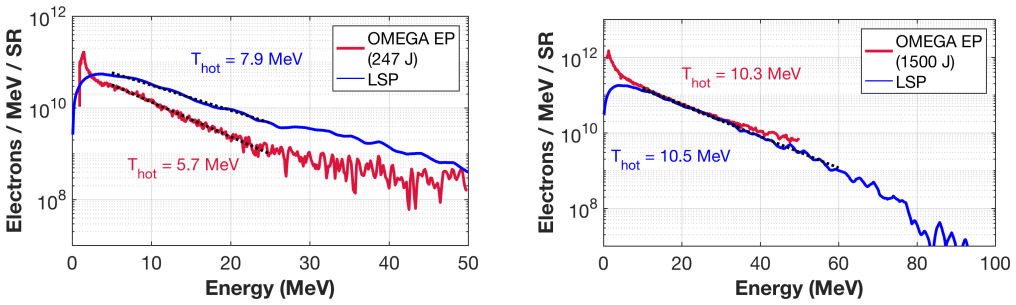


(a) (b)

Figure 6.8: Comparison of electron spectra for experiments and weighted source simulations, in absolute units, for (a) the low energy case, $E_{\text{laser}} = 247$ J, and (b) the high energy case, $E_{\text{laser}} = 1500$ J. Good agreement is found in the range of 10 – 50 MeV for the high energy case, which is the one of interest.

of 0.4. When plotted in absolute units in Figure 6.8b, however, the spectra agree well in the energy range of 10 - 50 MeV, which is a good indicator that the electron source is a reasonable approximation of experimental conditions. The lack of the high energy tail will cause a lower number of positrons to be produced, as the highest energy electrons produce a large amount of pairs, but will have a small impact on the evolution of the sheath field due to the low total charge. At low energies the EPPS data includes late-time particles that are not included in the simulated spectrum. Note that the LSP spectra were taken within a 13° cone centred around rear target normal to ensure enough signal. A similar result was found with a 25° cone. The electron temperature in the range of 10–50 MeV is also matches well, reflecting good agreement in the shape of the distribution. For reference, the simulated spectra for the input electron source and the escaping electron beam in the high energy case are shown in Figure 6.9.

### 6.3.2 Positron Spectral Features

The positron spectra from the constant scaling study are examined first. All cases were run to 40 ps except the 4× case, which was run to 34.5 ps due to numerical instability; this is expected to result in a reduction in signal only in

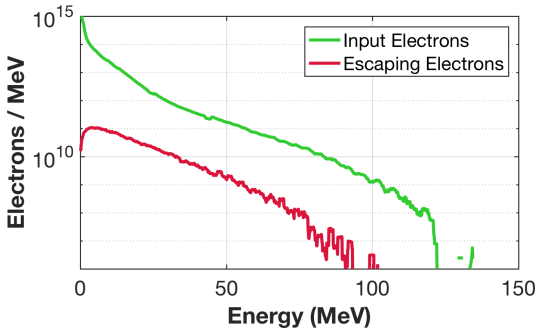


Figure 6.9: Comparison of simulated spectra for the input electron source and escaping electron beam, for the high energy case. Similar slopes are observed at higher energies, with the escaping electrons downshifted by the target potential, while at lower energies the injected electrons do not have sufficient energy to escape [29]. The input spectra was found by injecting the electron beam into vacuum with fields turned off. The escaping spectra was taken from the full simulation, and measured 4.25 mm from the rear of the target.

the low energy portion of the spectrum. Three distinct trends can be seen in Figure 6.10a. As the electron source energy increases: (1) The peak positron energy increases while the peak number also grows larger. (2) A low energy shoulder on the main peak becomes more pronounced. (3) Peaks appear to develop in the low energy side of the spectrum. The shifting of the main peak to higher energies is a known consequence of increasing charge causing stronger sheath fields, and hence more energetic positrons. This increase occurs even though the input hot electron temperature remains the same, which addresses one of the common misconceptions regarding TNSA: it is the hot electron *pressure*, not temperature alone, that drives acceleration.

Spectral features (2) and (3), the low energy shoulder and peak, have not been examined before. To isolate the origin of these features the time evolution of the 2× spectrum is plotted in Figure 6.10b; the 2× case was chosen rather then the 4× case because of instability in the 4× simulation that prevented it from running to 40 ps. The main, high energy peak develops early in time, by $t = 30$ ps, while the low energy features develop later over the next 10 ps. The origin of these late time features is explored further with weighted source simulations.

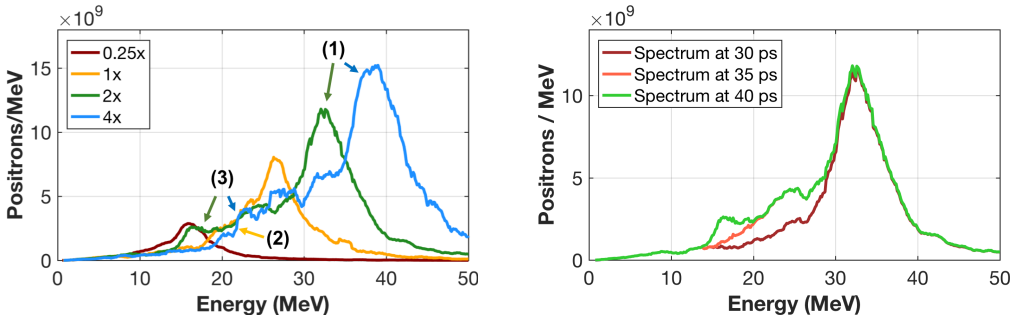


(a) (b)

Figure 6.10: (a) Positron spectra for constant scaling of electron source, showing (1) high energy peaks with (2) distinct low energy shoulders, and (3) low energy peaks. Note that the 4× case was only run to 34.5 ps due to numerical instability with the simulation, while the other cases were ran to ∼40 ps. (b) Time evolution of the 2× case. The low energy features develop late in time.

The simulated positron spectra from the weighted electron sources are shown in Figure 6.11, with their evolution in time displayed for 30 and 40 ps times. These runs attempted to match the variations in hot electron temperature and charge with laser intensity. In the low energy case the spectrum exhibits a single peak and the shape does not change over time. This reflects the fact that all escaping positrons experience the full sheath field potential, and this potential is approximately constant over the interaction time. For the high energy case two distinct peaks are present, in qualitative agreement with the experimental data (Figure 6.4). The high energy peak develops first, while the low energy peak grows later in time as the spectrum is filled in at decreasing energies. These peaks will henceforth be referred to as 'early' and 'late' time peaks. It should be noted that despite the differences in energies these peaks do not reflect a time of flight effect: all positrons in this energy range are highly relativistic and moving at ∼c, and the difference in travel times for 4.25 mm is ∼2 fs for the two peaks (E = 33.5 MeV and 21.8 MeV).

The electric field from the hot electron sheath is strongly peaked at the target surface (or the proton front, if protons are present), and rapidly decreases to zero inside the conducting target. Any positron that reaches the edge of

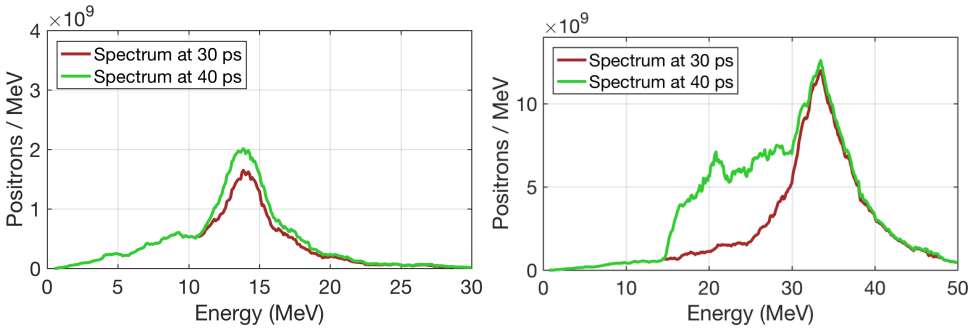


Figure 6.11: Time evolution of the simulated positron spectra for (a) the low energy case, $E_{laser}$ = 247 J, and (b) the high energy case, $E_{laser}$ = 1500 J. In these cases weighted electron source spectra were used, with different hot electron temperatures for the different laser intensities. Distinct early and late time peaks can be seen in the high energy case.

the target experiences this accelerating field and gains the total potential energy of the sheath at that time, and therefore there are no escaping positrons below this threshold energy: $E_{pos}(t) \geq e\phi_{\text{sheath}}(t)$. The time dependence of the sheath field can thus be seen in phase space plots of positron energy vs. distance from the target, with the minimum positron energy representing a time history of the sheath potential. The main phases of the sheath field development are shown in Figure 6.12, and consist of (1) target charging, (2) peak potential and (3) potential decay. The effect of TNSA proton expansion is also evident as the starting location of acceleration moved away from the initial target boundaries, following the proton beam front. The presence of TNSA protons affects the sheath field, which is discussed in the next section.

### Effect of Proton Contaminant Layer

The positron spectrum is modified by the presence of protons on the rear surface of the target. As the proton beam from TNSA expands outwards, charge separation occurs between the electron cloud and the protons at the beam front. This is the location of the peak sheath electric field, and it moves away from the target surface as the proton beam advances. Debye shielding

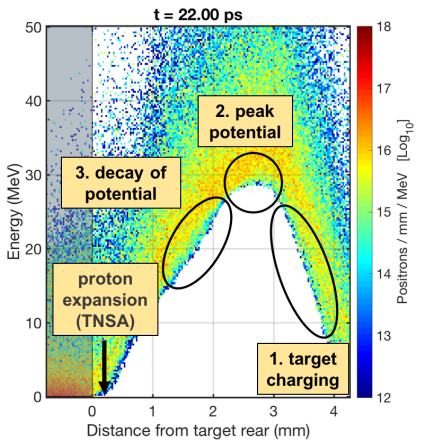


Figure 6.12: Positron energy phase space. Various stages of the sheath potential development are visible through their imprint on the minimum positron energy. Particles with $R \leq 2$ mm are included in the plot.

causes the electric field to decrease in strength with distance into the proton beam. This field behaviour is illustrated in Figure 6.13a, which shows a 2D plot of the $E_z$ sheath field when rear protons are simulated. When no proton contaminant layer is present the peak field remains located on the surface of the target until significant ion expansion occurs (Figure 6.13b). The electric field becomes quasi-static, and therefore the late time positron peak becomes more significant. It should be noted that the gold ionization is constant in the LSP simulation, and in reality some field ionization would be expected that in turn would lead to faster ion expansion.

To study the effect of the contaminant layer on the positron signal, simulations were run with and without the layer on the rear surface. The positron spectra for an $R = 1$ mm target (Figure 6.13c) show increased signal in the low energy, late time peak when no protons are present. The low energy shoulders on both peaks are also reduced compared to the proton case, due to redistribution of positrons to the peak energies. No enhancement is seen for the high energy peak; this is consistent with acceleration early in time, when negligible proton expansion has occurred and the field behaviour is similar in both cases. These effects are seen when a 10 ps electron source is used, as this gives a signif-

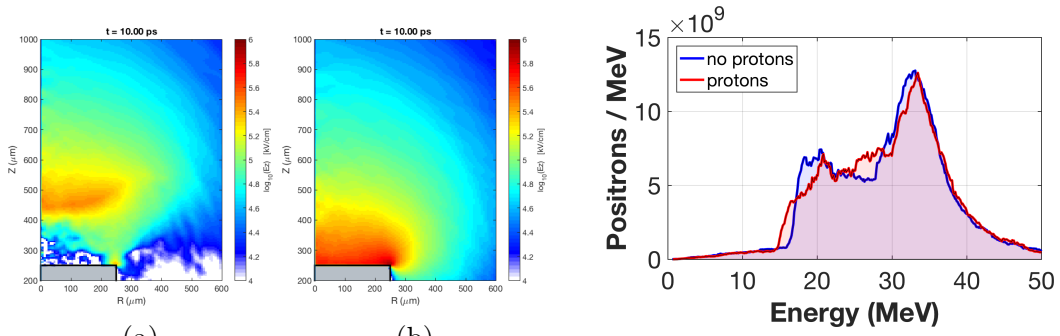


(a) (b) (c)

Figure 6.13: The sheath field $E_z$ on the rear surface of an Au target, with (a) a rear proton contaminant layer, (b) no initial proton contaminant layer. The translation and weakening of the peak field can be seen. (c) Positron spectra at 40 ps showing an enhancement of the low energy, late time positron peak when no proton contaminant layer is present, and a reduction in the low energy shoulders of both peaks.

icant amount of time for proton expansion to occur. No difference is expected for short, 1 ps pulses, again due to the lack of time for TNSA expansion of protons. The comparisons for other target sizes are shown in Figure 6.14, and are qualitatively similar: little change in the early time peaks, more prominent late time peaks. As the target size is decreased the early time peak remains at a similar energy while the late time peak shifts to higher energy; this shift in the low energy peak is discussed in Section 6.3.4. The presence of protons reduces the late time peak in all cases. For the $R = 0.25$ mm case the late time peak has merged into the early time peak, and the early peak itself has been modified due to 3D effects from the much reduced target.

Phase space plots of positron energy are shown in Figure 6.15 for both the proton layer and no proton layer cases. A change in the decay of the sheath potential is evident, as indicated by a difference in the slope of the minimum positron energy vs. position (here position is a proxy for time, with all particles moving at c). This change in behaviour is more evident for the no proton case, on the right. It appears that there is a quasi-static potential on the target, which is discussed in Section 6.3.2.

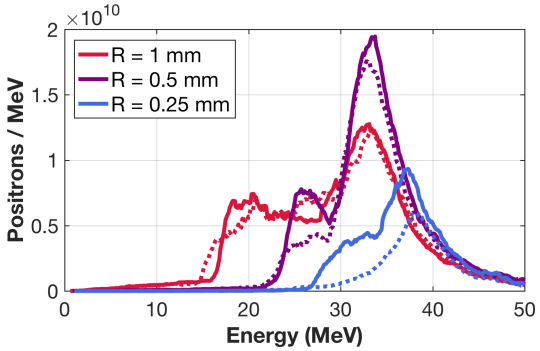


Figure 6.14: Positron spectra for targets with different radii at 40 ps. Solid lines indicate targets without protons on the rear, dashed lines have protons on the rear. The presence of protons has no effect on the early time peak but reduces the prominence of the late time peak. This trend is less clear for the $R = 0.25$ mm case, where the target aspect ratio is significantly altered.

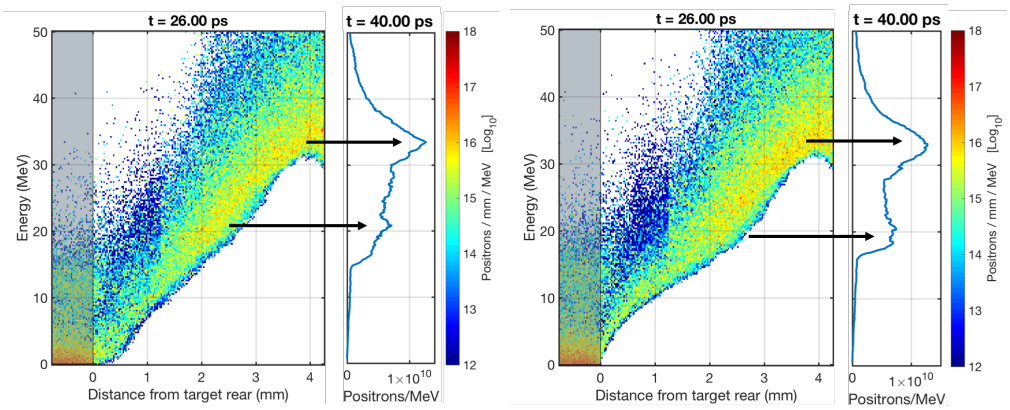


Figure 6.15: Positron energy phase space at early time and integrated spectrum at late times for two case. (a) Proton layer present on rear. (b) No proton layer. The initial target position is indicated by the grey box, and particles move from left to right. A change in the decay of the minimum positron energy reflects a change in the behaviour of the sheath field potential, and gives rise to two positron peaks.

### Evolution of the Sheath Field

The TNSA sheath field originates with hot electrons generated by ultra-intense LPI. The potential that results from these hot electrons can be separated into two parts [182]:

$$\phi_{\text{sheath}} = \phi_{\text{net charge}} + \phi_{\text{charge separation}} \tag{6.7}$$

Here $\phi_{\text{net charge}}$ is due to escaping hot electrons, which leave the target positively charged, and $\phi_{\text{charge separation}}$ is from trapped MeV-energy electrons, which drive charge separation and an ambipolar potential from their electron pressure. The evolution of these potentials has been studied by Poyé *et al.* in order to determine target charging and EMP generation [182]. At the same time, the target geometry influences the temporal evolution of the sheath field. Reflection of the hot electron cloud from the target edge and refluxing between the front and rear surfaces can both occur [110]. The interplay of these potentials and geometric effects can be complex, as they occur simultaneously and with different strengths and timescales.

The decay rates of the two potentials in Equation (6.7) are very different. As a first approximation the neutralization time for $\phi_{\text{net charge}}$ can be taken as $\tau_n \approx L/c$, where $L$ is the target holder length and c is the speed of light. For the OMEGA EP experiments the Au disk targets were mounted on 8 cm long glass stalks (2 mm in diameter and tapering to a 25–50 µm point), giving $\tau_n = 267$ ps. This ignores the inductance of the setup, which will increase the travel time of current on the holder. At the same time, neutralization current will begin to flow immediately, causing neutralization earlier then this estimate would suggest. The temperature of the hot electron cloud drives $\phi_{\text{charge separation}}$, and therefore its decay time is set by the time it takes for these electrons to cool. A lower estimate can be made by assuming continuous travel in Au, using the NIST total stopping power [21] to find the distance

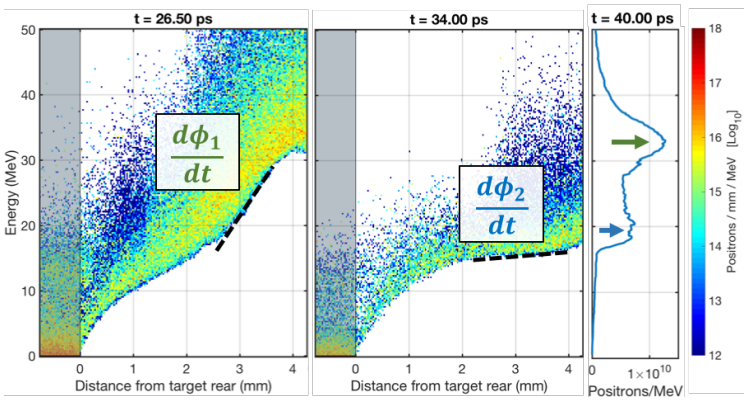


Figure 6.16: Positron energy phase space for a target with no rear protons, and the final positron spectrum. Two times in phase space are shown, with two different minimum energy decay rates. These correspond to the decay rates of $\phi_1 = \phi_{\text{charge separation}}$ and $\phi_2 = \phi_{\text{net charge}}$.

over which an electron loses the majority of its energy (see Figure 6.2a), and converting to a time using the speed of light (valid for relativistic, MeV electrons). Using this approach a 50 MeV electron will lose 99% of its energy in 7.5 mm of Au, for $\tau_d = 25$ ps. Significant refluxing through the target and scattering from the sheath cloud is known to occur, so this assumption is not unreasonable; however many other factors, such as adiabatic cooling and energy transfer to protons in the sheath, are neglected. These simple models provide order-of-magnitude estimates of the decay rates, and indicate that $\phi_{\text{net charge}}$ takes $\sim$10$\times$ longer to decay then $\phi_{\text{charge separation}}$. In the LSP simulations the target is freestanding, with no mounting stalk, and therefore there is no neutralization current to modify $\phi_{\text{net charge}}$; this simplification is justified by the long timescales for neutralization to occur ($\tau_n$) relative to the time of interest ($\sim$30 ps). These differing decay rates are reflected in the positron phase space plots in Figure 6.16.

The evolution of the accelerating sheath fields depends on the space charge of the trapped electrons and the dynamics of the electron cloud, which in turn depends on the target geometry. The first geometric factor to be considered is reflection of the sheath field from the side edges of the target, which occurs

when the expanding electron cloud encounters transverse electric fields. These fields are simply the sheath field normal to the side surface. Fast ignition studies of simulated cone and wire targets have shown that the expansion of hot electrons on the target surface mainly takes place outside the target, where the resistivity is low [177]. The electric sheath field directing electrons into the target is balanced by magnetic fields generated by the cold return current inside the target, establishing an equilibrium that is maintained until the electrons reach the end of the wire target and are reflected by the transverse sheath field. The timescale of sheath reflections can be calculated for a given target radius and sheath expansion velocity. From PIC simulations and experimental measurements the expansion velocity is between 0.75–0.95c [4, 177]. Using an average value of 0.85c and a target with R = 1 mm, a signal starting at r = 0 has a one-way travel time of 3.9 ps and a round-trip time of 7.8 ps. These timescales point toward one approach to isolating a reflection effect, which is to increase the target radius and therefore the reflection time.

Recirculation of hot electrons between the front and rear surfaces, known as refluxing, can occur when electrons are stopped and reflected by the sheath fields. For this discussion $d$ equals the thickness of the target, and electrons are assumed to move at $v = c$. Refluxing has been explored primarily for thin targets ($2d/c < \tau_{laser}$), where it enhances TNSA by increasing charge density in the electron cloud [183]. Refluxing is not typically considered for thick targets, but it has been shown by Chen *et al.* that electron refluxing must be included in LSP simulations to match experimental positron yields [72]. Experimental work done for this degree contributed to this research. The timescale of refluxing is set by the thickness of the target; for the d = 1 mm targets used at OMEGA EP a straight, round-trip journey takes $d/c = 6.7$ ps. The scattering of electrons cannot be ignored, however; the increase in path length travelled relative to a straight trip (the detour factor) is between 5–2× for 1–150 MeV electrons in solid density Au (see Figure 6.2b) [22].

The behaviour of the sheath field was examined by calculating the electric potentials on the front and rear surfaces of the target for each time step and radial position, $\phi_{front}(r,t)$ and $\phi_{rear}(r,t)$. The potentials were found by integrating $E_z$ from the edge of the grid to the target surface, $V_z(r,t) = \int_{\text{rear of target}}^{\text{edge of grid}} E_z(z,r,t)dz$. This distance was 4.25 mm. The rear potential is responsible for positron acceleration, while the front potential is useful to determine periodic effects such as refluxing. Sheath reflection is evident as diagonal bands of increased potential; the slope of these bands is the velocity of sheath expansion. To isolate the effect of target geometry, targets of different radii were simulated with the same electron source. Targets without protons were used to eliminate the complicating factor of TNSA sheath field expansion, and because these cases exhibit the clearest late time positron peaks. Radially averaged potential lineouts were taken, and averaged from R = 0 to 0.2 mm in all cases to avoid transverse non-uniformities.

Figure 6.17a and Figure 6.17b show the rear and front potentials, respectively, for an $R = 0.25$ mm target. There is no potential early in time because the electrons have not yet escaped the target. A distinct oscillation between the rear and front surfaces is seen. Radially averaged lineouts, plotted in Figure 6.17c, indicate a period of oscillation of $\tau_{osc} \approx 13$ ps. This is approximately twice the direct refluxing time of 6.7 ps, which is consistent with a detour factor of 2. Reflection of the sheath has a timescale of $2 \times 0.25$ mm$/0.85c = 2$ ps, and does not appear to occur. The limited lateral extent of the target does confine charge to a small volume, however, resulting in a higher final potential. Similar results are seen for the $R = 0.5$ mm target in Figure 6.18, with oscillations between the front and rear surfaces and no sheath reflection. The period of oscillation, 13–14 ps, is close to that of the $R = 0.25$ mm target.

Different behaviour occurs with the $R = 1$ mm target; for the first time reflection of the sheath field can be distinguished. Figure 6.19a shows the rear potential, with a dashed triangle indicating a signal moving at c and reflecting

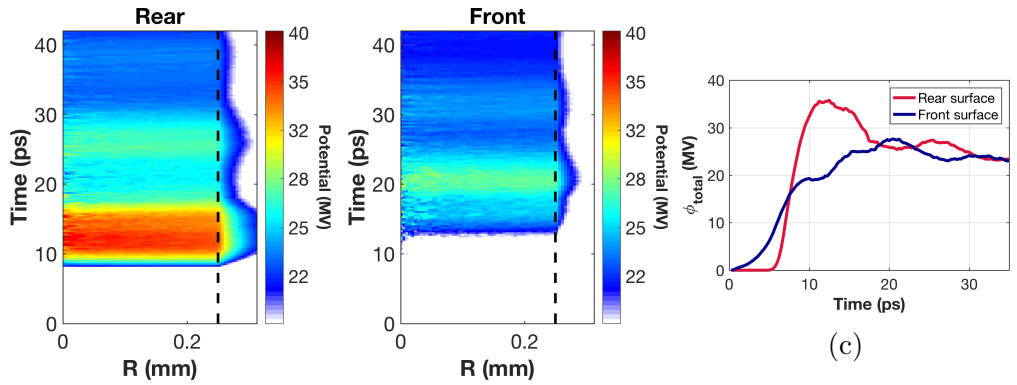


Figure 6.17: (a) Rear and (b) front sheath potentials for $R = 0.25$ mm target. Potential is indicated by the colour scale, and plotted vs. time and radial position on target. The radius of the target is denoted by the dashed line. There is clear refluxing of electrons between the front and rear surfaces. (c) Lineouts of front and rear potentials, averaged from R = 0 – 0.2 mm. An oscillation period of ∼13 ps is observed.

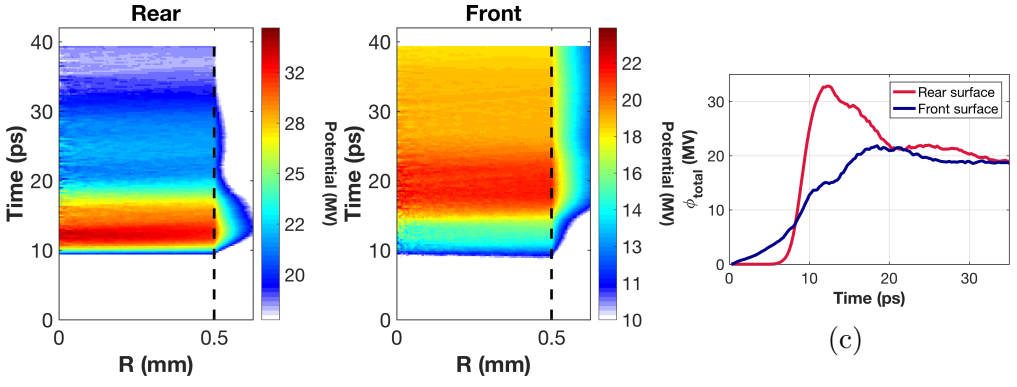


Figure 6.18: (a) Rear and (b) front sheath potentials for R = 0.5 mm target. Refluxing of electrons between the front and rear surfaces is seen. (c) Lineouts of front and rear potentials, averaged from R = 0 – 0.2 mm. A oscillation period of 13–14 ps is observed.

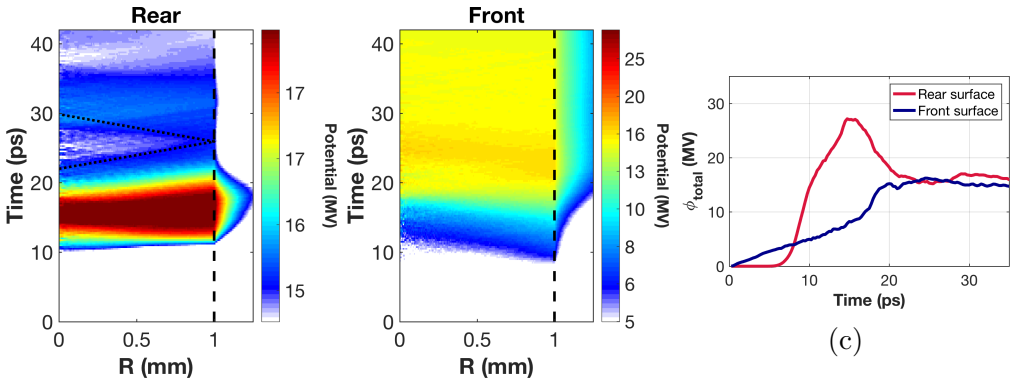


Figure 6.19: (a) Rear and (b) front sheath potentials for R = 1 mm target. Reflection of electrons from the edge of the target is evident, as well as weak refluxing. One reflection is highlighted by diagonal dashed lines, which indicate a signal traveling at c. (c) Lineouts of front and rear potentials, averaged from R = 0 – 0.2 mm.

from the target edge in 6.7 ps. It can be seen that the potential agrees well with these reflections. Refluxing may also be occurring, however with $\tau_{\text{reflux}} = 13$ ps as measured on smaller targets it will overlap with two reflection periods, $\tau_{\text{reflux}} = 2\tau_{\text{reflection}}$. The transverse motion of the potential (diagonal signal) is a signature of reflection.

For the $R = 2$ mm target the reflection time doubles to 13.3 ps, and reflection on this timescale can easily be distinguished in the rear potential, Figure 6.20a. The reflection time is now equal to the observed refluxing time and refluxing may contribute to the field oscillation, but once again the clear transverse motion of the potential indicates that reflection is significant. The area in which the hot electron beam breaks through the rear surface of the target ($R \approx 0.5$ mm) is small compared to the 2 mm radius of the target, and the expansion of the sheath field from $r = 1$ mm to $r = 2$ mm can be clearly observed. The velocity of this expansion is $\sim c$.

The lineouts of target potential display the effects of two sources: a large, transitory potential until 17–20 ps, then a quasi-static potential for later times. This agrees well with the two potentials in Equation (6.7). The effect of

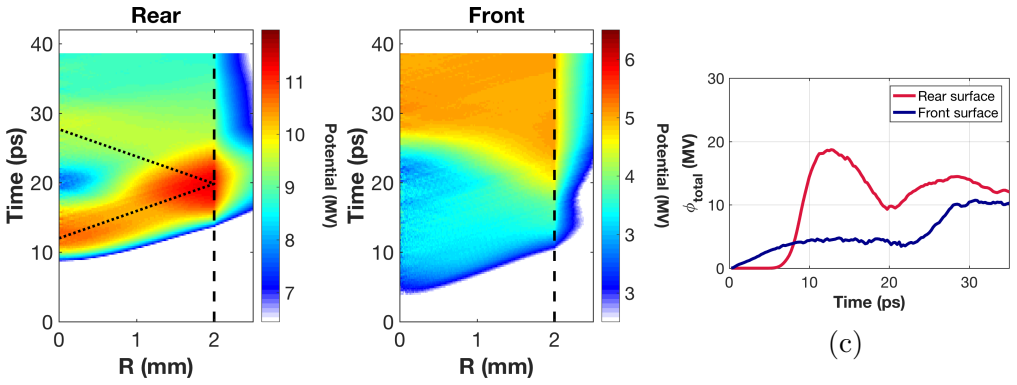


Figure 6.20: (a) Rear and (b) front sheath potentials for target with R = 2 mm. Clear reflection from the target edge is observed on the rear surface. The diagonal dashed lines indicate a signal traveling at c. (c) Lineouts of front and rear potentials, averaged from R = 0 – 0.2 mm.

electron cloud refluxing and reflection is evident in the late time potential, but only as perturbations on the late time value. The two peaks of the positron spectra are indicative of these two potentials.

### 6.3.3 Effect of Refluxing on Yield

While the temporal evolution of the sheath field is primarily responsible for the positron spectral peaks, it is possible that the time dependence of positron generation is a contributing factor. Electron refluxing is known to enhance positron yield [72], and can be examined directly in simulations. A key tool is the ability to disable fields in LSP, which stops sheath fields from forming and prevents charged particles from being confined to the target by electric potential. The time history of the number of electrons with $E > 10$ MeV within the full target is shown in Figure 6.21a, for the fields on and fields off cases and both forward and backward going particles. The energy threshold was chosen to select high energy electrons which are not significantly stopped or scattered within the target; these energetic electrons also dominant the production of positrons. A clear population of reflected, backward going electrons can be seen at t = 12 – 22 ps, which in turn gets reflected and increases the forward

going population for $t > 18$ ps. Backward going electrons are present in the no fields case due to scattering.

Of particular interest is the number of particles inside the target and near the rear surface, which have the most significant contribution to positron production and emission (i.e. those that can escape the target and contribute to the measured spectrum). To determine this population all electrons and positrons within 100 µm of the rear surface of the target and 500 µm in radius were recorded, then thresholded for $E_{e^-} > 10$ MeV and $E_{e^+} > 1$ MeV for electrons and positrons, respectively. An energy of 1 MeV was selected for positrons to ensure that the recorded particles escape to the edge of the target, which requires an energy of 0.35 MeV for $d$ =100 µm but increases due to scattering. The resulting electron numbers are shown in Figure 6.21b. The backward going population becomes significant when fields are on, and there is an increase in forward going electrons compared to the no fields case for $t > \sim$14 ps. After $t = 20$ ps the population of electrons inside and near the rear surface of the target is entirely due to confinement by fields.

The effect of fields and electron trapping on positron number is shown in Figure 6.21c. A secondary peak at $t = 14.5$ ps occurs when fields are on; this could be responsible for the middle peak in the experimental positron spectrum, which has otherwise not been accounted for with sheath fields. There is also a population of positrons late in time that is not present when fields are disabled. The number of positrons available for acceleration versus time is plotted along with the net target potential in Figure 6.22. The potential here was found by integrating the electric field at different times corresponding to a signal moving at c; this is the potential experienced by relativistic particles escaping the target. The population of particles at late times which contributes to the late time positron peak remains significant because of field effects.

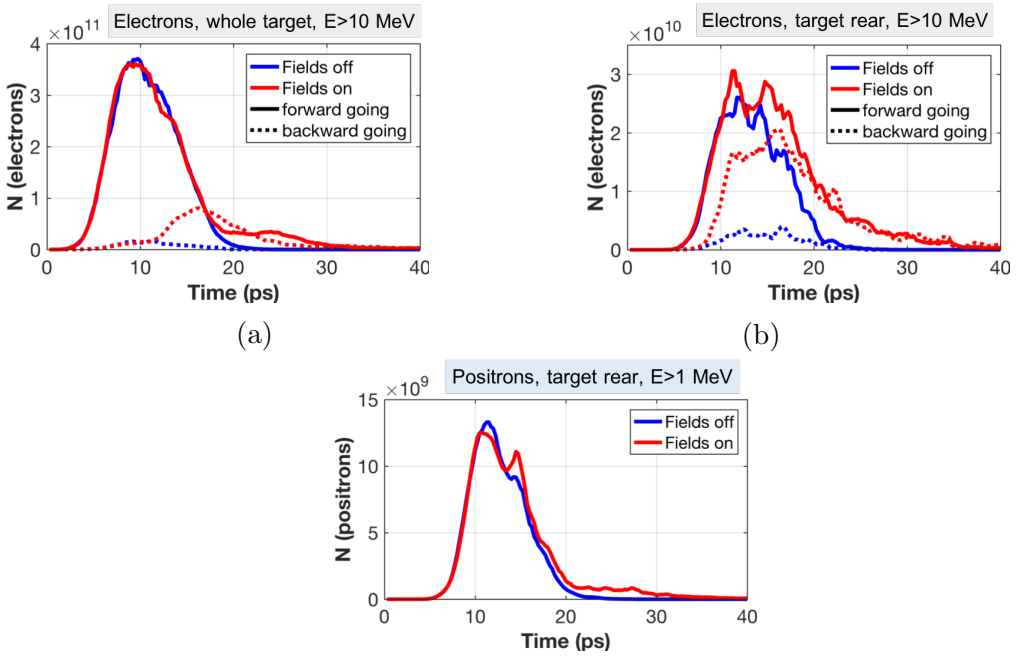


Figure 6.21: (a) Electrons in the whole target ($R = 1$ mm) with $E > 10$ MeV. With fields on, reflection of electrons by sheath fields leads to a larger backward going population and increased forward going electrons at late times. (b) Electrons within 100 µm of the rear surface of the target and R = 500 µm, with $E > 10$ MeV. The backward going population is significant when fields are on, and there is an increase in forward going electrons compared to the no fields case. (c) Positrons near the rear surface within the same 100 µm box and $E > 1$ MeV. With fields on there is a small secondary peak at 14.5 ps and slightly enhanced numbers at late times.

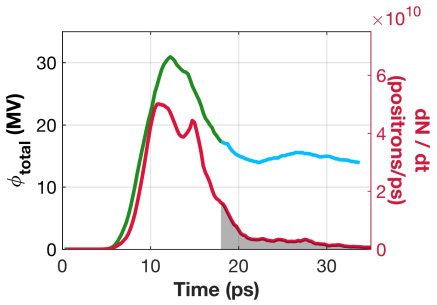


Figure 6.22: Total potential on the rear surface and positron number for an $R = 1$ mm target. The potential is given for a particle moving at c. The positrons were within 100 µm of the target rear surface and R = 500 µm, with $E > 1$ MeV. The green section of the potential is dominated by charge separation, the blue section by net charge. The number of positrons available at late time to form the late time peak is indicated by the shaded region.

### 6.3.4 Calculation of Target Charging

The net charging of a target can be calculated based on a simple capacitor model and a given electron source, as proposed by Tony Link [29]. This approach is used here to predict the energy of the late time positron peaks, which should correspond to $\phi_{\text{net charge}}$. The electron source is integrated in space to give a distribution in energy and time, $N_{\text{electrons}}(E, t)$. Stepping forward in time from $t = 0$ and moving from high to low energies, electrons are tested to see if they can escape the potential barrier of the target: $E_{\text{electrons}}(t) > \phi_{\text{target}}(t)$. Electrons that can escape increase the net charge of the target, and therefore increase the potential barrier for subsequent electrons. The change in potential due to a change in charge is determined by a structure's capacitance:

$$V = \frac{q}{C} \tag{6.8}$$

To calculate the capacitance of a target it is assumed to be a sphere with equivalent surface area to the original cylinder. This approximation was found to agree to within 3% for both escaping electron temperature and final charge distribution when compared to flat foils in LSP simulations [29]. The capacitance of an isolated sphere is that of two spherical shells with the second spherical plate at infinity, and is given by:

$$C_{\text{sphere}} = 4\pi\epsilon_0 R \tag{6.9}$$

The 1 mm thick targets used for positron generation are much thicker then standard TNSA targets, which are typically $< 50\,\mu\text{m}$, and therefore the electron energy loss must be accounted for to correctly calculate the net charging of the target. For each energy bin the projected range was found from tables in Monte Carlo calculations [22]; both the projected and CSDA (no scattering) range are plotted in Figure 6.2b. This projected range was used with the NIST ESTAR stopping power, including both collisional and radiative stop-

ping, to find the energy loss of each energy bin [21]. The resulting potential curves, Figure 6.23a, are characteristic of a target charging, where the most energetic particles occur at the peak of the pulse and no subsequent, lower energy particles can escape.

Reasonable agreement is found between the calculated potentials and the energies of the low energy positron peaks from LSP positron simulations for $R \leq 1$ mm targets, in Figure 6.23b. The deviation from the model for $R > 1$ mm targets occurs for several reasons. For these larger targets charge is no longer confined transversely on the rear surface, and the number of positrons available to be accelerated at late times drops. The approximation of a sphere also starts breaking down, causing the energy loss calculations to become less accurate. This approximation works best for the $R = 1$ mm case, where the radial and cylindrical extent of the target are equal and electrons travel approximately the equivalent range of 1 mm. Additionally, as the positron peaks have contributions from both the target potential and the positron birth energies, the net charging calculation somewhat underestimates the final potentials. Despite these factors, the calculated $\phi_{\text{net charge}}$ values match the simulated late time positron peak energies to within 25% for the indicated cases, which is impressive considering the highly simplified model used. This agreement suggests that the charging capacitor model captures the dominant physics that leads to this late time acceleration.

### 6.3.5 Target Size and Energy of Peaks

There is disagreement in the published literature regarding the relationship between the energy of the positron peak and target size, which LSP simulations can help resolve. As a target decreases in size the hot electron charge gets confined to a smaller area, increasing the charge density and consequently the strength of the sheath field. This is a well known effect in proton TNSA, where small, so-called "mass limited" targets have been used to increase proton cutoff

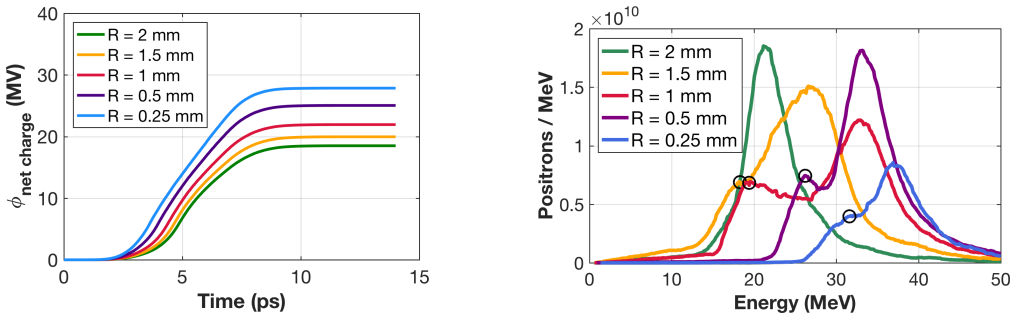


(a) (b)

Figure 6.23: (a) Calculated electrostatic potentials due to the net charging of targets, for targets of different radii. (b) Positron spectra for the corresponding target sizes, without protons. The positions of late time peaks are circled for the $R \leq 1.5$ mm targets. Reasonable agreement is found between the predicted net charging and the energy of the late time peaks for $R = 1$, 0.5 and 0.25 mm.

energies compared to large foil targets [184]. For positrons the increased fields will cause the peak to shift to higher energies. The scaling of this shift with target size is disputed. Chen *et al.* reported inverse scaling with surface area [30]:

$$E_{\text{peak (Chen)}} = 75\left(\frac{1}{A_{\text{cylinder}}}\right) + 4 \tag{6.10}$$

$$\rightarrow E_{\text{peak (Chen)}} \propto \frac{1}{2\pi R^2 + 2\pi HR} \tag{6.11}$$

where $R$ is the target radius and $H$ is the target height. Cylindrical Au targets were used, and the scaling was found by varying the diameter from 1 to 20 mm while keeping a constant 1 mm thickness. Data from both Titan (130 J in 1 ps, 8 µm spot) and OMEGA EP (~300-800 J in 10 ps, 50 µm spot) lasers fit this scaling. The intensities were 1–5 $\times$ $10^{20}$ W/cm$^2$.

More recently, Yan *et al.* reported scaling with inverse diameter [31]:

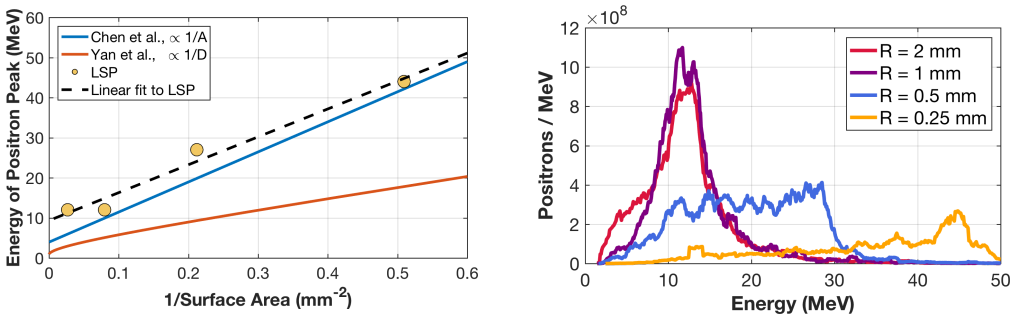


(a) (b)

Figure 6.24: (a) Comparison of peak positron energy with total target surface area. Chen *et al.* report scaling with inverse surface area [30], Yan *et al.* report scaling with inverse diameter [31]. Spectra from a parameter scan with LSP simulations are shown in (b) and the peak energies are plotted in (b). The LSP data is described well by a linear fit ($R^2 = 0.9743$).

$$E_{\text{peak (Yan)}} = 8.5\left(\frac{1}{D}\right) + 0.84 \tag{6.12}$$

$$\rightarrow E_{\text{peak (Yan)}} \propto \frac{1}{2R} \tag{6.13}$$

The targets used were also cylindrical Au discs, 1 mm thick and with diameters between 1 and 10 mm. The XingGuang III laser gave 100–200 J in ∼1 ps and a 20–30 µm spot, resulting in an intensity of $\sim 2 \times 10^{19}$ W/cm$^2$. The two scalings are shown in Figure 6.24a, plotted versus inverse surface area for comparison.

LSP can provide insight into these trends, as it can model realistic target sizes. A scaling study was carried out, with target radii of 0.25, 0.5, 1, and 2 mm. The target thickness was 1 mm, the same as the experiments, and a proton contaminant layer was present on the rear surface of the targets but not the side or front. The electron source used was 1 ps in duration, unscaled, and identical for each case. The resulting spectra are shown in Figure 6.24b, and the energies of the peaks are compared to the reported scalings in Figure 6.24a. The $R = 0.5$ mm case gave a broad spectrum that is not typical of positron spectrum; the highest energy cutoff was used as the peak energy. A linear

fit with inverse surface area matches the LSP results well, with $R^2 = 0.9743$. This is consistent with the inverse surface area scaling proposed by Chen *et al.* and the capacitor model put forward in [29]. In the charging model the potential established on the target due to escaping electrons is determined by the target capacitance, which in turn is set by the surface area. LSP simulations reported there had similar escaping hot electron distributions for both realistic disc targets and spherical targets of equivalent surface area. The results presented here support this model.

To interpret these results it is helpful to consider the surface area scaling of cylindrical targets. For small radii the surface area of the sides becomes significant and total surface area scales like $1/R$. For large radii the front and rear surfaces dominate and total surface area scales like $1/R^2$. The surface areas are 2.0, 4.7, 12.6 and 37.7 mm$^2$ for targets of radii 0.25, 0.5, 1 and 2 mm, respectively. It appears that for $R \geq 1$ mm the targets can effectively be considered semi-infinite in the transverse direction; this causes $\phi_{\text{net charge}}$ to become negligible and positron acceleration to be dominated by the initial hot electron pulse, $\phi_{\text{charge separation}}$. This potential is not significantly affected by target size, hence the constant peak energy for the $R = 1$ and 2 mm targets.

## 6.4 Conclusions and Future Work

Removal of the proton contaminant layer could provide an experimental test of the sheath evolution mechanisms detailed here, as well as provide an alternative route for enhancing positron yield. Most work done on optimizing laser-produced positrons has focused on the pair-production mechanism and maximizing the generation of hot electrons. This has involved calculating the optimal target thickness for a given hot electron temperature [161], the positron production rate for different materials [170] and scaling with laser parameters [72]. A rod geometry has been used to increase electron absorp-

tion relative to positrons, thereby increasing the positron-to-electron ratio [73]. Little work has been done regarding the sheath field and positron beams. Removing the contaminant layer could optimize the sheath field for positron acceleration.

There are several possible approaches to remove the contaminant layer in the laboratory. Cleaning a target from resistive heating has been experimentally demonstrated, in order to enhance the acceleration of heavier elements such as carbon [185]. Laser based heating has also been demonstrated, with continuous, several watt 532 nm lasers [131, 186]. Heating removes both front and rear surface protons, which would reduce the target preplasma scalelength and potentially decrease laser coupling to hot electrons and positrons. The injected source simulations do not account for any front surface LPI effects. Ion etching is another approach to removing contaminants that has been shown to selectively clean a surface [164]. This may be the preferred option to experimentally test this hypothesis, as the front surface preplasma will be maintained.

The role of electron refluxing in thick targets could be studied by measuring positron emission from the front surface, and scanning over target thickness. It is expected that front positron signal would decrease and eventually disappear as targets become thicker and refluxing becomes minimal. The positron signal from the rear of the target would decrease when changing from the optimal thickness, but with a different trend.

In conclusion, multiple positron spectral peaks were observed on experiment when the laser energy was increased to 1.5 kJ. These peaks were reproduced using LSP transport simulations and scaling the electron source in duration and magnitude to match the experiment. Simulations indicates that the peaks are caused by the time evolution of the sheath accelerating potential; the high energy peak develops early in time due to the trapped hot electron cloud, while the low energy peak develops late in time from the potential re-

sulting from the charging of the target. The energy of the low energy peak can be predicted with reasonable accuracy based on a simple, spherical capacitor model once electron energy loss is taken into account.

# Chapter 7
# Electrostatic Collisionless Shock Acceleration of Ions

A highly promising ion acceleration mechanism is collisionless electrostatic shockwave acceleration (CSA), which can generate high energy, monoenergetic ion beams. CSA occurs when a high pressure plasma expands into a lower pressure plasma and the background electron temperature is high; a shock will be established at the expansion front and ions ahead of the shock get reflected by the electric field present at the shock interface. The final velocity of the reflected ions can be up to twice the velocity of the shock. This process has been studied extensively in simulations [2] but is difficult to observe in the laboratory. Ultra-intense lasers can generate the conditions necessary for CSA when a laser interacts with a near-critical density plasma. Experimentally CSA has been reported with a 10 µm $CO_2$ laser and an $H_2$ gas jet target; monoenergetic protons beams up to ∼20 MeV with energy spreads of less than 1% were observed [133]. The total particle number in the beams was only $\sim 10^5$, however. Higher density plasmas are required to increase the density of the shock and the reflected beam, which has motivated research into driving shocks with shorter wavelength lasers and correspondingly higher $n_{\mathrm{crit}}$.

Three Titan experiments with two different approaches were conducted to try and demonstrate shock acceleration with a 1 µm laser. The first approach used a nanosecond beam to expand plastic foils, and carefully timed a picosecond pulse to drive a shock in the decompressing foil at the optimal density profile. The other approach used a cryogenic hydrogen jet to directly make a low density, ∼10 $n_{\mathrm{crit}}$ target. Both approaches were experimentally difficult, and consequently only one campaign succeeded. The first exploding foil ex-

periment and the hydrogen jet experiment used frequency doubling to increase the contrast level of the short pulse driver; however this appeared to reduce the laser $a_0$ below the threshold necessary to drive strong shocks. The second exploding foil experiment utilized the $1\omega$ beam and a plasma mirror to reach a higher $a_0$ while still maintaining a high contrast level. Distinct, high energy proton and ion peaks were observed in this final experiment. The properties of these peaks are consistent with collisionless electrostatic shockwave acceleration. This chapter will outline the theory behind CSA, the experimental approach used in the third, successful experiment, and analysis of the IPS ion data.

## 7.1 Theory of Shock Acceleration

A shock wave is a pressure discontinuity in a fluid, typically driven by density, across which the fluid properties undergo a step change [187]. This discontinuity arises when the energy transferred in a fluid exceeds the energy flux that can be supported by the sound speed, $C_s \times P_{max} \approx \rho C_s^3$. The region behind the shock is known as the downstream region; ahead of the shock is the upstream region. From the conservation of mass, momentum and energy the Rankine-Hugoniot jump condition can be derived, which relate the conditions before and after the shock, i.e the upstream and downstream regions:

$$\rho_1 u_1 = \rho_2 u_2 \tag{7.1}$$

$$\rho_1 u_1^2 + p_1 = \rho_2 u_2^2 + p_2 \tag{7.2}$$

$$\left[\rho_1 u_1 \left(\epsilon_1 + \frac{u_1^2}{2}\right) + p_1 u_1\right] = \left[\rho_2 u_2 \left(\epsilon_2 + \frac{u_2^2}{2}\right) + p_2 u_2\right] \tag{7.3}$$

where $\rho$, $u$, $p$ and $\epsilon$ are the density, velocity, pressure, and specific internal energies of the fluids, respectively; the indices indicate either the upstream

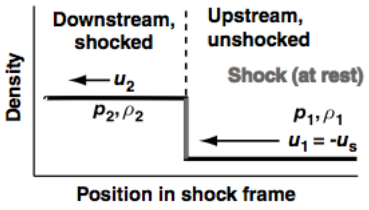


Figure 7.1: A shock wave.

(1) or downstream (2) regions. The result is that material after the shock becomes compressed, heated, and sped up - which is to say, the entropy increases. This dissipation of energy and corresponding increase in entropy is a key characteristic of a shock. These concepts are illustrated in Figure 7.1.

The shock velocity is defined as:

$$v_{\text{shock}} = MC_s \tag{7.4}$$

where $M$ is the Mach number and $C_s$ is the sound speed. In a plasma, $C_s$ is given by the ion acoustic velocity:

$$C_s = \left(\frac{ZT_e}{m_i}\right)^{1/2} \tag{7.5}$$

From Equation (7.5) it can be seen that the shock velocity depends upon the electron temperature, indicating that to reach high velocities the background plasma must be very strongly heated. This gives the first constraint to CSA: $E_{ion} \propto \frac{1}{2}m_i C_s^2 = \frac{1}{2}ZT_e$, from which it can be seen that to reach MeV-level ions, the electron temperature must also be $\sim$MeV.

A collisionless shock appears to be a contradiction, as the interaction of typical shocks with the background fluid is mediated by collisions. In plasmas, however, electromagnetic fields can play the same role, and this is a well-known phenomena in astrophysics where plasmas are often very low density. For an HED plasma with a density of $10^{22}$ cm$^{-3}$, however, it is not clear that collisionality can be neglected. The mean free paths for electron-ion and

ion-ion collisions are:

$$\lambda_{ei} = \frac{v_e}{\nu_{ei}} \approx \frac{c}{\nu_{ei}} \tag{7.6}$$

$$\lambda_{ii} = \frac{v_i}{\nu_{ii}} \approx \frac{C_s}{\nu_{ii}} \tag{7.7}$$

The electron-ion and ion-ion collision frequencies are given by:

$$\nu_{ei} = \frac{(2.53 \times 10^{-6}) n_e[cm^3] \mathrm{Z} \ln\Lambda}{T_{eV}^{3/2}} \tag{7.8}$$

$$\nu_{ii} = \frac{(4.8 \times 10^{-8}) n_e[cm^3] \mathrm{Z} \ln\Lambda}{T_{eV}^{3/2} (m_i/m_p)^{-1/2}} \tag{7.9}$$

For reasonable plasma values of $T_e = 500$ keV, $T_i = 100$ eV and $n_e = n_i = 10^{21}$ cm$^{-3}$, $\lambda_{ei} = 3.2$ m and $\lambda_{ii} = 111\,\mu$m. This is much larger than the shock interaction scale, which is 10's of µm, and therefore the shock can be considered collisionless.

An electrostatic collisionless shock forms from ion acoustic waves, which develop as the dense region expands upstream and rarefracts downstream. These waves lead to strong oscillations in the ion density, and for large enough density discontinuities the acoustic wave oscillations becomes nonlinear and trap particles. The leading oscillation is soliton-like and forms the collisionless shock. This situation is depicted in Figure 7.2 for the case in which the density discontinuity is hump-like; this most resembles that of laser plasmas and was studied extensively by Medvedev [32].

Charge separation occurs at the moving front, generating strong electric fields which can trap or reflect incoming ions. To understand ion reflection from the shock it is useful to consider a frame moving with the shock, in which the shock is stationary and upstream ions are impinging upon it at the shock velocity. These ions will climb the potential until they are either stopped

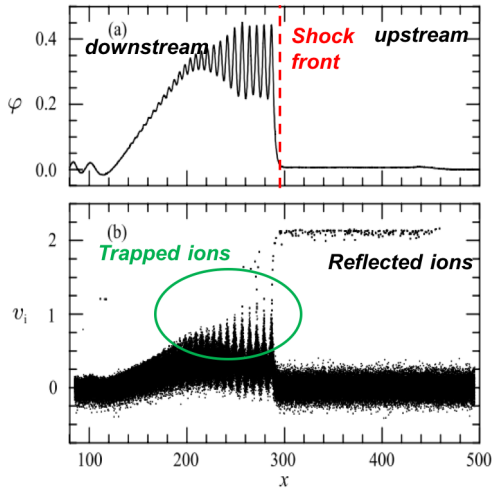


Figure 7.2: Results for a 1D simulation of a shock driven from a hump-like density discontinuity, with finite ion temperature $T_{i_0} = 0.01T_{e_0}$, at time $t = 200(m_i/4\pi Z_i e^2 n_{e_0})^{1/2}$. Top: Potential $\phi(x)$, showing oscillations behind the shock front due to ion acoustic waves in the trapped ions moving with the shock. Botton: Ion velocity phase space $(x, v_i)$ with the trapped ions and reflected ion populations indicated. The units for $x$, $v_i$ and $\phi$ are Debye length $\lambda_D$, ion acoustic velocity $C_s$, and $T_{e_0}/e$, respectively. From [32].

($v = 0$, as in the middle diagram) or pass over the barrier and through the shock. The reflection condition is therefore that the electrostatic potential barrier exceed the particle kinetic energy (which is non-relativistic for ions) [33]:

$$q_i \phi_{\text{shock}} > \frac{1}{2} m_i v_i^2 \tag{7.10}$$

Provided this condition is met, the ion will be stopped and accelerated down the potential. It will reach a final velocity equal to its initial speed in the shock frame, in the opposite direction. This is reflection from a shock. In the lab frame, if the particle starts are rest then the reflected ion will move at:

$$v_{\text{reflected}} = 2v_{\text{shock}} \tag{7.11}$$

For a more realistic case where the upstream plasma is expanding at some velocity $v_0$, the relative motion between the shock and the particle will be

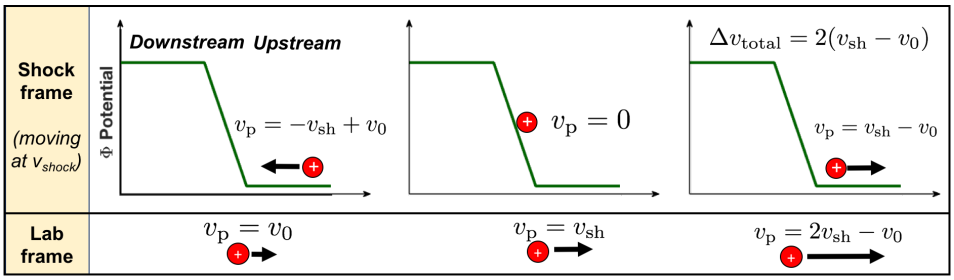


Figure 7.3: Ion reflection from a shock with an expanding upstream plasma.

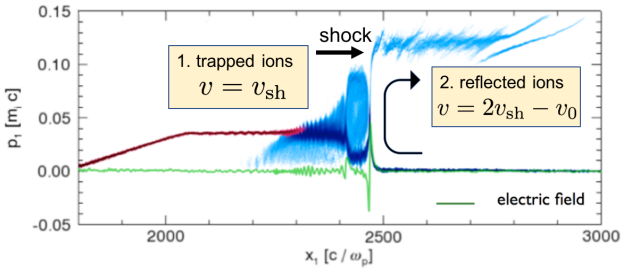


Figure 7.4: Ion phase space from a 1D PIC simulation, demonstrating the two populations of ions generated in a shock: (1) The trapped ions moving with the shock. (2) Reflected ions given a velocity of boost of twice the shock velocity. Simulation performed by Dr. Frederico Fiuza.

modified. The reflected ions will then move at:

$$v_{\text{reflected}} = 2v_{\text{shock}} - v_0 \tag{7.12}$$

The process of ion reflection from a shock is depicted in Figure 7.3 for the non-zero upstream velocity case.

The simplest shock acceleration scenario can produce two quasi-monoenergetic populations of particles: those trapped with the shock moving at the $v_{\text{shock}}$, and those reflected by the shock moving at $2v_{\text{shock}} - v_0$. In phase space this produces a distinctive fork-like structure, shown in Figure 7.4.

Ultra-intense lasers can be used to establish the conditions necessary for strong CSA. They do this in two ways: (1) radiation pressure drives density steepening in the region irradiated by the laser, creating the pressure discontinuity necessary for shock expansion. (2) Electrons are heated by the laser to MeV-level energies. Both of these processes occur most efficiently for near-

critical density targets. In particular, bulk heating of the background electrons is only possible when the interaction density, $\gamma n_{\text{crit}}$, approaches the peak target density, $n_0$. In this case the return current necessary to balance out the hot electron current can consist of the majority of the background electron population. As the return current electrons reach the interaction region they are heated by the laser, and provided that the target is thin enough for significant electron circulation to occur while the laser is on, efficient heating of the bulk electrons is possible.

One of the main challenges to observing CSA in the laboratory when using ultra-intense lasers is the presence of strong sheath fields, which both spectrally broaden the shock peaks and generate TNSA ion beams that can overwhelm the shock signal. These effects are demonstrated using PIC simulations in plots (a) and (b) of Figure 7.5. It has been proposed that an exponentially decreasing rear surface density profile could minimize the influence of TNSA, and allow shock peaks to be observed [33]. The strength of the electric field for a TNSA sheath is given by:

$$E_{TNSA} = \frac{k_B T_{e0}}{e L_n} \tag{7.13}$$

where $L_n$ is the rear plasma scalelength. By making $L_n$ large the peak TNSA field becomes small and relatively constant over a long spatial region. This reduces the energy gained by TNSA-accelerated particles, and also preserves the limited velocity spread of the shock particles by ensuring they are accelerated by a constant electric field. This tailored density profile case is shown in plots (c) and (d) of Figure 7.5, and can be achieved experimentally by laser irradiation and hydrodynamic expansion.

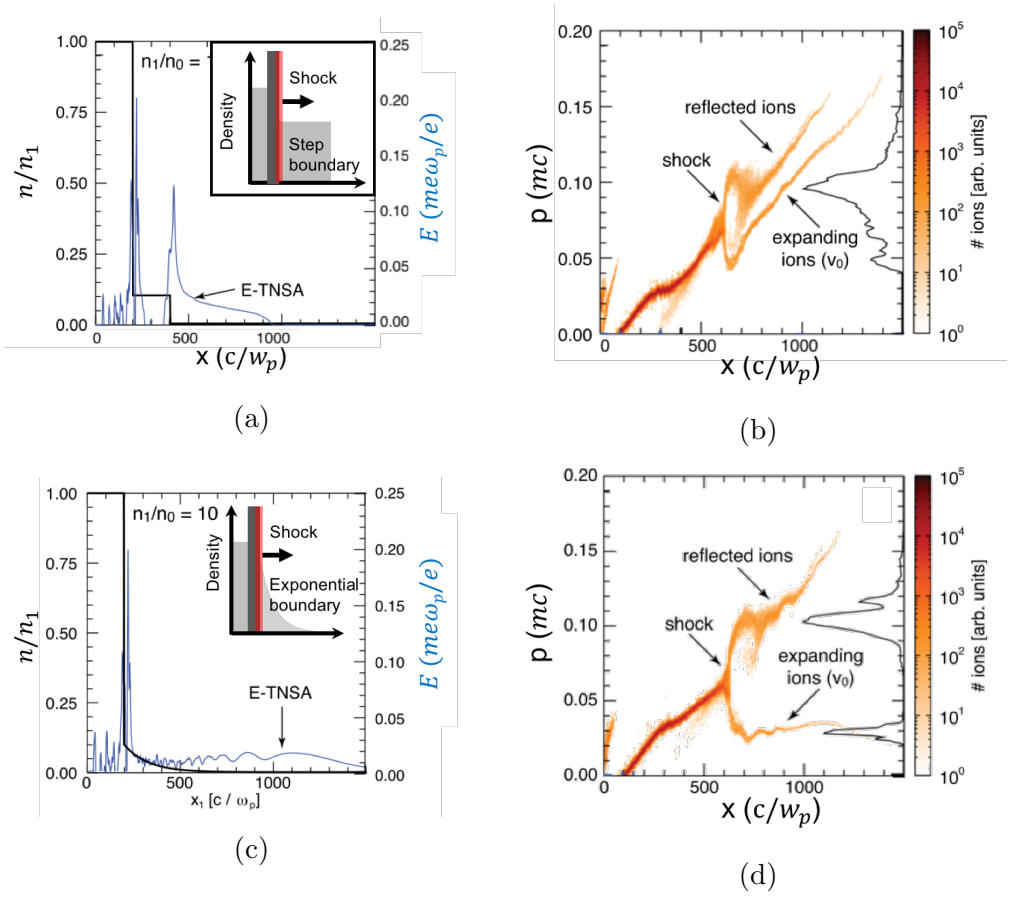


Figure 7.5: PIC simulations illustrating the effect of a step vs. exponential boundary, for shock and TNSA beams. Simulations were performed by Dr. Frederico Fiuza. (a) Density and electric field for a step boundary, with a strong TNSA field. (b) Ion phase space, with significant spectral broadening of the reflected ions. (c) An exponential boundary, showing significantly reduced electric fields (d) Reflected ions remain mono-energetic. Figures taken from [33].

## 7.2 Experimental Investigation

The experimental campaigns were carried out at the Titan laser. The setup described here and shown in Figure 7.6b is for the successful third experiment, but a similar setup (excluding the plasma mirror) was used for the first experiment using a $2\omega$ beam. The targets were 0.5 µm Mylar foils ($C_{10}H_8O_4$) stretched over 4 mm washers. Pure CH plastic was the preferred target material but Mylar was used by accident; the presence of oxygen was detrimental, and caused reduced target heating and ion sound speed. The tailored density profile was created by irradiating the target with the long pulse (LP) beam, and delaying the short pulse (SP) arrival until the target had expanded and decompressed to the desired density. The optimal density profile was evaluated by matching the peak density to the expected $a_0$ of 10, taking into account relativistic transparency, so that $n_{max} = 10n_{\text{crit}}$. Asymmetric front and rear scalelengths developed naturally due to the one-sided irradiation and hydrodynamic expansion. The short scalelength on the front surface was beneficial to reducing beam filamentation and maximize density steepening. A LP-SP timing delay of 4 ns was found to produce peak density $\sim 10n_{\text{crit}}$, as determined by 2D HYDRA simulations of the target expansion from Tony Link (Figure 7.6a). The $1\omega$ long pulse ablation beam was 10 ns in duration, 8.5 J and used a phase plate to create a smooth 500 µm diameter spot. The resulting intensity was $\sim 4 \times 10^{10}$ W/cm$^2$. This low value was chosen to minimize the target expansion velocity, and therefore reduce the effect of timing jitter on the density profile interacted with by the SP beam. The $1\omega$ SP was ~80 J in 0.7–1 ps (nominal duration) and a 20 µm diameter spot containing half the energy, giving a peak $a_0$ of 8.6.

The contrast ratio of the short pulse laser was a critical parameter, as a significant nanosecond prepulse would greatly disrupt the density profile of the target and inhibit the formation of a strong shock. The first experiment

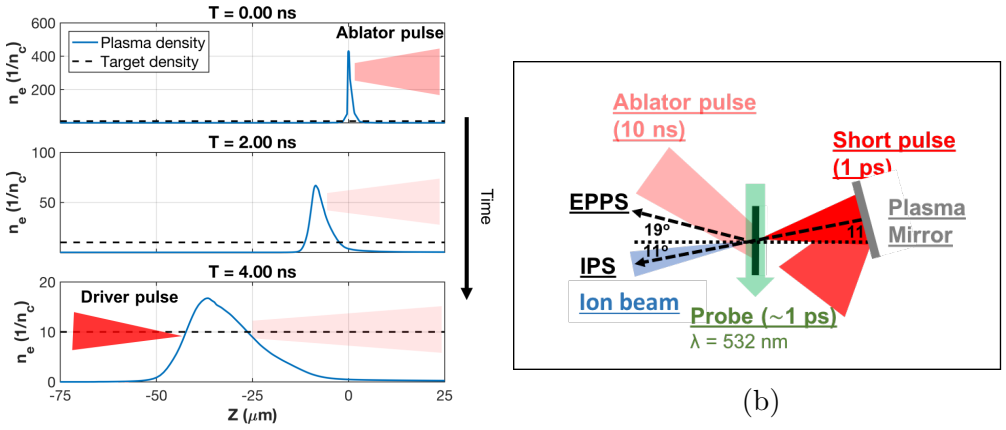


(a) (b)

Figure 7.6: (a) HYDRA profiles of the target at different times. These profiles were used to guide the delay between the ablator and short pulses. The simulations performed by Dr. Anthony Link. (b) Titan experimental setup.

utilized frequency doubling to improve the Titan contrast, which is on the order of $10^{-4}$ to $10^{-5}$ for $1\omega$ (5 – 10 mJ). Unfortunately, this reduced the hot electron production in two ways: (1) the 20 cm, sub-aperture doubling crystal gave <40% conversion from $1\omega$ to $2\omega$ light, and (2) the $I\lambda^2$ ponderomotive scaling of electron temperature (Equation (6.5)), caused $T_e$ to be reduced by a factor of 0.25 for $\lambda = 527$ nm compared to $\lambda = 1054$ nm. Additionally, issues with the compressor likely resulted in reduced temporal compression of the beam. Inconsistent, weak proton peaks at 1–2 MeV were observed. The second experiment used $2\omega$ and a cryogenic hydrogen jet, developed by SLAC [188], as the target. The intrinsic density of the jet is $5\times10^{22}$ cm$^{-3}$, making it a promising target for shock acceleration, but the difficulty of fielding the jet with the Titan laser and the aforementioned issues with $2\omega$ electron acceleration led to poor data. Only a small proton peak at 1.1 MeV was observed, which could be due to various non-shock acceleration mechanisms [56].

For the third, successful experiment a plasma mirror (PM) was used to increase the contrast level of the $1\omega$ short pulse. Anti-reflection coated, 1" fused silica mirrors were used for the PM, which was located 4 cm from TCC. The mirror was ~90% reflective in the fluence operating range of 60 - 80 J/cm$^2$,

with a 1.4 cm spot diameter on the PM. Spectralon measurements of the reflected profile indicated an F/3 beam, similar to that of the incident beam. The spectralon images were also used to give feedback on the contrast enhancement: with the PM in place the imaged spot was highly speckled, indicating that the surface features of the target survived long enough to scatter the laser. Similar profiles were observed with the low contrast $2\omega$ pulse, while the $1\omega$ beam with no PM gave smooth profiles due to the presence of significant preplasma. The contrast of the beam after the PM was not measured directly, but similar setups have reported contrast enhancements of up to $10^{-2}$ [141].

### 7.2.1 Electron Measurements

To measure the electron spectrum an Electron-Proton-Positron Spectrometer (EPPS) was used. It was located 741 mm $\pm$1 mm from TCC, 30.1° from the rear laser axis. The measured spectra showed increased coupling into hot electrons for near-critical density targets compared to solid targets (Figure 7.7a), which validates one of the goals of using such targets. However, the escaping electron temperatures for near-critical targets were not correlated well with different calculated laser intensities (before self-focusing). This could indicate that self-focusing is dominating the interaction. Another possibility is that the hot escaping electrons are mainly generated in the underdense region of the density profile, which is insensitive to timing changes between the long pulse and short pulse. The relationship between the escaping electron temperature and the bulk electron temperature was also of interest, as the bulk electron temperature determines the ion sound speed and therefore the energy of the shock accelerated ions. While it was found that the measured $T_{\mathrm{hot}}$ did not correlate with the proton peak velocities (see Section 7.3.1), simulations were performed to give more insight into this relation. Analysis was performed on a 2D LPI simulation (setup by Tony Link), with a realistic density profile and laser spot size. Escaping electrons were measured at a plane 100 µm

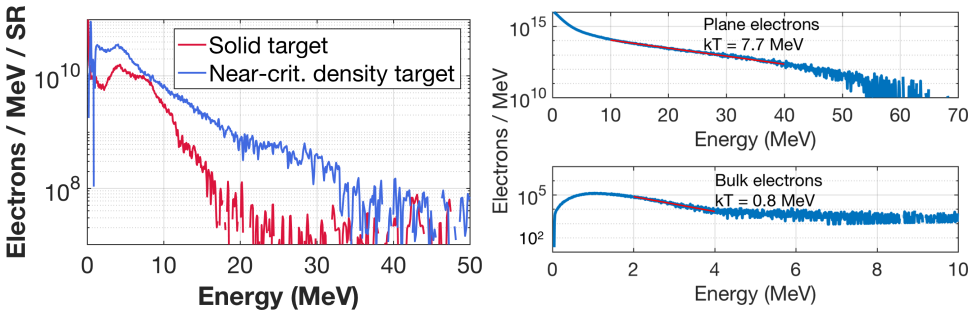


(a) (b)

Figure 7.7: (a) Measured electron spectra showing enhanced coupling to hot electrons for near-critical density target. (b) Simulated escaping and bulk electron temperatures from 2D LPI PIC, showing a ∼1/10 relationship.

from peak density, while bulk electrons were measured in a 10 µm box around the ion front. It was found that the bulk electrons were much cooler than the escaping electrons (Figure 7.7b), with $T_{e(\text{bulk})} \approx 1/10 \times T_{e(\text{escaping})}$. The background electrons are still highly energetic, however, at $T_e > 0.8$ MeV and much higher temperature than for a solid target.

### 7.2.2 IPS Measurements

The primary ion diagnostic was the Imaging Proton Spectrometer (IPS). The 5 cm height of the IPS entrance slit allowed for relatively large angular coverage in the vertical direction (±2.7°), which was important to capture the spatially inhomogeneous proton beams. The spectrometer was placed along the laser axis, 530 mm ±1 mm from TCC, and 11° off of rear-target normal. Data was collected primarily on the rear image plate (IP), to view > 2 MeV protons. Initially a 50 µm aluminum filter was placed on the IP to block heavy ions and ensure proton signal up to 16 MeV (see Figure 5.3). To measure higher energy protons a 250 µm Al foil was added to half of the IP, for a total thickness of 300 µm. By comparing the signals from the two filter channels protons could be distinguished from heavier ions, allowing for simultaneous proton and ion measurements over wide angular ranges. Protons were measured up to 49 MeV

on the 300 µm channel with no overlaid ion signal, and $C^{6+}/O^{8+}$ ions broke through on the 50 µm channel starting at $E_{\text{carbon}} = 75$ MeV/$E_{\text{protons}} = 25$ MeV (with potential overlap with proton signals). Significant variations in IPS signal were observed off the central axis of the IP, necessitating analysis of the full 2D spectrum. The dewarping procedure used is outlined in Section 5.1.4. A Thomson Parabola (TP) was fielded beside the IPS, but problems with arcing and the small pinhole size made capturing data unreliable. The main result from the TP data was the conclusion that the charge states of the ions was primarily $C^{6+}$ and $O^{8+}$.

Scans were performed varying SP-LP delay and SP focal position in order to find conditions for shock acceleration. When near-critical density targets were shot, modified proton spectra were produced, with reduced TNSA-like exponential signal and a variable number of quasi-monoenergetic proton peaks. The 2D IPS rear IP data is shown in Figure 7.8 for a reference SP only shot and a near-critical density target. The reference TNSA spectrum from the SP only shot is inset; an exponential fall-off to a clear cutoff at around 17 MeV can be seen. For this shot the target was offset by 200 µm, which would give a focal spot of >50 µm. Near-critical density shots with two distinct proton peaks are shown in Figure 7.9. They were taken with a delay of 4 ns and SP offset in axial focal position of 200, 150 and 250 µm (after focal point). The highest energy quasi-monoenergetic proton peak observed was 17 MeV, for shot 79, with an energy spread of 6%. Shots with single proton peaks in the 5 - 10 MeV energy range were common, typically at the end of a TNSA-like spectrum. The proton spectra were highly variable, with identical conditions giving very different results. This was interpreted as uncertainty in the plasma conditions from the long pulse pointing and timing, as well as laser variability from self-focusing and plasma mirror effects.

To find the number of protons in the monoenergetic beams both spatial and spectral limits of integration must be defined. Gaussian curves were first

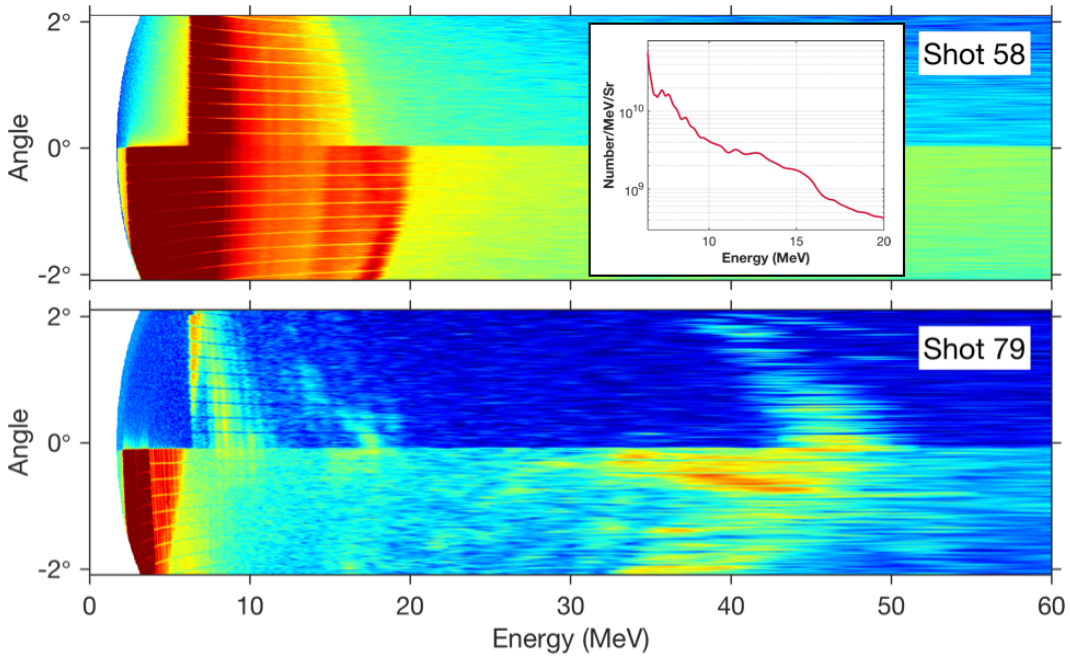


Figure 7.8: Dewarped rear image plate data from the IPS. Shot 58 was a single beam, TNSA shot. Shot 79 was two beam, shock acceleration. The spectrum for shot 58 is inset, showing a typical TNSA distribution.

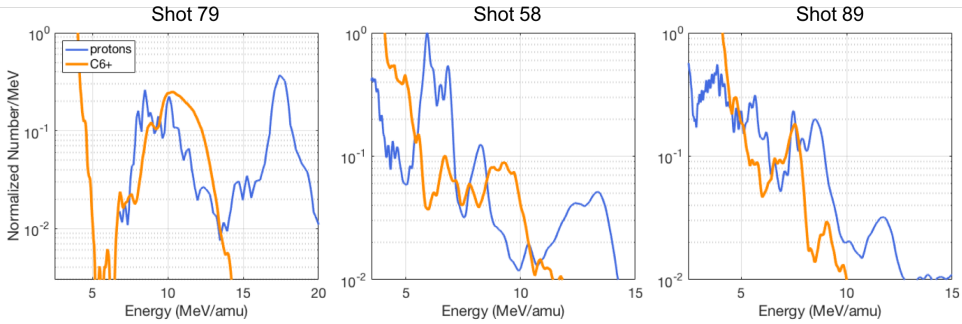


Figure 7.9: Proton and ion ($C^{6+}$ or $O^{8+}$) spectra, for tailored density targets with two proton peaks. The targets were offset 150, 200 and 250 µm behind the SP focal position, respectively.

fitted to the spectral peaks, and energy cutoffs were set at 0.2 of the Gaussian maximum signals (Figure 7.11). The spectra were then integrated within this range to get protons/steradian. The TNSA signal was integrated in the same energy region to provide a direct comparison of yield. The final number of protons in the beam was determined from the beam footprint, as measured by radiochromic film. A cone with a half angle of 30° was found to encompass the shock signal (Figure 7.10), for a proton energy of ∼11 MeV. The spatial uniformity of the beam was low, however, with a high degree of filamentation (see discussion below). It was therefore necessary to define a fill factor, corresponding to the variation in signal (after background subtraction) in the beam region. This was found to be $40 \pm 20\%$. Using these values, the maximum number of protons in a beam was $2 \pm 1 \times 10^9$. Typical values were on the order of $10^8 - 10^9$ protons. This is $10^3 - 10^4$ times more then the number reported in [133], although it should be noted that some of this enhancement comes from the increased solid angle and energy spread and not increased particles per steradian per MeV. The total number of protons in the lower energy peak is 1/7 that in the same spectral range for the reference TNSA shot using the plasma mirror; the total number in the higher energy peak is 2× TNSA for the same spectral range. The reference shot was not taken under optimal TNSA conditions, however, due to the high contrast and defocused beam (although the effects of a large beam spot may under some circumstances enhance TNSA [100]). A comparison to a TNSA shot under more optimal conditions (low contrast, 10 µm Au target, best focus) indicates that the shock beams had ∼1/35 protons in a comparable spectral range.

The beam structure in Figure 7.10 was indicative of the general shock-accelerated proton beam quality. The filamentation is believed to occur due to Weibel-induced magnetic fields in the long scalelength plasma. Experimental and computational work has suggested that Weibel instabilities can develop under these conditions due to the hot electron beam and corresponding return

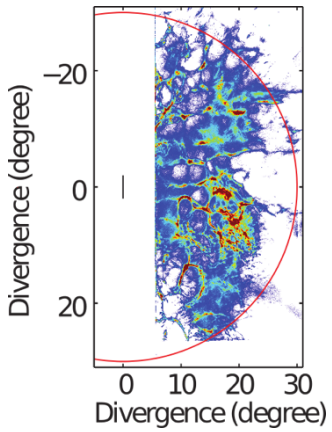


Figure 7.10: RCF image of the shock-accelerated proton beam footprint, generated by Dr. Art Pak. The black vertical line indicates the approximate acceptance angle of the IPS, and the proton energy is ∼11 MeV.

current [189, 190].

### 7.2.3 Carbon Data

As discussed earlier, CSA will accelerate heavier ions as well as protons provided the reflection condition, Equation (7.10), is met. For $C^{6+}$ and $O^{8+}$, which have half the charge-to-mass ratio of protons, twice the potential is needed for reflection to occur. In the ideal case ions moving with or reflected by a shock will have the same velocity as protons, but a larger energy due to their mass. Ions were measured in the 50 µm channel of the IPS. The spectra are shown in Figure 7.9 overlaid with protons, where they have been plotted as MeV/amu to better compare velocity with protons. The ion signal has been corrected for the filter effect (Section 5.1.2). It can be seen that the ion peaks generally agree well with the lower energy proton peaks and do not show signal for the higher energy peaks. The number of ions is typically 20-30× lower then protons, although for shot 79 the number is comparable. As the IPS cannot differentiate between species with the same charge-to-mass ratio, the ion signal could be either $C^{6+}$ or $O^{8+}$ (Mylar contains both species). The species was taken to be $C^{6+}$ for PSL to ion number conversion, as there are published

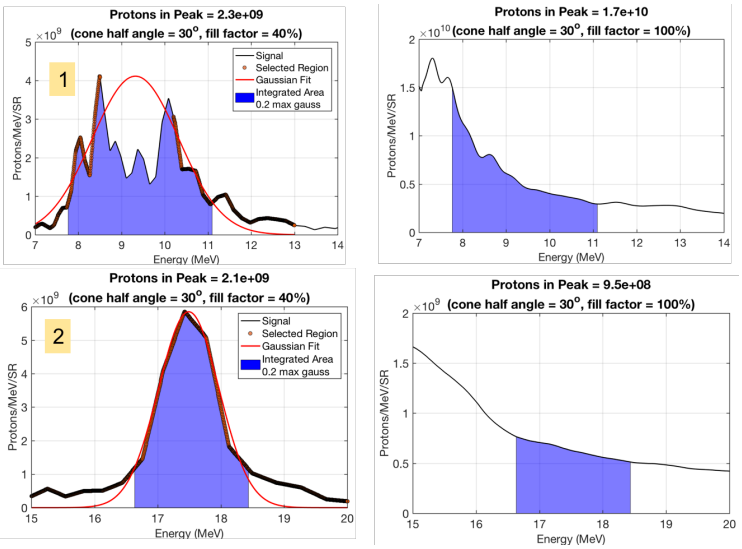


Figure 7.11: Calculation of protons/SR for the shock peaks (left) and corresponding energy regions for TNSA (right).

conversion factors for carbon.

## 7.3 Interpretation of Ion Peaks

The measured high energy proton peaks, up to 17 MeV, cannot be well explained by any acceleration mechanism other then CSA for the experimental laser and target conditions. Radiation pressure acceleration (RPA) and hole boring can only efficiently drive ions when coupling to the target is poor and reflectivity is high, for maximum momentum transfer, while the background electrons are cold [191]. Schemes to realize these mechanism use circularly polarized light to minimize electron heating and thin (<200 nm) targets, very different conditions from those of shock acceleration. Calculated ideal proton hole boring energies (assuming 100% laser reflection) for a range of $a_0$ and electron densities is shown in Figure 7.12 [34]. The estimated ranges of experimental parameters is highlighted. Assuming optimal hole boring conditions, such that self-focusing doubles $a_0$ from 9 to 18 and a peak electron density $n_e = 1 \times 10^{21}$ cm$^{-3}$ is reached, a maximum proton energy of 7.6 MeV

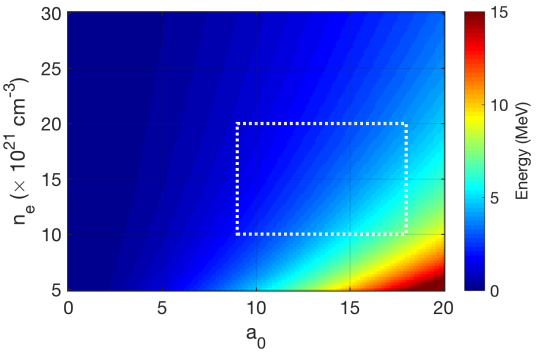


Figure 7.12: Relativistically corrected, mixed species calculation of proton hole boring energies, based on [34]. The estimated experimental parameter range is indicated by the dashed box, which has a mean proton energy of 3.2 MeV and a maximum of 7.6 MeV. These values are much less then the maximum experimental energy of 17 MeV.

is expected. This is significantly less then the observed maximum peak energy of 17 MeV, and also a large overestimate based on the high absorption (low reflectivity) expected for the real interaction. Breakout afterburner (BOA) is not expected to occur as the target is not relativistically transparent, which is necessary for the mechanism [192].

### 7.3.1 Acceleration Scenarios

The exact reason for the observation of two proton peaks in some shots is difficult to determine exactly. The dynamics of the shock acceleration process can be complex, and the presence of non-negligible TNSA fields adds an additional complication. First, it is assumed that the protons in the highest energy peak are due to reflection from a shock, which is supported by PIC simulations; it is likely that they were partially accelerated by TNSA fields, however. The lower energy peaks could then have several possible sources:

1. **Particles that are trapped and moving with the shock.** This scenario is seen in Figure 7.4 for a 1D PIC simulation, and is typically observed for simple simulations (1D, single species). The velocities of the two proton peaks should then follow the relationship given by Equa-

tion (7.12).

2. **Reflection from multiple shocks.** 2D PIC simulations have shown that multiple reflections can occur over the course of a single interaction, in the following manner: a strong early shock reflects both protons and ions, while a shock later in time just reflects protons. The potential associated with the second reflection is smaller, but the upstream protons have significant expansion velocities by this time from TNSA and therefore can be reflected. For two proton peaks to be output from this scenario the two reflections must not coexist for a significant amount of time; if they do, particles will experience acceleration from both shocks and the net result will be a single final energy.

3. **TNSA.** When the rear density profile is exponential the sheath field is approximately constant in space and the protons accelerated by it can form a peak, as shown in Figure 7.5d for a 1D PIC simulation. The trapped shock ions may have energies comparable to those from TNSA.

A further challenge in interpreting the data is determining the energy contributions of CSA vs. TNSA. Depending upon the temporal dynamics of the acceleration process, either or both mechanisms can contribute to the energy gained by a given particle. If a shock is driven through an expanding plasma accelerated by the sheath field, the relative motion between the shock and the upstream plasma is reduced and the reflected ions are boosted less. If the shock acceleration phase ends before the shock and reflected populations reach significant sheath fields, they will be accelerated further by TNSA in a second phase. Their final energies will therefore have contributions from both shock and sheath field acceleration. These scenarios are summarized in Figure 7.13, with the lower energy peak labelled 'peak 1' and the higher energy peak labelled 'peak 2'.

Two dimensional PIC simulations performed by Dr. Frederico Fiuza sug-

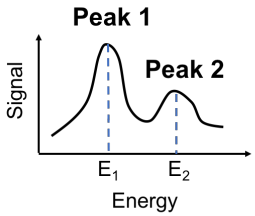


| Peak 1 scenarios | Peak 2 scenarios |
|---|---|
| **1. Trapped shock particles** $E_1 = E_{CSA\ (shock)} \pm E_{TNSA\ 1}$ | $E_2 = E_{CSA\ (reflection\ 2)} \pm E_{TNSA\ 2}$ |
| **2. Multiple reflections** $E_1 = E_{CSA\ (reflection\ 1)} \pm E_{TNSA\ 1}$ | |
| **3. TNSA for exponential $n_p$** $E_1 = E_{TNSA\ 1}$ | |

Figure 7.13: Possible scenarios for energy gain of the observed proton peaks. $E_{\text{CSA (reflection)}}$ and $E_{\text{TNSA}}$ may not be equal for peaks 1 and 2, and $E_{\text{TNSA}}$ may be zero or negligible.

gest that the CSA process is highly sensitive to the initial density profile. Multiple reflections (scenario 2) appear to be the dominate process for an idealized CH profile, with a peak density of $n_e = 1 \times 10^{22}$ cm$^{-3}$, a linear increase over 10 µm on the front surface and an exponential decrease on the rear surface with a scalelength $L_n = 20$ µm. The laser was 1 ps in duration with a peak $a_0 = 8.5$. Ion phase space plots for this case at two interaction times are given in Figure 7.14a, and show that a two shock feature appears to arise from species separation of the $H^+$ and $C^{6+}$ ions. Early in time a strong shock is driven, with enough of a potential barrier to reflect both proton and carbons. TNSA occurs rapidly, such that the shock was propagating through an expanding plasma. Later in time a weaker shock is driven in the expanding plasma, which is strong enough to reflect protons but not carbons. The second, higher energy proton peak arises from this second reflection. In this case the velocity of the second peak is $v_2 = 2v^*_{\text{shock}} + v_{\text{TNSA}}$, where $v^*_{\text{shock}} = v_s - v_{\text{TNSA}}$ is the shock velocity in the upstream frame (see Table B.2). When the peak density is decreased to $n_e = 5 \times 10^{21}$ cm$^{-3}$ and the idealized CH profile is maintained, a much higher energy proton peak is observed. The reduced target mass allows for increased electron heating, stronger TNSA and a faster shock. The energy of the resulting reflected proton beam is $E \approx 100$ MeV, close to the theoretical scaling [33]. It should be noted that plane wave irradiation was used instead of a finite laser spot.

When a more realistic density CH profile is used, the dominant CSA process changes. The profile, taken from a HYDRA simulation, had a peak density of $n_e = 1.1 \times 10^{22}$ cm$^{-3}$ and two different rear scalelengths: a small scalelength from peak density to approximately critical density, and a large scalelength afterwards (see Figure 7.15a). Reflection from a shock occurs early in time, as compared to the ideal case the plasma is less strongly heated and the shock velocity is lower. The proton and carbon spectra are again similar to those observed on experiment, with two proton peaks and a carbon peak at a similar velocity to the lower energy proton peak (see Figure 7.15b). In this case, however, the lower energy proton peak is associated with protons moving with the shock (scenario 1). Strong species separation occurs between $H^+$and $C^{6+}$due to the collisionless nature of the simulations, and consequently similar results are seen in both CH and H only cases.

The experimental data is consistent with a scenario 1 interpretation, although it is offers limited information on the interaction dynamics and cannot provide a definite conclusion. Relationships were calculated between the measured proton peak velocities and the sound speed inferred from the escaping electron temperature for the scenarios outlined above. The derivations are given in Appendix B, with care taken to distinguish the lab and upstream frames. As discussed in Section 7.2, from 2D PIC simulations the escaping electron temperature appears to overestimate the bulk electron temperature by $\sim$10$\times$, and consequently the measured $T_e$ were scaled by 1/10 when calculating $C_s$. Additional assumptions were that the expansion velocity is equal to the sound speed, and that the Mach number was 1.5 (based on typical simulation values [33]). The three scenarios are depicted graphically in Figure 7.16, Figure 7.17 and Figure 7.18. In all scenarios two cases are give: either CSA and TNSA occur separately, with CSA first, or CSA and TNSA occur simultaneously (i.e. a shock is driven through an expanding plasma). The experimental data points from the three double peak shots are overlaid.

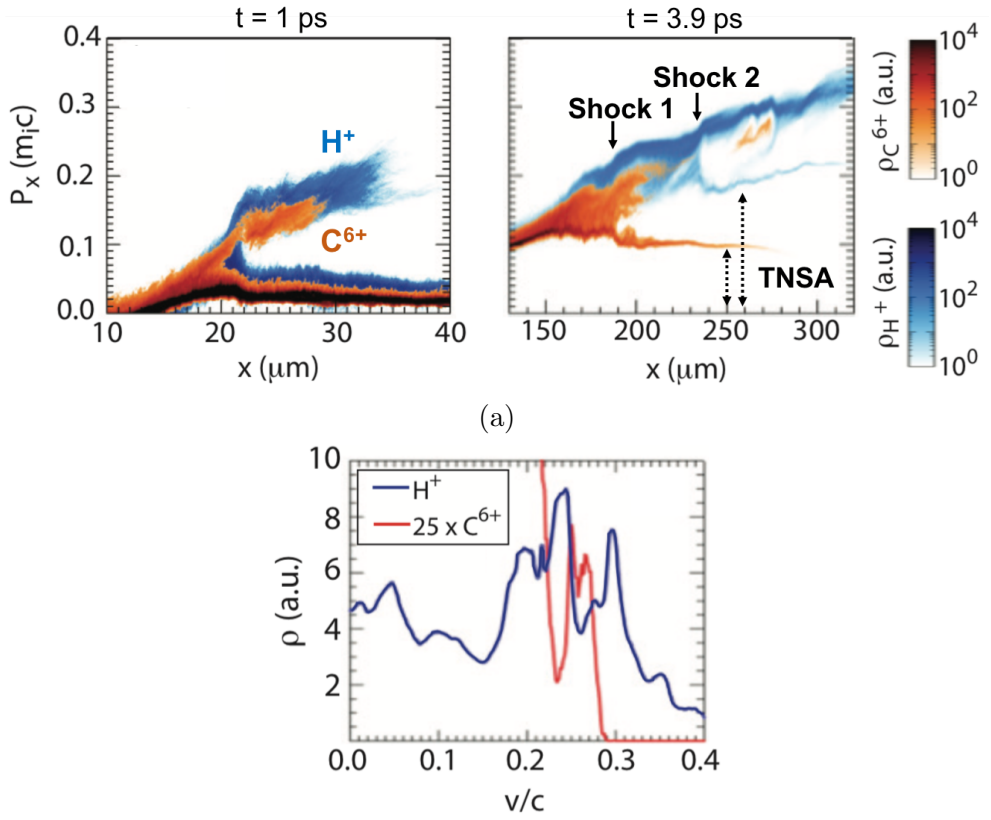


Figure 7.14: Results from 2D PIC simulations using an idealized density profile with a peak density of $n_e = 1 \times 10^{22}$ cm$^{-3}$, and a 1 ps laser with $a_0 = 8.5$. (a) Ion phase space plots. Two times are shown: 1 ps (left) and 3.9 ps (right) after the start of the laser pulse. $H^+$ ions are shown in blue, $C^{6+}$ ions in orange. A strong shock early in time reflects both ion species, while a weaker shock later in time only reflects protons. Simulations and diagrams from by Dr. Frederico Fiuza. (b) Ion spectra at late time, showing a double proton peak and single carbon peak similar to that observed on experiment.

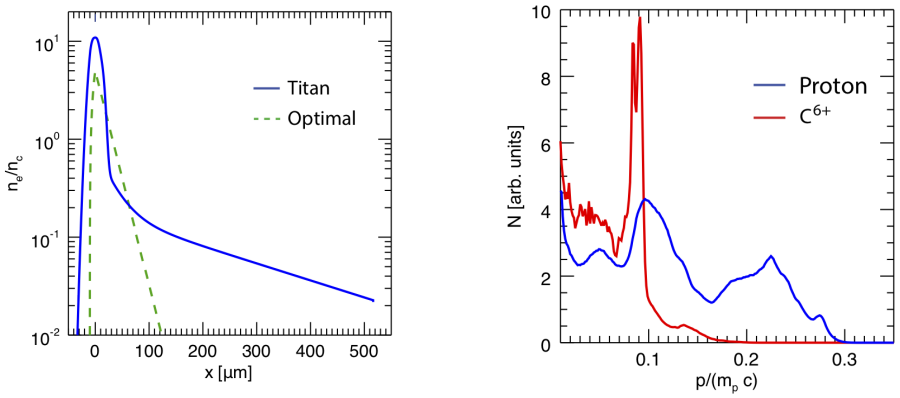


(a) (b)

Figure 7.15: (a) Density profiles used in 2D PIC simulations. The 'Titan' profile is taken from a HYDRA simulation and approximates the experimental conditions. (b). Proton and carbon spectra for the Titan profile, displaying features similar to experiment. Simulations and diagrams from Dr. Frederico Fiuza.

Scenario 2, depicted in Figure 7.17, has too many free variables to be tested with the same data and assumptions. The evidence for it comes from the interpretation of PIC simulations, as discussed above. Of the cases that can be tested from experimental data, scenario 1 (CSA then TNSA) and scenario 2 (CSA and TNSA) are in best agreement with the data based on calculated $\chi^2$ values. The $\chi^2$ values are calculated from the difference between the expected ion sound speed (background colourmap) and the speed calculated from experimental measurements (scatter point colours). The low number of experimental data points, however, does not give a high degree of confidence in these results. Of these three possibilities, scenario 1 was judged to be the most likely due to the agreement of the realistic density profile PIC simulation. In this process the low energy proton peak originates with protons moving with the shock and the high energy proton peak is due to from reflection from this shock.

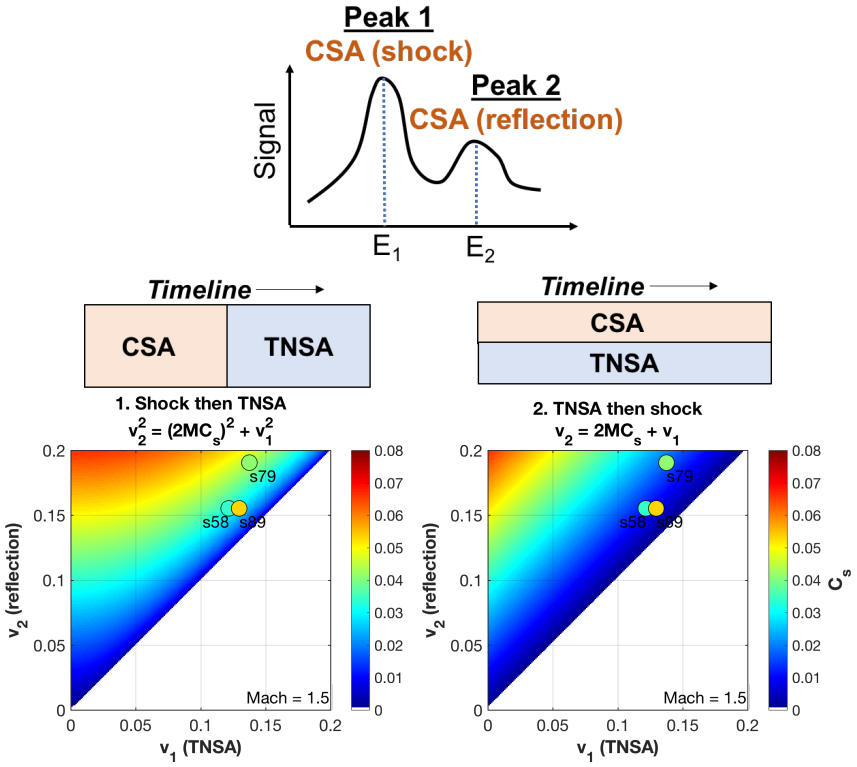


Figure 7.16: Scenario 1 velocity phase space plots, with peak 1 due to shock from CSA. The plot indicates calculated sound speeds for reflection and TNSA contributions. Scatter points are experimentally measured peak velocities, with sound speeds found from 0.1× the escaping electron temperature and Mach = 1.5. The $\chi^2$ values are 0.01 and 0.11. Note that shot 58 is offset to the right by 0.01 to prevent overlap with shot 89.

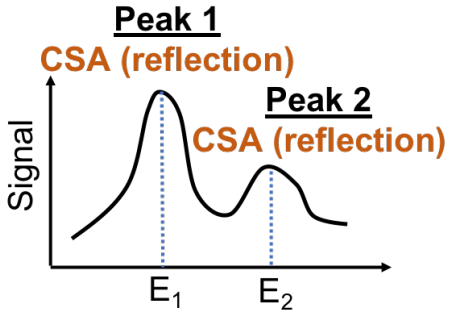


Figure 7.17: Scenario 2, in which peak 1 is due to reflection from CSA. This is the scenario indicated by PIC simulations in Figure 7.14.

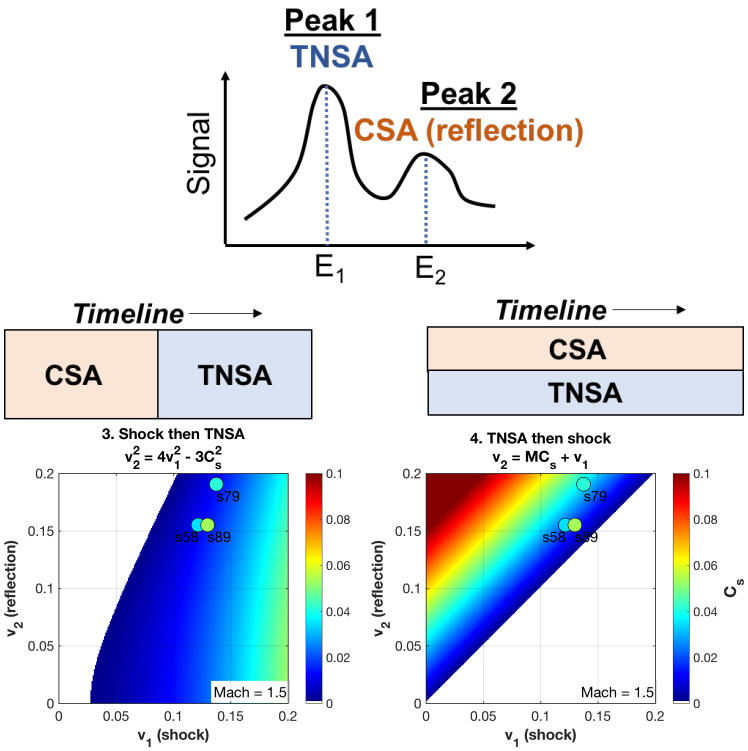


Figure 7.18: Scenario 3 velocity phase space plots, in which peak 1 is from TNSA. The $\chi^2$ values are 0.06 and 0.02.

### 7.3.2 Single Shot Analysis

Shot 79 was the strongest shot, based on energy and signal level of the ions peaks, and therefore was examined further. If the observed ion spectral peaks have some energy contribution from both CSA and TNSA then the ratio of the peak velocities will not accurately indicate the shock signature. This assumes scenario 1, with CSA and TNSA occurring as distinct phases and CSA finishing before TNSA occurs. To try and deconvolve these effects, Figure 7.19 plots proton energy as a function of relative velocity contributions of shock and sheath acceleration, from 0 to 100%. The ratios of the shock velocity components of the peaks are also plotted. The measured velocities of the peaks are $v_1 = 0.14$c and $v_2 = 0.19$c for $E_1 = 9.0$ MeV and $E_2 = 17.5$ MeV, respectively, giving a ratio of $v_2/v_1 = 1.36$. If there is a TNSA contribution to the energies of the peaks, the components due to CSA decrease and the ratio of the shock velocities increases. One possible choice for maximum TNSA velocity contribution is $v_{\mathrm{TNSA}} \approx 0.11$c, which is the velocity corresponding to the cutoff energy of proton signal below the first proton peak; this value gives $v_{2,\mathrm{shock}}/v_{1,\mathrm{shock}} = 1.9$, $v_{\mathrm{carbon,\ shock}}/v_{1,\mathrm{shock}} = 1.1$ and $v_{\mathrm{carbon,shock}}/v_{2,\mathrm{shock}} = 0.6$. These ratios are consistent with CSA, with peak 1 being shock ions, peak 2 being reflection from this shock moving at approximately twice the shock velocity and carbon ions co-moving with protons in the shock.

Scenario 2, in which peak 1 is due to a second reflection and CSA and TNSA occur concurrently, can also be evaluated on this shot. In PIC simulations the shock velocity in the upstream frame, $v^*_{\mathrm{shock}}$, was seen to be relatively constant in time. The TNSA velocity of carbon was roughly half that of hydrogen in the simulation: $v_{\mathrm{TNSA},\ C^{6+}} \approx 0.5 v_{\mathrm{TNSA},\ H^+}$. The ratio of the final velocities for proton peak 1 and the carbon peak is then:

$$\frac{v_{\mathrm{final},H+}}{v_{\mathrm{final},C^{6+}}} = \frac{2v^*_{\mathrm{shock}} + v_{\mathrm{TNSA},\ H^+}}{2v^*_{\mathrm{shock}} + v_{\mathrm{TNSA},\ H^+}/2} \tag{7.14}$$

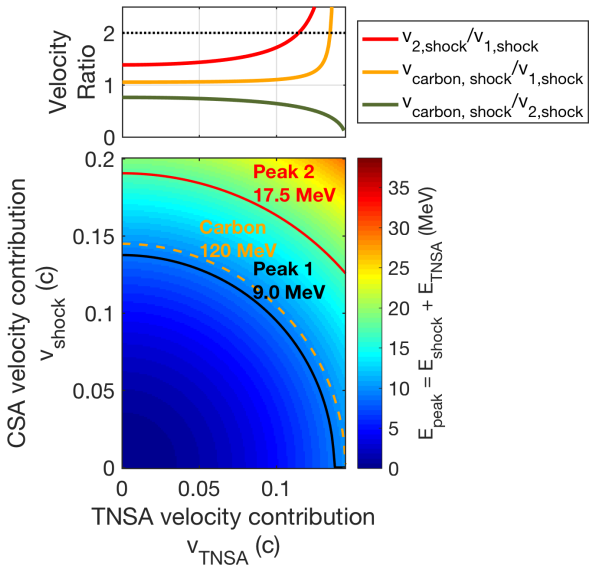


Figure 7.19: Velocity contribution ranges from CSA and TNSA, for shot 79. The velocity ratios of the shock components are plotted above, using the some velocity scale. For scenario 1 – peak 1 is due to a shock, peak 2 is due to reflection from this shock – a ratio of $v_{2,\mathrm{shock}}/v_{1,\mathrm{shock}}{\sim}2$ is expected. For a TNSA contribution of $v_{\mathrm{TNSA}} \approx 0.11$c, based on the experimental cutoff before the first peak, a ratio of $v_{2,\mathrm{shock}}/v_{1,\mathrm{shock}} = 1.9$ is found.

When the shock contribution dominates, it can be seen that $v_{\mathrm{final},H+}/v_{\mathrm{final},C^{6+}}{\sim}1$. The value from simulation was ∼1.16 and from shot 79 was ∼1.1, which suggests significant shock acceleration in this scenario.

In summary, the most reasonable explanation for the ion peaks observed is that they are due to acceleration from CSA. No other explanation can explain the high energies of the peaks for the conditions at the time of the interaction. This is validated by 2D PIC simulations which give details of the interaction, indicating that CSA is dominant with some additional acceleration from residual TNSA effects. The detailed contribution of TNSA cannot be determined from the present experiments due to limited number of data shots and the variety of possible interaction scenarios, as discussed.

## 7.4 Conclusions and Future Work

Using a two beam setup, quasi-monoenergetic proton peaks up to 17 MeV were observed from expanded foil, near-critical density targets. Multiple proton peaks were observed, as well as single carbon peaks at similar velocities to the lower energy proton peaks. The interaction conditions and high peak energies suggest that electrostatic collisionless shockwaves (CSA) was the primary acceleration mechanism. Low energy proton peaks ($E < 1$ MeV) attributed to CSA have been previously published with a $\lambda = 1054$ nm laser and a gas jet target with $n_e \approx n_{\text{crit}}$ [193], but the results reported here show greatly enhanced proton energies. They open up the possibility of higher flux, high energy, quasi-monoenergetic ion beams at various facilities around the world.

Future work is necessary to find the optimal conditions for shock acceleration. A more planar shock could give a more uniform or energetic beam, and may be possible to achieve by defocusing the driver beam. The highly filamented spatial quality of the beam is an issue for any potential applications, and therefore finding a way to reduce or eliminate the filamentation is crucial. One potential approach is to increase the rear scalelength, such that the growth of the fields decreases and the proton beam deflection is reduced.

Lastly, alternative targets offer another promising avenue to explore. Low density foam, high pressure gas jets and micro-structured, 3D-printed targets can all reach near-critical densities without the difficulties associated with foil expansion. Foams ranging from $0.9 - 30 n_{\text{crit}}$ (densities of $3 - 100$ mg/cm$^{-3}$) have been shot at OMEGA EP [194]. To reduce TNSA fields a pre-tailored, exponential profile could be constructed. Alternatively, a thin, high-Z layer with surface contaminants removed could be placed behind the foam layer, as shown in Figure 7.20. The lack of light species on the clean rear surface would constrain the sheath field to the surface of the high-Z layer, where it would evolve on the timescale of the heavy, high Z ions. The resulting

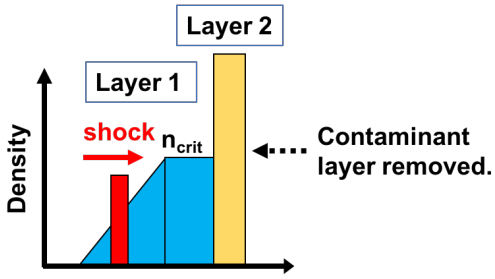


Figure 7.20: Double layer target concept. Layer 1 is pre-formed and near-critical density, either foam or 3D-printed. Layer 2 is a thin, high-Z foil with the rear contaminant layer removed. A shock is driven in layer 1, and the shock-accelerated particles travel through layer 2 and are further accelerated by constrained sheath fields on the rear.

localized fields should preserve the quasi-monoenergetic energies of the shock-accelerated particles to a higher degree then standard TNSA fields; a similar concept has demonstrated in computational work [195].

# Chapter 8
# Conclusions and Future Work

## 8.1 Conclusions

The generation and acceleration of energetic proton and positron beams from ultra-intense laser-plasma interactions has been studied, both experimentally and computationally. Beams of relativistic positrons were produced in thick (∼mm), high-Z targets and the energy gain through target normal sheath acceleration (TNSA) was investigated. In the first part of this thesis, it was proposed that these positron beams can act as probes of the accelerating fields on the target, and a computational study was performed to connect the observed positron spectral features with the underlying field behaviour. For the second part of this thesis, an experimental study was undertaken to demonstrate collisionless shockwave acceleration (CSA) of ions driven by an ultrashort laser pulse at a wavelength of $\lambda = 1.054$ µm laser. In this case a high intensity laser pulse drives an electrostatic shock in a near critical density plasma, that can reflect ions in its path as it propagates forward. These reflected ions can result in quasi-monoenergetic ion beams, which are desirable for many applications. Ion spectra with properties consistent with shock acceleration were observed.

The computational study of positrons was motivated by experimental results from the OMEGA EP laser, where the positron spectra evolved from a single, quasi-monoenergetic peak to multiple peaks when the laser energy was increased from 250 J to 1.5 kJ in 10 ps. It was hypothesized that the spectral features were the result of transient phenomena in the accelerating sheath fields, present only when the target was highly charged, and that the positrons could be an effective probe of these fields. Particle-in-cell simulations

were carried out using the LSP code to test this hypothesis. The simulations were implicit, 2D cylindrical, and hybrid, with both kinetic and fluid particles. An electron source was injected to model the laser heating of electrons, and scaled in duration and charge to approximate the experimentally measured escaping electron spectra. The targets were 1 mm thick Au foils, the laser pulse duration was ∼10 ps, and the simulations were run to 40 ps to capture the full interaction. The oscillation of the electron cloud in space was studied by varying the target radius from 0.25 mm to 2 mm. The simulations indicate that the positron peaks are caused by the time evolution of the sheath accelerating potential, with the high energy peaks developing early in time due to the trapped hot electron cloud and the low energy peaks developing late in time from the potential resulting from the charging of the target. The electron cloud oscillations introduce perturbations on top of the general potential evolution. The target must also be small enough ($R \leq 1$ mm) such that the confinement of electrons remains significant at late times during the interaction. Lastly, the energy of the low energy peak can be predicted with reasonable accuracy based on a simple, spherical capacitor model once electron energy loss in the thick targets is taken into account.

The experimental shock acceleration work was performed using the Titan laser in the Jupiter Laser Facility. A 0.5 µm thick Mylar foil target was ablated with a nanosecond laser at $I \approx 10^{10}$ W/cm$^2$, then allowed to decompress to near-critical density. The shock was then initiated by a $\lambda = 1054$ nm, picosecond laser with $I > 10^{19}$ W/cm$^2$. A steep density profile on the front surface was necessary to maximize coupling, and this was realized by a plasma mirror. Quasi-monoenergetic proton peaks up to 17 MeV were measured using the Imaging Proton Spectrometer. For several shots multiple proton peaks were observed, as well as single carbon peaks at similar velocities to the lower energy proton peaks. PIC simulations indicate that these peaks occur due to reflections from multiple shocks, with the carbon species playing a key role

in the formation of the second shock. Alternative acceleration mechanisms, such as hole boring, cannot easily explain the data and thus CSA is the most probable mechanism for the generation of the ion beams. This is believed to be the first observation of multi-MeV proton beams from CSA with a wavelength of $\lambda = 1054$ nm laser, which allows much higher beam fluxes than past work.

## 8.2 Future Work

In the LSP simulations of positron beams, the presence of a proton contaminant layer on the rear target surface was found to have a significant effect on the positron acceleration. Removal of the contaminant layer in simulations led to increased signal in the lower energy, late time positron peak, as the hot electrons remained confined to the target at late times instead of co-moving with the proton beam. Conducting an experiment with this proton layer removed could provide a further test of the simulations and interpretations described in this thesis. In addition, it could optimize the sheath field for positron acceleration and may therefore enhance position yield. Experimentally, the contaminant layer could be removed by resistive heating of the target, laser heating, or ion etching. Of these options, ion etching is likely the preferred choice; it allows selective cleaning of the rear surface without removing the contaminant layer on the front surface, and therefore does not affect the preplasma or laser absorption.

One potential application of in situ positron probing of sheath fields is in the area of multi-pulse TNSA, which is of interest due to the possibility of highly efficient proton acceleration under certain conditions [121]. The evolution of the sheath field is hard to diagnose on sub-picosecond timescales, and therefore the full effects of multiple pulse irradiation are still unclear. Positron pulses can be generated and accelerated on a comparable timescale, and could give insight into this area.

Much work remains to achieve the optimal conditions for shock acceleration. The maximum proton energy predicted from simulations for $a_0 = 9$ is ∼100 MeV [33], while the maximum energy measured experimentally with a similar $a_0$ was 17 MeV. Applications such as proton radiotherapy require $E > 200$ MeV beams [6], and therefore achieving more effective CSA is critical. Simulations suggest that the discrepancy is primarily due to the non-ideal plasma density profile realized on experiment, which had a slower shock and reduced TNSA. To overcome these limitations, alternative targets could be developed. Low density foams and micro-structured, 3D-printed targets are promising options; they can reach near critical densities and have pre-made, tailored density profiles that avoid the complications and uncertainty of multi-beam setups. High pressure gas jets and cryogenic jets are also intriguing options, as allow for high repetition rates. Increasing shot rate is necessary to deliver useful doses in a reasonable amount of time; a typical medical treatment is on the order of $10^{11}$ protons [6], while the proton number in the measured quasi-monoenergetic beams was $10^8 - 10^9$. Lastly, more complicated targets combining foam and solid layers may be worth exploring, as they could enhance the beam energy.

In addition to target modifications, there are several other possible areas of improvement for CSA. Enlarging the beam spot of the short pulse laser could drive a more planar shock, that in turn could give a more uniform and energetic ion beam. To maintain laser intensity, however, more energy would be necessary. An externally imposed axial magnetic field is another option for improving performance, as it would reduce lateral plasma expansion and therefore the divergence of the shock. Improving the spatial uniformity of the ion beam is also necessary for any potential applications. The high filamentation seen in the beam is believed to occur from instability growth on the rear surface [189], which may be reduced for longer rear scalelengths that give weaker fields. In all cases, advanced simulations of expected performance,

similar to those carried out in this thesis, will help to guide and optimize such studies.

# References


[1] H. Chen, A. U. Hazi, R. van Maren, S. N. Chen, J. Fuchs, M. Gauthier, S. Le Pape, J. R. Rygg, and R. Shepherd, "An imaging proton spectrometer for short-pulse laser plasma experiments." *The Review of Scientific Instruments*, vol. 81, 10D314, 2010. https://doi.org/10.1063/1.3483212 [Not cited.]

[2] F. Fiuza, A. Stockem, E. Boella, R. A. Fonseca, L. O. Silva, D. Haberberger, S. Tochitsky, C. Gong, W. B. Mori, and C. Joshi, "Laser-driven shock acceleration of monoenergetic ion beams," *Physical Review Letters*, vol. 109, 215001, 2012. https://doi.org/10.1103/PhysRevLett.109.215001 [Cited on pages 30 and 91.]

[3] "NASA Space Radiation Laboratory User Guide." https://www.bnl.gov/nsrl/userguide/bragg-curves-and-peaks.php [Cited on page 2.]

[4] K. Quinn, P. A. Wilson, C. A. Cecchetti, B. Ramakrishna, L. Romagnani, G. Sarri, L. Lancia, J. Fuchs, A. Pipahl, T. Toncian, O. Willi, R. J. Clarke, D. Neely, M. Notley, P. Gallegos, D. C. Carroll, M. N. Quinn, X. H. Yuan, P. McKenna, T. V. Liseykina, A. MacChi, and M. Borghesi, "Laser-Driven ultrafast field propagation on solid surfaces," *Physical Review Letters*, vol. 102, 194801, 2009. https://doi.org/10.1103/PhysRevLett.102.194801 [Cited on pages 3 and 80.]

[5] K. Quinn, L. Romagnani, B. Ramakrishna, G. Sarri, M. E. Dieckmann, P. A. Wilson, J. Fuchs, L. Lancia, A. Pipahl, T. Toncian, O. Willi, R. J. Clarke, M. Notley, A. Macchi, and M. Borghesi,

"Weibel-Induced Filamentation during an Ultrafast Laser-Driven Plasma Expansion," *Physical Review Letters*, vol. 108, 135001, 2012. https://doi.org/10.1103/PhysRevLett.108.135001 [Cited on page 3.]

[6] V. S. Khoroshkov and E. I. Minakova, "Proton beams in radiotherapy," *European Journal of Physics*, vol. 19, 523, 1998. https://doi.org/10.1088/0143-0807/19/6/006 [Cited on pages 4, 5, and 116.]

[7] M. Roth, T. E. Cowan, M. H. Key, S. P. Hatchett, C. Brown, W. Fountain, J. Johnson, D. M. Pennington, R. A. Snavely, S. C. Wilks, K. Yasuike, H. Ruhl, F. Pegoraro, S. V. Bulanov, E. M. Campbell, M. D. Perry, and H. Powell, "Fast ignition by intense laser-accelerated proton beams," *Physical Review Letters*, vol. 86, 436, 2001. https://doi.org/10.1103/PhysRevLett.86.436 [Cited on pages 8 and 9.]

[8] J. J. Honrubia and M. Murakami, "Ion beam requirements for fast ignition of inertial fusion targets," *Physics of Plasmas*, vol. 22, 012703, 2015. https://doi.org/10.1063/1.4905904 [Cited on pages 8 and 9.]

[9] K. G. Estabrook, E. J. Valeo, and W. L. Kruer, "Two-dimensional relativistic simulations of resonance absorption," *Physics of Fluids*, vol. 18, 1151, 1975. https://doi.org/10.1063/1.861276 [Cited on page 16.]

[10] P. Gibbon and A. R. Bell, "Collisionless absorption in sharp-edged plasmas," *Physical Review Letters*, vol. 68, 1535, 1992. [Cited on page 16.]

[11] J. E. Crow, P. L. Auer, and J. E. Allen, "The expansion of a plasma into a vacuum," *Journal of Plasma Physics*, vol. 14, 65, 1975. https://doi.org/10.1017/S0022377800025538 [Cited on page 22.]

[12] P. Mora, "Plasma Expansion into a Vacuum," *Physical Review Letters*, vol. 90, 185002, 2003. https://doi.org/10.1103/PhysRevLett.90.185002 [Cited on pages 20 and 22.]

[13] L. J. Waxer, D. N. Maywar, J. H. Kelly, T. J. Kessler, B. E. Kruschwitz, S. J. Loucks, R. L. Mccrory, D. D. Meyerhofer, S. F. B. Morse, C. Stoeckl, and J. D. Zuegel, "High-Energy Petawatt Capability for the Omega Laser," *Optics and Photonics News*, vol. 16, 30, 2005. https://doi.org/10.1364/OPN.16.7.000030 [Cited on pages 35 and 36.]

[14] H. Chen, A. J. Link, R. Van Maren, P. K. Patel, R. Shepherd, S. C. Wilks, and P. Beiersdorfer, "High performance compact magnetic spectrometers for energetic ion and electron measurement in ultraintense short pulse laser solid interactions." *The Review of Scientific Instruments*, vol. 79, 10E533, 2008. https://doi.org/10.1063/1.2953679 [Cited on pages 39 and 68.]

[15] C. K. Birdsall and A. B. Langdon, *Plasma Physics Via Computer Simulation*. McGraw-Hill Book Company, 1985. [Cited on page 43.]

[16] D. Welch, R. Clark, C. Thoma, N. L. Bruner, T. C. Genoni, C. Mostrom, E. Madrid, C. Miller, W. Zimmerman, and D. Rose, "Advanced Particle-in-Cell Techniques for HEDP Simulation - LSP," Tech. Rep., 2011. [Cited on page 45.]

[17] A. Mancić, J. Fuchs, P. Antici, S. A. Gaillard, and P. Audebert, "Absolute calibration of photostimulable image plate detectors used as (0.5-20 MeV) high-energy proton detectors." *The Review of Scientific Instruments*, vol. 79, 073301, 2008. https://doi.org/10.1063/1.2949388 [Cited on pages 55, 56, and 185.]

[18] T. Bonnet, M. Comet, D. Denis-Petit, F. Gobet, F. Hannachi, M. Tarisien, M. Versteegen, and M. M. Aleonard, "Response functions of Fuji imaging plates to monoenergetic protons in the energy range 0.6-3.2 MeV," *Review of Scientific Instruments*, vol. 84, 013508, 2013. http://dx.doi.org/10.1063/1.4775719 [Cited on pages 40, 55, 56, and 185.]

[19] D. Doria, S. Kar, H. Ahmed, A. Alejo, J. Fernandez, M. Cerchez, R. J. Gray, F. Hanton, D. A. MacLellan, P. McKenna, Z. Najmudin, D. Neely, L. Romagnani, J. A. Ruiz, G. Sarri, C. Scullion, M. Streeter, M. Swantusch, O. Willi, M. Zepf, and M. Borghesi, "Calibration of BAS-TR image plate response to high energy (3-300 MeV) carbon ions," *Review of Scientific Instruments*, vol. 86, 123302, 2015. http://dx.doi.org/10.1063/1.4935582 [Cited on pages 56 and 185.]

[20] J. F. Ziegler, J. P. Biersack, and M. D. Ziegler, *SRIM: The Stopping and Range of Ions in Matter*. Morrisville, NC: Lulu Press Co, 2008. [Cited on pages 57 and 58.]

[21] M. Berger, J. Coursey, M. Zucker, and J. Chang, "ESTAR, PSTAR, and ASTAR: Computer Programs for Calculating Stopping-Power and Range Tables for Electrons, Protons, and Helium Ions (version 1.2.3)," 2005. http://physics.nist.gov/Star [Cited on page 67.]

[22] T. Tabata, P. Andreo, K. Shinoda, and R. Ito, "Range distributions and projected ranges of 0.1- to 100-MeV electrons in elemental absorbers," *Nuclear Instruments and Methods B*, vol. 108, 11, 1996. https://doi.org/10.1016/0168-583X(95)00625-7 [Cited on pages 67 and 86.]

[23] H. Chen, A. Link, Y. Sentoku, P. Audebert, F. Fiuza, A. Hazi, R. F. Heeter, M. Hill, L. Hobbs, A. J. Kemp, G. E. Kemp, S. M. Kerr, D. D. Meyerhofer, J. Myatt, S. R. Nagel, J. Park, R. Tommasini, and G. J. Williams, "The scaling of electron and positron generation in intense laser-solid interactions," *Physics of Plasmas*, vol. 22, 056705, 2015. https://doi.org/10.1063/1.4921147 [Cited on pages 10, 48, 63, 67, 68, and 187.]

[24] A. Pukhov, Z.-M. Sheng, and J. Meyer-ter Vehn, "Particle acceleration

in relativistic laser channels," *Physics of Plasmas*, vol. 6, 2847, 1999. https://doi.org/10.1063/1.873242 [Cited on pages 66 and 68.]

[25] Y. Ping, R. Shepherd, B. Lasinski, M. Tabak, H. Chen, H. Chung, K. Fournier, S. Hansen, A. J. Kemp, D. Liedahl, K. Widmann, S. C. Wilks, W. Rozmus, and M. Sherlock, "Absorption of Short Laser Pulses on Solid Targets in the Ultrarelativistic Regime," *Physical Review Letters*, vol. 100, 085004, 2008. https://doi.org/10.1103/PhysRevLett.100.085004 [Cited on page 72.]

[26] A. J. Kemp and L. Divol, "Interaction Physics of Multipicosecond Petawatt Laser Pulses with Overdense Plasma," *Physical Review Letters*, vol. 109, 195005, nov 2012. https://doi.org/10.1103/PhysRevLett.109.195005 [Cited on pages 71 and 72.]

[27] P. M. Nilson, A. A. Solodov, J. F. Myatt, W. Theobald, P. A. Jaanimagi, L. Gao, C. Stoeckl, R. S. Craxton, J. A. Delettrez, B. Yaakobi, J. D. Zuegel, B. E. Kruschwitz, C. Dorrer, J. H. Kelly, K. U. Akli, P. K. Patel, A. J. MacKinnon, R. Betti, T. C. Sangster, and D. D. Meyerhofer, "Scaling hot-electron generation to long-pulse, high-intensity lasersolid interactions," *Physics of Plasmas*, vol. 18, 235001, 2011. https://doi.org/10.1063/1.3560569 [Cited on page 72.]

[28] M. H. Key, M. D. Cable, T. E. Cowan, K. G. Estabrook, B. A. Hammel, S. P. Hatchett, E. A. Henry, D. E. Hinkel, J. D. Kilkenny, J. A. Koch, W. L. Kruer, A. B. Langdon, B. F. Lasinski, R. W. Lee, B. J. MacGowan, A. MacKinnon, J. D. Moody, M. J. Moran, A. A. Offenberger, D. M. Pennington, M. D. Perry, T. J. Phillips, T. C. Sangster, M. S. Singh, M. A. Stoyer, M. Tabak, G. L. Tietbohl, M. Tsukamoto, K. Wharton, and S. C. Wilks, "Hot electron production and heating by hot electrons in fast ignitor research," *Physics of*

*Plasmas*, vol. 5, 1966, 1998. https://doi.org/10.1063/1.872867 [Cited on page 72.]

[29] A. J. Link, R. R. Freeman, D. W. Schumacher, and L. D. Van Woerkom, "Effects of target charging and ion emission on the energy spectrum of emitted electrons," *Physics of Plasmas*, vol. 18, 053107, 2011. https://doi.org/10.1063/1.3587123 [Cited on pages 19, 26, 75, 84, and 86.]

[30] H. Chen, S. C. Wilks, D. D. Meyerhofer, J. D. Bonlie, C. Chen, S. Chen, C. Courtois, L. Elberson, G. Gregori, W. L. Kruer, O. Landoas, J. Mithen, J. F. Myatt, C. D. Murphy, P. M. Nilson, D. F. Price, M. B. Schneider, R. Shepherd, C. Stoeckl, M. Tabak, R. Tommasini, and P. Beiersdorfer, "Relativistic Quasimonoenergetic Positron Jets from Intense Laser-Solid Interactions," *Physical Review Letters*, vol. 105, 015003, 2010. https://doi.org/10.1103/PhysRevLett.105.015003 [Cited on pages 64, 87, and 88.]

[31] Y. Yan, Y. Wu, J. Chen, M. Yu, K. Dong, and Y. Gu, "Positron acceleration by sheath field in ultra-intense lasersolid interactions," *Plasma Physics and Controlled Fusion*, vol. 59, 045015, 2017. https://doi.org/10.1088/1361-6587/aa5f77 [Cited on page 88.]

[32] Y. V. Medvedev, "Evolution of a density disturbance in a collisionless plasma," *Plasma Physics and Controlled Fusion*, vol. 56, 025005, 2014. https://doi.org/10.1088/0741-3335/56/2/025005 [Cited on page 95.]

[33] F. Fiuza, A. Stockem, E. Boella, R. A. Fonseca, L. O. Silva, D. Haberberger, S. Tochitsky, W. B. Mori, and C. Joshi, "Ion acceleration from laser-driven electrostatic shocks," *Physics of Plasmas*, vol. 20, 056304, 2013. https://doi.org/10.1063/1.4801526 [Cited on pages 30, 95, 98, and 116.]

[34] A. P. L. Robinson, P. Gibbon, M. Zepf, S. Kar, R. G. Evans, and C. Bellei, "Relativistically correct hole-boring and ion acceleration by circularly polarized laser pulses," *Plasma Physics and Controlled Fusion*, vol. 51, 024004, 2009. https://doi.org/10.1088/0741-3335/51/2/024004 [Cited on pages 28 and 104.]

[35] L. Willingale, K. Krushelnick, A. G. R. Thomas, F. J. Dollar, A. Maksimchuk, C. Zulick, H. Chen, A. U. Hazi, G. J. Williams, P. Nilson, R. S. Craxton, T. Sangster, V. Glebov, C. Stoeckl, W. Nazarov, J. Cobble, and P. Norreys, "Relativistic laser interactions with near-critical density plasmas," in *APP Division of Plasma Physics Annual Meeting*, 2012. [Cited on page 167.]

[36] A. Gilmour, *Klystrons, Traveling Wave Tubes, Magnetrons, Crossed-Field Amplifiers and Gyrotrons*. Artech House, 2011. [Cited on page 178.]

[37] H. Bethe, "Zur Theorie des Durchgangs schneller Korpuskularstrahlen durch Materie," *Annalen der Physik*, vol. 397, 325, 1930. https://doi.org/10.1002/andp.19303970303 [Cited on page 1.]

[38] F. Bloch, "Zur Bremsung rasch bewegter Teilchen beim Durchgang durch Materie," *Annalen der Physik*, vol. 408, 285, 1933. https://doi.org/10.1002/andp.19334080303 [Cited on page 1.]

[39] M. Borghesi, A. Schiavi, D. H. Campbell, M. G. Haines, O. Willi, A. J. MacKinnon, L. A. Gizzi, M. Galimberti, R. J. Clarke, and H. Ruhl, "Proton imaging: a diagnostic for inertial confinement fusion/fast ignitor studies," *Plasma Physics and Controlled Fusion*, vol. 43, A267, 2001. https://doi.org/10.1088/0741-3335/43/12A/320 [Cited on page 2.]

[40] A. J. Mackinnon, P. K. Patel, R. P. Town, M. J. Edwards, T. Phillips, S. C. Lerner, D. W. Price, D. Hicks, M. H. Key, S. Hatchett, S. C. Wilks, M. Borghesi, L. Romagnani, S. Kar, T. Toncian, G. Pretzler,

O. Willi, M. Koenig, E. Martinolli, S. Lepape, A. Benuzzi-Mounaix, P. Audebert, J. C. Gauthier, J. King, R. Snavely, R. R. Freeman, and T. Boehlly, "Proton radiography as an electromagnetic field and density perturbation diagnostic," *Review of Scientific Instruments*, vol. 75, 3531, 2004. https://doi.org/10.1063/1.1788893 [Cited on page 2.]

[41] L. Romagnani, J. Fuchs, M. Borghesi, P. Antici, P. Audebert, F. Ceccherini, T. Cowan, T. Grismayer, S. Kar, A. MacChi, P. Mora, G. Pretzler, A. Schiavi, T. Toncian, and O. Willi, "Dynamics of electric fields driving the laser acceleration of multi-MeV protons," *Physical Review Letters*, vol. 95, 195001, 2005. https://doi.org/10.1103/PhysRevLett.95.195001 [Cited on pages 2 and 27.]

[42] N. L. Kugland, D. D. Ryutov, C. Plechaty, J. S. Ross, and H.-S. S. Park, "Relation between electric and magnetic field structures and their proton-beam images," *The Review of Scientific Instruments*, vol. 83, 101301, 2012. https://doi.org/10.1063/1.4750234 [Cited on page 2.]

[43] C. K. Li, F. H. Séguin, J. A. Frenje, J. R. Rygg, R. D. Petrasso, R. P. J. Town, P. A. Amendt, S. P. Hatchett, O. L. Landen, A. J. MacKinnon, P. K. Patel, V. A. Smalyuk, J. P. Knauer, T. C. Sangster, and C. Stoeckl, "Monoenergetic proton backlighter for measuring e and B fields and for radiographing implosions and high-energy density plasmas," *Review of Scientific Instruments*, vol. 77, 10E725, 2006. https://doi.org/10.1063/1.2228252 [Cited on page 3.]

[44] J. R. Rygg, A. B. Zylstra, F. H. Séguin, S. Lepape, B. Bachmann, R. S. Craxton, E. M. Garcia, Y. Z. Kong, S. F. Khan, B. J. Lahmann, P. W. Mckenty, R. D. Petrasso, H. G. Rinderknecht, D. B. Sayre, and H. W. Sio, "Note : A monoenergetic proton backlighter for the National Ignition Facility Note : A monoenergetic proton backlighter for the

National Ignition Facility," *Review of Scientific Instruments*, vol. 86, 116104, 2015. http://dx.doi.org/10.1063/1.4935581 [Not cited.]

[45] R. Clarke, S. Dorkings, D. Neely, and I. Musgrave, "The production of patient dose level 99m Tc medical radioisotope using laser-driven proton beams," in *SPIE Optics + Optoelectronics*, E. Esarey, C. B. Schroeder, W. P. Leemans, K. W. D. Ledingham, and D. A. Jaroszynski, Eds. International Society for Optics and Photonics, 2013, 87791C. https://doi.org/10.1117/12.2016971 [Cited on pages 3 and 4.]

[46] J. Tollefson, "Reactor shutdown threatens world's medical-isotope supply," *Nature*, 2016. https://doi.org/10.1038/nature.2016.20577 [Cited on page 3.]

[47] B. Neilly, S. Allen, J. Ballinger, J. Buscombe, R. Clarke, B. Ellis, G. Flux, L. Fraser, A. Hall, H. Owen, A. Paterson, A. Perkins, and A. Scarsbrook, "Future Supply of Medical Radioisotopes for the UK Report 2014," British Nuclear Medicine Society and Science & Technology Facilities Council, Tech. Rep. December, 2014. https://arxiv.org/pdf/1501.03071.pdf [Cited on page 3.]

[48] X. Fu, Q. Liu, P. Li, Z. Sui, T. Liu, and M. Gong, "High-efficiency 2 J, 20 Hz diode-pumped Nd:YAG active-mirror master oscillator power amplifier system," *Applied Physics Express*, vol. 8, 092702, 2015. https://doi.org/10.7567/APEX.8.092702 [Cited on page 4.]

[49] E. Sistrunk, T. Spinka, A. Bayramian, P. Armstrong, S. Baxamusa, S. Betts, R. Bopp, and S. Buck, "All Diode-Pumped , High-repetition-rate Advanced Petawatt Laser System ( HAPLS )," in *CLEO: Science and Innovations 2017*, 2017. https://doi.org/10.1364/CLEO{_}SI.2017.STh1L.2 [Cited on page 4.]

[50] H. Takahashi, S. I. Okihara, M. Fujimoto, S. Ohsuka, K. Matsukado, S. Okazaki, T. Ito, S. I. Aoshima, and Y. Tsuchiya, "Production of short-lived positron-emitting radioactive nuclei using a 2.4 TW, 50 fs tabletop laser," *Japanese Journal of Applied Physics, Part 2: Letters*, vol. 44, 425, 2005. https://doi.org/10.1143/JJAP.44.L425 [Cited on page 4.]

[51] K. Nemoto, A. Maksimchuk, S. Banerjee, K. Flippo, G. Mourou, D. Umstadter, and V. Y. Bychenkov, "Laser-triggered ion acceleration and table top isotope production," *Applied Physics Letters*, vol. 78, 595, 2001. https://doi.org/10.1063/1.1343845 [Cited on page 4.]

[52] B. Damato, A. Kacperek, M. Chopra, I. R. Campbell, and R. D. Errington, "Proton beam radiotherapy of choroidal melanoma: The Liverpool-Clatterbridge experience," *International Journal of Radiation Oncology Biology Physics*, vol. 62, 1405, 2005. https://doi.org/10.1016/j.ijrobp.2005.01.016 [Cited on page 4.]

[53] R. Miralbell, A. Lomax, and M. Russo, "Potential role of proton therapy in the treatment of pediatric medulloblastoma/primitive neuro-ectodermal tumors: Spinal theca irradiation," *International Journal of Radiation Oncology*Biology*Physics*, vol. 38, 805, 1997. https://doi.org/10.1016/S0360-3016(97)00005-9 [Cited on page 4.]

[54] D. Brooks, "Is proton beam therapy for prostate cancer worth the cost?" http://blogs.cancer.org/expertvoices/2013/02/20/is-proton-beam-therapy-for-prostate-cancer-worth-the-cost/ [Not cited.]

[55] U. Linz and J. Alonso, "What will it take for laser driven proton accelerators to be applied to tumor therapy?" *Physical Review Special Topics - Accelerators and Beams*, vol. 10, 094801,

2007. https://doi.org/10.1103/PhysRevSTAB.10.094801 [Cited on pages 4 and 5.]

[56] M. Gauthier, J. B. Kim, C. B. Curry, B. Aurand, E. J. Gamboa, S. Göde, C. Goyon, A. Hazi, S. Kerr, A. Pak, A. Propp, B. Ramakrishna, J. Ruby, O. Willi, G. J. Williams, C. Rödel, and S. H. Glenzer, "High-intensity laser-accelerated ion beam produced from cryogenic micro-jet target," *Review of Scientific Instruments*, vol. 87, 11D827, 2016. https://doi.org/10.1063/1.4961270 [Cited on page 187.]

[57] P. L. Poole, C. D. Andereck, D. W. Schumacher, R. L. Daskalova, S. Feister, K. M. George, C. Willis, K. U. Akli, and E. a. Chowdhury, "Liquid crystal films as on-demand, variable thickness (50-5000 nm) targets for intense lasers," *Physics of Plasmas*, vol. 21, 063109, 2014. http://scitation.aip.org.proxy.lib.umich.edu/content/aip/journal/pop/21/6/10.1063/1.4885100 [Not cited.]

[58] R. E. Kidder, "Energy gain of laser-compressed pellets-a simple model calculations," *Nuclear Fusion*, vol. 16, 405, 1976. https://doi.org/10.1088/0029-5515/16/3/003 [Cited on page 6.]

[59] J. Meyer-ter Vehn, "On energy gain of fusion targets: The model of kidder and bodner improved," *Nuclear Fusion*, vol. 22, 561, 1982. https://doi.org/10.1088/0029-5515/22/4/010 [Cited on page 6.]

[60] S. Atzeni, A. Schiavi, and J. R. Davies, "Stopping and scattering of relativistic electron beams in dense plasmas and requirements for fast ignition," *Plasma Physics and Controlled Fusion*, vol. 51, 015016, 2009. https://doi.org/10.1088/0741-3335/51/1/015016 [Not cited.]

[61] M. Tabak, J. Hammer, M. E. Glinsky, W. L. Kruer, S. C. Wilks, J. Woodworth, E. M. Campbell, M. D. Perry, and R. J. Mason, "Ignition and high gain with ultrapowerful lasers," *Physics of Plasmas*,

vol. 1, 1626, 1994. https://doi.org/10.1063/1.870664 [Cited on pages 6 and 7.]

[62] J. Meyer-ter Vehn, "Fast ignition of ICF targets: an overview," *Plasma Physics and Controlled Fusion*, vol. 43, A113, 2001. https://doi.org/10.1088/0741-3335/43/12A/308 [Cited on page 7.]

[63] S. Atzeni, "Inertial fusion fast ignitor: Igniting pulse parameter window vs the penetration depth of the heating particles and the density of the precompressed fuel," *Physics of Plasmas*, vol. 6, 3316, 1999. https://doi.org/10.1063/1.873571 [Cited on pages 7 and 8.]

[64] T. Bartal, M. E. Foord, C. Bellei, M. H. Key, K. A. Flippo, S. A. Gaillard, D. T. Offermann, P. K. Patel, L. C. Jarrott, D. P. Higginson, M. Roth, A. Otten, D. Kraus, R. B. Stephens, H. S. McLean, E. M. Giraldez, M. S. Wei, D. C. Gautier, and F. N. Beg, "Focusing of short-pulse high-intensity laser-accelerated proton beams," *Nature Physics*, vol. 8, 139, 2011. https://doi.org/10.1038/nphys2153 [Cited on pages 8 and 69.]

[65] J. C. Fernández, B. J. Albright, F. N. Beg, M. E. Foord, B. M. Hegelich, J. J. Honrubia, M. Roth, R. B. Stephens, and L. Yin, "Fast ignition with laser-driven proton and ion beams," *Nuclear Fusion*, vol. 54, 54006, 2014. https://doi.org/10.1088/0029-5515/54/5/054006 [Cited on page 8.]

[66] B. A. Remington, "Modeling Astrophysical Phenomena in the Laboratory with Intense Lasers," *Science*, vol. 284, 1488, 1999. https://doi.org/10.1126/science.284.5419.1488 [Cited on pages 9 and 10.]

[67] C. M. Huntington, F. Fiuza, J. S. Ross, A. B. Zylstra, R. P. Drake, D. H. Froula, G. Gregori, N. L. Kugland, C. C. Kuranz, M. C. Levy, C. K. Li, J. Meinecke, T. Morita, R. Petrasso, C. Plechaty, B. A.

Remington, D. D. Ryutov, Y. Sakawa, A. Spitkovsky, H. Takabe, and H.-S. Park, "Observation of magnetic field generation via the Weibel instability in interpenetrating plasma flows," *Nature Physics*, vol. 11, 173, 2015. https://doi.org/10.1038/nphys3178 [Cited on page 9.]

[68] B. A. Remington, R. P. Drake, and D. D. Ryutov, "Experimental astrophysics with high power lasers and Z pinches," *Reviews of Modern Physics*, vol. 78, 755, 2006. https://doi.org/10.1103/RevModPhys.78.755 [Cited on page 9.]

[69] E. Waxman, "Gamma-rayburst afterglow: supporting the cosmological fireball model, constraining parameters, and making predictions," *The Astrophysical Journal Letters*, vol. 485, 1997. https://doi.org/10.1086/310809 [Cited on page 10.]

[70] K.-I. Nishikawa, J. Niemiec, P. E. Hardee, M. Medvedev, H. Sol, Y. Mizuno, B. Zhang, M. Pohl, M. Oka, and D. H. Hartmann, "Weibel Instability and Associated Strong Fields in a Fully Three-Dimensional Simulation of a Relativistic Shock," *The Astrophysical Journal*, vol. 698, L10, 2009. https://doi.org/10.1088/0004-637X/698/1/L10 [Cited on page 10.]

[71] H. Chen, S. A. Wilks, J. D. Bonlie, E. P. Liang, J. Myatt, D. F. Price, D. D. Meyerhofer, and P. Beiersdorfer, "Relativistic Positron Creation Using Ultraintense Short Pulse Lasers," *Physical Review Letters*, vol. 102, 105001, 2009. https://doi.org/10.1103/PhysRevLett.102.105001 [Cited on pages 10 and 63.]

[72] H. Chen, F. Fiuza, A. Link, A. Hazi, M. Hill, D. Hoarty, S. James, S. Kerr, D. D. Meyerhofer, J. Myatt, J. Park, Y. Sentoku, and G. J. Williams, "Scaling the Yield of Laser-Driven Electron-Positron Jets to Laboratory Astrophysical Applications," *Physical Review Letters*, vol.

114, 215001, 2015. https://doi.org/10.1103/PhysRevLett.114.215001 [Cited on pages 10, 66, 71, 80, 84, 89, and 187.]

[73] E. Liang, T. Clarke, A. Henderson, W. Fu, W. Lo, D. Taylor, P. Chaguine, S. Zhou, Y. Hua, X. Cen, X. Wang, J. Kao, H. Hasson, G. Dyer, K. Serratto, N. Riley, M. Donovan, and T. Ditmire, "High e+/e Ratio Dense Pair Creation with 1021W.cm-2 Laser Irradiating Solid Targets," *Scientific Reports*, vol. 5, 13968, 2015. https://doi.org/10.1038/srep13968 [Cited on pages 10 and 89.]

[74] J. K. Crane, G. Tietbohl, P. Arnold, E. S. Bliss, C. Boley, G. Britten, G. Brunton, W. Clark, J. W. Dawson, S. Fochs, R. Hackel, C. Haefner, J. Halpin, J. Heebner, M. Henesian, M. Hermann, J. Hernandez, V. Kanz, B. McHale, J. B. McLeod, H. Nguyen, H. Phan, M. Rushford, B. Shaw, M. Shverdin, R. Sigurdsson, R. Speck, C. Stolz, D. Trummer, J. Wolfe, J. N. Wong, G. C. Siders, and C. P. J. Barty, "Progress on converting a NIF quad to eight, petawatt beams for advanced radiography," *Journal of Physics: Conference Series*, vol. 244, 032003, 2010. https://doi.org/10.1088/1742-6596/244/3/032003 [Cited on page 10.]

[75] H. Shiraga, S. Fujioka, M. Nakai, T. Watari, H. Nakamura, Y. Arikawa, H. Hosoda, T. Nagai, M. Koga, H. Kikuchi, Y. Ishii, T. Sogo, K. Shigemori, H. Nishimura, Z. Zhang, M. Tanabe, S. Ohira, Y. Fujii, T. Namimoto, Y. Sakawa, O. Maegawa, T. Ozaki, K. Tanaka, H. Habara, T. Iwawaki, K. Shimada, H. Nagatomo, T. Johzaki, A. Sunahara, M. Murakami, H. Sakagami, T. Taguchi, T. Norimatsu, H. Homma, Y. Fujimoto, A. Iwamoto, N. Miyanaga, J. Kawanaka, T. Jitsuno, Y. Nakata, K. Tsubakimoto, N. Morio, T. Kawasaki, K. Sawai, K. Tsuji, H. Murakami, T. Kanabe, K. Kondo, N. Sarukura, T. Shimizu, K. Mima, and H. Azechi, "Fast ignition integrated experiments with Gekko

and LFEX lasers," *Plasma Physics and Controlled Fusion*, vol. 53, 124029, 2011. https://doi.org/10.1088/0741-3335/53/12/124029 [Cited on page 10.]

[76] R. Wilson, M. King, R. J. Gray, D. C. Carroll, R. J. Dance, C. Armstrong, S. J. Hawkes, R. J. Clarke, D. Neely, P. Mckenna, R. Wilson, M. King, R. J. Gray, D. C. Carroll, R. J. Dance, and C. Armstrong, "Ellipsoidal plasma mirror focusing of high power laser pulses to ultra-high intensities Ellipsoidal plasma mirror focusing of high power laser pulses to ultra-high intensities," *Physics of Plasmas*, vol. 23, 033106, 2016. http://dx.doi.org/10.1063/1.4943200 [Cited on page 10.]

[77] M. N. Saha, "LIII. Ionization in the solar chromosphere," *Philosophical Magazine Series 6*, vol. 40, 472, 1920. https://doi.org/10.1080/14786441008636148 [Not cited.]

[78] P. Gibbon and E. Förster, "Short-pulse laser plasma interactions," *Plasma Physics and Controlled Fusion*, vol. 38, 769, 1996. https://doi.org/10.1088/0741-3335/38/6/001 [Not cited.]

[79] S. Le Pape, Y. Y. Tsui, A. Macphee, D. Hey, P. Patel, A. Mackinnon, M. Key, M. Wei, T. Ma, F. N. Beg, R. Stephens, K. Akli, T. Link, L. Van-Woerkom, and R. R. Freeman, "Characterization of the preformed plasma for high-intensity laser-plasma interaction." *Optics Letters*, vol. 34, 2997, 2009. https://doi.org/10.1364/OL.34.002997 [Cited on pages 13 and 35.]

[80] P. Sprangle, C. M. Tang, and E. Esarey, "Relativistic self-focusing of short-pulse radiation beams in plasmas," *IEEE Transactions on Plasma Science*, vol. 15, 145, 1987. https://doi.org/10.1109/TPS.1987.4316677 [Cited on page 14.]

[81] L. Schlessinger and J. Wright, "Inverse-bremsstrahlung absorption rate in an intense laser field," *Physical Review A*, vol. 20, 1934, 1979. https://doi.org/10.1103/PhysRevA.20.1934 [Cited on page 15.]

[82] S. C. Wilks and W. L. Kruer, "Absorption of ultrashort, ultra-intense laser light by solids and overdense plasmas," *IEEE Journal of Quantum Electronics*, vol. 33, 1954, 1997. https://doi.org/10.1109/3.641310 [Cited on page 15.]

[83] J. P. Freidberg, R. W. Mitchell, R. L. Morse, and L. I. Rudsinski, "Resonant absorption of laser light by plasma targets," *Physical Review Letters*, vol. 28, 795, 1972. https://doi.org/10.1103/PhysRevLett.28.795 [Cited on page 15.]

[84] N. G. Denisov, "On a Singularity of the Field of an Electromagnetic Wove," *Soviet Physics JETP*, vol. 4, 544, 1957. www.jetp.ac.ru/cgi-bin/dn/e{_}004{_}04{_}0544.pdf [Cited on page 15.]

[85] F. Brunel, "Not-So-Resonant, Resonant Absorption," vol. 59, 52, 1987. https://doi.org/10.1103/PhysRevLett.59.52 [Cited on page 16.]

[86] P. Gibbon, *Short Pulse Laser Interactions with Matter: An Introduction*. Imperial College Press, 2005. [Cited on page 17.]

[87] W. L. Kruer and K. Estabrook, "JxB heating by very intense laser light," *Physics of Fluids*, vol. 28, 430, 1985. https://doi.org/10.1063/1.865171 [Cited on page 17.]

[88] B. Bezzerides, S. Gitomer, and D. Forslund, "Randomness, Maxwellian Distributions, and Resonance Absorption," *Physical Review Letters*, vol. 44, 651, 1980. https://doi.org/10.1103/PhysRevLett.44.651 [Cited on page 18.]

[89] S. C. Wilks, W. L. Kruer, M. Tabak, and A. B. Langdon, "Absorption of ultra-intense laser pulses," *Physical Review Letters*, vol. 69, 1383, 1992. https://doi.org/10.1103/PhysRevLett.69.1383 [Cited on pages 18, 28, and 66.]

[90] E. Clark, K. Krushelnick, and J. Davies, "Measurements of energetic proton transport through magnetized plasma from intense laser interactions with solids," *Physical Review Letters*, vol. 96, 249201, 2000. https://doi.org/10.1103/PhysRevLett.84.670 [Cited on page 18.]

[91] R. A. Snavely, M. H. Key, S. P. Hatchett, T. E. Cowan, M. Roth, T. W. Phillips, M. a. Stoyer, E. A. Henry, T. C. Sangster, M. S. Singh, S. C. Wilks, A. J. MacKinnon, A. Offenberger, D. M. Pennington, K. Yasuike, a. B. Langdon, B. F. Lasinski, J. Johnson, M. D. Perry, and E. M. Campbell, "Intense high-energy proton beams from Petawatt-laser irradiation of solids." *Physical review letters*, vol. 85, 2945, 2000. https://doi.org/10.1103/PhysRevLett.85.2945 [Cited on page 18.]

[92] S. P. Hatchett, C. G. Brown, T. E. Cowan, E. A. Henry, J. S. Johnson, M. H. Key, J. A. Koch, a. B. Langdon, B. F. Lasinski, R. W. Lee, A. J. Mackinnon, D. M. Pennington, M. D. Perry, T. W. Phillips, M. Roth, T. C. Sangster, M. S. Singh, R. a. Snavely, M. a. Stoyer, S. C. Wilks, and K. Yasuike, "Electron, photon, and ion beams from the relativistic interaction of Petawatt laser pulses with solid targets," *Physics of Plasmas*, vol. 7, 2076, 2000. http://link.aip.org/link/PHPAEN/v7/i5/p2076/s1{&}Agg=doi [Cited on page 18.]

[93] S. C. Wilks, A. B. Langdon, T. E. Cowan, M. Roth, M. Singh, S. Hatchett, M. H. Key, D. Pennington, A. MacKinnon, and R. A. Snavely, "Energetic proton generation in ultra-intense lasersolid

interactions," *Physics of Plasmas*, vol. 8, 542, 2001. https://doi.org/10.1063/1.1333697 [Cited on pages 19, 20, and 22.]

[94] D. T. Offermann, K. A. Flippo, S. A. Gaillard, D. C. Gautier, S. Letzring, J. C. Cobble, G. Wurden, R. P. Johnson, T. Shimada, D. S. Montgomery, R. P. Gonzales, T. Hurry, F. Archuleta, M. J. Schmitt, S.-M. Reid, T. Bartal, M. S. Wei, D. P. Higginson, F. N. Beg, M. Geissel, and M. Schollmeier, "Carbon ion beam focusing using laser irradiated, heated diamond hemispherical shells," *Journal of Physics: Conference Series*, vol. 244, 022053, 2010. https://doi.org/10.1088/1742-6596/244/2/022053 [Cited on page 20.]

[95] P. Mora, "Thin-foil expansion into a vacuum," *Physical Review E*, vol. 72, 056401, 2005. https://doi.org/10.1103/PhysRevE.72.056401 [Cited on pages 21 and 23.]

[96] J. Fuchs, P. Antici, E. D'Humières, E. Lefebvre, M. Borghesi, E. Brambrink, C. A. Cecchetti, M. Kaluza, V. Malka, M. Manclossi, S. Meyroneinc, P. Mora, J. Schreiber, T. Toncian, H. Pépin, and P. Audebert, "Laser-driven proton scaling laws and new paths towards energy increase," *Nature Physics*, vol. 2, 48, 2006. https://doi.org/10.1038/nphys199 [Cited on page 175.]

[97] L. Robson, P. T. Simpson, R. J. Clarke, K. W. D. Ledingham, F. Lindau, O. Lundh, T. McCanny, P. Mora, D. Neely, C.-G. Wahlström, M. Zepf, and P. McKenna, "Scaling of proton acceleration driven by petawatt-laserplasma interactions," *Nature Physics*, vol. 3, 58, 2006. https://doi.org/10.1038/nphys476 [Cited on pages 23 and 27.]

[98] C. Perego, A. Zani, D. Batani, and M. Passoni, "Extensive comparison among Target Normal Sheath Acceleration theoretical models," *Nuclear Instruments and Methods in Physics Research, Section A: Accelerators,*

*Spectrometers, Detectors and Associated Equipment*, vol. 653, 89, 2011. https://doi.org/10.1016/j.nima.2011.01.100 [Cited on pages 23 and 24.]

[99] S. Buffechoux, J. Psikal, M. Nakatsutsumi, L. Romagnani, A. Andreev, K. Zeil, M. Amin, P. Antici, T. Burris-Mog, A. Compant-La-Fontaine, E. D'Humières, S. Fourmaux, S. A. Gaillard, F. Gobet, F. Hannachi, S. Kraft, A. Mancić, C. Plaisir, G. Sarri, M. Tarisien, T. Toncian, U. Schramm, M. Tampo, P. Audebert, O. Willi, T. E. Cowan, H. Pépin, V. Tikhonchuk, M. Borghesi, and J. Fuchs, "Hot electrons transverse refluxing in ultraintense laser-solid interactions," *Physical Review Letters*, vol. 105, 015005, 2010. https://doi.org/10.1103/PhysRevLett.105.015005 [Cited on page 26.]

[100] C. M. Brenner, P. McKenna, and D. Neely, "Modelling the effect of laser focal spot size on sheath- accelerated protons in intense laserfoil interactions," *Plasma Physics and Controlled Fusion*, vol. 56, 084003, 2014. https://doi.org/10.1088/0741-3335/56/8/084003 [Not cited.]

[101] A. Yogo, K. Mima, N. Iwata, S. Tosaki, A. Morace, Y. Arikawa, S. Fujioka, T. Johzaki, Y. Sentoku, H. Nishimura, A. Sagisaka, K. Matsuo, N. Kamitsukasa, S. Kojima, H. Nagatomo, M. Nakai, H. Shiraga, M. Murakami, S. Tokita, J. Kawanaka, N. Miyanaga, K. Yamanoi, T. Norimatsu, H. Sakagami, S. V. Bulanov, K. Kondo, and H. Azechi, "Boosting laser-ion acceleration with multi-picosecond pulses," *Scientific Reports*, vol. 7, 42451, 2017. https://doi.org/10.1038/srep42451 [Cited on pages 23 and 71.]

[102] M. Passoni and M. Lontano, "Theory of light-ion acceleration driven by a strong charge separation," *Physical Review Letters*, vol. 101, 115001, 2008. https://doi.org/10.1103/PhysRevLett.101.115001 [Cited on page 24.]

[103] M. Passoni, L. Bertagna, and A. Zani, "Target normal sheath acceleration: theory, comparison with experiments and future perspectives," *New Journal of Physics*, vol. 12, 045012, 2010. https://doi.org/10.1088/1367-2630/12/4/045012 [Cited on page 24.]

[104] J. Schreiber, F. Bell, F. Grüner, U. Schramm, M. Geissler, M. Schnürer, S. Ter-Avetisyan, B. M. Hegelich, J. Cobble, E. Brambrink, J. Fuchs, P. Audebert, and D. Habs, "Analytical Model for Ion Acceleration by High-Intensity Laser Pulses," *Physical Review Letters*, vol. 97, 045005, 2006. https://doi.org/10.1103/PhysRevLett.97.045005 [Cited on page 24.]

[105] K. Zeil, S. D. Kraft, S. Bock, M. Bussmann, T. E. Cowan, T. Kluge, J. Metzkes, T. Richter, R. Sauerbrey, and U. Schramm, "The scaling of proton energies in ultrashort pulse laser plasma acceleration," *New Journal of Physics*, vol. 12, 045015, 2010. https://doi.org/10.1088/1367-2630/12/4/045015 [Cited on page 24.]

[106] P. McKenna, D. C. Carroll, O. Lundh, F. Nrünberg, K. Markey, S. Bandyopadhyay, D. Batani, R. G. Evans, R. Jafer, S. Kar, D. Neely, D. Pepler, M. N. Quinn, R. Redaelli, M. Roth, C. G. Wahlström, X. H. Yuan, and M. Zepf, "Effects of front surface plasma expansion on proton acceleration in ultraintense laser irradiation of foil targets," *Laser and Particle Beams*, vol. 26, 591, 2008. https://doi.org/10.1017/S0263034608000657 [Cited on page 25.]

[107] A. J. Mackinnon, M. Borghesi, S. Hatchett, M. H. Key, P. K. Patel, H. Campbell, A. Schiavi, R. Snavely, S. C. Wilks, and O. Willi, "Effect of Plasma Scale Length on Multi-MeV Proton Production by Intense Laser Pulses," *Physical Review Letters*, vol. 86, 1769, 2001. https://doi.org/10.1103/PhysRevLett.86.1769 [Cited on page 25.]

[108] D. Batani, R. Jafer, M. Veltcheva, R. Dezulian, O. Lundh, F. Lindau, A. Persson, K. Osvay, C.-G. Wahlström, D. C. Carroll, P. McKenna, A. Flacco, and V. Malka, "Effects of laser prepulses on laser-induced proton generation," *New Journal of Physics*, vol. 12, 045018, 2010. https://doi.org/10.1088/1367-2630/12/4/045018 [Cited on page 25.]

[109] M. Schollmeier, A. B. Sefkow, M. Geissel, A. V. Arefiev, K. A. Flippo, S. A. Gaillard, R. P. Johnson, M. W. Kimmel, D. T. Offermann, P. K. Rambo, J. Schwarz, and T. Shimada, "Laser-to-hot-electron conversion limitations in relativistic laser matter interactions due to multi-picosecond dynamics," *Physics of Plasmas*, vol. 22, 043116, 2015. https://doi.org/10.1063/1.4918332 [Cited on pages 25, 49, and 50.]

[110] C. P. Ridgers, M. Sherlock, R. G. Evans, A. P. L. Robinson, and R. J. Kingham, "Superluminal sheath-field expansion and fast-electron-beam divergence measurements in laser-solid interactions," *Physical Review E - Statistical, Nonlinear, and Soft Matter Physics*, vol. 83, 036404, 2011. https://doi.org/10.1103/PhysRevE.83.036404 [Cited on pages 26 and 79.]

[111] P. McKenna, D. C. Carroll, R. J. Clarke, R. G. Evans, K. W. D. Ledingham, F. Lindau, O. Lundh, T. McCanny, D. Neely, A. P. L. Robinson, L. Robson, P. T. Simpson, C. G. Wahlström, and M. Zepf, "Lateral electron transport in high-intensity laser-irradiated foils diagnosed by ion emission," *Physical Review Letters*, vol. 98, 145001, 2007. https://doi.org/10.1103/PhysRevLett.98.145001 [Cited on page 26.]

[112] M. Kaluza, J. Schreiber, M. I. Santala, G. D. Tsakiris, K. Eidmann, J. Meyer-Ter-Vehn, and K. J. Witte, "Influence of the laser prepulse on proton acceleration in thin-foil experiments," *Physical Review Letters*, vol. 93, 045003, 2004. https://doi.org/10.1103/PhysRevLett.93.045003 [Cited on page 26.]

[113] D. Neely, P. Foster, A. Robinson, F. Lindau, O. Lundh, A. Persson, C. G. Wahlström, and P. McKenna, "Enhanced proton beams from ultrathin targets driven by high contrast laser pulses," *Applied Physics Letters*, vol. 89, 021502, 2006. https://doi.org/10.1063/1.2220011 [Cited on page 26.]

[114] P. Neumayer, B. Aurand, M. Basko, B. Ecker, P. Gibbon, D. C. Hochhaus, A. Karmakar, E. Kazakov, T. Kühl, C. Labaune, O. Rosmej, A. Tauschwitz, B. Zielbauer, and D. Zimmer, "The role of hot electron refluxing in laser-generated K-alpha sources," *Physics of Plasmas*, vol. 17, 103103, 2010. https://doi.org/10.1063/1.3486520 [Cited on page 26.]

[115] P. M. Nilson, J. R. Davies, W. Theobald, P. A. Jaanimagi, C. Mileham, R. K. Jungquist, C. Stoeckl, I. A. Begishev, A. A. Solodov, J. F. Myatt, J. D. Zuegel, T. C. Sangster, R. Betti, and D. D. Meyerhofer, "Time-Resolved Measurements of Hot-Electron Equilibration Dynamics in High-Intensity Laser Interactions with Thin-Foil Solid Targets," *Physical Review Letters*, vol. 108, 085002, 2012. https://doi.org/10.1103/PhysRevLett.108.085002 [Cited on page 26.]

[116] J. Psikal, V. T. Tikhonchuk, J. Limpouch, and O. Klimo, "Lateral hot electron transport and ion acceleration in femtosecond laser pulse interaction with thin foils," *Physics of Plasmas*, vol. 17, 013102, 2010. https://doi.org/10.1063/1.3276524 [Cited on page 27.]

[117] P. Antici, J. Fuchs, M. Borghesi, L. Gremillet, T. Grismayer, Y. Sentoku, E. D'Humières, C. A. Cecchetti, A. Mančić, A. C. Pipahl, T. Toncian, O. Willi, P. Mora, and P. Audebert, "Hot and Cold Electron Dynamics Following High-Intensity Laser Matter Interaction," *Physical Review Letters*, vol. 101, 105004, 2008. https://doi.org/10.1103/PhysRevLett.101.105004 [Cited on page 27.]

[118] M. Coury, D. C. Carroll, A. P. L. Robinson, X. H. Yuan, C. M. Brenner, M. Burza, R. J. Gray, M. N. Quinn, K. L. Lancaster, Y. T. Li, X. X. Lin, O. Tresca, C.-G. Wahlström, D. Neely, and P. McKenna, "Influence of laser irradiated spot size on energetic electron injection and proton acceleration in foil targets," *Applied Physics Letters*, vol. 100, 074105, 2012. https://doi.org/10.1063/1.3685615 [Cited on page 27.]

[119] A. P. L. Robinson, D. Neely, P. McKenna, and R. G. Evans, "Spectral control in proton acceleration with multiple laser pulses," *Plasma Physics and Controlled Fusion*, vol. 49, 373, 2007. https://doi.org/10.1088/0741-3335/49/4/002 [Cited on page 27.]

[120] K. Markey, P. McKenna, C. M. Brenner, D. C. Carroll, M. M. Günther, K. Harres, S. Kar, K. Lancaster, F. Nürnberg, M. N. Quinn, a. P. L. Robinson, M. Roth, M. Zepf, and D. Neely, "Spectral Enhancement in the Double Pulse Regime of Laser Proton Acceleration," *Physical Review Letters*, vol. 105, 195008, 2010. https://doi.org/10.1103/PhysRevLett.105.195008 [Cited on page 27.]

[121] C. M. Brenner, A. P. L. Robinson, K. Markey, R. H. H. Scott, R. J. Gray, M. Rosinski, O. Deppert, J. Badziak, D. Batani, J. R. Davies, S. M. Hassan, K. L. Lancaster, K. Li, I. O. Musgrave, P. A. Norreys, J. Pasley, M. Roth, H.-P. Schlenvoigt, C. Spindloe, M. Tatarakis, T. Winstone, J. Wolowski, D. Wyatt, P. McKenna, and D. Neely, "High energy conversion efficiency in laser-proton acceleration by controlling laser-energy deposition onto thin foil targets," *Applied Physics Letters*, vol. 104, 081123, 2014. https://doi.org/10.1063/1.4865812 [Cited on pages 27 and 116.]

[122] L. Volpe, J.-L. Feugeas, P. Nicolaï, J. J. Santos, M. Touati, J. Breil, D. Batani, and V. Tikhonchuk, "Controlling the fast electron divergence in a solid target with multiple laser pulses," *Physical Review E*,

vol. 90, 1–8, 2014. https://doi.org/10.1103/PhysRevE.90.063108 [Cited on page 27.]

[123] A. Macchi, F. Cattani, T. Liseykina, and F. Cornolti, "Laser Acceleration of Ion Bunches at the Front Surface of Overdense Plasmas," *Physical Review Letters*, vol. 94, 165003, 2005. https://doi.org/10.1103/PhysRevLett.94.165003 [Cited on page 28.]

[124] A. Macchi, M. Borghesi, and M. Passoni, "Ion acceleration by superintense laser-plasma interaction," *Reviews of Modern Physics*, vol. 85, 751, 2013. https://doi.org/10.1103/RevModPhys.85.751 [Cited on page 28.]

[125] T. Esirkepov, M. Borghesi, S. V. Bulanov, G. Mourou, and T. Tajima, "Highly Efficient Relativistic-Ion Generation in the Laser-Piston Regime," *Physical Review Letters*, vol. 92, 175003, 2004. https://doi.org/10.1103/PhysRevLett.92.175003 [Cited on page 29.]

[126] A. Macchi, S. Veghini, and F. Pegoraro, "Light Sail Acceleration Reexamined," *Physical Review Letters*, vol. 103, 085003, 2009. https://doi.org/10.1103/PhysRevLett.103.085003 [Cited on page 29.]

[127] T. V. Liseykina, M. Borghesi, A. Macchi, and S. Tuveri, "Radiation pressure acceleration by ultraintense laser pulses," *Plasma Physics and Controlled Fusion*, vol. 50, 124033, 2008. https://doi.org/10.1088/0741-3335/50/12/124033 [Cited on page 29.]

[128] A. P. L. Robinson, M. Zepf, S. Kar, R. G. Evans, and C. Bellei, "Radiation pressure acceleration of thin foils with circularly polarized laser pulses," *New Journal of Physics*, vol. 10, 013021, 2008. https://doi.org/10.1088/1367-2630/10/1/013021 [Cited on page 29.]

[129] C. A. J. Palmer, N. P. Dover, I. Pogorelsky, M. Babzien, G. I. Dudnikova, M. Ispiriyan, M. N. Polyanskiy, J. Schreiber, P. Shkolnikov,

V. Yakimenko, and Z. Najmudin, "Monoenergetic Proton Beams Accelerated by a Radiation Pressure Driven Shock," *Physical Review Letters*, vol. 106, 014801, 2011. https://doi.org/10.1103/PhysRevLett.106.014801 [Cited on page 29.]

[130] L. Yin, B. J. Albright, B. M. Hegelich, K. J. Bowers, K. A. Flippo, T. J. T. Kwan, and J. C. Fernandez, "Monoenergetic and GeV ion acceleration from the laser breakout afterburner using ultrathin targets," *Physics of Plasmas*, vol. 14, 056706, 2007. https://doi.org/10.1063/1.2436857 [Cited on page 29.]

[131] D. Jung, L. Yin, D. C. Gautier, H.-C. Wu, S. Letzring, B. Dromey, R. Shah, S. Palaniyappan, T. Shimada, R. P. Johnson, J. Schreiber, D. Habs, J. C. Fernández, B. M. Hegelich, and B. J. Albright, "Laser-driven 1 GeV carbon ions from preheated diamond targets in the break-out afterburner regime," *Physics of Plasmas*, vol. 20, 083103, 2013. https://doi.org/10.1063/1.4817287 [Cited on pages 29 and 89.]

[132] X. Q. Yan, T. Tajima, M. Hegelich, L. Yin, and D. Habs, "Theory of laser ion acceleration from a foil target of nanometer thickness," *Applied Physics B*, vol. 98, 711, 2009. https://doi.org/10.1007/s00340-009-3707-5 [Cited on page 29.]

[133] D. Haberberger, S. Tochitsky, F. Fiuza, C. Gong, R. A. Fonseca, L. O. Silva, W. B. Mori, and C. Joshi, "Collisionless shocks in laser-produced plasma generate monoenergetic high-energy proton beams," *Nature Physics*, vol. 8, 95, 2012. http://dx.doi.org/10.1038/nphys2130 [Cited on pages 30 and 91.]

[134] D. Strickland and G. Mourou, "Compression of amplified chirped optical pulses," *Optics Communications*, vol. 55, 447, 1985. https://doi.org/10.1016/0030-4018(85)90151-8 [Cited on page 31.]

[135] A. Dubietis, G. Jonušauskas, and A. Piskarskas, "Powerful femtosecond pulse generation by chirped and stretched pulse parametric amplification in BBO crystal," *Optics Communications*, vol. 88, 437, 1992. https://doi.org/10.1016/0030-4018(92)90070-8 [Cited on page 32.]

[136] I. N. Ross, J. L. Collier, P. Matousek, C. N. Danson, D. Neely, R. M. Allott, D. A. Pepler, C. Hernandez-Gomez, and K. Osvay, "Generation of terawatt pulses by use of optical parametric chirped pulse amplification," *Applied Optics*, vol. 39, 2422, 2000. https://doi.org/10.1364/AO.39.002422 [Cited on page 32.]

[137] R. W. Boyd, *Nonlinear Optics*, 3rd ed. Academic Press, 2008. [Cited on pages 32 and 33.]

[138] B. C. Stuart, J. D. Bonlie, J. A. Britten, J. A. Caird, R. Cross, C. A. Ebbers, M. J. Eckart, A. C. Erlandson, W. A. Molander, A. Ng, P. K. Patel, and D. F. Price, "The Titan Laser at LLNL - Technical Digest (CD)," in *Conference on Lasers and Electro-Optics/Quantum Electronics and Laser Science Conference and Photonic Applications Systems Technologies*. Long Beach, California: Optical Society of America, 2006, JTuG3. https://www.osapublishing.org/abstract.cfm?uri=QELS-2006-JTuG3 [Cited on page 33.]

[139] Y. Kato, K. Mima, N. Miyanaga, S. Arinaga, Y. Kitagawa, M. Nakatsuka, and C. Yamanaka, "Random phasing of high-power lasers for uniform target acceleration and plasma-instability suppression," *Physical Review Letters*, vol. 53, 1057, 1984. https://doi.org/10.1103/PhysRevLett.53.1057 [Cited on page 35.]

[140] C. Dorrer, A. Consentino, D. Irwin, J. Qiao, and J. D. Zuegel, "OPCPA front end and contrast optimization for the OMEGA

EP kilojoule, picosecond laser," *Journal of Optics*, vol. 17, 2015. https://doi.org/10.1088/2040-8978/17/9/094007 [Cited on page 36.]

[141] G. Doumy, F. Quéré, O. Gobert, M. Perdrix, P. Martin, P. Audebert, J. C. Gauthier, J. P. Geindre, and T. Wittmann, "Complete characterization of a plasma mirror for the production of high-contrast ultraintense laser pulses," *Physical Review E - Statistical, Nonlinear, and Soft Matter Physics*, vol. 69, 026402, 2004. https://doi.org/10.1103/PhysRevE.69.026402 [Cited on pages 37 and 99.]

[142] Y. Amemiya and J. Miyahara, "Imaging plate illuminates many fields." *Nature*, vol. 336, 89, 1988. https://doi.org/10.1038/336089a0 [Cited on page 39.]

[143] A. L. Meadowcroft, C. D. Bentley, and E. N. Stott, "Evaluation of the sensitivity and fading characteristics of an image plate system for x-ray diagnostics." *The Review of Scientific Instruments*, vol. 79, 113102, 2008. https://doi.org/10.1063/1.3013123 [Cited on page 40.]

[144] H. Chen, N. L. Back, T. Bartal, F. N. Beg, D. C. Eder, A. J. Link, A. G. MacPhee, Y. Ping, P. M. Song, A. Throop, and L. D. Van Woerkom, "Absolute calibration of image plates for electrons at energy between 100 keV and 4 MeV." *The Review of Scientific Instruments*, vol. 79, 033301, 2008. https://doi.org/10.1063/1.2885045 [Cited on page 40.]

[145] S. Devic, J. Seuntjens, E. Sham, E. B. Podgorsak, C. R. Schmidtlein, A. S. Kirov, and C. G. Soares, "Precise radiochromic film dosimetry using a flat-bed document scanner," *Medical Physics*, vol. 32, 2245, 2005. https://doi.org/10.1118/1.1929253 [Cited on page 41.]

[146] J. Sorriaux, A. Kacperek, S. Rossomme, J. A. Lee, D. Bertrand, S. Vynckier, and E. Sterpin, "Evaluation of Gafchromic® EBT3 films characteristics in therapy photon, electron and proton beams." *Physica*

*medica*, vol. 29, 599, 2013. https://doi.org/10.1016/j.ejmp.2012.10.001 [Cited on page 41.]

[147] S. Agostinelli, J. Allison, K. Amako, J. Apostolakis, H. Araujo, P. Arce, M. Asai, D. Axen, S. Banerjee, G. Barrand, F. Behner, L. Bellagamba, J. Boudreau, L. Broglia, A. Brunengo, H. Burkhardt, S. Chauvie, J. Chuma, R. Chytracek, G. Cooperman, G. Cosmo, P. Degtyarenko, A. Dell'Acqua, G. Depaola, D. Dietrich, R. Enami, A. Feliciello, C. Ferguson, H. Fesefeldt, G. Folger, F. Foppiano, A. Forti, S. Garelli, S. Giani, R. Giannitrapani, D. Gibin, J. J. Gomez Cadenas, I. Gonzalez, G. Gracia Abril, G. Greeniaus, W. Greiner, V. Grichine, A. Grossheim, S. Guatelli, P. Gumplinger, R. Hamatsu, K. Hashimoto, H. Hasui, A. Heikkinen, A. Howard, V. Ivanchenko, A. Johnson, F. W. Jones, J. Kallenbach, N. Kanaya, M. Kawabata, Y. Kawabata, M. Kawaguti, S. Kelner, P. Kent, A. Kimura, T. Kodama, R. Kokoulin, M. Kossov, H. Kurashige, E. Lamanna, T. Lampen, V. Lara, V. Lefebure, F. Lei, M. Liendl, W. Lockman, F. Longo, S. Magni, M. Maire, E. Medernach, K. Minamimoto, P. Mora de Freitas, Y. Morita, K. Murakami, M. Nagamatu, R. Nartallo, P. Nieminen, T. Nishimura, K. Ohtsubo, M. Okamura, S. O'Neale, Y. Oohata, K. Paech, J. Perl, A. Pfeiffer, M. G. Pia, F. Ranjard, A. Rybin, S. Sadilov, E. di Salvo, G. Santin, T. Sasaki, N. Savvas, Y. Sawada, S. Scherer, S. Sei, V. Sirotenko, D. Smith, N. Starkov, H. Stoecker, J. Sulkimo, M. Takahata, S. Tanaka, E. Tcherniaev, E. Safai Tehrani, M. Tropeano, P. Truscott, H. Uno, L. Urban, P. Urban, M. Verderi, A. Walkden, W. Wander, H. Weber, J. P. Wellisch, T. Wenaus, D. C. Williams, D. Wright, T. Yamada, H. Yoshida, and D. Zschiesche, "GEANT4 - A simulation toolkit," *Nuclear Instruments and Methods in Physics Research, Section A: Accelerators, Spectrometers, Detectors and Associated Equipment*, vol. 506, 250, 2003. https://doi.org/10.1016/S0168-9002(03)01368-8 [Not

cited.]

[148] J. F. Ziegler, M. D. Ziegler, and J. P. Biersack, "SRIM - The stopping and range of ions in matter (2010)," *Nuclear Instruments and Methods in Physics Research, Section B: Beam Interactions with Materials and Atoms*, vol. 268, 1818, 2010. http://dx.doi.org/10.1016/j.nimb.2010.02.091 [Not cited.]

[149] D. R. Welch, D. V. Rose, M. E. Cuneo, R. B. Campbell, and T. A. Mehlhorn, "Integrated simulation of the generation and transport of proton beams from laser-target interaction," *Physics of Plasmas*, vol. 13, 063105, 2006. https://doi.org/10.1063/1.2207587 [Not cited.]

[150] D. Welch, D. Rose, R. Clark, T. Genoni, and T. Hughes, "Implementation of an non-iterative implicit electromagnetic field solver for dense plasma simulation," *Computer Physics Communications*, vol. 164, 183, 2004. https://doi.org/10.1016/j.cpc.2004.06.028 [Cited on page 45.]

[151] D. R. Welch, D. V. Rose, B. V. Oliver, and R. E. Clark, "Simulation techniques for heavy ion fusion chamber transport," *Nuclear Instruments and Methods in Physics Research, Section A: Accelerators, Spectrometers, Detectors and Associated Equipment*, vol. 464, 134, 2001. https://doi.org/10.1016/S0168-9002(01)00024-9 [Cited on pages 44 and 46.]

[152] D. W. Hewett and A. Bruce Langdon, "Electromagnetic direct implicit plasma simulation," *Journal of Computational Physics*, vol. 72, 121, 1987. https://doi.org/10.1016/0021-9991(87)90075-1 [Cited on page 45.]

[153] M. E. Jones, D. S. Lemons, R. J. Mason, V. a. Thomas, and D. Winske, "A Grid-Based Coulomb Collision Model for PIC

Codes," *Journal of Computational Physics*, vol. 123, 169, 1996. https://doi.org/10.1006/jcph.1996.0014 [Cited on page 46.]

[154] T. Takizuka and H. Abe, "A binary collision model for plasma simulation with a particle code," *Journal of Computational Physics*, vol. 25, 205, 1977. https://doi.org/10.1016/0021-9991(77)90099-7 [Cited on page 47.]

[155] K. Nanbu, "Theory of cumulative small-angle collisions in plasmas," *Physical Review E*, vol. 55, 4642, 1997. https://doi.org/10.1103/PhysRevE.55.4642 [Cited on page 47.]

[156] Y. T. Lee and R. M. More, "An electron conductivity model for dense plasmas," *Physics of Fluids*, vol. 27, 1273, 1984. https://doi.org/10.1063/1.864744 [Not cited.]

[157] M. P. Desjarlais, "Practical Improvements to the Lee-More Conductivity Near the Metal-Insulator Transition," *Contributions to Plasma Physics*, vol. 41, 267, 2001. [Not cited.]

[158] A. M. Russell and D. W. Schumacher, "Extending the Nanbu Collision Algorithm to Non-Spitzerian Systems and Application to Laser Heating and Damage," *Physics of Plasmas*, vol. 080702, 1–5, 2017. https://doi.org/10.1063/1.4995268 [Not cited.]

[159] C. Li and R. D. Petrasso, "Effects of scattering upon energetic ion energy loss in plasmas," *Plasma Physics*, vol. 2, 2460, 1995. https://doi.org/10.1063/1.871271 [Cited on page 47.]

[160] B. C. Franke, R. P. Kensek, and T. W. Laub, "ITS Version 6: The Integrated TIGER Series of Coupled Electron/Photon Monte Carlo Transport Codes," Tech. Rep., 2008. http://prod.sandia.gov/techlib/access-control.cgi/2008/083331.pdf [Cited on page 47.]

[161] J. F. Myatt, J. A. Delettrez, A. V. Maximov, D. D. Meyerhofer, R. W. Short, C. Stoeckl, and M. Storm, "Optimizing electron-positron pair production on kilojoule-class high-intensity lasers for the purpose of pair-plasma creation," *Physical Review E*, vol. 79, 066409, 2009. https://doi.org/10.1103/PhysRevE.79.066409 [Cited on pages 48 and 89.]

[162] D. P. Higginson, "Ultra-High-Contrast Laser Acceleration of Relativistic Electrons in Solid Targets," Ph.D. dissertation, 2011. https://escholarship.org/content/qt2xc140kf/qt2xc140kf.pdf [Cited on page 49.]

[163] D. P. Higginson, A. Link, H. Sawada, S. C. Wilks, T. Bartal, S. Chawla, C. D. Chen, K. A. Flippo, L. C. Jarrott, M. H. Key, H. S. McLean, P. K. Patel, F. Pérez, M. S. Wei, and F. N. Beg, "High-contrast laser acceleration of relativistic electrons in solid cone-wire targets," *Physical Review E - Statistical, Nonlinear, and Soft Matter Physics*, vol. 92, 063112, 2015. https://doi.org/10.1103/PhysRevE.92.063112 [Cited on page 49.]

[164] M. Allen, P. K. Patel, A. Mackinnon, D. Price, S. Wilks, and E. Morse, "Direct experimental evidence of back-surface ion acceleration from laser-irradiated gold foils," *Physical Review Letters*, vol. 93, 265004, 2004. https://doi.org/10.1103/PhysRevLett.93.265004 [Cited on pages 49 and 90.]

[165] F. Beg, "Private communication," 2017. [Not cited.]

[166] F. Wagner, O. Deppert, C. Brabetz, P. Fiala, A. Kleinschmidt, P. Poth, V. A. Schanz, A. Tebartz, B. Zielbauer, M. Roth, T. Stöhlker, and V. Bagnoud, "Maximum Proton Energy above 85 MeV from the Relativistic Interaction of Laser Pulses with Micrometer Thick CH2 Targets," *Physical Review Letters*, vol. 116, 205002, 2016. https://doi.org/10.1103/PhysRevLett.116.205002 [Cited on page 58.]

[167] A. M. Rasmus, A. U. Hazi, M. J.-E. Manuel, C. C. Kuranz, S. R. Klein, P. X. Belancourt, J. R. Fein, M. J. MacDonald, R. P. Drake, B. B. Pollock, J. Park, G. J. Williams, and H. Chen, "Detailed characterization of the LLNL imaging proton spectrometer," *Review of Scientific Instruments*, vol. 87, 11D831, 2016. http://dx.doi.org/10.1063/1.4962045 [Not cited.]

[168] T. Piran, "Gamma-ray bursts and the fireball model," *Physics Reports*, vol. 314, 575, 1999. https://doi.org/10.1016/S0370-1573(98)00127-6 [Cited on page 63.]

[169] C. D. Chen, A. J. Kemp, F. Perez, A. Link, F. N. Beg, S. Chawla, M. H. Key, H. S. McLean, A. Morace, Y. Ping, A. Sorokovikova, R. B. Stephens, M. Streeter, B. Westover, and P. K. Patel, "Comparisons of angularly and spectrally resolved Bremsstrahlung measurements to two-dimensional multi-stage simulations of short-pulse laser-plasma interactions," *Physics of Plasmas*, vol. 20, 052703, 2013. https://doi.org/10.1063/1.4804348 [Cited on page 63.]

[170] G. J. Williams, D. Barnak, G. Fiksel, A. Hazi, S. Kerr, C. Krauland, A. Link, M. J.-E. Manuel, S. R. Nagel, J. Park, J. Peebles, B. B. Pollock, F. N. Beg, R. Betti, and H. Chen, "Target material dependence of positron generation from high intensity laser-matter interactions," *Physics of Plasmas*, vol. 23, 123109, 2016. http://dx.doi.org/10.1063/1.4971235 [Cited on pages 63, 89, and 187.]

[171] W. Heitler, *The Quantum Theory of Radiation*. Oxford: Clarendon Press, 1954. [Not cited.]

[172] T. E. Cowan, M. D. Perry, M. H. Key, T. R. Ditmire, S. P. Hatchett, E. A. Henry, J. D. Moody, M. J. Moran, D. M. Pennington, T. W. Phillips, T. C. Sangster, J. A. Sefcik, M. S. Singh, R. A. Snavely,

M. A. Stoyer, S. C. Wilks, P. E. Young, Y. Takahashi, B. Dong, W. Fountain, T. Parnell, J. Johnson, A. W. Hunt, and T. Kühl, "High energy electrons, nuclear phenomena and heating in petawatt laser-solid experiments," *Laser and Particle Beams*, vol. 17, 773, 1999. https://doi.org/10.1017/S0263034699174238 [Cited on page 63.]

[173] H. W. Koch and J. W. Motz, "Bremsstrahlung cross-section formulas and related data," *Reviews of Modern Physics*, vol. 31, 920, 1959. https://doi.org/10.1103/RevModPhys.31.920 [Cited on page 64.]

[174] J. A. Bearden and A. F. Burr, "Reevaluation of X-ray atomic energy levels," *Reviews of Modern Physics*, vol. 39, 125, 1967. https://doi.org/10.1103/RevModPhys.39.125 [Cited on page 64.]

[175] J. W. Motz, H. A. Olsen, and H. W. Koch, "Pair production by photons," *Reviews of Modern Physics*, vol. 41, 581, 1969. https://doi.org/10.1103/RevModPhys.41.581 [Cited on page 65.]

[176] G. J. Williams, B. B. Pollock, F. Albert, J. Park, and H. Chen, "Positron generation using laser-wakefield electron sources," *Physics of Plasmas*, vol. 22, 093115, 2015. https://doi.org/10.1063/1.4931044 [Not cited.]

[177] H. Sawada, D. P. Higginson, A. Link, T. Ma, S. C. Wilks, H. S. McLean, F. Perez, P. K. Patel, and F. N. Beg, "Characterizing the energy distribution of laser-generated relativistic electrons in cone-wire targets," *Physics of Plasmas*, vol. 19, 103108, 2012. https://doi.org/10.1063/1.4759163 [Cited on pages 69, 79, and 80.]

[178] J. M. C. Robles, E. Ogando, and F. Plazaola, "Positron lifetime calculation for the elements of the periodic table," *Journal of Physics: Condensed Matter*, vol. 19, 176222, 2007. https://doi.org/10.1088/0953-8984/19/17/176222 [Not cited.]

[179] J. Peebles, M. S. Wei, A. V. Are, C. Mcguffey, R. B. Stephens, W. Theobald, D. Haberberger, and L. C. Jarrott, "Investigation of laser pulse length and pre-plasma scale length impact on hot electron generation on OMEGA-EP," vol. 19, 023008, 2017. https://doi.org/10.1088/1367-2630/aa5a21 [Not cited.]

[180] J. Green, V. Ovchinnikov, R. Evans, K. Akli, H. Azechi, F. Beg, C. Bellei, R. Freeman, H. Habara, R. Heathcote, M. Key, J. King, K. Lancaster, N. Lopes, T. Ma, A. MacKinnon, K. Markey, A. McPhee, Z. Najmudin, P. Nilson, R. Onofrei, R. Stephens, K. Takeda, K. Tanaka, W. Theobald, T. Tanimoto, J. Waugh, L. Van Woerkom, N. Woolsey, M. Zepf, J. Davies, and P. Norreys, "Effect of Laser Intensity on Fast-Electron-Beam Divergence in Solid-Density Plasmas," *Physical Review Letters*, vol. 100, 015003, 2008. https://doi.org/10.1103/PhysRevLett.100.015003 [Cited on page 73.]

[181] V. M. Ovchinnikov, D. W. Schumacher, M. McMahon, E. A. Chowdhury, C. D. Chen, A. Morace, and R. R. Freeman, "Effects of Preplasma Scale Length and Laser Intensity on the Divergence of Laser-Generated Hot Electrons," *Physical Review Letters*, vol. 110, 065007, 2013. https://doi.org/10.1103/PhysRevLett.110.065007 [Cited on page 73.]

[182] A. Poyé, J. L. Dubois, F. Lubrano-Lavaderci, E. D'Humières, M. Bardon, S. Hulin, M. Bailly-Grandvaux, J. Ribolzi, D. Raffestin, J. J. Santos, P. Nicolaï, and V. Tikhonchuk, "Dynamic model of target charging by short laser pulse interactions," *Physical Review E - Statistical, Nonlinear, and Soft Matter Physics*, vol. 92, 043107, 2015. https://doi.org/10.1103/PhysRevE.92.043107 [Cited on page 77.]

[183] A. J. Mackinnon, Y. Sentoku, P. K. Patel, D. W. Price, S. Hatchett, M. H. Key, C. Andersen, R. Snavely, and R. R. Freeman, "Enhancement

of proton acceleration by hot-electron recirculation in thin foils irradiated by ultraintense laser pulses," *Physical Review Letters*, vol. 88, 215006, 2002. https://doi.org/10.1103/PhysRevLett.88.215006 [Cited on page 80.]

[184] O. Tresca, D. C. Carroll, X. H. Yuan, B. Aurand, V. Bagnoud, C. M. Brenner, M. Coury, J. Fils, R. J. Gray, T. Kühl, C. Li, Y. T. Li, X. X. Lin, M. N. Quinn, R. G. Evans, B. Zielbauer, M. Roth, D. Neely, and P. McKenna, "Controlling the properties of ultraintense laserproton sources using transverse refluxing of hot electrons in shaped mass-limited targets," *Plasma Physics and Controlled Fusion*, vol. 53, 105008, 2011. https://doi.org/10.1088/0741-3335/53/10/105008 [Cited on page 87.]

[185] P. McKenna, K. W. D. Ledingham, J. M. Yang, L. Robson, T. McCanny, S. Shimizu, R. J. Clarke, D. Neely, K. Spohr, R. Chapman, R. P. Singhal, K. Krushelnick, M. S. Wei, and P. A. Norreys, "Characterization of proton and heavier ion acceleration in ultrahigh-intensity laser interactions with heated target foils," *Physical Review E - Statistical, Nonlinear, and Soft Matter Physics*, vol. 70, 036405, 2004. https://doi.org/10.1103/PhysRevE.70.036405 [Cited on page 89.]

[186] D. T. Offermann, K. A. Flippo, J. Cobble, M. J. Schmitt, S. A. Gaillard, T. Bartal, D. V. Rose, D. R. Welch, M. Geissel, and M. Schollmeier, "Characterization and focusing of light ion beams generated by ultra intensely irradiated thin foils at the kilojoule scale," *Physics of Plasmas*, vol. 18, 056713, 2011. https://doi.org/10.1063/1.3589476 [Cited on page 89.]

[187] R. P. Drake, *High-Energy-Density Physics*. Springer, 2006. [Cited on page 92.]

[188] J. B. Kim, S. Göde, and S. H. Glenzer, "Development of a cryogenic hydrogen microjet for high-intensity, high-repetition rate experiments," *Review of Scientific Instruments*, vol. 87, 11E328, 2016. https://doi.org/10.1063/1.4961089 [Cited on page 187.]

[189] S. Göde, C. Rödel, K. Zeil, R. Mishra, M. Gauthier, F. Brack, T. Kluge, M. J. MacDonald, J. Metzkes, L. Obst, M. Rehwald, C. Ruyer, H. P. Schlenvoigt, W. Schumaker, P. Sommer, T. E. Cowan, U. Schramm, S. Glenzer, and F. Fiuza, "Relativistic electron streaming instabilities modulate proton beams accelerated in laser-plasma interactions," vol. 118, 194801, 2017. https://doi.org/10.1103/PhysRevLett.118.194801 [Cited on page 117.]

[190] G. G. Scott, C. M. Brenner, V. Bagnoud, R. J. Clarke, B. Gonzalez-Izquierdo, J. S. Green, R. I. Heathcote, H. W. Powell, D. R. Rusby, B. Zielbauer, P. McKenna, and D. Neely, "Diagnosis of Weibel instability evolution in the rear surface density scale lengths of laser solid interactions via proton acceleration," *New Journal of Physics*, vol. 19, 043010, 2017. https://doi.org/10.1088/1367-2630/aa652c [Not cited.]

[191] M. Borghesi, "Laser-driven ion acceleration: State of the art and emerging mechanisms," *Nuclear Instruments and Methods in Physics Research, Section A: Accelerators, Spectrometers, Detectors and Associated Equipment*, vol. 740, 6, 2014. http://dx.doi.org/10.1016/j.nima.2013.11.098 [Cited on page 103.]

[192] B. M. Hegelich, D. Jung, B. Albright, J. Fernandez, D. Gautier, C. Huang, T. Kwan, S. Letzring, S. Palaniyappan, R. Shah, H.-C. Wu, L. Yin, A. Henig, R. Hörlein, D. Kiefer, J. Schreiber, X. Yan, T. Tajima, D. Habs, B. Dromey, and J. Honrubia, "Experimental demonstration of particle energy, conversion efficiency and spectral shape required

for ion-based fast ignition," *Nuclear Fusion*, vol. 51, 083011, 2011. https://doi.org/10.1088/0029-5515/51/8/083011 [Not cited.]

[193] S. N. Chen, M. Vranic, T. Gangolf, E. Boella, P. Antici, M. Bailly-Grandvaux, P. Loiseau, H. Pépin, G. Revet, J. J. Santos, A. M. Schroer, M. Starodubtsev, O. Willi, L. O. Silva, E. D'Humières, and J. Fuchs, "Collimated protons accelerated from an overdense gas jet irradiated by a 1 m wavelength high-intensity short-pulse laser," *Scientific Reports*, vol. 7, 13505, 2017. http://doi.org/10.1038/s41598-017-12910-6 [Cited on page 111.]

[194] L. Willingale, P. M. Nilson, A. G. R. Thomas, S. S. Bulanov, A. Maksimchuk, W. Nazarov, T. C. Sangster, C. Stoeckl, and K. Krushelnick, "High-power, kilojoule laser interactions with near-critical density plasma," *Physics of Plasmas*, vol. 18, 056706, 2011. https://doi.org/10.1063/1.3563438 [Cited on page 111.]

[195] B. S. Wettervik, T. C. DuBois, and T. Fülöp, "Vlasov modelling of laser-driven collisionless shock acceleration of protons," *Physics of Plasmas*, vol. 23, 053103, 2015. https://doi.org/10.1063/1.4948424 [Not cited.]

[196] A. Grassi, L. Fedeli, A. Sgattoni, and A. Macchi, "Vlasov simulation of laser-driven shock acceleration and ion turbulence," *Plasma Physics and Controlled Fusion*, vol. 034021, 1–14, 2016. http://arxiv.org/abs/1507.08585 [Cited on page 164.]

[197] M. Schnürer, A. A. Andreev, F. Abicht, J. Bränzel, C. Koschitzki, K. Y. Platonov, G. Priebe, and W. Sandner, "The beat in laser-accelerated ion beams," *Physics of Plasmas*, vol. 20, 1–5, 2013. [Cited on page 164.]

[198] A. Mancic, J. Robiche, P. Antici, P. Audebert, C. Blancard, P. Combis, F. Dorchies, G. Faussurier, S. Fourmaux, M. Harmand, R. Kodama,

L. Lancia, S. Mazevet, M. Nakatsutsumi, O. Peyrusse, V. Recoules, P. Renaudin, R. Shepherd, and J. Fuchs, "Isochoric heating of solids by laser-accelerated protons: Experimental characterization and self-consistent hydrodynamic modeling," *High Energy Density Physics*, vol. 6, 21–28, 2010. http://dx.doi.org/10.1016/j.hedp.2009.06.008 [Cited on page 164.]

[199] D. Jung, R. Hrlein, D. C. Gautier, S. Letzring, D. Kiefer, K. Allinger, B. J. Albright, R. Shah, S. Palaniyappan, L. Yin, J. C. Fernndez, D. Habs, and B. M. Hegelich, "A novel high resolution ion wide angle spectrometer," *Review of Scientific Instruments*, vol. 82, 1–5, 2011. [Cited on page 164.]

[200] D. G. Hicks, C. K. Li, F. H. Séguin, J. D. Schnittman, A. K. Ram, J. A. Frenje, R. D. Petrasso, J. M. Soures, D. D. Meyerhofer, S. Roberts, C. Sorce, C. Stöckl, T. C. Sangster, and T. W. Phillips, "Observations of fast protons above 1 MeV produced in direct-drive laser-fusion experiments," *Physics of Plasmas*, vol. 8, 606–610, 2001. [Cited on pages 165 and 172.]

[201] D. G. Hicks, C. K. Li, R. D. Petrasso, F. H. Seguin, B. E. Burke, J. P. Knauer, S. Cremer, R. L. Kremens, M. D. Cable, and T. W. Phillips, "Design of an electronic charged particle spectrometer to measure $\rho$R on inertial fusion experiments," *Review of Scientific Instruments*, vol. 68, 589, 1997. http://scitation.aip.org/content/aip/journal/rsi/68/1/10.1063/1.1147660 [Cited on page 165.]

[202] J. D. Jackson, *Classical Electrodynamics*, 3rd ed. Wiley, 1998. [Cited on page 167.]

[203] F. H. Séguin, C. K. Li, M. J. E. Manuel, H. G. Rinderknecht, N. Sinenian, J. A. Frenje, J. R. Rygg, D. G. Hicks, R. D. Petrasso, J. Delettrez,

R. Betti, F. J. Marshall, and V. A. Smalyuk, "Time evolution of filamentation and self-generated fields in the coronae of directly driven inertial-confinement fusion capsules," *Physics of Plasmas*, vol. 19, 1–12, 2012. [Cited on page 174.]

[204] P. Stoltz, S. Veitzer, R. Cohen, A. Molvik, and J.-L. Vay, "Simulation of Heavy Ion Induced Electron Yield at Grazing Incidence." *Physical Review Special Topics - Accelerators and Beams*, vol. 7, 103201, 2004. [Cited on page 177.]

[205] J. R. M. Vaughan, "Multipactor," *Electron Devices, IEEE Transactions on*, vol. 35, 1172–1180, 1988. [Cited on page 178.]

[206] A. Poyé, S. Hulin, M. Bailly-Grandvaux, J. L. Dubois, J. Ribolzi, D. Raffestin, M. Bardon, F. Lubrano-Lavaderci, E. D'Humières, J. J. Santos, P. Nicolaï, and V. Tikhonchuk, "Physics of giant electromagnetic pulse generation in short-pulse laser experiments," *Physical Review E - Statistical, Nonlinear, and Soft Matter Physics*, vol. 91, 043106, 2015. https://doi.org/10.1103/PhysRevE.91.043106 [Cited on page 179.]

[207] A. Pak, S. Kerr, N. Lemos, A. Link, P. Patel, F. Albert, L. Divol, B. B. Pollock, D. Haberberger, D. Froula, M. Gauthier, S. H. Glenzer, A. Longman, L. Manzoor, R. Fedosejevs, S. Tochitsky, C. Joshi, and F. Fiuza, "Collisionless shock acceleration of narrow energy spread ion beams from mixed species plasmas using 1 $\mu$m lasers," 2018. [Not cited.]

[208] X. Vaisseau, A. Debayle, J. J. Honrubia, S. Hulin, A. Morace, H. Sawada, B. Vauzour, D. Batani, F. N. Beg, J. R. Davies, R. Fedosejevs, R. J. Gray, G. E. Kemp, S. M. Kerr, K. Li, A. Link, P. Mckenna, H. S. Mclean, M. Mo, P. K. Patel, J. Park, J. Peebles, Y. J. Rhee, A. Sorokovikova, V. T. Tikhonchuk, L. Volpe, M. Wei, and J. J. Santos, "Enhanced Relativistic-Electron-Beam Energy Loss in Warm

Dense Aluminum," *Physical Review Letters*, vol. 095004, 1–6, 2015. https://doi.org/10.1103/PhysRevLett.114.095004 [Cited on page 187.]

[209] X. Vaisseau, A. Morace, M. Touati, M. Nakatsutsumi, S. D. Baton, S. Hulin, P. Nicolaï, R. Nuter, D. Batani, F. N. Beg, J. Breil, R. Fedosejevs, J. Feugeas, C. Fourment, S. Fujioka, L. Giuffrida, S. Kerr, H. S. Mclean, H. Sawada, V. T. Tikhonchuk, and J. J. Santos, "Collimated Propagation of Fast Electron Beams Accelerated by High-Contrast Laser Pulses in Highly Resistive Shocked Carbon," *Physical Review Letters*, vol. 205001, 1–6, 2017. https://doi.org/10.1103/PhysRevLett.118.205001 [Cited on page 187.]

[210] H. Friesen, H. F. Tiedje, D. S. Hey, M. Z. Mo, A. Beaudry, R. Fedosejevs, Y. Y. Tsui, A. J. Mackinnon, H. S. McLean, and P. K. Patel, "Kirkpatrick-Baez microscope for hard X-ray imaging of fast ignition experiments." *The Review of scientific instruments*, vol. 84, 023704, 2013. https://doi.org/10.1063/1.4776670 [Cited on page 187.]

[211] H. Chen, J. C. Sheppard, D. D. Meyerhofer, A. U. Hazi, A. J. Link, S. Anderson, H. A. Baldis, R. Fedosejev, J. Gronberg, N. Izumi, S. M. Kerr, E. Marley, J. Park, R. Tommasini, S. C. Wilks, and G. J. Williams, "Emittance of positron beams produced in intense laser plasma interaction," *Physics of Plasmas*, vol. 20, 013111, 2013. https://doi.org/10.1063/1.4789621 [Cited on page 187.]

[212] M. Z. Mo, Z. Chen, S. Fourmaux, A. Saraf, S. Kerr, K. Otani, R. Masoud, J. Kieffer, Y. Tsui, A. Ng, and R. Fedosejevs, "Measurements of ionization states in warm dense aluminum with betatron radiation," *Physical Review E*, vol. 95, 053208, 2017. https://doi.org/10.1103/PhysRevE.95.053208 [Cited on page 187.]

[213] S. R. Nagel, H. Chen, J. Park, M. Foord, A. U. Hazi, T. J. Hilsabeck,

S. M. Kerr, E. V. Marley, and G. J. Williams, "Two-dimensional time-resolved ultra-high speed imaging of K-alpha emission from short-pulse-laser interactions to observe electron recirculation," *Applied Physics Letters*, vol. 110, 144102, 2017. https://dx.doi.org/10.1063/1.4979802 [Cited on page 187.]

[214] N. F. Brejnholt, T. A. Decker, R. M. Hill, H. Chen, G. J. Williams, J. Park, J. B. Alameda, M. Fernández-Perea, M. J. Pivovaroff, R. Soufli, M.-A. Descalle, J. Peebles, and S. M. Kerr, "Reflective multilayer optic as hard X-ray diagnostic on laser-plasma experiment." *The Review of scientific instruments*, vol. 86, 013110, 2015. https://doi.org/10.1063/1.4906509 [Cited on page 187.]

[215] H. Chen, M. Bitter, K. W. Hill, S. M. Kerr, E. Magee, S. R. Nagel, J. Park, M. B. Schneider, G. Stone, G. J. Williams, and P. Beiersdorfer, "A high-resolution imaging x-ray crystal spectrometer for high energy density plasmas," *Review of Scientific Instruments*, vol. 85, 11E606, 2014. https://doi.org/10.1063/1.4891053 [Cited on page 187.]

# Appendices

# Appendix A
# Investigation of IPS Modulations

An investigation was undertaken to try and determine the origin of the modulations in the IPS ion spectral data. Published observations of modulations from other diagnostics are summarized in Section A.1. Numerous experimental tests were performed on the IPS; these tests are described in Section A.2 and summarized in Table A.1. It should be noted that the properties of the proton beams varied significantly for these tests, and therefore it would be best to repeat these tests using a constant proton source before drawing any definitive conclusions. Lastly, Section A.3 covers LSP PIC simulations of the IPS and TNSA source.

## A.1 Observations in Literature

Modulations in proton signal from laser-generated beams have been observed and published previously, though rarely directly addressed. A fundamental question is whether the phenomenon originates in the diagnostic or the beam source/transport. One suggestion is that the $2\omega$ hot electrons bunches produced by J $\times$ B heating could cause density modulations in the background plasma when interacting with bunches reflected by the sheath field [196]. Schnürer *et al.* observed low level oscillations in a TNSA spectrum and attributed them to the imprint of these electron dynamics [197]. This behaviour was only seen for very high laser contrast and fs pulse durations, however, very different experimental conditions from those used with the IPS. Mancic *et al.* published proton data with spectral oscillations (Fig. 3) for 320 fs, 30 J pulses, but did not provide an explanation [198]. The spectrometer used had a

5 mm slit entrance, and the oscillations occurred out to 1.2 MeV. The ion wide angle spectrometer (iWASP), built and fielded at the Trident laser, is another slit-based diagnostic that displayed artifacts in TNSA proton spectra for 550 fs, 80 J pulses [199]. These artifacts were in the imaging direction and not the energy direction, however, and were claimed to be due to non-uniformities in the 20 µm wide slit. Hicks *et al.* observed spectral modulations in $< 1$ MeV protons with 1 ns duration beams, multi-kJ energies and $I = 1 \times 10^{15}$ W/cm$^2$, and suggested it could be due to ion acoustic perturbations in an expanding plasma [200]. The magnetic spectrometer used had a slit entrance [201]. It is interesting to note that spectral modulations seem to be associated with spectrometers that have slit entrance holes. Finally, weak modulations have been observed with a Thomson Parabola at Titan, but without the regularity of the IPS.

## A.2 Experimental Tests

Various analysis techniques were used to characterize the modulations. The simplest approach was to find the location and separation of the peaks in energy space. Similar analysis was done in time by converting proton energy to velocity and then using the source distance to calculate arrival time. Fourier analysis was performed on the proton spectrum, now defined in time, to extract the dominant temporal frequencies. This has the disadvantage of integrating over all time, making time-dependent frequency shifts difficult to detect. Wavelet analysis was therefore also performed; this technique decomposes the signal in terms of finite-time functions ('wavelets'), and is therefore better suited to giving time-dependent frequency information. The 'morse' wavelet was used was for all wavelet analysis. In all cases the data was first cubicly interpolated to reduce the effect of pixel noise (peaks may consist of 3-4 pixels at 50 µm scanning resolution). A higher scanning resolution of 25 µm

| | **Test** | **Result** | **Comment** |
|---|---|---|---|
| 1 | Number of protons in beam varied | Stronger modulations for higher proton number | Modulations are dependent upon incident current |
| 2 | Source-diagnostic distance increased | Energy spacing decreases while temporal spacing is unchanged | Modulations are imposed by the IPS at a set frequency |
| 3 | Thin foils placed in path of beam | Modulations removed, very weak for high energy protons and 0.5 µm foil | Low beam emittance is critical to observing modulations |
| 4 | Co-moving electrons removed with B-field | Oscillations unchanged | Co-moving electrons have no effect on modulations |
| 5 | Slit dimensions changed; plastic slit used | Oscillations unchanged | Resonance in the slit does not cause the modulations |
| 6 | Body slot geometry changed | Oscillations unchanged | Body slot is not primary source of modulations |
| 7 | Carbon ions are modulated | Frequency is less then that of co-timed protons | Unclear. |
| 8 | TNSA measured at Orion laser | Modulations with similar frequency to Titan | Chamber EMP characteristics are not critical |

Table A.1: Summary of tests and observations regarding the IPS spectral modulations. It should be noted that the proton source (target, laser conditions, IPS position) was not kept constant for all tests, as IPS testing was a lower priority then the primary goals of the experiments.

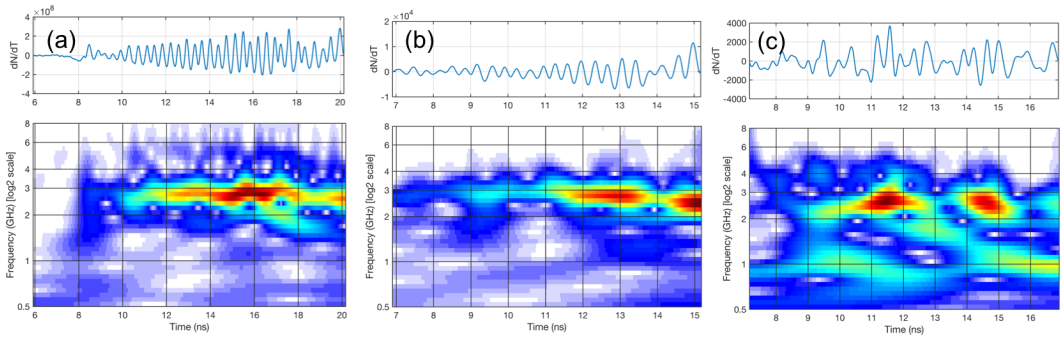


Figure A.1: Sample wavelet analysis for various shots at Titan. (a) Shot 5 from Feb. 2013, on 25 µm Cu (data collected by Dr. Louise Willingale [35]). (b) Shot 10 from Sep. 2016, on 10 µm Au. (c) Shot 23 from May 2017, on 10 µm Au.

is in fact necessary to fully resolve the oscillations, but this was only realized after all data was taken.

Wavelet frequency analysis of representative shots from different experiments is shown in Figure A.1. When the IPS is located on or near rear normal with good TNSA conditions (thin foil targets, high laser energy) a single frequency response dominates the spectrum. This frequency is between 2 - 3 GHz, as seen in plots (a) and (b). When the TNSA beam is non-ideal, due to either IPS placement or sub-optimal target conditions, the modulations in the spectra become highly variable. An example is given in plot (c).

### A.2.1 Effect of Source Distance

When the IPS position and shot conditions are kept constant the oscillation features are highly consistent, in both energy value and energy width. TNSA shots on Au foils (4-10 µm, 120-125 J in 1 ps) from the Sep. 2016 shock campaign were analyzed to quantify the effect of distance on the modulations. The IPS was positioned along rear target normal. The spectra are shown in Figure A.2(a), and the peak energy and temporal widths are plotted in Figure A.2(b) and (c). It can be seen that the modulations of shots 1 and 3 (distance = 20.3 cm) follow a different trend then shots 7, 8 and 10 (distance =

49.7 cm) when plotted in energy width. When converted to temporal duration, however, the width of each shot becomes relatively constant, between 0.3 - 0.4 ns. This finding is consistent with a modulation imposed by the diagnostic at a constant frequency. A TNSA proton beam has a range of velocities that cause it to be significantly stretched out in space and time when it reaches the IPS (up to 10's - 100's of ns, see Section A.3). If a diagnostic effect then bunches the proton beam at a set frequency, it will have both spatial and spectral modulations. If the beam travels further it will be stretched more in space, resulting in different spectral modulations for the same spatial/temporal bunching. This process is outlined in Figure A.3. On the other hand, if the beam modulations originated at or near the target at a set frequency additional travel time would not alter the peak width in energy space. Consider if a modulation occurred close to the target, between 4 MeV and 5 MeV protons; these protons will separate in space as they travel but keep the same 1 MeV energy difference. The IPS only measures the energy spacing of the beam, which is set at the modulation point.

### A.2.2 Resonant Cavity Tests

The average duration of the analyzed peaks was $0.34 \pm 0.03$ ns, equivalent to a frequency of $2.94 \pm 0.26$ GHz. For a rectangular waveguide with dimensions of $a$ and $b$ the TE mode cutoff frequencies are given by [202]:

$$f_{mn} = \frac{1}{2\pi\sqrt{\mu\epsilon}}\sqrt{\left(\frac{m\pi}{a}\right)^2 + \left(\frac{n\pi}{b}\right)^2} \qquad m, n = 0, 1, ... \tag{A.1}$$

The lowest frequency TE mode is m = 1, n = 0, and for $a = 5$ cm the frequency is $f_{10} = 3$ GHz, approximately the same as that observed in the Sep. 2016 data. Several distances in the IPS entrance geometry are 5 cm. The IPS slit is formed by two tungsten alloy (Hev-Met) plates separated by Al spacers, and has a height of 5 cm, length of 6.35 mm (1/4 inch, the thickness of the plates)

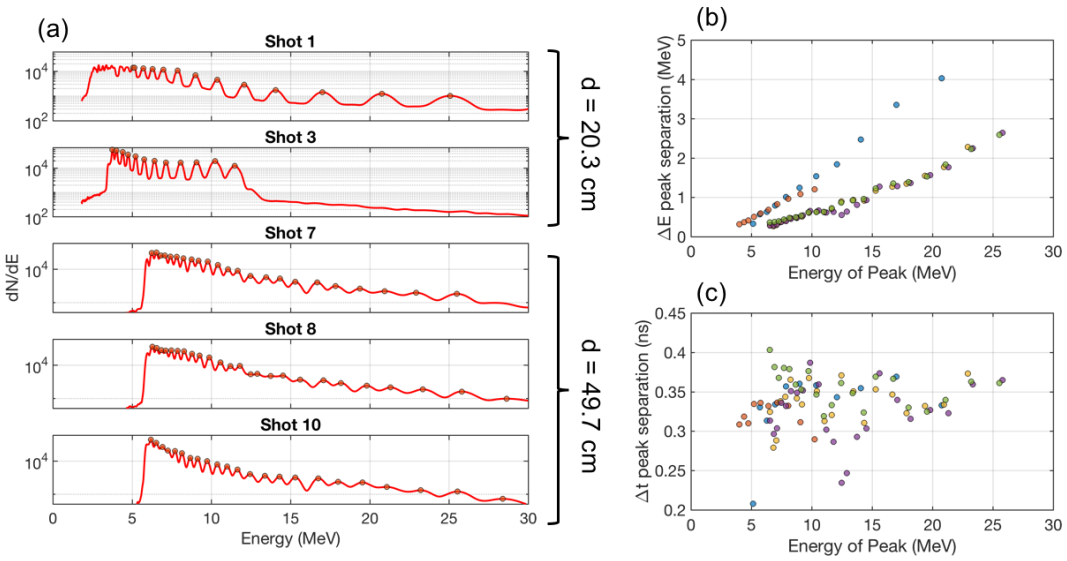


Figure A.2: Data from Sep. 2016, showing the effect of source-to-IPS distance. (a) Spectra, with peaks marked by yellow circles and the distance to TCC shown on the right. (b) Energy separation of peaks, showing two different trends depending on distance. (c) Temporal separation, which is effectively constant with distance and energy.

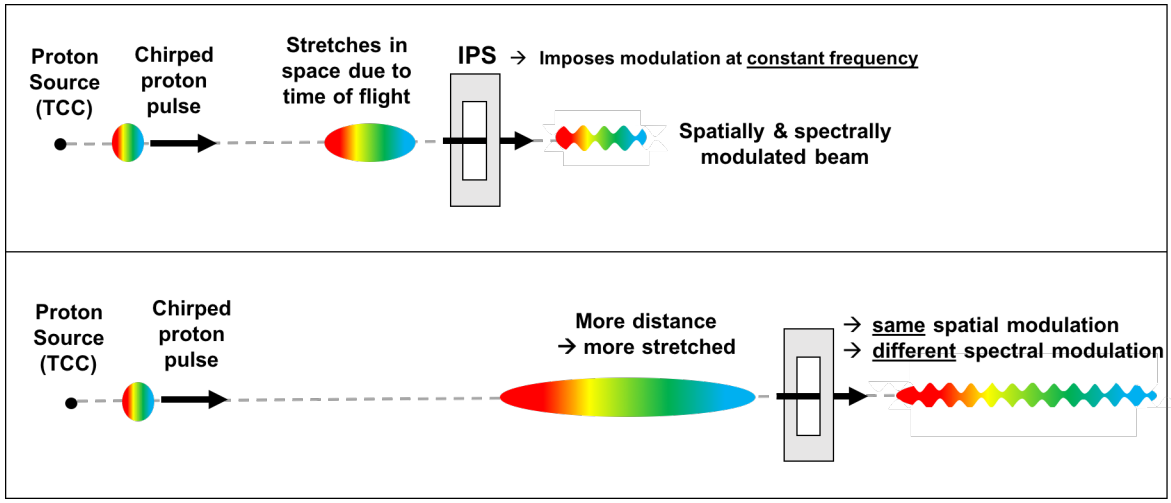


Figure A.3: Illustration of how modulation spacing in energy could be determined by the distance of the IPS from the proton source, while temporal spacing remains constant.

and width of 100 µm (as set by the spacers). The entrance slot of the IPS body is ∼5 cm tall, 7 mm wide and 1.3 cm deep. Both features were investigated to determine if they were supporting resonant modes that were modulating the proton beam.

To test the slit its heigh was varied by changing the spacer distance, from 5 cm to 1 mm, while keeping the IPS distance constant. If a resonant mode was imprinting on the beam it would be expected that the oscillation frequencies would vary between 3 and 150 GHz, with periods from 0.33 to 0.01 ns, respectively. In the highest frequency case this period would be beyond the resolution of the detector, and no oscillations would be expected to be observed. The IPS was 0.7215 m from TCC and 33.5° from rear target normal. The resulting data is shown in Figure A.4 along with Fourier spectral analysis, which has the advantage of not requiring peak fitting or width definitions. The data was taken from line-outs that were 50 pixels wide, an increase from the standard 8 pixels to compensate for the low signal-to-noise ratio. It can be seen that the data has a peak frequency around ∼2 GHz for all slit heights, and no clear trend with decreasing height. No strong signals above 5 GHz were observed. The modulations were significantly weaker and noisier then those recorded in Sep. 2016 (Figure A.2), resulting is more uncertainty in the frequency analysis. This uncertainty may account for the inconsistency between the observed peak frequencies.

Additional data was collected with a plastic slit, which is non-conducting and would not create a resonant cavity. The slit was formed from two teflon plates separated by Al spacers, and was 100 µm wide, 5 cm tall and 1.3 cm deep. Most of the signal was blocked due angular misalignment of the slit, but the unblocked portion clearly showed oscillations - see Figure A.5. From these tests it was concluded that a resonance in the slit is not responsible for the oscillations, although it may still be a contributing factor. The depth of modulation appears to be smaller with the plastic slit compared to the

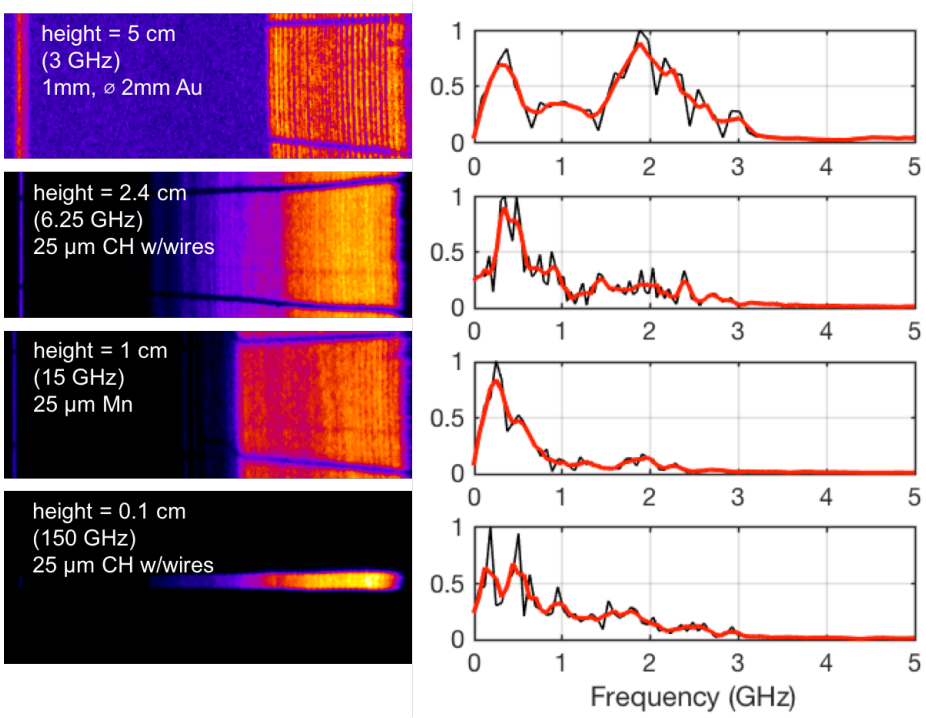


Figure A.4: Test of the resonant slit hypothesis, with the slit height varied from 5cm to 1mm. Left: Raw data, showing oscillations for all slit heights. Right: FFT analysis of the data (black = raw, red = averaged), showing no trend with slit size.

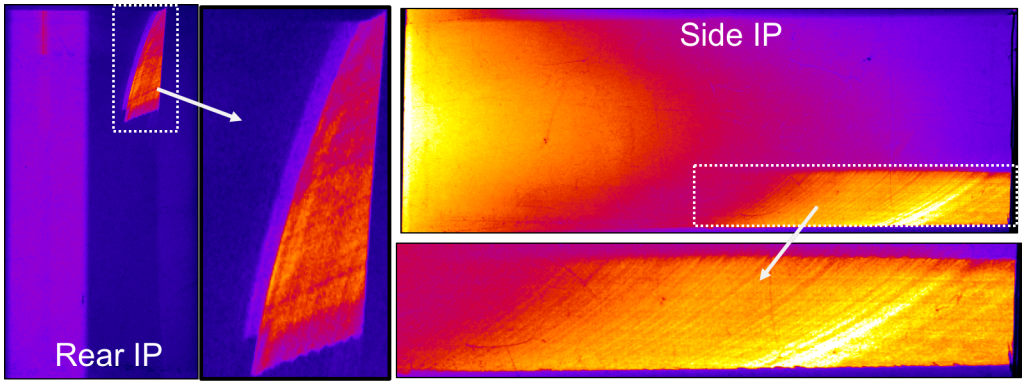


Figure A.5: Data taken with a plastic slit, showing oscillations despite the lack of a metal cavity.

metal slit, but the proton source was not constant between shots and therefore making a comparison is difficult.

The entrance slot of the IPS body is ∼5 cm tall, thereby offering another potential cavity with the appropriate dimensions for a 3 GHz resonance. To test the effect of this geometry an Al structure was inserted into the slot, thereby reducing the entrance size to 2 mm wide and 1.5 cm high. This would have the effect of significantly increasing the resonant frequency of this cavity. There was no significant change in the spectral modulations when this structure was present, suggesting that the IPS body slot geometry is not responsible for the phenomenon.

### A.2.3 Foil and Magnet Tests

Tests were performed by placing foils on the entrance of the IPS, on the surface of the metal plates, before the slit and after the plastic shielding. When a foil was attached no oscillations were observed in the region it shadowed (Figure A.6). The same result was found for all foils used, from 6 µm carbon to 0.5 µm $B_4C$ and 1.5 µm Al. A foil preceding the slit will have two effects: (1) the low energy, co-moving electrons (keV-range) will be significantly slowed and stopped, (2) protons will be scattered due to collisions within the foil,

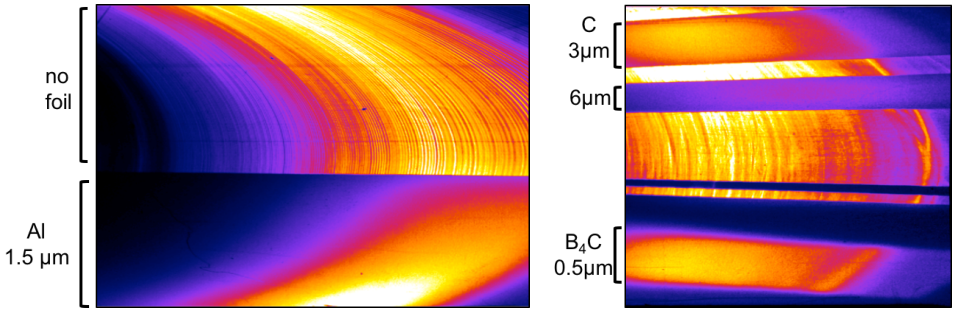


(a) (b)

Figure A.6: Foils placed on the entrance of the IPS, before the slit, eliminate the oscillatory features in the proton signal. Data is from the low energy side image plate. (a) $r$ = 1.5 mm, t = 1 mm Au target, 319 J in 10 ps. Data collected by Dr. Andy Hazi. (b) $r$ = 125 µm, t = 25 µm Au target, 26 J in 2 ps, defocused. Data collected by Dr. Hui Chen, Nov./Dec. 2009.

increasing the emittance of the beam. It is not obvious which of these two effects is critical to the oscillations. The scattering of protons could support the source/transport hypothesis that oscillations are present in the beam before it arrives at the IPS, and these features becomes blurred by the foils.

To deconvolve the dual effects of the foils, magnets were placed between the IPS and TCC and oriented with their magnetic field parallel to that of the IPS. This had the effect of sweeping away the cold co-moving electrons while maintaining the proton beam emittance. An array of 10 ceramic puck magnets (6mm diameter) was used, with two groups of 5 magnets separated by 1 cm. The magnets were located 4 cm in front of the IPS, and the magnetic field between them was greater then 300 G. The resulting spectrum is shown in Figure A.7. Oscillations are clearly present at all energies, and qualitatively comparable to shots without the magnets. This implies that the emittance of the proton beam is the key property being destroyed by thin foils.

### A.2.4 Other Tests and Observations

Ions other then hydrogen are also modulated in the IPS data, as can be seen by the carbon breakthrough signal in Figure A.8. The filter used was 100 µm

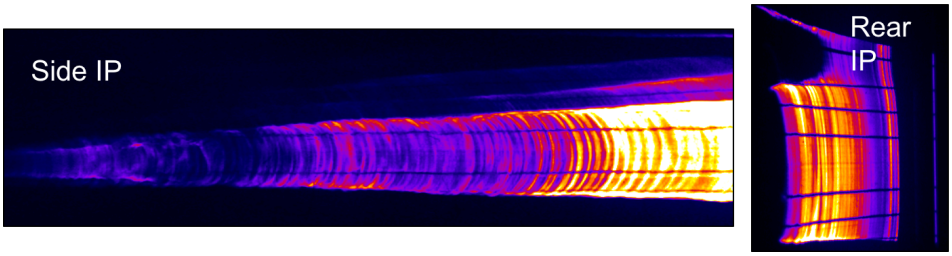


Figure A.7: Spectrum with a magnetic field removing the co-moving electrons before they enter the IPS. The narrowing of the signal in the side IP is due to the increased field closer to the magnets, which bent the lower energy protons away from the slit.

Al, which $C^{6+}$breaks through at $E_{proton}$ = 25 MeV. Only 2–3 oscillations are present in each shot, making peak separation the necessary analysis technique. Plotting the spectra vs. time allows the carbons oscillations to be compared with those of protons that arrive at the same time. It can be seen that the modulations are longer for carbon ions then protons. This is perhaps consistent with the carbon ions being driven by a weaker Lorentz force from the reduced q/m ratio for $C^{6+}$, such as would be experienced due to an electric field generated in a resonant cavity.

Modulations with similar characteristics were observed when a second IPS was fielded at the Orion laser, located in AWE, UK. The target was a 15 µm thick Au disc with a diameter of 225 µm, and the IPS was located 30 cm from the target along the rear normal. The laser energy was 390 J in ∼1 ps and a 20 µm spot. Strong modulations were seen in the 5 - 15 MeV range, with a central frequency around 2.75 GHz. This suggests that the chamber EMP characteristics are not important to the modulation frequency, although it is possible that similar EMP signatures are generated in both Orion and Titan setups. The effect of EMP at Titan was tested by shielding the IPS in a freestanding 15 µm Al foil housing. No difference in modulations was seen.

Ion acoustic waves could be responsible for proton spectral modulations with properties similar to those observed, in which case the features originate in the beam transport and not the diagnostic. Following the argument of Hicks

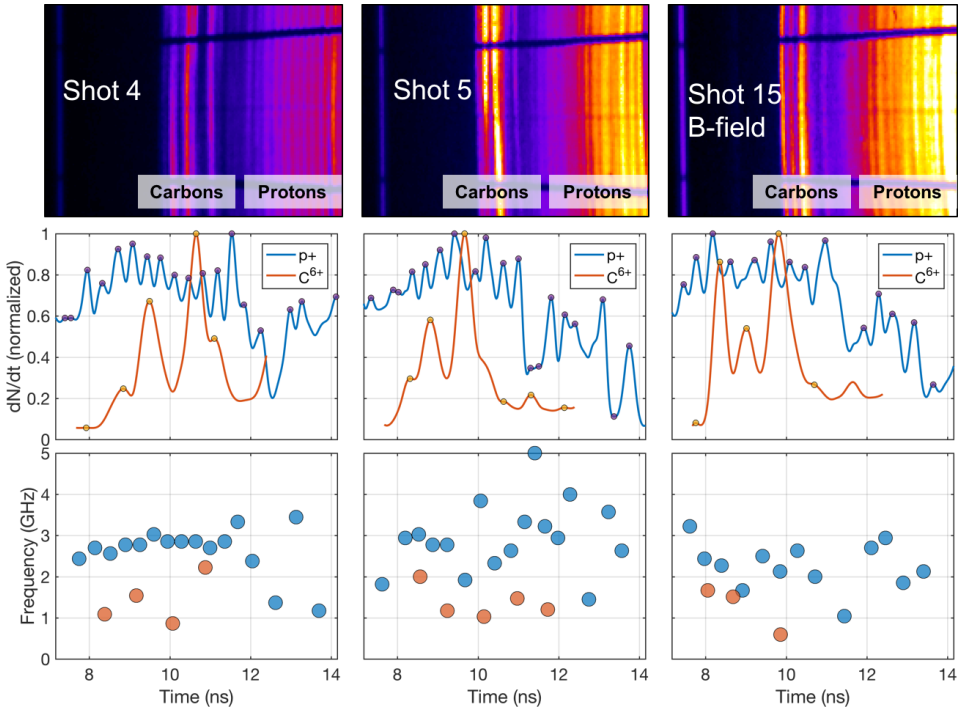


Figure A.8: Modulations are seen in the carbon spectra for ions breaking through a 100 µm Al foil. Upper row: raw IPS data. Middle row: carbon and proton signals versus arrival time. Modulations are seen in both, but the temporal duration is longer for carbon ions. Lower row: Frequency of modulations versus arrival time.

*et al.* [200], density peaks from ion acoustic waves in an expanding plasma will have a range of velocities if the wave velocity is constant and the background plasma expansion velocity varies. Such a variation occurs in the isothermal model of TNSA, where protons near the front have more energy then protons further from the front. In this case the velocity between peaks, $\Delta V$, will be proportional to the velocities of the peaks: $\Delta V \propto V$. This argument has been invoked by Séguin *et al.* to possibly explain proton radiographs of imploding capsules at OMEGA, which appear to show shells of charge [203].

## A.3 LSP Modelling

The long, narrow entrance slit of the IPS is the one of its unique aspects: it is 5 cm tall, 6.35 mm long and 50 – 100 µm wide depending on the Al spacers used. This is a key feature distinguishing the IPS and other magnetic spectrometers, such as Thomson Parabolas, which use pinholes and do not exhibit consistent spectral oscillations. From the summary of published oscillations in Section A.1 there is also evidence that spectral modulations have been observed for other slit-based instruments. Several ideas were proposed for how the slit could produce spectral modulations. It was hypothesized that the IPS slit is acting as a form of linear accelerator, producing fields in the mm to sub-mm region (microwave to terahertz frequencies) which in turn produce spatial bunching of the proton beam. Another hypothesis was that the slit is generating a resonant TE mode, in the 5 cm, vertical direction, which is somehow responsible for the modulations. These hypotheses were investigated using LSP in Section A.3.1 and Section A.3.2, respectively.

Lastly, it cannot be dismissed that a beam generation or transport effect is responsible for the spectral features. Section A.3.3 covers simulations of the TNSA proton source.

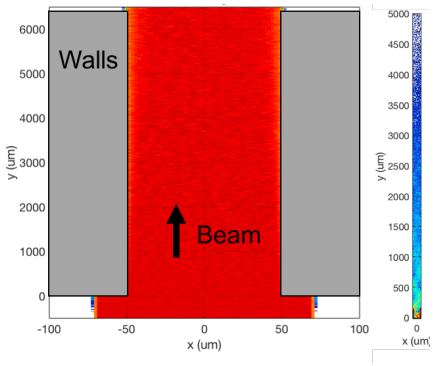


Figure A.9: Left: Setup of 2D slit simulation. Right: simulation grid to scale.

### A.3.1 2D Slit Simulations

The linear accelerator hypothesis was tested by simulating the slit in 2D, and injected a proton beam that approximates a TNSA beam into one opening. It was assumed that the 5 cm height of the slit was effectively infinite compared to the 100 µm width, and could be neglected; as will be reported in Section A.3.2 this may not be an accurate assumption. The simulations were run in both implicit and explicit modes. The setup is shown in Figure A.9.

The slit walls were simulated as pure Tungsten, ignoring the 6% Ni and 4% Cu that are present in Tungsten heavy met alloy. Two options are available for a metal region in LSP: (1) A conducting object can be defined, which will generate fields through Ohm's law and a realistic conductivity, but absorbs all particles incident on it without charging. (2) Fluid particles can be used to create a solid density, energy-conserving plasma. This setup has the advantage that it can realistically handle local charge imbalances, but it is much more costly and prone to instability issues. Both approaches were tried. The TNSA beam was modelled by injecting equal densities of proton and electrons; a constant density of $10^{11}$ cm$^{-3}$ was used, which approximates the average beam density. The typical TNSA spectrum decreases exponentially in density, but this was assumed to not be critical to the modulation phenomenon as experimentally oscillations are seen across several orders of signal levels.

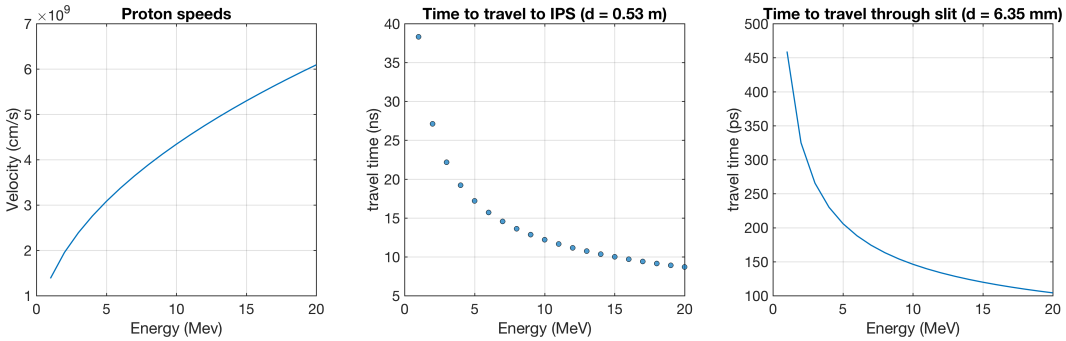


Figure A.10: Relevant timescales for a proton beam incident on the IPS. The beam is assumed to be generated instantaneously and then travel to the detector with no energy loss.

The temporal duration of the pulse is set by the emission properties of a TNSA beam and the geometry of the experimental setup. The acceleration of a TNSA protons occurs over a time period similar to the laser pulse duration [96], which for the Titan laser is 0.7-10 ps. A 20 MeV proton moves at $6.09\times10^7$ m/s and travels 0.5 m in 8.2 ns (see Figure A.10a). As this travel time is six orders of magnitude larger then the acceleration time, emission of the protons can be considered instantaneous. The exponential spread of energies for TNSA protons introduces spatial chirp through differing times of flight, with the energy range of the pulse determining the pulse duration. Figure A.10b shows the travel times for a proton beam, with 1-20 MeV protons having a pulse duration of 30 ns (20 ns for 2-20 MeV). Experimentally, oscillations are seen at higher and lower proton energies, but this energy range was selected as a representative sample for this study. The proton energies were converted to $\gamma\beta$, the input unit for the temporal momentum function in LSP, a decreasing exponential was fit to determine the temporal profile, and defined in LSP using a python script.

When properly defined, 2D simulations showed no oscillatory behaviour with either fluid particle or conducting object walls. Proton and electron densities are shown in Figure A.11a for conducting walls, and Figure A.11b for fluid particle walls. The electron beam charge was chosen to neutralize the

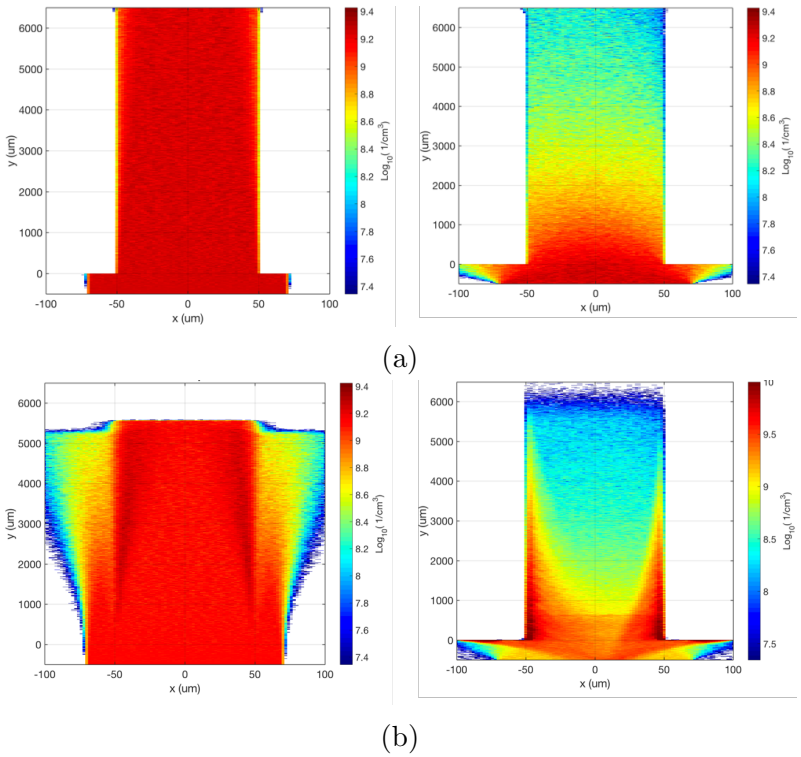


(a)

(b)

Figure A.11: Proton (left) and electron (right) beam densities. (a) Conducting walls at t = 2.86 ns. (b) Fluid particle walls at t = 0.66 ns. No external magnetic field was included in both cases.

proton beam charge, and the beams were initialized with the same velocity. It should be noted that improper simulation setups created false oscillations due to charge trapping. This occurred when a small but non-zero gap (30 µm) was included between the front or rear of the slit and the grid boundaries. Charge from the injected beam was trapped in these regions, leading to exponential, unbounded growth in fields and artificial modulations imposed upon the injected beam. This unstable behaviour disappeared when the gaps were increased to several hundred micrometers. These results do not support the linear accelerator hypothesis.

The simulations did not include secondary particle emission, which could be important factor. Ions incident at grazing angles upon stainless steel have been shown to emit 100's - 1000's of electrons/ion, depending upon the angle, energy and species of the ion [204]. This extra source of charge was not

accounted for in these simulations. LSP is capable of modelling secondary particle emission, and this is a potential area of future investigation.

### A.3.2 3D Slit Simulations

As discussed in Section A.2.2 the full 3D slit could act like a waveguide, with current from the hot electrons and TNSA beam driving transverse electric (TE) resonant modes. These physics are not present in the 2D simulations discussed above, and require a full 3D treatment to be simulated. The extension from 2D to 3D in LSP is straightforward, and the main computational difference was an increase in cell size to allow for the full-size, 5 cm vertical entrance dimension. To reduce computation time only conducting object walls were used for the 3D simulations.

Figure A.12 shows the induced electric field in the slit for an injected beam. No fields were defined on the grid or at the boundaries; this field is created by the current of the beam and the geometry of the conducting cavity. It matches well with a single frequency, resonant TE mode for a 5 cm cavity. For comparison, a second simulation was run with an artificial, TE01 (f = 3 GHz) drive model for the top and bottom boundaries, and no injected beam. The field probe results are overlaid, and have good agreement.

The field direction from this resonant TE mode is directed toward the walls of the slit, and therefore will not bunch or modify the velocity of the protons in the longitudinal direction (the direction of travel). Indeed, no bunching was observed in the protons in the 3D simulations. One hypothesis as to how such a directed field could result in spectral modulations is the multipactor effect. When the travel time between walls equal to the half the period of a TE mode, secondary electrons generated on one wall are accelerated towards the other wall, where they make more secondary electrons. This has a cascading effect that can built up charge under the right conditions [205]. The multipactor effect is illustrated in Figure A.13, and is a known vacuum

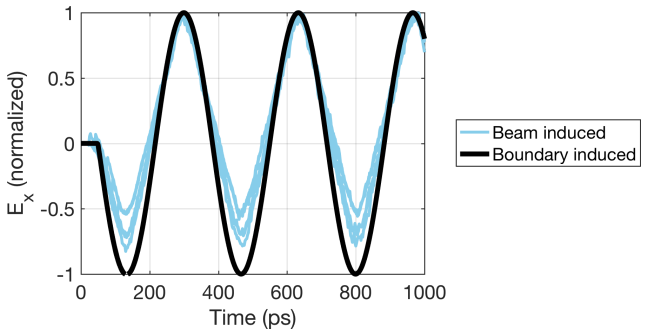


Figure A.12: Point probes showing the time history of $E_x$, the electric field directed towards the walls of the slit; for the beam induced case probes at several positions are shown. The electric fields in other directions were noise. The electron-proton beam in the cavity induces a single frequency response, $f \approx 3$ GHz, corresponding to the resonant TE01 mode in a 5 cm cavity. For comparison the fields from a TE01 mode driven by grid boundary conditions is shown (no injected beam).

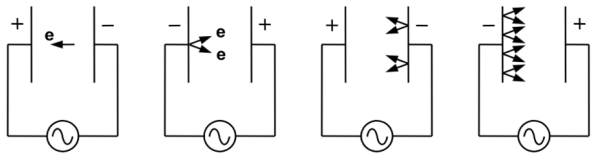

Figure A.13: The multipactor effect, where a cascade of secondary electrons occurs when the travel time between electrodes matches half the period of the AC voltage. From [36].

breakdown mechanism. As no secondary electron generation was modelled in the LSP simulations, this effect was not studied computationally. It could be explored in future work.

### A.3.3 TNSA Proton Source

If the modulations are not being introduced by the instrument then they are due to physics occurring in the TNSA beam, either during its creation or transport. In particular the acceleration phase of TNSA has the highest electron charge density and therefore could generate the strongest fields, which in turn may introduce proton density perturbations. This possibility was explored using 2D cylindrical LSP simulations. The long timescale involved with

beam transport (10's of ps) made LPI simulations impractical, and therefore an injected electron source was used. This source was the same Titan-like source used in the positron simulations (Chapter 6) with a 1 ps duration, and includes $2\omega$ electron bunches. A 50 µm thick, 2 mm diameter Au target was used to provide a typical TNSA target while minimizing front surface effects (such as laser acceleration of recirculating electrons) which are not accounted for with an injected electron source.

In order to investigate spectral and spacial modulations on the proton beam, it is important to avoid numerical effects that could cause similar results. The cells within the initial proton layer can imprint on the proton beam, as discussed in Section 4.2.1. To minimize this effect a high resolution run was performed, with 10 nm cells in a 1 µm thick proton layer (100 cells). The base grid cell size of 2 µm was smoothly decreased to this value, and increased afterwards. The proton density was $n = 10^{20}$ cm$^{-3}$. Due to computational issues this simulation was only run to 9 ps. In order to allow the beam to evolve further, a lower resolution run was performed. This simulation had cell sizes of 0.25 µm in the proton layer (4 cells), and was run to 37 ps.

The high and low resolution cases were compared to see if numerical effects were influencing the proton spectrum. The evolution of the TNSA beam was tracked using the maximum proton energy, which is expected to asymptotically reach a constant value once the acceleration phase is over. From Figure A.14a it can be seen that a large part of the acceleration occurs over the first ∼3 ps, but a further increase in energy of ∼50% occurs over the next 30 ps. After 33 ps the most energetic protons start leaving the rear of the grid, causing the maximum proton energy to decrease. The low resolution case tracks the high resolution case closely to the end of the latter's runtime, at 9 ps. Figure A.14b displays the proton spectra for the two cases at two different times, with the spectra taken from all the particles on the grid. The spectra at 9 ps are shown for both low and high resolution cases, and give identical results. Along with

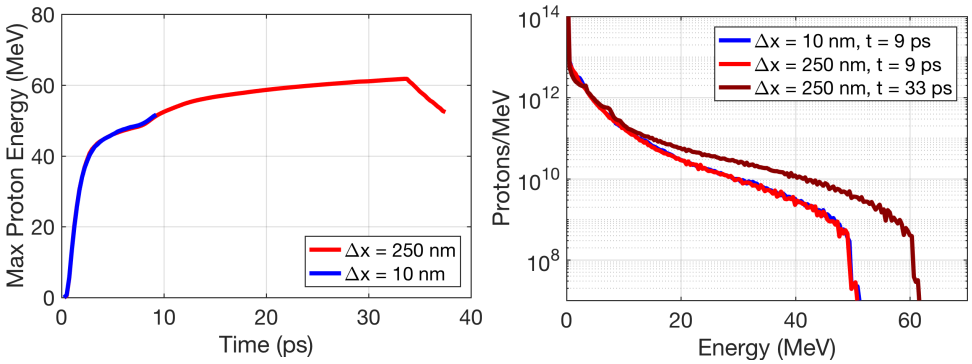


(a) (b)

Figure A.14: (a) Maximum proton energy (anywhere on the grid) vs. time. A large part of the acceleration occurs over the first ∼3 ps, although a significant fraction (∼50%) occurs over the next 30 ps. (b) TNSA beam at late times. The proton spectrum and density do not show modulations.

the matching maximum energy evolutions, this gives some confidence in the accuracy of the low resolution case, and motivates looking at the proton beam at late time. The third spectrum is at t = 33 ps for the low resolution run. No significant spectral modulations are seen. This late time observation (t = $30\tau_{\text{laser}}$) suggests that the IPS oscillations do not originate near the target, in the acceleration phase of TNSA.

Perhaps the most significant phenomenon missing in these simulations is the EMP generated by the neutralization current to the target, which causes the target assembly to act like a quarter-wavelength dipole antenna [206]. The target in LSP is freestanding, and therefore cannot create EMP in this way. The Debye length of electrons with $T_e = 10$ keV and $n = 1 \times 10^{20}$ cm$^{-3}$ is ∼2 cm, which is on the order of the TNSA beam itself; it is therefore expected that an external electric field would not be shielded out of the TNSA plasma. Further investigation is needed to determine what effect, if any, EMP has on the TNSA beam during transport.

# Appendix B

# Shock Frames

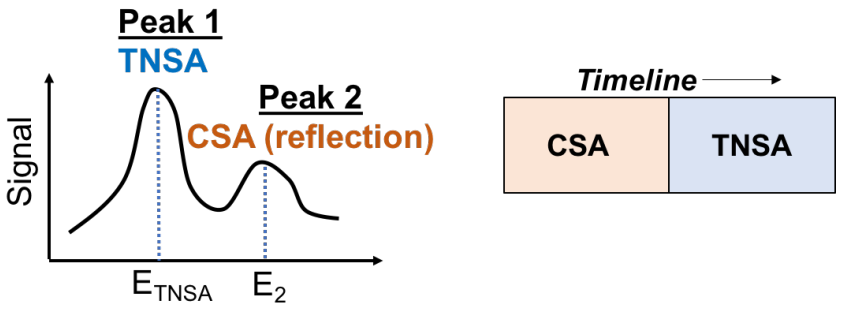


Figure B.1: Case 1 – Peak 1 is from TNSA, peak 2 is from CSA reflection. CSA and TNSA are two distinct phases with CSA occurring first, then TNSA. TNSA field is assumed to be constant in time.

**Lab Frame**

Same as upstream frame ($v_{\text{exp}} = v_{\text{TNSA}} = 0$ during shock acceleration).

| | | |
|---|---|---|
| Shock | $v_{\text{shock}}$ | $= MC_s$ |
| Peak 1 (TNSA) | $E_1$ | $= E_{\text{TNSA}}$ |
| | | $\rightarrow v_1 = v_{\text{TNSA}}$ |
| Peak 2 (CSA, reflection) | $E_2$ | $= E_{\text{reflection}} + E_{\text{TNSA}}$ |
| | | $\rightarrow v_2^2 = v_{\text{reflection}}^2 + v_{\text{TNSA}}^2$ |
| | | $\rightarrow v_2^2 = (2MC_s)^2 + v_1^2$ |

Table B.1: Case 1 – Shock velocity relationship.

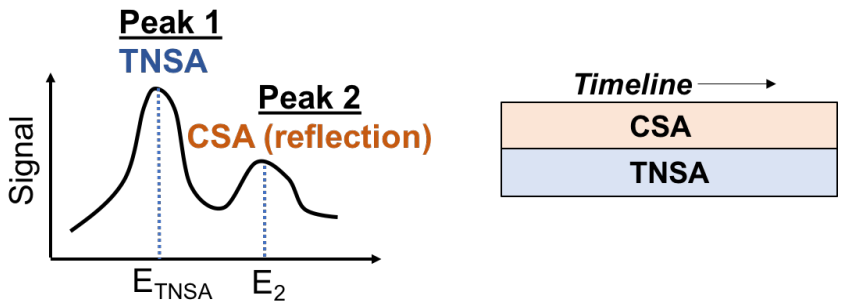


Figure B.2: Case 2 – Peak 1 is from TNSA, peak 2 is from CSA reflection. CSA occurs concurrently with TNSA expansion.

| **Lab Frame** | | | **Upstream Frame [*]** (moving at $v_{\text{TNSA}} = v_1$) | |
|---|---|---|---|---|
| Shock | $v_{\text{shock}}$ | | Shock | $v^*_{\text{shock}} = v_{\text{shock}} - v_1$ |
| Peak 1 (TNSA) | $E_1$ | $= E_{\text{TNSA}}$ | | $\rightarrow v_{\text{shock}} = v^*_{\text{shock}} + v_1$ |
| | | $\rightarrow v_1 = v_{\text{TNSA}}$ | | |
| Peak 2 (CSA, reflection) | $v_2$ | $= 2v_{\text{shock}} - v_{\text{TNSA}}$ | Peak 1 | $v^*_1 = 0$ |
| | | $= 2v_{\text{shock}} - v_1$ | Peak 2 | $v^*_2 = 2v_{\text{shock}} - 2v_1$ |
| | | | | $v^*_2 = 2v^*_{\text{shock}}$ |
| Substituting in $v^*_{\text{shock}}$ from the upstream frame to get Mach number $M$: | | | Mach # | $v^*_{\text{shock}} = MC_s$ |
| $v_2 = 2v_{\text{shock}} - v_1$ | | | | $\rightarrow M = \frac{v^*_{\text{shock}}}{C_s}$ |
| $= 2v^*_{\text{shock}} + v_1$ | | | | $\rightarrow M = \frac{v_{\text{shock}} - v_1}{C_s}$ |
| $= 2MC_s + v_1$ | | | | |

Table B.2: Case 2 – Shock velocity relationship.

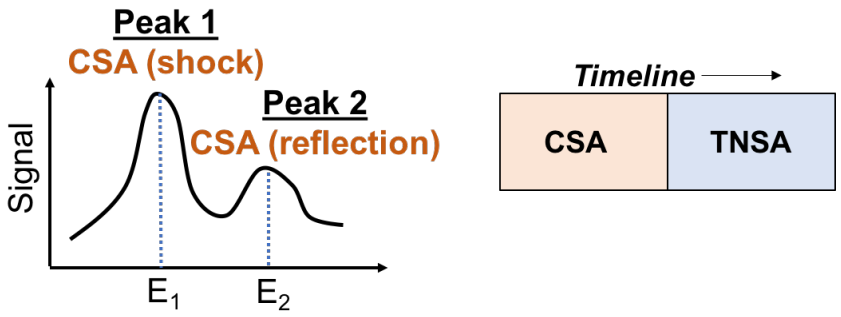


Figure B.3: Case 3 – Peak 1 is from CSA shock, peak 2 is from CSA reflection. CSA and TNSA are two distinct phases with CSA occurring first, then TNSA. TNSA field is assumed to be constant in time.

**Lab Frame**

Same as upstream frame ($v_{\text{exp}} = 0$ during shock acceleration).

| | | |
|---|---|---|
| Shock | $v_{\text{shock}}$ | $= MC_s$ |
| TNSA | $v_{\text{TNSA}}$ | $\approx C_s$ |
| Peak 1 (shock) | $v_1^2$ | $= v_{\text{shock}}^2 + v_{\text{TNSA}}^2$ |
| | | $= (MC_s)^2 + C_s^2$ |
| Peak 2 (reflection) | $v_2^2$ | $= v_{\text{reflected}}^2 + v_{\text{exp}}^2$ |
| | | $= (2MC_s)^2 + C_s^2$ |
| | | $= (4M^2 + 1)C_s^2$ |
| | | $= \left(4\left(\frac{v_1^2}{C_s^2} - 1\right) + 1\right) C_s^2$ |
| | | $= 4v_1^2 - 3C_s^2$ |

Table B.3: Case 3 – Peak 1 is from CSA, shock. CSA and TNSA are two distinct phases with CSA occurring first, then TNSA.

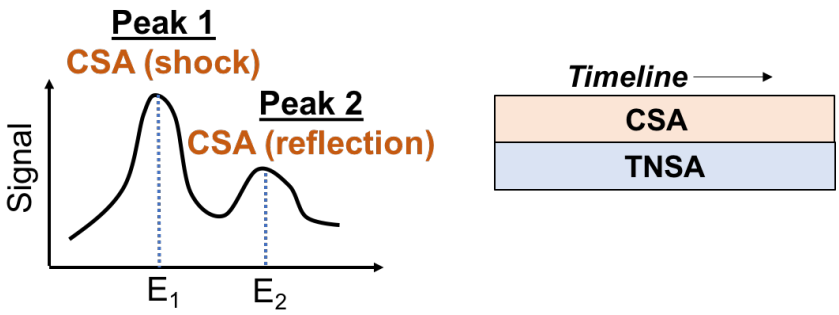


Figure B.4: Case 4 – Peak 1 is from CSA shock, peak 2 is from CSA reflection. CSA occurs concurrently with TNSA expansion.

**Lab Frame**

| | | |
|---|---|---|
| TNSA | $v_{\text{exp}}$ | |
| Peak 1 (shock) | $v_1$ | $= v_{\text{shock}}$ |
| Peak 2 (reflection) | $v_2$ | $= 2v_{\text{shock}} - v_{\text{exp}}$ |

Substituting Mach # from the upstream frame:

$$\begin{aligned} v_2 &= 2v_1 - v_{\text{exp}} \\ &= 2v^*_{\text{shock}} + v_{\text{exp}} \\ &= 2MC_s + v_1 - MC_s \\ &= MC_s + v_1 \end{aligned}$$

**Upstream Frame [*]**
(moving at $v_{\text{TNSA}}$)

| | |
|---|---|
| Peak 1 | $v^*_{\text{shock}} = v_1 - v_{\text{exp}}$ |
| | $\rightarrow v_1 = v^*_{\text{shock}} + v_{\text{exp}}$ |
| Peak 2 | $v^*_2 = 2v_1 - 2v_{\text{exp}}$ |
| | $v^*_2 = 2v^*_{\text{shock}}$ |
| Mach # | $v^*_{\text{shock}} = MC_s$ |
| | $\rightarrow M = \dfrac{v^*_{\text{shock}}}{C_s}$ |
| | $\rightarrow M = \dfrac{v_1 - v_{\text{exp}}}{C_s}$ |
| | $\rightarrow v_{\text{exp}} = v_1 - MC_s$ |

Table B.4: Case 4 – Shock velocity relationships.

# Appendix C
# Code & Analysis Tools

## C.1 Code on Github

Scripts generated in the course of my thesis that may be of interest to others in the field are listed below. They are hosted on a publicly available Github repository:

https://github.com/Nuahaun/ThesisCode

**SRIM files**

1. LoadSRIMFile.m - Loads particle properties from SRIM input and output files.
2. SaveTRIMFile.m - Writes a TRIM input file for a particle distribution with given energies, positions and directions.
3. Alfilters_GenerateParticleDistribution.m - Generates a particle distribution, which is saved by SaveTRIMFile.m.

**Laser beam spot analysis**

1. Beam Analysis GUI - A tool for determining beam spot size and energy distribution. All functions in the folder are necessary for the tool to run.
2. BeamSpotFunction.m - The analysis function which is called by the analysis GUI. It can be run separately and modified for use.

**Image plates ion response**

1. psl2protons.m - Converts from PSL to protons using published image plate response curves in Mancic *et al.* [17] or Bonnet *et al.* [18].

2. psl2carbons.m - Converts from PSL to carbon ions using published image plate response curves from Doria *et al.* [19].

3. ProtonIPFading - Compensates for PSL decay with scan time for image plates. Uses the proton formula from Bonnet *et al.* [18].

4. IonFilterCompensation - Corrects for energy loss of protons or carbon ions travelling through an aluminum filter onto an image plate.

## C.2 YAMP

YAMP is a graphical user interface (GUI) I built in Matlab to allow easier visualization and analysis of LSP simulations. The GUI is shown in Figure C.1. It provides real-time visualization of 1D, 2D and 3D LSP data, with easy switching between time steps, species and data types. Scalar, field and particle files can be plotted, as well as history and extraction plane data. Phase space plots can be generated from particle files, and subsets of particles easily selected based on user parameters. YAMP has been used by students and scientists at the University of Alberta, LLNL and UCSD.

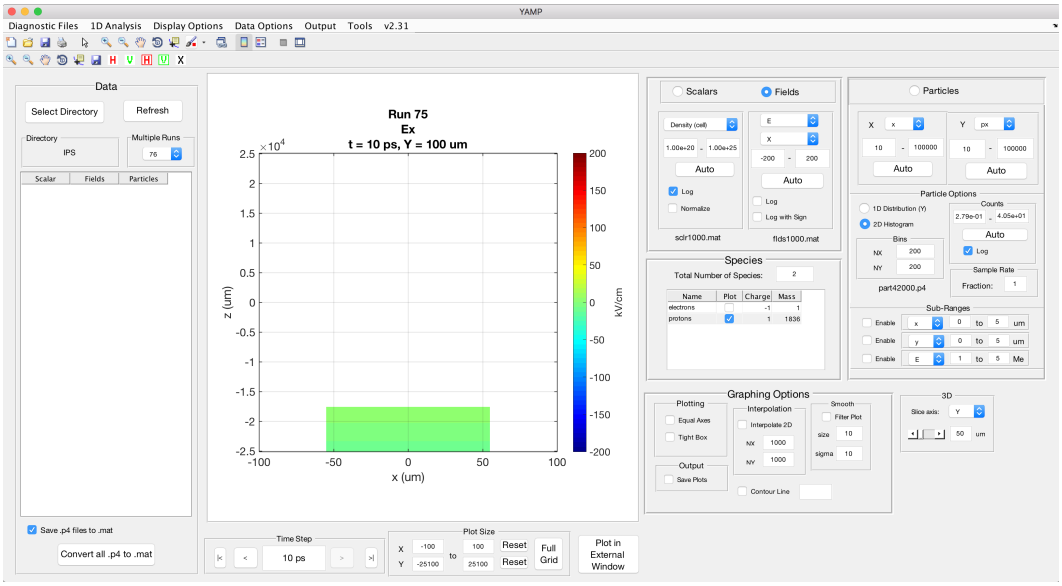


Figure C.1: YAMP (Yet Another Matlab Plotter), the visualization tool build to facilitate LSP visualization and analysis. A sample screenshot is shown here.

# Appendix D
# Other Research Contributions

Extensive experimental work was conducted over the course of this degree, in collaboration with numerous researchers, and this appendix outlines the publications that have subsequently been produced. Work not included in the main body of the thesis is also reported below.

The positron computational study in Chapter 6 is being prepared for publication. The shock acceleration study in Chapter 7 has been submitted for publication and is under review [207].

The transport of relativistic electron beam in matter was studied, in a collaboration led by researchers at the University of Bordeaux, with several publications resulting [208, 209]. The author fielded a Kirkpatrick-Baez (KB) x-ray microscope [210] at both the Titan laser and the LULI2000 facility at the École Polytechnique, France.

A large number of experiments were conducted at the Titan laser to study the physics of positron generation from ultra-intense LPI, which produced publications on positron scaling with target material [170], scaling with laser parameters [23, 72] and beam emittance [211]. The author contributed in all aspects of the experimental work.

The author contributed to an experiment at the Advanced Laser Light Source (ALLS) facility in Montreal, in which betatron x-rays from wakefield electron bunches were used to probe ionization states [212].

The acceleration of particles from a cryogenic hydrogen jet [188] was studied [56], as well as time-resolved x-ray information from relativistic electrons [213]. The author also aided with the diagnostic development of multilayer x-ray optics [214] and an x-ray crystal spectrometer [215].